Studies on Functionalization of Poly(lactic acid) for Textile Applications

Thesis submitted in partial fulfillment of the requirements for the degree of

DOCTOR OF PHILOSOPHY

Submitted by

DOLI HAZARIKA

Roll No. – 176107021

Department of Chemical Engineering

Indian Institute of Technology Guwahati,

Guwahati– 781039, Assam, India

This Thesis
is dedicated
to my beloved parents
Who has been my source of inspiration
strength, Who continuely provide their moral,
emotional, and financial support.

Department of Chemical Engineering

Indian Institute of Technology-Guwahati

CERTIFICATE

This is to certify that the thesis entitled "**Studies on Functionalization of Poly(lactic acid) for Textile Applications**", being submitted by **Doli Hazarika** for the award of Ph.D. The degree has been carried out by her at the Chemical Engineering Department, Indian Institute of Technology Guwahati, under our guidance and supervision. The work documented in this thesis has not been submitted to any other University or Institute for the award of any degree or diploma.

Prof. Vimal Katiyar
Professor
Department of Chemical Engineering
Indian Institute of Technology
Guwahati - 781039, India.

Dr. Amit Kumar
Associate Professor
Department of Chemical Engineering
Indian Institute of Technology
Guwahati - 781039, India.

Thesis Acknowledgment

Foremost, I would like to express my sincere gratitude to my supervisors **Prof. Vimal Katiyar** and **Dr. Amit Kumar** for their continuous support during my Ph.D. study and research, along with their patience, motivation, enthusiasm, and immense knowledge. Their guidance has helped me be confident in doing my work independently and precisely during my Ph.D. duration to complete my work within the stipulated time. It was a great privilege to work under them as I could not have imagined having such a better advisor and mentor for my Ph.D. study.

Besides my supervisor, I would also like to thank the rest of my doctoral committee members; **Prof. G. Pugazhenthi** (Department of Chemical Engineering)**, Prof. Parameswar Krishnan Iyer** (Department of Chemistry), and **Prof. A. S. Achalkumar** (Department of Chemistry)**,** for their insightful comments, brilliant suggestions, questions and encouragement during the Ph.D. course.

I am also extending my heartful gratitude to **Center of Excellence for Sustainable Polymers (CoE-SuSPol),** Department of Chemical Engineering, Analytical Lab, and **Central Instruments Facility (CIF), IIT Guwahati,** for the availability of all the facilities of the sophisticated instruments. I would also sincerely thanks to the Department of Science and Technology (DST) Govt. of India, for the necessary grants provided for smooth running of the current research work. Even, I would also like to thank the head and all the authorities for letting me utilize all the required facilities during my research work. I am extremely thankful to the technical staff (teaching and non-teaching) of the chemical engineering department, particularly Mr. Harsaraj Biswanath, Mr. Pankaj Kumar, Mr. Debojit, Ms. Ritumoni Kalita, Mr. Jayanta Kumar, Mr. Lukumoni, Mr. Prasun, and non-technical staff like Mr. Shoilen, Mr. Deep and Mr. Bhagya for their kind cooperation during the Ph.D. course. I would also like to thank a few CIF operators

particularly, Mr. Bhaskar, and Mr. Milan for their immense help in analyzing all the morphological analyses. I am also fortunate to have friends in the lab as well as in the hostel. I am very much thankful to all my co-research fellows, especially my seniors like Dr. Gourhari Chakraborty, Dr. Arvind Gupta, Dr. Narendren S., Dr. Siddhartha Mohan Bhasney, Dr. Neha Mulchandani, Dr. Rahul Patwa, Dr. Tabli Ghosh, Dr. Monika, Dr. Shasanka Sekhar Borkotoky, Dr. Surendra Singh Gaur, Dr. Kiron Kumar Gali for all kinds of help and morale support made available to me in the lab as seniors when I require any help or suggestions. I would like to thank fellow labmates Kona Mandal, Durlov Pait, Bhanupriy Das, Pankaj Baruah, Chethana Mudenur, Munmi Das, Devleena Bose, Md. Modu Aji for helping a lot when required and making my stay at IIT Guwahati cheerful and memorable.

The selflessness and countless sacrifices made by my wonderful parents made it possible for me to reach this stage in my life. I would like to thank my dear husband Dr. Naba Kumar Kalita for being the pillar of support and positive energy in my life. Finally, I would like to thank the almighty God, for letting me overcome all the difficulties to move forward.

Abstract

The idea of a sustainable environment has led to a path to reduce utilization of fossil fuel-based petroleum products. Enough evidence shows that synthetic fibers, and other plastics do not degrade fully in waste water treatment plants, landfills, and the environment. Sustainable polymers have facile degradation pathways and, in many cases, can be obtained from renewable resources, making them promising alternatives to conventional plastics. Poly(lactic acid),(PLA) is one of the most widely studied sustainable polymers that possess several properties that are comparable to conventional polymers. The present work is a systematic, descriptive study of PLA-based composites in the field of textiles. The reinforcement phase of textile materials developed in this work consists of hybrid materials with modified structure and shape such that resulting products are non-toxic, ecological, and biodegradable. Material selection while designing sustainable products also plays an important role in the engineering field. The hybrid materials are a combination of two materials (organic and inorganic) that can offer benefits to conventional textiles with functional characteristics in order to develop smart textiles for waste water treatment as well as healthcare applications. The combination of organic and inorganic parts deals with both strong (covalent, ionic covalent bond) and weaker (hydrogen, electrostatic, and van der Waals force) interactions. Nanotechnology in textile design is currently based on electrospun polymeric nanofabric to obtain functional properties like high hydrophobicity, high hydrophilicity, self-cleaning ability, dye degradability, shrinkage free characteristic, shimmer, antibacterial, and antiviral properties. The smart components are added to the substrate during fiber spinning, fabric formation level, or during finishing level. PLA functionalization has been carried out by in situ incorporation of nanohybrid fillers during polymerization followed by electrospinning to obtain the multifunctional properties for application in waste water

treatment for a sustainable environment. The thesis also discusses the functionalization finishing approach by obtaining a polymer-hybrid composite solution where electrospun fabric is impregnated into this solution for application in the the healthcare sector. The choice of a hybrid solution will lead to a shimmery nanofinish layer over electrospun PLA nanofabric to tune the properties. Further, for PLA nanofabric, as the big challenge is to achieve dyeing, stability, and superhdrophilicity, the introduction of stereocomplexity on subsequent annealing can be a novel approach using nano-metal oxide to overcome such problems. The modification of crystallization behaviour of highly hydrophobic PLA nanofabric by the incorporation of nanohybrid fillers into the electrospun solution has also been investigated in this work. The presence of biopolymer nanocrystals with metal oxide acting as nucleating agent results in the change in crystallization behaviour.

Another fact lies on proper disposal of PLA under specific environmental conditions is important along with its high-cost production during monomer formation. In this thesis, we report another pathway for degradation of PLA using a hybrid catalyst that can reduce the environmental disposal as well as energy and material input during their production. Here, we have demonstrated the capability of the hybrid catalyst for the production and degradation of PLA.

Keywords: PLA; Stereocomplex PLA; electrospun nanofabric; Smart textile; Chemical degradation.

Table of Contents

List of Figures

List of Tables

Abbreviations

LA	**Lactide**
PLA	**Poly(lactic Acid)**
sc PLA	**Stereocomplex Poly(lactic Acid)**
STPP	**Sodium Tripoly Phosphate**
WCA	**Water Contact Angle**
GPC	**Gel Permeation Chromatography**
MWD	**Molecular Weight Distribution**
FTIR	**Fourier Transform Infrared Spectroscopy**
NMR	**Nuclear Magnetic Resonance**
DSC	**Differential Scanning Calorimetry**
TGA	**Thermogravimetric Analysis**
UV	**Ultraviolet**
XRD	**X-Ray Powder Diffraction**
FESEM	**Field Emission Scanning Electron Microscope**
FETEM	**Transmission Electron Microscopy**
POM	**Polarized Optical Microscope**
PCL	**Poly(ε-caprolactone)**
ZL	**Zinc olio lactate**
nCS	**Nanochitosan**
PP	**Polypropylene**
SNC	**Silk Nanocrystal**
ZnO	**Zinc oxide**
TiO_2	**Titanium dioxide**

Notations

Mn	**Number Average molecular weight**
Mw	**Weight Average molecular weight**
Da	**Dalton**
T_g	**Glass transition temperature**
T_m	**Melting Temperature**
TCC	**Cold crystallization temperature**
ΔH_m	**Enthalpy of Melting**
ΔH_{cc}	**Enthalpy of Crystallization**
X_t	**Relative Crystallinity**
R^2	**Regression Coefficient**
$t_{0.5}$	**Crystallization Half Time**

CHAPTER 1

INTRODUCTION AND LITERATURE REVIEW

Abstract: This chapter focuses on human's demanding nature along with comfort and fashion, which made researchers oriented towards flourishing functional textile products. They are now trying to introduce extraordinary functional properties like dye removal, UV resistance, shrinkage-free, shimmery, antimicrobial properties, antiviral and self-cleaning properties that are different from conventional textiles. Most of the manmade fibers used in the textile industry are petroleum-based which are depleting the natural resources and destructing the ecological balance at a constant rate. In this regard, utilizing sustainable polymers for smart textiles would serve as a promising candidate thereby solving the problem of discarded textiles. The current chapter, therefore, aims at providing insights into the utilization of biodegradable polymers in smart textiles. But alone the polymer cannot fulfill the required functional properties. Thereby, this chapter includes an introduction of preferable and desirable addition of new materials, and approach like stereocomplexation. Also, attention to fabricate functional scPLAfibers is possible by incorporating various bio nanofillers which will be discussed in this chapter. Eventually, the application of such smart textiles is also concerned towards the safety of human beings which will be very useful for academics and for the industries to cope up with the new concept of smart fabrics using biodegradable polymer.

Publications: Hazarika, D., Kumar, A., & Katiyar, V. (2020). Mimicking Smart Textile by Fabricating Stereocomplex Poly (Lactic Acid) Nanocomposite Fibers.In *Advances in Sustainable Polymers* (pp. 341-362).Springer, Singapore

1.1 Introduction

Fibers are the main foundation in textile industry which was spun into yarns or fabrics to obtain textile products. The textile fibers are classified as natural fibers (asbestos, cotton, silk, wool, etc.) and manmade fibers (Polyesters, rayon, nylon, acrylic, etc.). Such fibers have various applications in the fields like geo textiles, industrial fabrics (floor mats, seat fabrics, and seat cushions), wipes, clothing, and home furnishing. The natural fibers, which are made of cellulose and proteins, have a porous structure, which invites appropriate conditions for the growth of bacteria and microbes, retaining moisture and in turn leading to the deterioration of textiles. The excessive moisture absorbability weakens materials made from natural fibers (a decreased adhesion), and at the same time, it favors the growth of microorganisms (fungi, molds, bacteria). Non-wettable textiles with a high WCA, particularly the superhydrophobic ones (i.e., those with WCA >150°), are a contemporary research topic [1]. Enormous attention has been made to use the synthetic antibacterial agents like nitro compounds, dyes, oxidizing agents, metal-based, and halogen compounds. Moreover, in the textile industry service of laundry is consuming enough electricity as well as contaminates water resources [2]. The cultivation of natural fibers requires excessive water, land, pesticides, and fertilizers also synthetic fibers like nylon, polyester is non-renewable and toxicity is obtained from polymers[3]. Polymers are derived from fossil fuels, like crude oil and natural gas which are also well known as petrochemical-based polymers. They are obtained from cheap feedstock, possess low specific density, are usually light in weight, and are easily processed to obtain the desired complicated products to make them advantageous over other materials like metals ceramics. But excessive use of petro-based products in industries and for domestic purposes has increased their trend of demand everywhere[4]. Petrochemical-based polymers have advantageous characteristics like high strength,

good oxygen barrier properties, high heat sealability, low production cost over the alternatives, which shows them the path towards usage in most of the industries. On the other hand, the disadvantages of petroleum-based polymers such as the decline in gas oil resources, migration of toxic material while using them for packaging applications, environmental pollution regarding their degradation, inflation of prices altogether prohibit them from their uses in different fields. Such issues have made technologies deal with their recycling so that the problem is fixed but their recycling rates remain low [5]. Green economy together with sustainable development is the only solution in solving the problem of using fossil-based resources. Bioplastics or biopolymers obtained from plants, animals, and microorganisms, became more popular not only because they are environment friendly but also due to their strategic nature. Release of toxic and greenhouse gases e.g. CO_2, is in the way of reduction by use of proper agriculture-based products like cellulose, starch, wood, etc., for polymer production which confirms the good impact of bioplastics on nature alongwith less energy consumption while producing [4].

For centuries human has been using manmade fibers to make yarn and wool into textile by using handmade processes. Now in the 20^{th}century, polyester fibre with its low capacity production has contributed to a rapid share of production in the market. Today almost in every sector of the textile industry, the idea of the potential use of nanotechnology is a growing interest. Starting from the fabrication of nanofibers using different spinning techniques to the fabrication of fiber composites using various nanomaterials is now a booming topic for technologists. The conventional fibers used in the textile industry that people have been conventionally using are facing the problem of long-lasting, bacterial, and microbial attacks even using chemicals or detergents for removing stains which is harmful to marine animals[6]. Owing to solve such serious problems and keeping in mind

the demand for getting extraordinary functionalities into the textile industries, researchers have started thinking of impregnating nanoparticles into the fibers to obtain a functional composite fiber.

1.2 Bioplastics/ Bio based biodegradable plastics-

Currently, the total production of plastics in the whole world has been significantly marked up by the use of bioplastics. The major disposing problem owing to the use of petroleum-based plastics is that they are not biodegradable as they are produced by chemical extraction.

The bio-based plastics are differentiated accordingly -

- Biopolymers are kinds of polymers that are occurred in nature using biological actions like starch, cellulose, natural rubbers, proteins, and poly (hydroxyalkanoates).
- Bio-based polymers are polymers that are based on the polymerization of monomers that are biomass-derived like Poly (lactic acid).

Thereby plastics can be termed as bioplastics if they are either biobased, biodegradable, or consist of both properties having a biological source whether completely or significantly. They can be biodegradable or non-biodegradable depending on different standards where biodegradability, disintegrate and compostability conditions need to be followed. Consequently, bioplastics can also be recycled or reutilized to avoid plastic pollution [7].

Bio compostable plastics/polymers are degraded by biological means during composting conditions to yield CO_2, H_2O, inorganic compounds, and biomass at a consistent rate without leaving distinguishable or hazardous residues [4, 8]. The classification of bioplastics is shown in **Figure 1.**

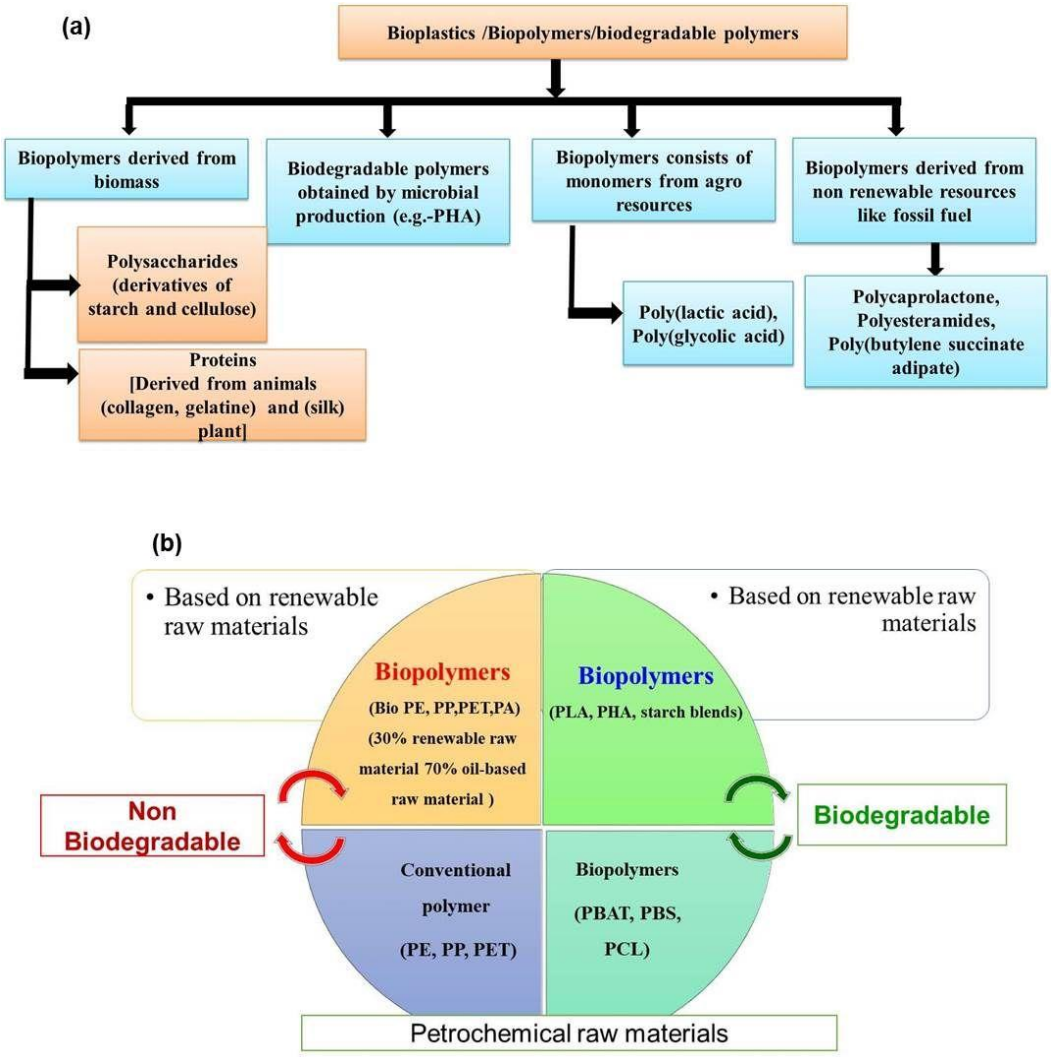

Figure 1: (a) Flowchart of different kinds of bioplastics, and (b) differentiation between bioplastics and Petroleum-based bioplastics.

1.2.1 Global production of Bioplastics

Environment-friendly products demand is increasing in the market as shown in **Figure 2.** The global bioplastics market was estimated at 3,123.24 kilo tons by 2021 and expected to grow to a CAGR of 26.03 %, during the period (2021- 2023). The presence of a large amount of feedstock causes the highest production of bioplastics in Asia-Pacific.The global production capacity of bioplastics reported by the European Bioplastics Association is 2.11 million tons in 2020, due to the growing demands from countries, like

China, India, South Korea, and Japan. Concerning the pros and cons that though bioplastics are the remedies for solving global problems but biodegradability is also an important agenda that is to be followed. Out of the various bioplastics Poly(lactic acid) is more advantageous because of its natural feedstock and biodegradable and compostable nature. The global market value of poly(lactic acid) (PLA) was USD 698.27 million, by revenue, in 2021, and estimated to reach USD 2,091.29 million by 2023, at an estimated CAGR of 20.06%[9, 10].

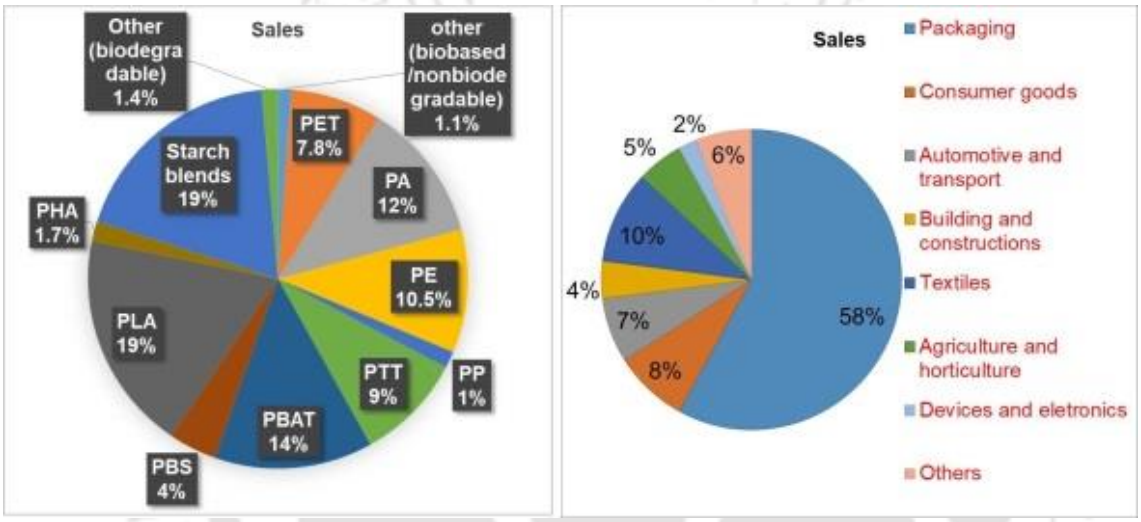

Figure 2: Bioplastic market in 2020 as per European bioplastics data, global production capacities of bioplastics for various applications by 2022.

1.3 Smart Textile

The textile industry has given the global world a shield from cold and rain which is the main function of original textile. But recently, adapting to the environment a new discipline of interactive textile has been risen in the textile sector. A new generation of textile has been discovered which has the potential to provide us comfort at all times together with proper protection by warning us against any danger. Such materials are termed as smart or functional textiles which are like ordinary clothes but they provide special extraordinary functionalities for the desired application. Therefore the smart textiles are defined as textiles which are having the potential to react or sense the stimuli

(mechanical, chemical, electrical, optical, biological, or other sources) created by the environment in a predetermined way as shown in **Figure 3**.

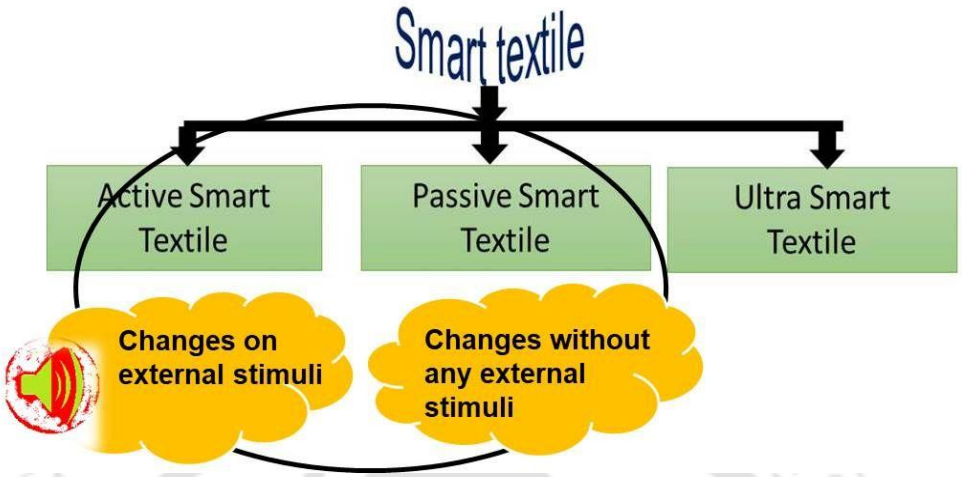

Figure 3: Smart features of smart textile.

1.3.1 Types of smart textiles in terms of different functionalities

Active smart textiles: These are the 2nd generation of smart textiles which include actuators and sensors. These materials include new functionalities such as shape memory effect, chameleonic effect, water-resistant ability, hydrophilic/ nonporous vapor permeability, heat storage, thermo regulation, vapor absorption and heat evolving fabrics and suits have electrically heated features.

Passive smart textiles: These are the 1st generation of smart textiles particularly providing various features in passive mode with the environment. For example, if considered a highly insulating coat it would adapt to the outside temperature and remain insulating. Anti-microbial, anti-odor, anti-static, bullet-proofs are included in this category.

Ultra smart textiles: These are the 3rd generation of smart textiles which work like a brain with capacities of reasoning and activating features. They mainly involve multidisciplinary properties such as sensing, actuation, advanced processing, provide help

in communication, act as artificial intelligence for mimicking human behavior. The conductive yarns and fibers which are different in their functionalities than the natural fibers are obtained from using conducting materials into the fibers.

1.3.2 Applications of smart textiles

The smart components form an integrated part when incorporated into the textile structure by behaving smartly. Those are added into the substrate which may include fiber spinning, fabric formation level, or during finishing level. In terms of health, these smart fabrics act like strain fabric sensors, sensitized garments to measure heart rhythm and respiration, life belt for pregnant women to analyze vital signs at any time. Smart fabrics may be used in defense applications as they can increase protection by alertness from environmental hazards. Moreover, in the fashion and entertainment world for giving dazzling effect, invisible coatings and advanced fibers have been developed to get dramatic change in the textile appearance. Another important area is for the athletes or sportsmen where monitoring of heart beat, steps count, breathing, and body temperature reading are important parameters for the development of smart clothing [11].

1.4 Nanotechnology

Nanotechnology has come up with an idea for researchers to assist as an environment benefiter. Nanomaterial has immense surface properties considering high surface to volume ratio which has marked them very much different from the bulky additives and materials. The relevant contribution of nanotechnology has potential applications in different sectors like packaging, textile (apparel, commodity as well as medical treatments), etc. [12]. They are classified into two classes namely organic and inorganic nanoparticle

1.4.1 Organic nanoparticle

Organic particles are solid particles that are mostly derived from natural resources. They have more reinforcing ability than inorganic fillers. They are abundantly found in nature, have low density, have higher mechanical properties, and are also biodegradable.

1.4.1.1 Polysaccharides

Chitosan: Chitosan is the second most available linear polysaccharide after cellulose which is produced by the deacetylation of chitin. It is a composition of glucosamine and N-acetyl glucosamine units having a linkage of 1–4 glucosidic bonds. They are insoluble in water, alkali, and acid systems but soluble in organic acid, acetic acid, lactic acid, and formic acid[13]. Chitosan possesses unique properties like biocompatible, non-toxic, antifungal activity, and antibacterial properties which makes it an attractive choice for the functional modification of textiles. Chitosan nanoparticles are produced by the ionic gelation of chitosan with sodium triphosphate (STPP), where STPP polyanions (negative)interact with amine groups of chitosan [14]. In the textile industry, green bioactive nano-chitosan has been a new concept and is gaining importance. Chitosan nanoparticles have also been known to be made by polymerization of methacrylic acid (MAA) using $K_2S_2O_8$ as initiator followed by centrifugation [15].

1.4.1.2 Proteins

Silk: Silk is the most precious fiber given to us by nature over the past few decades which has had an enormous impact on the textile industry. Silk fiber structure possesses tenacity with a range from 3.5 – 5.0 g/d when in dry condition and may lose up to 20 percent of its strength under wet conditions. Silk has no elastic behavior when it is stretched to a certain amount and it never regains to its original position. Considering the current preferences along with the increase in demand for natural fibers, silk has made a well-known platform in the textile industry due to the optimum properties in terms of human comfort and wear

ability because of its eco-friendly nature. Silk is the family of *Lepidoptera and Araeneaein* with a continuous form of spun filaments having the structure of the orthorhombic unit cell and high packing density[16]. Silk is obtained from varieties of insects like silkworms and spiders. The spider silk has the fibroins on inside and a protective coating of sericin with gum-like properties, wild silk-like tassar, eri and muga silk which is the outer cover of silk cocoon. But the amorphous region application i.e. sericin layer should be removed to obtain only the crystalline region i.e. fibroin by chemical treatment (degumming process). The process continues firstly from silk to microfibrils and secondly from microfibrils to nanofibrils under proper conditions. Fibroin is a component of silk fiber with repetitive and ordered structural units termed as β-sheets. The fibroin part gives strength thereby imparting antibacterial, UV resistant, moisture regulating properties which contributes to the textile industry. Acid hydrolysis is the proper treatment that has been used by many researchers to fabricate silk nanocrystals from wild silk [17, 18]. The sequential units in silk fibroin (SF) are glycine–alanine–glycine–alanine–glycine–serine (GAGAGS), which composes the crystal regions in the SF polychain shown in **Figure 4**[19]. The highly crystalline region of silk provides the strength but the presence of strong hydrogen bonding makes it insoluble in many solvents like dilute acids, alkalis, and water. These sheets play an important role in strengthening and stiffening the silk fibers[20]. It has been reported that the presence of only β-sheets i.e. crystalline regions which are having ~50 nm diameter possess high crystallinity, usually more than 90% [18].

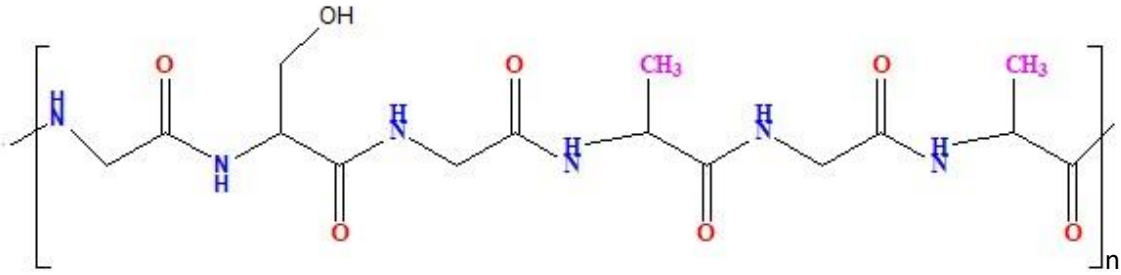

Figure 4: Structure of Silk Nanocrystal backbone.

1.4.2 Inorganic nanoparticles

The natural or conventional fibers are more prone to staining from a spilled drink, itching because of uncontrolled microbial growth, and adhered micron-dust, static energy generation which has made researchers to make efforts on studying the control of human hygienic living standards to replace harmful or toxic chemicals. The introduction of new technologies by utilization of both inorganic and organic nanoparticles has delivered new opportunities for the development of improved multifunctional properties for textile applications. The inorganic nanomaterials include metallic like silver, copper, gold, platinum, gallium, and metal oxides like silver oxide, zinc oxide, titanium oxide, iron oxide, magnesium oxide, silicon oxide, zinc oxide; and others such as clay nanoparticles, carbon nanotubes. A few important are discussed below.

1.4.2.1 Titanium oxide (TiO_2)

This nanomaterial has remarkable properties in terms of high stability, long-lasting nature, safe and anti-biotic properties which have made it promising for targeted properties like self-cleaning, anti-bacterial activity, UV resistance, dye degradation in textile effluents. Mainly, the photo activity effect depends on the structure, purification, and crystalline nature[21]. The three forms of TiO_2 available in nature are anatase, rutile and brookite. Out of the three phases, anatase form is a metastable state with more photo

catalytic nature than rutile whereas rutile is more thermodynamically stable than rutile and booklite. TiO_2 when irradiated by the source of light forms electron-hole pairs which induce redox reaction over the TiO_2surface. The active oxygen species (O^{2-}) oxidizes the organic compounds of the bacterial cell and convert them into carbon dioxide (CO_2) and water (H_2O) molecules thereby acting as photo active agent. Different preparation techniques have been employed out of which the sol-gel method is mostly applicable to obtain a stable anatase form of TiO_2[22]. The electron excitation i.e. light absorption range can be extended from UV (<387.5 nm.) to visible light (>400 nm) by creating a local electricfield using gold and silver nanomaterial thereby increasing the photocatalytic effect.

1.4.2.2 Zinc complex

Zinc Oxide (ZnO): ZnO nano-particles are more advantageous to silver nano-particle in comparison with low cost, white in appearance also are having UV-blocking properties, to make it useful as UV light-emitting device, sun-screens, UV absorbers, and photo-catalyst[23]. Researchers have studied the potential application of ZnO nanoparticles on dye removing from when considered under UVC light from textile effluent [24]. It has been reported that with a sweat concentration of 11 g/L ZnO making artificial sweat solution by considering alkaline, acidic, and inorganic salt the anti-bacterial activity of nano-ZnO when functionalized on cotton fabric was observed better salt and alkaline resistances than acid resistances sweat solution[25]. Even more ZnO nano-rod was incorporated using the dip-pad-cure process on cotton fabric samples with the addition of a hydrophobic agent to fabricate a hydrophobic fabric[26].

Zinc oligo lactate (ZL): Zinc is a metal that has been purported to have antimicrobial properties. Zinc oligo lactate, a salt obtained from reacted zinc and lactic acid (by bacterial fermentation). Various mechanisms are reported that show antimicrobial

properties of lactic acid and their salts as in an acidic environment, they act as ionophores and decrease the intracellular pH in bacteria [27, 28]. ZL may possess a protective effect and adjuvant therapy of COVID- 19 infection for the whole world. From the report, zinc is considered as a potential supportive treatment in the therapy of COVID-19 infection due to its antiviral effect and immune-modulatory effect [29].

1.5 Poly (lactic acid)

PLA is observed to be as linear thermoplastic polyester derived from 100 % renewable and degradable resources (corn, sweet potato, and starch-rich product like rice) by fermentation that can help to mitigate the energy crisis together with the reduction of CO_2. In 1932 by Carothers (DuPont) produced a low molecular weight PLA only by heating lactic acid under vacuum conditions [30]. In 1954 Du Pont obtains a higher molecular weight PLA. Moreover, poly(lactic) acid is biodegradable and compostable but under standard conditions only [31]. PLA may be amorphous or semi-crystalline in solid-state, which depends on the stereochemistry and the thermal history. The polymerization of PLA takes place by either direct polycondensation of lactic acid under certain conditions like using high vacuum and high temperature or by ring-opening polymerization of lactide which is due to the opening of dimer rings under mild conditions. The direct polycondensation technique uses a solvent to extract the water and obtain low to polymer of intermediate molecular weight [32]. Another polymerization method is ring-opening polymerization performed under mild conditions via the opening of lactide rings resulting in high molecular weight polymer. The direct condensation technique is often accompanied by several drawbacks such as the formation of low molecular weight polymer, use of large reactors, use of solvent and evaporation, problem of solvent recovery. Ring-opening mechanism of lactide by two-step process: (a) Oligomerization of lactic acid of molecular weight approximately 1-4 kDa, depolymerized to obtain lactide.

(b) Production of high molecular weight PLA by ring-opening polymerization. Different types of catalysts like metal, cationic, and organic (stannous octoate, dibutyl tin methoxide, zinc stearate, and one co-initiator, triphenylphosphine) were used to attain high molecular weight with high optical purity [33]. The polymerization reaction was mostly carried out by preferring stannous octoate as it provides a high reaction rate, high conversion rate, together with high molecular weights, just using mild polymerization conditions as shown in **Figure 5**.

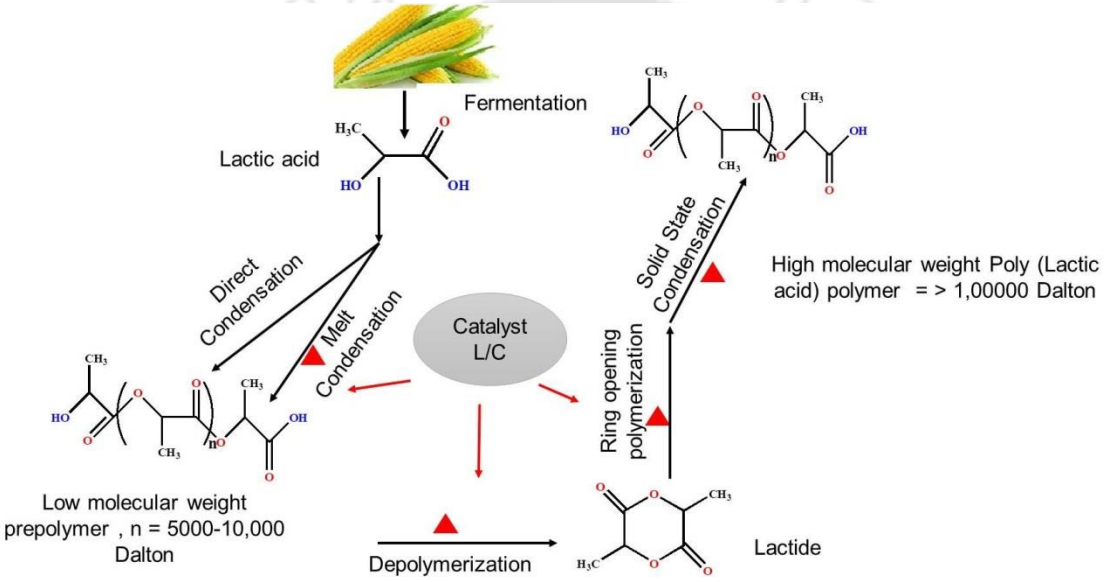

Figure 5: Schematic diagram of the synthesis of poly(lactic acid).

1.5.1 Stereocomplex Poly(lactic acid)

From 50 years onwards humans have been using synthetic and petroleum-derived non-biodegradable polymers that remarked the scientists to focus more on biomass-derived poly(lactic acid). Researchers have taken innovative initiation to improve the thermal stability and decelerate the hydrolytic degradation of PLA. PLA consists of asymmetric carbon atoms where two optically active enantiomers exist in its skeletal chain namely poly(L-lactic acid) (PLLA) and poly(D-lactic acid) (PDLA). In 1987, it has been first reported by Ikada et al. that melt and solution blending of homocrystals of PLLA and

PDLA in equal (1:1) molar ratio stereocomplex PLA was formed[34]. It was also reported that PDLA with low molecular weight cannot form stereocomplex crystallites as they cannot act as a nucleation site due to a large surface area. Whereas when a high molecular weight PDLA chain with increased content was added to PLLA chain then large strereocrystallites were found to be formed[35]. The various report has been made on the formation of stereocomplexation using external solvent for blending use of a nano-sized nucleating agent which may cost higher for industrial purposes[36, 37]. Recently, many studies have been carried out to investigate the stereocomplex type poly(lactic acid) (scPLA) because it has improved characteristic features in terms of thermal, mechanical, hydrolysis resistance and high melting point (T_m) (approximately 50°C higher than both enantiomers) [38]. The studies carried out on the formation and properties of scPLA include homopolymer molecular weight, blending ratio of PLLA to PDLA, blending temperature, and optical purity [39]. During the formation of stereocrystals, both the PLLA and PDLA chains force a larger diffusion path than that of conventional folding crystallization mechanisms conditions. The enhanced stability of PLA originates from the high crystallinity in PLA stereocomplex (SC) because of stronger hydrogen bonds and dipole−dipole interactions between the enantiomeric PLA chains formed due to their complementary helical chain structures, results in tie chains between the crystallites and dense packing of chains. An important evidence of the stronger hydrogen bonds and dipole−dipole interactions between the enantiomeric PLA chains in scPLA is depicted by the enhanced resistant of PLLA/PDLA blends toward hydrolytic degradation compared to plain PLLA copolymers [40]. Tsuji et al. has tried wet and dry spun stereocomplex PLA by mixing it with chloroform and then studied the stereocomplex crystallites formation using differential Scanning Calorimeter without formation of any homocrystallites when they are hot drawn and spunned into fibers[41]. They also reported the enhancement of

stereocomplex crystallization by hot drawing to high ratio which was due to chain expansion and interaction between PLLA and PDLA. Besides the modification with other polymers or various nanofillers, formation of stereocomplex crystallite (SC), which shows the remarkable feature of high melting point (Tm), ~ 50 °C higher than that of poly(l-lactic acid) (PLLA) or poly(d-lactic acid) (PDLA) homocrystallite (HC) has been proven to be another successful way to improve the properties of PLA, such as heterogeneous nucleation crystallization thermal stability and hydrolysis resistance[42]. The latter character limits their use in conjunction with hydrophobic polymers that are industrially attractive due to the poor dispersion and the occurrence of aggregations. Thermal property and crystallization behavior of PLLA, when blended with 1-5 % of PDLA, was studied and found that stereocomplex crystallites act as nucleation sites on PLLA matrix. Masaki et al. reported the exclusive formation of scPLA pellets and fibers, by controlling the temperature around 200 °C, assuming transesterification due to the presence of catalyst remnant from polymerization of homopolymers. These authors showed that by drawing and annealing of the as-spun fibers, with certain amount of initial scPLA, fibers containing mainly scPLA could be obtained as depicted in **Figure 6 and 7**[43].

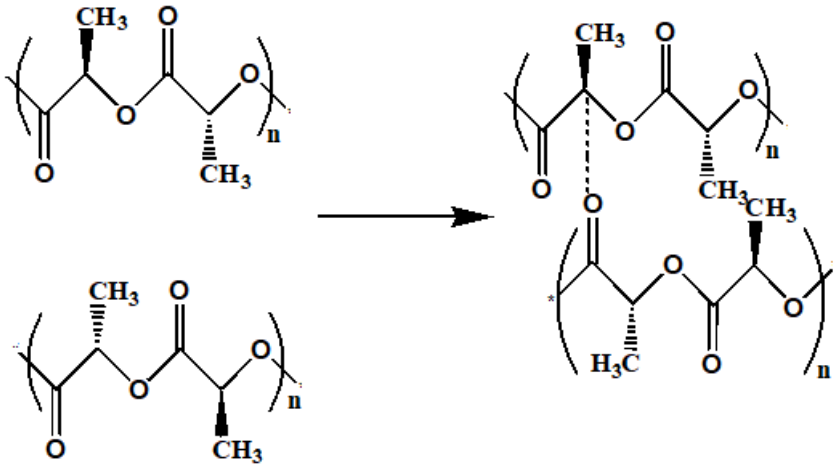

Figure 6: Structure of Poly(L-lactic acid), Poly(D-lactic acid), Stereocomplex PLA.

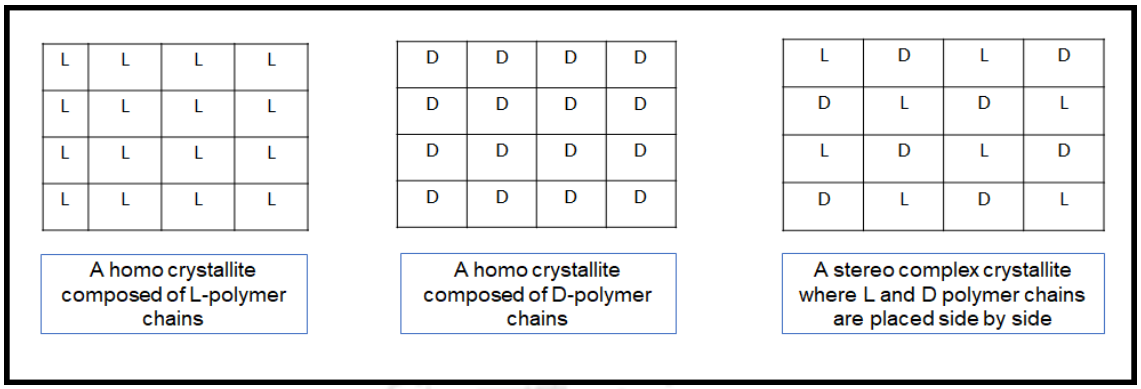

Figure 7: Lattice arrangement of L and D units in the stereocomplex PLA**.**

1.6 Polymer degradation and recycling

PLA is one of the most frequently used biobased polymers that has been used in commodity applications to substitute the non-degradable poly(ethylene terephthalate) (PET), polystyrene (PS), polypropylene (PP), and others in the future. The misunderstanding of PLA biodegradability that it gets readily degraded in a natural environment can even lead to mismanagement of creating a plastic polluted environment. Under soil or domestic composting conditions, it can take up to years at 20 °C and maybe within 12 weeks under > 25°C[44]. Even degradation under marine conditions is also a challenging task. The report has been made on mimicking static sea water where no degradation takes place within a year but weight loss has been found when considered a simulated dynamic seawater environment[45]. Even PLA does not tend to get degraded at ambient temperature even though an accelerated environment has been mimicked[46].PLA can be composted under industrial conditions, and at the end-of-life degraded into CO_2 and biomass serving as carbon-sink into the environment. A suitable required temperature, the moisture content in the composting system is favorable for PLA degradation when degradation of higher molecular weight to intermediate low molecular weight by random chain scission followed by assimilation of those low molecular weight

chains by activated microbes under ASTM standards[47]. Polymer degradation causes changes in electrical, mechanical using discoloration, phase separation, cracking by a leading chain, side chain, and intersectional chains scissioning. Further degradation of PLA involves ester bond linkage scission through non-abiotic and abiotic processes like hydrolysis, thermal, oxidation, pyrolysis and microorganisms respectively. In such cases the specimen characterization in terms of degree of crystallinity, molecular weight, morphology plays an important role [48]. Industrial composting has been identified as the worst end-of-life option from a climate perspective as neither energy recovery nor improvement in compost quality takes place leading to the generation of more greenhouse gases. Studies reported PLA recycling leads to higher environmental benefits than thermal treatment of PLA waste[49].

In the case of the chemical recycling of PLA polymers break down into constituent parts that can be utilized for other applications. This is more beneficial in terms of valuable chemical recovery and tolerance to contamination with other plastics by reducing the separation cost. Further, the stereochemistry of PLA can be maintained even after recycling to obtain an enantiopure PLA[50]. Various processes are available for chemical recycling of PLA using hydrolytic or alcoholic depolymerization by using miscible systems of PLA/ solvent/reactant for monomer recovery at higher and even lower temperatures in an efficient and environmentally-friendly manner. The process also allows easy implementation and cost-effective operation and proper identification of catalyst that adheres to the circular economy.

1.7 Literature Review

A group of researchers has reported the formation of nanocellulose-titania nanoparticles hybrids with high inorganic content by adsorption of TiO_2 nanoparticles on wood-derived nanofibrillated cellulose. As transparent coatings, these hybrids demonstrated high wear

resistance and UV activity [51]. SF/TiO_2 nanocomposite films were prepared by sol-gel technique using butyl titanate precursor for titania which produced high crystalline, improvement in mechanical, thermal properties with a decrease in water solubility [52]. Yang et al. has prepared 7-10 nm gold (Au) nanoparticles embedded in silk fibroin fibers (SFF) by solution impregnation technique [53]. Patwa et al. has prepared iron oxide (Fe_3O_4) magnetic CSN for applicable in therapeutics and implants. TiO_2/Cellulose nanowhiskers-based nanohybrid was prepared by sol-gel process using $Ti(O_2CH_5)_4$ where they had a promising photodegradation ability [54]. A convenient biomineralization technique has been developed to form and assemble flowerlike zinc oxide (ZnO) on silk fibroin fiber (SFF). The prepared material has also had bacteria repellency and anti-ultraviolet radiation functions. Thus, the obtained ZnO particles have potential applications in biomolecular detection, antibacterial agents, and anti-ultraviolet-radiation fibers[55]. A study was performed by fabricating zerovalent iron (ZVI) nanoparticles supported on cellulose nanocrystals for dye reduction, organic conversion as well as chemo- magnetic propulsion [56]. Using Zn powder, a cheap and easily available catalyst with microwave technique was used to produce moderate molecular weight polylactic acid with high purity [57]. Research was made on antimicrobial hybrid materials consisting of poly(lactic acid) as nonwoven fabrics, using phosphoro-organic compound-fosfomycin as a coating and modifying agent. Nonwoven mats made of a poly(lactic acid)/chitosan (PLA/CS) blend and a PLA/CS blend containing silver (Ag) nanoparticles (Ag/PLA/CS) were prepared using an electrospinning technique. The PLA/CS blends containing silver nanoparticles are better than CS in the PLA/CS blend that exhibited good antibacterial activity against the gram-negative bacteria *E. coli* and the gram-positive bacteria *S. aureus* [58]. A study was performed using electrospinning to prepare PLA/TiO_2 nanofibers where it was found that the antibacterial activity improved under

UV-A irradiation, and nanofibers and films with 0.75 wt.% TiO_2 content exhibited inhibition zones of 4.86 ± 0.50 and 3.69 ±0.40 mm for *E. coli* and 4.63±0.45 and 5.98 ± 0.77 mm for *S. aureus*, respectively [59]. Another study was performed using activated charcoal (A.C.) reinforced polylactic acid (PLA) nanofibre membranes produced by the electrospinning technique. It was found that Bacterial Filtration Efficiency (BFE) (% and Submicron Particle Filtration Efficiency (%) is ≥98%, which may act as personal protective equipment. PLA has been degraded using H_2SO_4 within temperature range 150 °C and 190 °C within 2h with high conversion of alkyl lactates [60]. To avoid acid-base catalysis PLA degradation another report focused on the use of ionic liquids for the methanolysis of PLA [61]. Luis et al. has reported an imino monophenolate $Zn(1)_2$ catalyst to degrade PLA into methyl lactate using THF as solvent and methanol as an aprotic source. The effect of temperature, catalyst concentration, and PLA concentration are also important factors [62].

CHAPTER 2

MATERIALS EXPERIMENTAL SECTION AND FABRICATION TECHNIQUE

2.1 Materials

L-lactic acid was purchased from Corbion, PURAC®, India, Tin(II) 2-ethylhexanoate (tin octoate) procured from Sigma Aldrich for synthesis of PLLA with specific rotation = [-157]$^{T=25^{\circ}C}_{\lambda=589nm}$ (at temperature 25ºC and wavelength 589 nm). The waste cocoons of *Antheraea assama*, popularly known as Muga silk, was used as silk fibroin source, received from Regional Muga Silk Station, Central Silk Board, Boko, Assam, India. The precursor Titanium (IV) butoxide (TTB) (99%) was supplied by Aldrich Chemical Co., Milwaukee, WI, Absolute alcohols were used as a solvent (Sigma Chemical Co., St. Louis, MO). Distilled water was used to initiate and complete the hydrolysis reaction. Nitric acid (HNO_3) (69% pure Himedia) was used as both a catalyst and a peptizing agent, for hydrolysis and peptization, respectively. Analytical grade chemicals like sodium carbonate (Na_2CO_3) (>99% purity), sulfuric acid (H_2SO_4) (>99%), and methylene blue (MB) was procured from SRL Chemicals, Mumbai, India, Absolute ethanol without further purification. PLA (grade 2003D, D-lactic acid: 1.4%, L-lactic acid: 98.6%, in granules form, the density of 1.24 g/cm^3) with number-average molecular weight (Mn) of ~134000 Da and weight-average (Mw) of ~222000 Da, respectively) was supplied by Nature works, U.S.A. ε-caprolactone, purchased from SUOYA (Tangshan) Biological Technology Co. Ltd., China. Chloroform (analytical grade, procured from Spectrochem, HPLC grade), N, N-Dimethyl formamide, DMF (EMPLURA®). Acetic acid glacial (HIMEDIA), Zinc Oxide Extrapure (SRL), Zinc powder pure (Merk), Chitosan (medium molecular weight, deacetylated chitin), Polypropylene nonwoven fabric *(50 GSM* SSMMS (Spunbond x 2, Meltblown x 2 and Spunbond x 1) hydrophobic, supplied by KTEX NONWOVENS, Benzyl Alcohol, from Merk, India, Ethylene Glycol,

Tetrahydrofuran (THF), HPLC grade Methanol from Sigma Aldrich, Acetic acid glacial (HIMEDIA).

2.2 Experimental Methods

2.2.1 Fabrication of TiO_2 doped SNC (ana-TCS) nanohybrid with post-treatment

Hydrolysis of the alkoxide precursor TTB was carried out in an alcoholic medium using the acid catalyst HNO_3 as a hydrolysis agent. For the sol-gel process, firstly 0.1 g SNC, 2.5 mL HNO_3, and 50 mL absolute ethanol were kept in a sonication bath for 1 h to promote uniform dispersion of SNC in the medium. Then, placed in a two-neck round bottom flask (RB) for 4h, maintained at a temperature of 45 °C. 1 mL TTB was added dropwise with continuous stirring until it turns to a white gel-like in appearance. Then 5-fold times DI water was added to stop any further reaction and centrifuged using DI water at 6000 rpm for 15 min to obtain the slurry. Thereafter, dialysis was performed as shown in **Figure 8.** The presence of the –NH group in SNC chains might have resulted in a color change. Using cellulose acetate membrane (Sigma-Aldrich, India) it was dialyzed in DI water for 3 days to obtain neutral pH. The freeze-dried (-100 °C) sample was dried at 70 °C for 2 h for aging to promote the crystallization of the anatase phase, and calcined at 300 °C (below the degradation temperature of SNC) for 3 h to obtain pure crystalline anatase- TiO_2 powder.

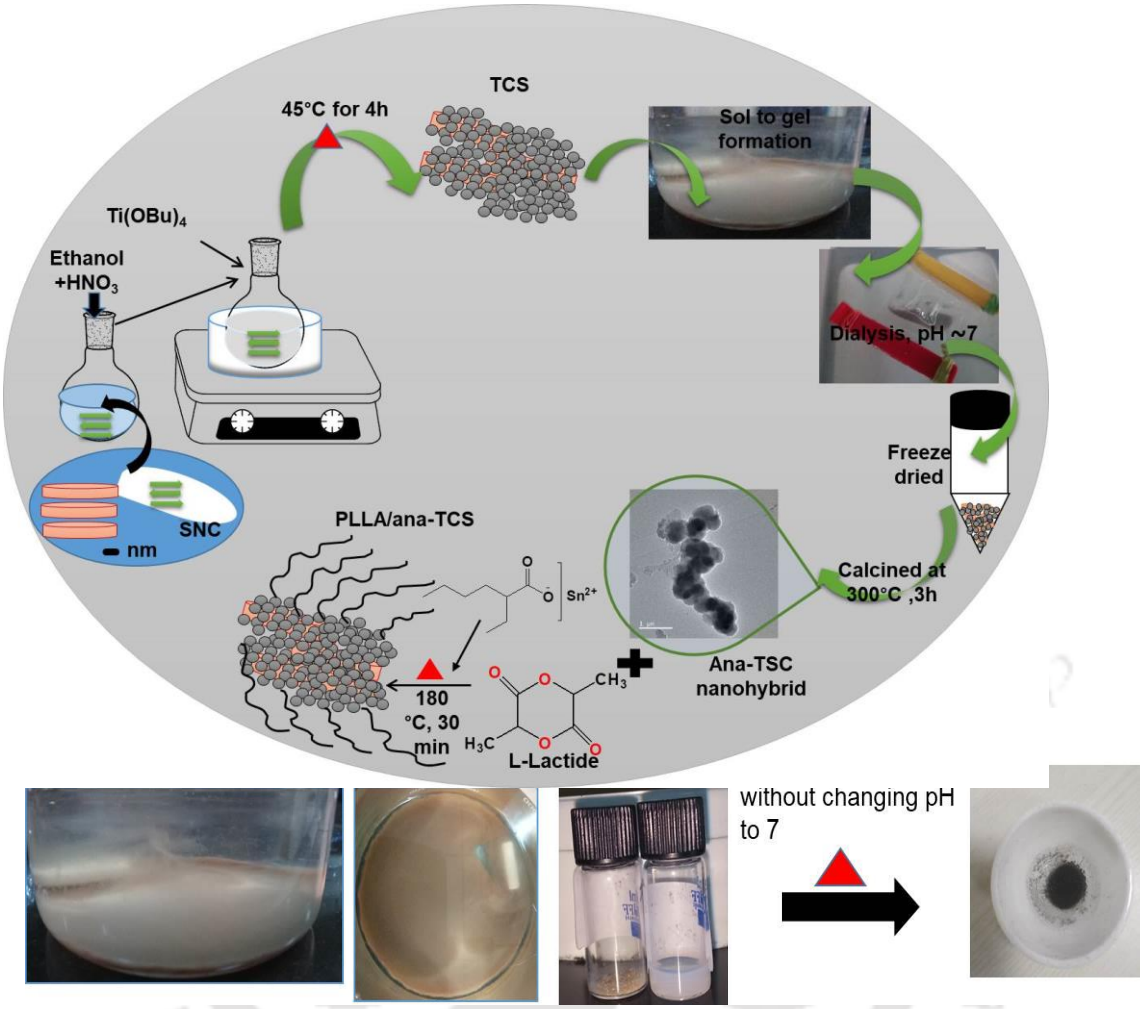

Figure 8: Synthesis of in situ polymerized PLLA/ana-TiO_2-SNC (PLLA/anaTCS), (a) ana-TCS in DI water, (b) aged ana-TCS (c) left dried powder, (c) right in DI water after drying to check for any visual changes after aging, (d) Change in color seen after annealing.

2.2.2 Fabrication of in situ *polymerization of PLLA/ana-TCS nanocomposite into electrospun nanofabric*

The dried and finely powdered ana-TCS was then placed in one neck 50 mL RB, inside stirred by a magnetic bar with an oil bath set over a hot plate. For the polymerization step, prepared lactide (moisture content = 0.06 ppm) was taken in the RB. The amount of monomer/ initiator [M/C] ratio was taken as 2500/1 molar ratio, and the whole material was left overnight under full vacuum with nitrogen purging condition. Before carrying at

reaction temperature 180˚C, the material was again left for drying at 40˚C for 1h so as no moisture leftover and maintained the reaction time for 30 min at the mentioned reaction temperature. The catalyst taken was poured inside RB using a 250 µL syringe with a calculated amount and considered lactide amount to be a batch of 15g. The nanohybrid concentration taken was 0.5 wt. % to check its effect over polymerized PLLA. The solid mass obtained was then stored in an oven, set at 40˚C for 24h to remove moisture. The purification step was avoided to omit the use of any harmful chemicals, and then those were converted into pellets form, further supported by different characteristic methods to evaluate its structural condition. Further, the electrospinning technique was used to fabricate the prepared nanocomposite into a non-woven nanofibrous mat over aluminum (substrate). 10 %(wt. /vol.) PLLA/ana-TCS solution was prepared in chloroform: DMF (70:30) solvent mixture stirred at 50 °C for 6 h. Parameters used during electrospinning were as follows: 12 kV voltage, tip distance from the collector was maintained at 12 cm using a 6 mL syringe for spinning the solution to the collector. The electrospun nanofibers were then dried in a vacuum oven at 40 ˚C for 12 h. The schematic diagram of preparation and fabrication of electrospun nanofabric is as shown in **Figure 9.**

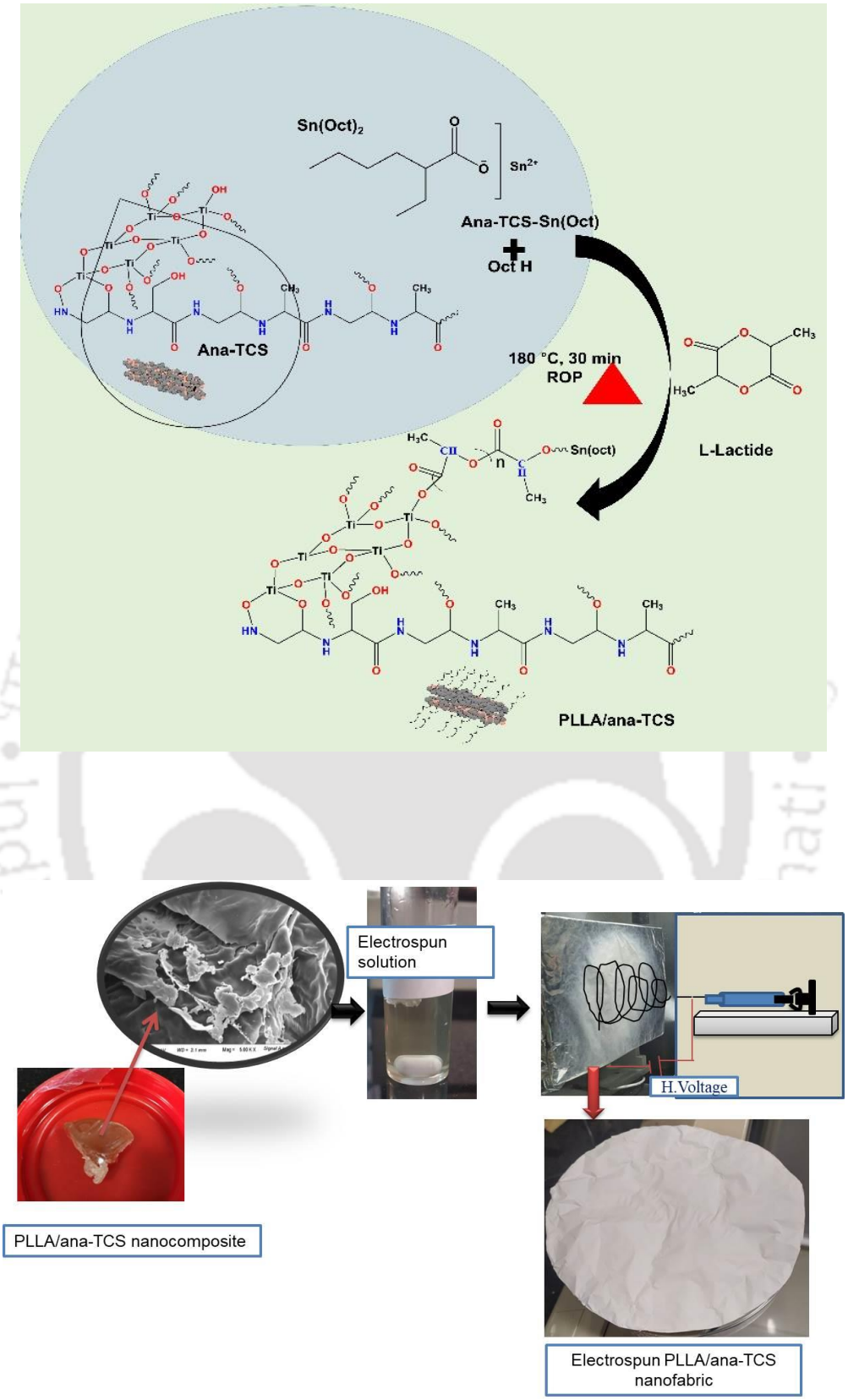

Figure 9: Schematic diagram depicting grafting of ana-TCS with PLLA and fabrication of electrospun PLLA/ana-TCS nanofabric.

2.2.3 Synthesis of zinc oligo lactate (ZL) by microwave heating:

Zinc powder and lactic acid were taken in the ratio of 1:10 (wt. /wt. %) with proper mixing in a round-bottom flask (RBF) with a glass rod before the synthesis. The prepared mixture was placed inside microwave purging using an N_2 atmosphere. Microwave heating was used to achieve higher reaction rate and high product yield. Condensation polymerization reaction was performed for preparation of ZL in a microwave at 140 °C for 1h at 240 W under "convection cum microwave" mode. A heating belt (temperature ~100 °C), was connected between RBF and condenser. This usually avoids condensation of unbound water and any other by products during reaction under the inert atmosphere. After completion of the reaction, solid mass was taken out of the RB, dried at 50 °C for 12 h in an oven and 5mL of the distilled product was collected after reaction. For purification, the ZL was stirred in DI water for 1 h at room temperature to remove any unwanted lactic acid present. The white precipitate found was centrifuged at 5000 rpm for 5 min, and then dried in an oven at 60°C overnight and ground to powder. This powder was dispersed in water and was found that it forms white precipitation with water at room temperature. Subsequently, it was used as filler with varying percentages for the preparation of PLA/Zinc lactate bio-nanocomposite mat.

2.2.4 Preparation of PLA/ZL-SNC nanocomposite solutions by Electrospinning

The Electrospinning technique was used to prepare samples of PLA, PLA/ZL, and PLA/ZL/SNC nanofibre nonwoven mat over PP substrate. Separately 10 % (wt./v) PLA solution was prepared by dissolving PLA in Chloroform: DMF (70:30) solvent mixture in a conical flask. Accordingly, the desired parameters taken are parameters (solution mixing temperature: 45°C), flow rate: 1 (mL/h), working distance 12 (cm), high voltage: 12 (kV) were used for the preparation of nano-fibrous mat as shown in **Figure 10.**

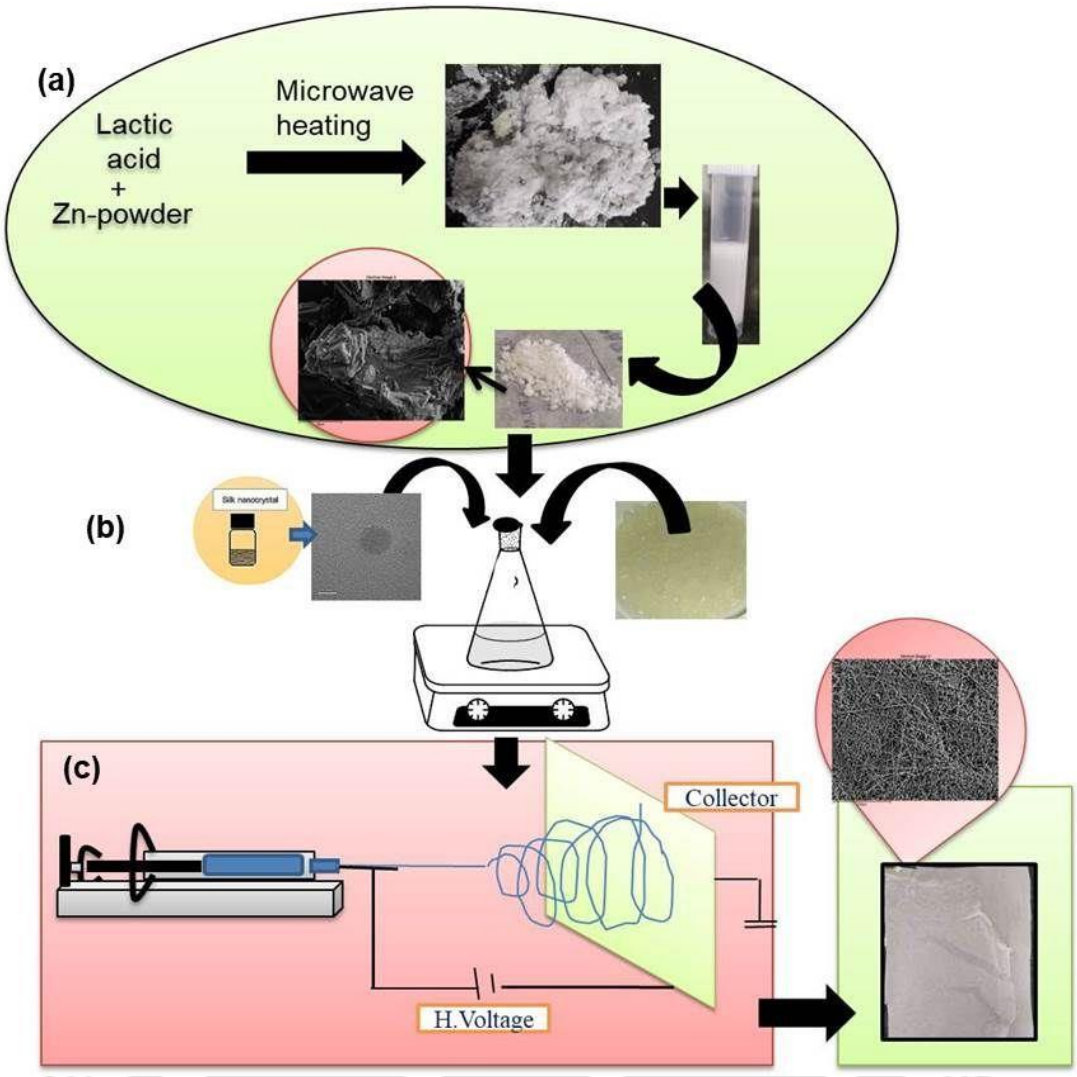

Figure 10: Schematic diagram for **(a)** microwave synthesized zinc oligo lactate, **(b)** preparation of electrospun PLA based solution, and **(c)** fabrication of PLA based electrospun nanofabric.

2.2.5 Preparation of nanochitosan (nCS) using STPP by ionic gelation method

Chitosan nanoparticles are synthesized by medium molecular weight commercial obtained chitosan using cross-linker Sodium triphosphate, STPP as a cross-linker. Firstly, a solution of chitosan (1w/v %) has been prepared to dissolve in dilute aqueous acetic acid solution (1v/v %) with continuous stirring for 24 h. A volume of 100 mL of 0.10% STPP solution is then dropped into the solution of 100mL of chitosan solution. The formulation has been stirred for 3 h till a white milky emulsion is produced as shown in

Figure 11. The formation of nanoparticles consisted of a spontaneous reaction mechanism between cationic chitosan and anionic STPP cross-linking as shown in the scheme diagram. Here, the addition of chitosan (solubilized in acetic acid) and the addition of STPP solution resulted by a cross-linked electrostatic interaction between NH_3^+ groups of chitosan and O^- groups of STPP into a stabilized polyelectrolyte complex. The three-dimensional entanglement was in precipitated form and turns into gel-like particles. The interaction occurred due to pH-sensitive glucosamine groups with pKa ≈ 6, where they are converted into a soluble form of protonated amine ($R–NH_3^+$) groups. The precipitated nCS particles have been separated using centrifugation at 5000 rpm for 10 min and washed with distilled water followed by freeze-drying in lyophilizer as shown in **Figure 12.**

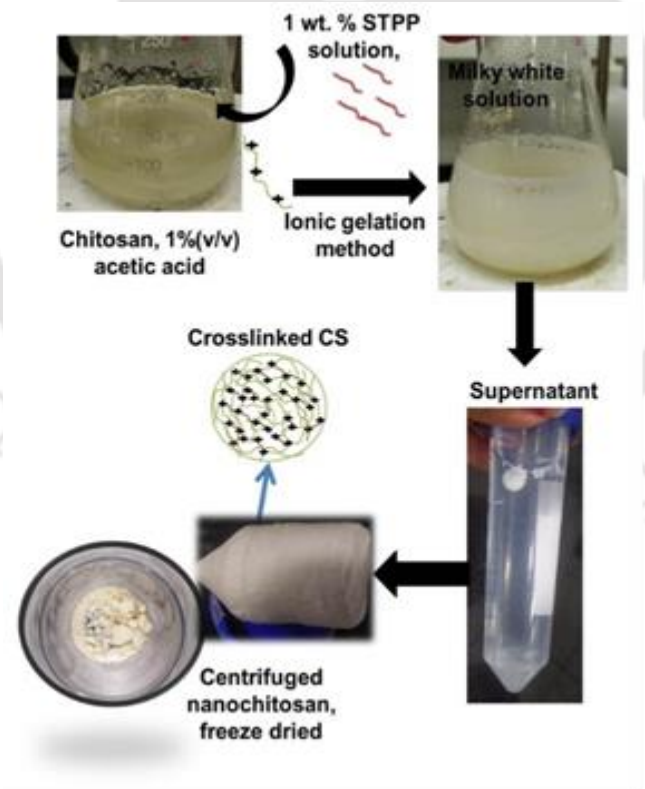

Figure 11: Fabrication of nanochitosan using Sodium triphosphate by ionic-gelation method.

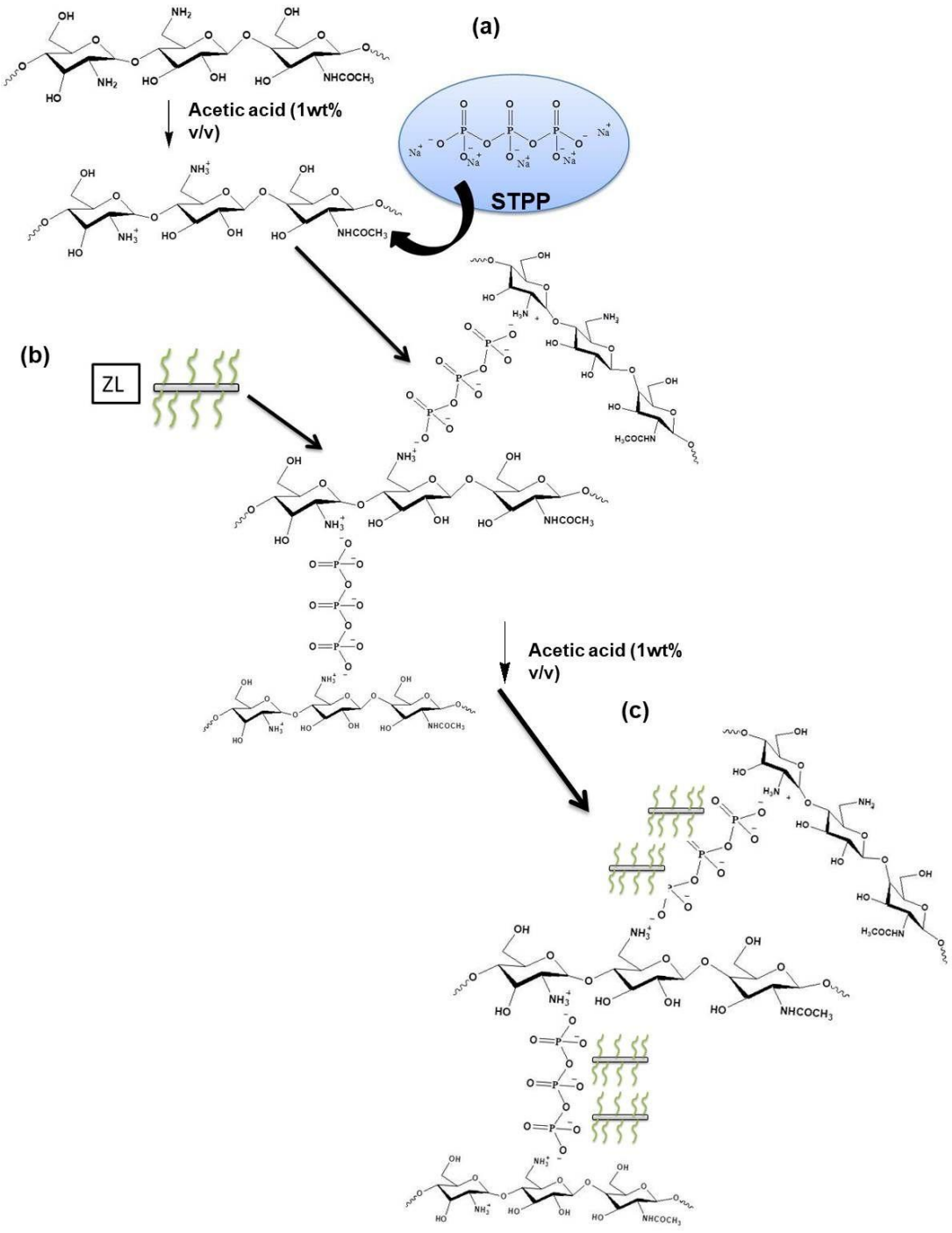

Figure 12: Schematic illustration of the chitosan-STPP complex.

2.2.6 Fabrication of nCS-ZL nanofinish over PLA electrospun nanofabric

For the preparations of PLA/nCS-ZL nanofabrics, 9 wt.% of PLA beads were first dispersed in 30 mL using a binary solution of DMF and $CHCL_3$. The solution was stirred for 6h untilled the polymer beads get completely dissolved into the solution. Fabrication of PLA nanofabrics was carried out using E-spin electrospinning instrument from Nanotech, India. The solution was jet out by a 5mL syringe, 20G SS needle, flow rate 1 mL/h with a positive voltage (10kV). The oriented fibers were collected in an aluminum foil collector, placed at a distance of 13 cm from the tip of needle at a temperature 32 °C and 45% relative humidity. Thereafter, the nanofabrics are dipped inside the prepared solution of varying compositions of nCS and ZL and both. nCS, nCS/ZL is picked up by the nanofabric which was later dried to form a thin film as depicted in **Figure 13**.

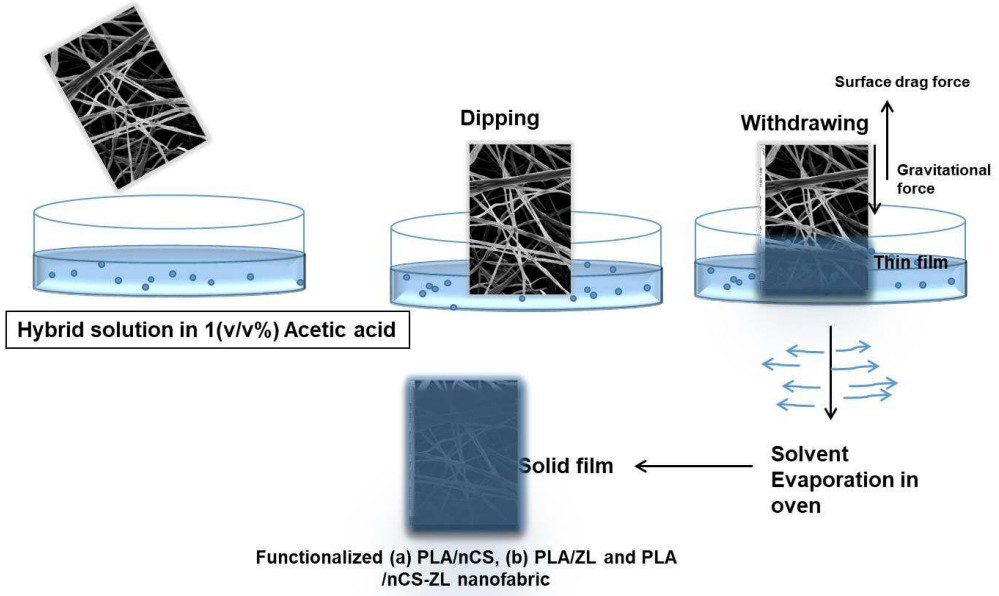

Figure 13: Dip coating process for the formation of nanolayers of nCS-ZL on PLA nanofabric.

2.2.7 One-pot synthesis of green silk nanocrystal/zinc oxide nanohybrid using precipitation method

The accurate weight of 0.75 g ZnO powder was dissolved in 100 mL of 1% (v/v) acetic acid so that it can be changed into zinc cations. To this solution, 1 gm of silk nanocrystal was added. The mixture was sonicated for 30min for proper dispersion. This solution was kept under magnetic stirring where 1M NaOH solution was added drop by drop till the pH of the solution attained ~11. The solution was then heated in a water bath at 80°C for about 3 h to appear white precipitation of the solution. It was then centrifuged at 5000 rpm for 5 min to separate the mass and washed with distilled water several times the supernatant was decanted. The mass obtained was then dried in an oven at 50°C for 12 hr and ground in a mortar pestle to obtain in a fine powder form.

2.2.8 Fabrication of electrospun in situ *PLA/SNC-ZNO nanofabric*

To prepare electrospun PLA fibrous mat, PLA pellets were dissolved in a binary mixture of chloroform: DMF directly. Considered three varying percentage of nanohybrid that was taken for preparation of three different PLA nanocomposite solutions as mentioned in Table 3. The appropriate weight of PLA was dissolved in the mixture and stirred for 5 h to obtain a transparent colloid solution. The following compositions are also prepared accordingly, in the same manner, were obtained. Finally, pure PLA and its composite fibrous mats were made from the electrospinning unit. The electrospun fibrous mats were dried overnight in the oven at 50°C. The schematic diagram shows the fabrication of the nanohybrid and PLA/SNC-ZnO nanofabric in **Figure 14**.

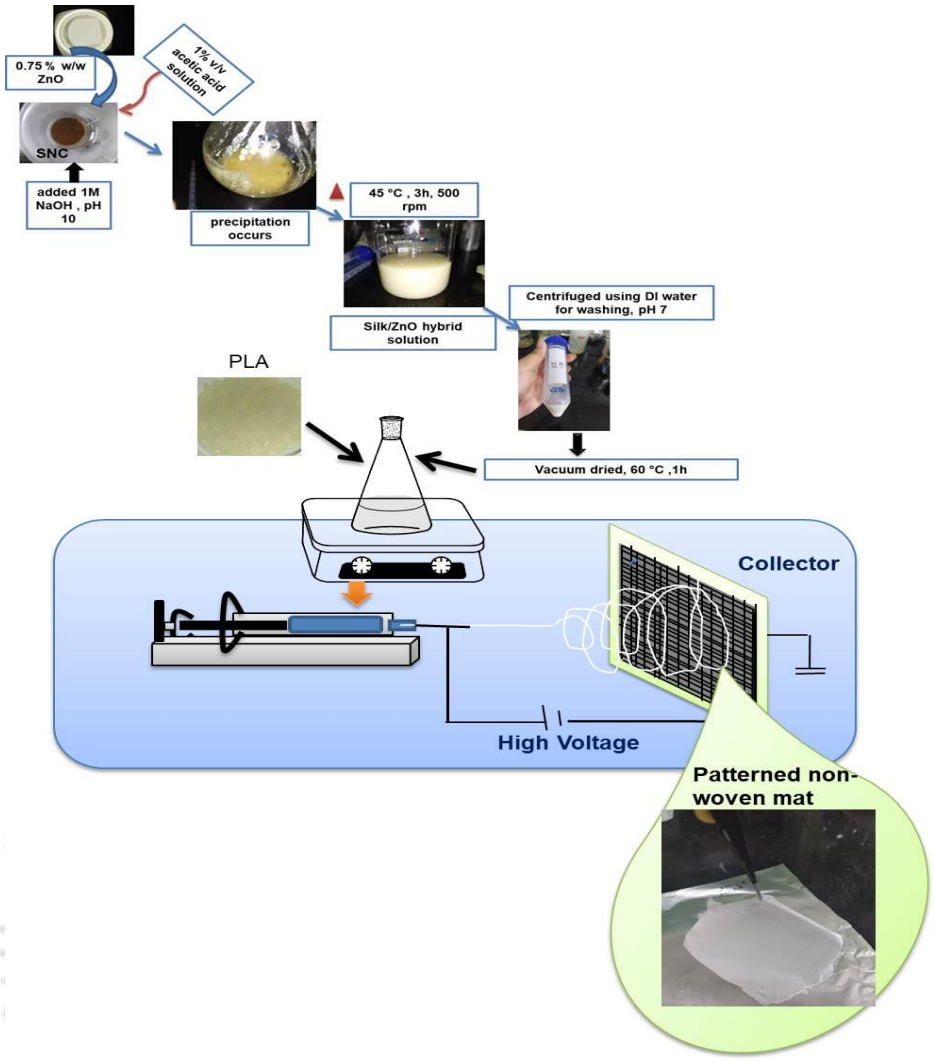

Figure 14: Schematic picture of preparation of ZnO-SNC nanohybrid and fabrication of non-woven mimic of patterned shaped PLA/SNC-ZnO nanofabric

2.2.9 Synthesis of anatase nano-TiO_2 using sol-gel method

The hydrolysis of alkoxide precursor TTB was performed under an alcoholic medium using an acid catalyst as a hydrolysis agent. To prepare the TiO_2 sol, first HNO_3 acid (5mL, 0.1M) and ethanol (100 mL) were mixed under vigorous stirring for 20 min until the solution became homogeneous. Then TTB (10 mL) was added dropwise slowly into the mixture to form a sol phase. The whole solution was then stirred for 1 h at 80 $^{\circ}$C. After the time ceases the solution turns into a white precipitate gel which was centrifuged at 5000 rpm for 5 min to separate the gel from the solution. Further, calcination was done

at an elevated temperature 500 °C for 1h can change the amorphous phase of TiO_2 to a highly crystalline anatase phase (a-TiO_2).

2.2.10 Fabrication of electrospun non-woven PLA/a-TiO_2 using three different cases

PLLA and PDLA with molecular weight as mentioned in **Table 1** were solutions blended in chloroform for 12 h at 60 °C. A long time of stirring upon dilution can dissolve homocrytsal but cannot dissolve stereocomplex crystallites on the same solvent. High molecular weight PLLA/ PDLA (1/1, wt./wt.%) was then dissolved in a binary mixture of $CHCl_3$/ HFIP (7/3, v/v%) at 60 °C for 6 h having a concentration of 20 mg/mL. The light whitish suspension was obtained when mixed at room temperature, which was treated to form a clear solution by stirring above the glass transition temperature of homo PLLA/PDLA for one hour. The electrospinning was operated on a commercial electrospinning instrument (Nanotech, India), using a syringe needle. Process parameters were fixed for a needle with a syringe diameter of 13.6 mm, an applied voltage of 15 kV at 25 °C. The distance of the needle tip to the collector plate (aluminum foil) is 15 cm with a feed speed of 1 mL/h.

Table 1: Molecular weight analysis of synthesized PLLA and PDLA

Matrix	**M_n (kDa)**	**M_w (kDa)**	**PDI**
PLLA	113	203	1.79
PDLA	109	205	1.88

For comparison, scPLA, and solutions of scPLA/a-TiO_2 solutions were prepared in three different cases using three different compositions as shown in **Figure 15** with the distribution of a-TiO_2. Then, electrospun nanofibrous fabrics were vacuum-dried for 12 h. For **case (I)** nanomaterial and scPLA solution were prepared in a single system and

electrospunned into nanofibrous over aluminum foil substrate. For **case (II),** a separate a-TiO_2 ethanol solution was made to electrospray over the scPLA nanofibrous fabric. Whereas, for **case (I), (II)** the electrospun scPLA nanofibrous fabric was dipped into a-TiO_2/ethanol solution of 1 mg/mL and 10 min ultrasonication. While using dip-coating method different a-TiO_2 loadings were used followed by withdrawal and evaporation at 60 °C causing deposition of a-TiO_2 over the scPLA nanofibers. Nano-morphology of the scPLA fibrous surface has influenced in fixing of a-TiO_2 nanoparticles for the **case (III)**.

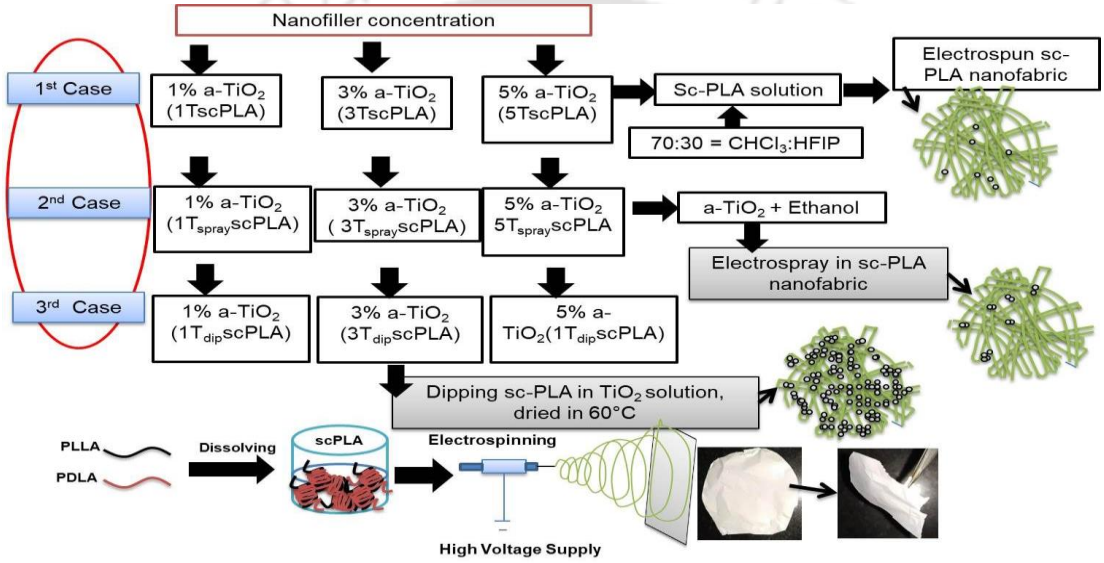

Figure 15: Different case studies on fabrication of stereocomplex PLA/ a-TiO_2 nanofabric.

2.2.11 Ring-opening polymerization of L-lactide and ε-Caprolactone using ZL as catalyst (a solvent-free approach)

The polymerization reaction was carried out in a 10 mL glass ampoule. The glass ampoule was flashed with inert gas (N_2 99.99% purity) before any chemical charging so that no contamination occurred before carrying the reaction. A series of experiments have been performed using ZL as initiator and with or without BA as co-initiator. The optimized conditions are given as shown in the table give the molecular weight of the synthesized polymers. Ɛ-caprolactone and twice recrystallized L-Lactide were used after vacuum drying for 24 hr before using. An alternate supply of 5 min vacuum and 5 min N_2 purging was done and sealed after placing in an oil bath at 60°C for 1 h. The ROP was

done by raising the temperature to 180 °C and vigorously stirring for 30 min using different monomer to catalyst ratios [M/C]. Further, a volatilization process of 1 h at 110 °C was performed to remove any unreacted lactide in the synthesis process.

Whereas for ROP reaction of PCL, co-initiator ethylene glycol and catalyst ZL has been charged into the ampoule maintaining the [M/I/C] molar ratio and stirring allowed for 10 min at room temperature. As soon as the monomer was charged the reaction temperature was raised to 150 °C and continued for 1 h till the viscosity shoots up and stopped the magnetic bead for further. A similar attempt was made to remove any unreacted monomer by extending the reaction time for 20 min at 110°C. Proper caution has been considered while maintaining the reaction temperature inside the ampoule.

2.2.12 Depolymerization of high molecular weight PLA and PLA nanocomposite waste by Chemical degradation (methanolysis) using ZL as a catalyst

Commercial high molecular weight PLA and outdoor stored waste medium molecular weight PLA composite have been utilized for the study. Here the synthesized zinc grafted short PLA chains have been used as a catalyst and dissolved in THF assisted by heating and stirring for dissolution. Here, we have reported the use of ZL for transesterification reaction where alcohol used is methanol for degradation of high molecular weight PLA and outdoor stored waste PLA nanocomposite to very low molecular weight methyl lactate. A simple experimental setup with optimized condition parameters has motivated to scale up the process to the industrial level. To increase the green credentials of the process we have omitted chlorinated compounds. For this experiment under inert atmosphere, the reaction has been performed in a 2 neck RB. 12.5 g PLA beads are taken with 250 mL THF and 50 mL chloroform and degradation temperature and time required with varying catalyst concentrations are noted in Table 3. In the absence of any catalyst, there is no change in molecular weight at 3h. But in presence of 4% ZL at 50°C, it can be

found that a drastic change in molecular weight can be seen after 3h reaction time with complete dissolution of PLA beads into the binary solution. Further at different time intervals 2 mL solutions were pipetted out from the RB and dropped in glass slides for drying for further molecular weight analysis of the residue.

After the methanolysis reaction was completed, the reactor was cooled down at room temperature and filtered by drying over a filter paper using an Erlenmeyer flask. The PLA conversion and yield of methyl lactate were defined as follows.

Conversion of PLA:

$$\frac{W_p-(W_R-W_C)}{W_P}\times 100\% \quad \text{.....(i)}$$

Yield of oligomer methyl lactate**:**

$$\frac{W_R}{W_P}\times\frac{M_P}{M_M}\times 100 \quad \text{.....(ii)}$$

Here, W_R denotes residues after the degradation, W_P denotes weight of PLA, W_C denotes weight of catalyst, M_P molar weights of PLA (72g/mol), M_M (104g/mol) molar weights of methyl lactate repeating units respectively.

2.3 Characteristics Measurements

2.3.1 Molecular weight analysis

Gel permeation chromatography (GPC) supplied by Shimazdu, Japan, was used to determine the molecular weight of the prepared samples. HPLC-grade chloroform is chosen as the eluent with a flow rate of 1.0 mL min^{-1} having a column oven temperature set to 40°C equipped with PL gel 5 µm mixed D columns (Agilent supplied) with detector refractive index detector, RID (10A). For calibration of the whole system monodispersed polystyrene (PS) with a polydispersity index (PDI = 1) standard range 370Da-500kDa has

been used. For the preparation of the sample, 20mg/mL was first dissolved in the same eluent until proper dissolution and filtered through 0.25 μm PTFE syringe filters, which were placed in glass vials into the autosampler.

2.3.2 Structural analysis

2.3.2.1 Fourier transform infrared spectrometer (FTIR)

The spectroscopic method for chemical structure analysis was done using infrared spectroscopy by Fourier transform infrared spectrometer, IR Affinity (Shimadzu, Japan). For powder samples, the diffuse reflection spectroscopy (DRS) method was used where samples were mixed properly with oven-dried Potassium bromide (KBr) powder of 1:100 ratio in the range 400-4000 cm^{-1} with 8 scans rate. The samples were finely pressed in an agate mortar and pestle for getting uniform powder pellet and then put in a forming pellet frame under hydraulic press of 10 tons. Whereas for the nanocomposite, they are transformed into films of dimensions (2×2) cm and analyzed under attenuated total internal reflection mode (ATR) of range 650-4000 cm^{-1} with 4 cm^{-1} resolution and 16 rates of scans.

2.3.2.2 Nuclear Magnetic Resonance (NMR)

The structural linkage of the prepared nanocomposite in the macromolecular level was studied by dissolving it in deuterated chloroform ($CDCl_3$) taking concentration of 20mg in 1 mL $CDCl_3$ and vortexed at lower speed. The proton ^1H NMR spectra for the nanocomposite were recorded by Bruker NMR spectrometer, 600 MHz with 500 scans at room temperature with spectral range 0-10 ppm after filtering with PTFE 0.25 μm syringe filter for performing the analysis.

2.3.3 Optical polarity

For identifying isotactic polyenantiomers of PLLA for obtaining the specific and optical rotations, AUTOPOL II polarimeter (Rudolph Research Laboratory) at a wavelength of

589 nm using a self-calibrated manually set mechanism. The polymer samples were measured as 100 mg was dissolved in 10 mL of HPLC grade chloroform to avoid any impurity present and filtered with a 0.25 μm filter before analysis.

2.3.4 Crystalline measurement

X-ray diffraction (XRD) spectra were analyzed using Rigaku SmartLab® X-ray diffraction system equipped with Cu−Kα radiation of x-ray wavelength, λ = 0.1541 nm with the supply of 40 kV,40 mA at scan rate of 5° per min in 2θ range 5°-80°. The XRD patterns were recorded by PDXL software where x-ray was allowed to the incident through a slit of 1 mm with 15 min exposure. Thereby JCPDS library was used to match further the formation of the polymer with the existed polymer library.

2.3.5 Raman spectroscopy

The vibration mode of molecules that gives structural fingerprint for identification of the molecules was supported by Raman spectroscopy. Raman spectra were measured by (make: Horiba Jobin Vyon with model LabRam HR, Japan, equipped with 1-W, Nd: YAG with a diode-pumped laser) Raman spectrophotometer. The excitation wavelength of 785nm was considered with 1024 scans having 10s of exposure time and 50X magnification.

2.3.6 Water race analysis

For the water race analysis, contact angle measurement was preferred using Kruss, DSA-25, Expert model (Germany). For the dried powder has been transformed into pellet form with a diameter of 2.5 cm using a hydraulic press and placed in a glass slide for analysis. In the case of the nanocomposite, it has been made in film form of (1×1) cm (L×B) and ~100 μm thickness prepared by solvent casting in a Petri dish, glued by double-side glue transparent tape. The instrument settings were set at 27°C, and water dropped amount at a single time as 2 μL distilled water with a drop rate 0.16 ml/min. Thereby the water

dropping by syringe over the specimen was captured using a video mode, and measurement was made for different times using Young's Laplace equation.

2.3.7 Morphological analysis

2.3.7.1 Surface structure morphology

The compound's internal crystalline bulk morphology was studied using high-resolution transmission electron microscope (HRTEM) supplied by (JEM-2100, JEOL, MA, U.S.A) at 200 kV. Powder samples were dropped cast by preparing a suspension of 0.01 wt. % dropped by 200 µL micro syringe. Thin slices of fabricated samples were then placed into a carbon film of 300 mesh copper grid in the oven, overnight. Images were taken at high resolution and magnification of 5 nm scale, whereas the selected area electron diffraction patterns (SAED) for the samples were captured for determining crystalline rings. The average dimensional calculations were done using Image J® software.

The topography view for powder and the nanocomposite samples were performed using Field Emission Scanning Electron Microscope (FESEM) (Sigma, Zeiss, GmbH, 2-4 kV accelerated voltage) treated with conductive gold sputtering unit for the 30s before being placed under the equipped microscope. For the powder sample preparation, a suspension as (0.01 wt. %) was made and sonicated for 10 min, drop cast over an aluminum foil-covered glass slide of 3*3 mm dimension adhered over the stub.

For examining the elemental composition with mapping for observing elemental distribution energy dispersive X-ray (EDX) spectroscopy (Oxford Instruments, UK) operated at ~20 kV. (SAED) has been used. The powdered samples (~2 mg) were floated over carbon black tape and blown with an air blower for spreading treated with gold sputtering for 30s and placed for analysis.

2.3.8 Polarizing Optical microscopy (POM) for spherulite growth analysis

For the determination of optical images with spherulite growth, polarized optical microscope (POM) with Model Eclipse LV100N POL, Nikon Co., (Japan) connected with a hot stage setup (Instec TST350) from Linkam Scientific Instrument was used. The isothermal condition was maintained and the sample preparation was 0.001 g, sandwiched between two cover slips over the hot stage. This was melted to 190 °C for 3 min to take time for the chain arrangement then an isothermal temperature was maintained at 120 °C, 10 °C /min cooling rate for 7 min. The setting for the analysis was set so that image will capture in each 5 seconds and continues for 7 min. In between manual adjustment is preferable for good images, recorded by a digital camera.

2.3.9 Thermal analysis

The thermal characteristic of and nanocomposite pellets was examined using differential scanning calorimeter (DSC) supplied by Germany modeled as Phoenix-DSC 204, F1 NETZSCH, GmbH, under continuous nitrogen atmosphere. A weighted amount of around ~ 7.5 mg was taken in the platinum crucible. The program was set by heating 20 to 200 °C and kept under isothermal conditions at 200 °C for 2 min to wipe out thermal history. The material was then cooled to 20 °C at a rate of 10 °C·min^{-1}. Then it was heated again to 200 °C, maintaining the same rate. The obtained curve gives the information of glass transition temperature (T_g), cold crystallization temperature (T_{cc}), melting temperature (T_m), enthalpy of crystallization (H_{cc}), and enthalpy of fusion (H_m) for the samples.

Moreover, thermal degradation behavior was analyzed using thermogravimetric analysis (TGA) supplied by PerkinElmer, TGA4000, MA. Here for analysis, a sample weight of ~ 6.5 was taken in an unladen alumina crucible and set program to heat it from 30 to 700 °C at 20 mL/min continuous N_2 flow rate.

2.3.10 Kinetics study by Melt crystallization

Generally, cold crystallization and melt crystallization are the two types of crystallization that occur in polymers. Mostly, the physical and mechanical properties of polymers are directly or indirectly dependent on the crystallization behavior of the material. The different models and the related equations for studies of non-isothermal crystallization kinetics are mentioned below.

The percentage crystallinity (%X_c) of all the samples were determined using the following equations

$$\%X_c = 100\times\left(\frac{\Delta H_m}{\Delta H_m^0\times\left(1-\left(\frac{wt.\%filler}{100}\right)\right)}\right) \quad \text{.....(iii)}$$

Where, ΔH_m is the enthalpy heat of fusion from DSC and ΔH_m^0 is the heat of enthalpy of fusion for fully crystalline PLA (93.6 J/g).

2.3.10.1 Relative Crystallinity, (X_t)

It can be expressed in terms of the time of crystallization (t) where integrating the exotherms of melt crystallization for the different compositions.

The relative crystallinity as a function of temperature can be expressed as given below

$$X_t = \frac{\int_T^{T_o}\frac{H_c}{dT}dT}{\int_T^{T\infty}\frac{TH_c}{dT}dT} \quad \text{.....(iv)}$$

Here T_o denotes the onset and T_∞ denotes final melt crystallization temperature. At crystallization time (t), T is the temperature which is related as:

$$t = \frac{T-T_o}{\beta} \text{ and } \beta \text{ is the heating rate} \quad \text{.....(v)}$$

Further crystallization half time ($t_{0.5}$) is the time required for the sample to reach 50% crystallization for crystallization rate prediction

2.3.10.2 Avrami Model

Kinetic parameters are investigated using this model for non-isothermal crystaliization of polymers:

$$X_t = 1\text{-}\exp(-kt^n) \quad \text{.....(vi)}$$

$$\text{Log}[-\ln(1\text{-}X_t)] = \text{Log}k + n\text{Log}t \quad \text{.....(vii)}$$

Where, X_t denotes relative crystallinity at t time, denotes crystallization rate constant and n denotes Avrami exponent where n and k values are calculated from the slope and intercepts of the straight line obtained from $\log[-\ln(1-X_t)]$ vs logt. Here n signifies the nucleation mechanism and growth of crystals. By plotting $\ln[\ln(1-X_t)]$ versus ln t for each cooling rate, a straight line is fitted, based on which Z_t and n are calculated from the intercept and slope, respectively. Jeziorny further modified the parameter by introducing the cooling rate and the modified parameter as follows[63].

$$\ln Z_c = \ln Z_t / \beta \quad \text{.....(viii)}$$

2.3.10.3 Ozawa model

It is the modified version of Avrami model where the time variable is replaced by the cooling rate. The expression goes as followed:

$$1\text{-}X_t = \exp\left[\frac{-K(T)}{\beta^m}\right] \quad \text{.....(ix)}$$

here $X(T)$ denotes relative crystallinity degree, $K(T)$ is the kinetic parameter (at T temperature), β signifies cooling rate, and m as Ozawa exponent where the equation can be rearranged

$$\text{Log}[-\text{Log}(1\text{-}X(T)] = \text{log}K(T) - m\text{Log}\beta \quad \text{.....(x)}$$

The graphs plotted between $\log[-\ln(1-X(T)]$ vs $\log\beta$ gives of $K(T)$ and 'm' from the intersection with the Y-axis and slope of the line.

2.3.10.4 Mo Model

It gives the relation between Avrami and Ozawa model. In case of Avrami model the relationship exists between X_t with t and in Ozawa model X(T) with β. Here relationship between t and β can be established using the two terms the equation is as follows.

$$t = \frac{T_o - T}{\beta} \text{.....(xi)}$$

Where T_o is the initial crystallization temperature and T is the temperature at t time. The following equation was developed from the Avrami and Ozawa model assumption.

$$\text{Log } K_t + n \text{ nLogt} = \text{Log K(T)-m Log } \beta \text{.....(xii)}$$

$$\text{Log } \beta = (1/m) \text{ Log[K(T)K(t)]-(n/m)Logt.....(xiii)}$$

$$\text{Log } \beta = \text{Log F(T)-a Logt.....(xiv)}$$

where $F(T)=[K(T)/K(t)]^{1/m}$ and a=n/m, and the values of a and Log F(T) were calculated from the linear graph.

2.3.10.5 Tobin Model

In the system, whole process crystallization can be described by Tobin model that helps in understanding both the primary and secondary crystallization alongwith phase transformation kinetics and growth impingement. As Avrami model only gives the initial kinetics idea. The various expressions related to Tobin model are given below

$$X_t = \frac{K_t t^n T}{1 + K_t t^n T}$$

Taking logarithm on both sides,

$$Log \left\{\frac{X_t}{1-X_t}\right\} = Log\ K_t + n^T\ Logt \text{.....(xv)}$$

Here X_t, denotes relative crystallinity at t time, n^T denotes Tobin exponential responsible for different nucleation and growth mechanism, and K_t denotes Tobin parameter for crystallization rate constant.

The graph plotted between $Log\left\{\frac{X_t}{1-X_t}\right\}$ vs Log t the values of 'K_t' and 'n^T' can be calculated from the intercept and slope of the linearly fitted lines

2.3.11 UV-visible spectroscopy

The dye degradation and photocatalytic catalytic activity have been studied and were carried out with a UV-Vis spectrophotometer (Perkin-Elmer, USA) in the wavelength range of 200–800 nm.

2.3.12 Color intensity properties

To calculate optical parameters chroma (c*) and Hue angle (hue), CIE-L*a*b* coordinates (L* indicates black (0) to white (100); a* indicates red (+) to green (−) and b* indicates yellow (+) to blue (−)) were measured from the bionanocomposites using a colorimeter CR 410 (Minolta Co., Tokyo, Japan) with a 10 mm diameter window and D65 illuminant/10◦ observer. The measurements were taken on a white background standard and the color difference values are given by the equation as follows:

$$\Delta E^*_{ab} = \sqrt{(L^*_2\text{-}L^*_1)^2\text{-}(a^*_2\text{-}a^*_1)^2\text{-}(b^*_2\text{-}b^*_1)} \quad \text{.....(xvi)}$$

2.3.13 Photo degradation effect

The photocatalytic oxidative activities study for the samples were performed using synthetic dye methylene blue (MB) to check the reduction of the methylene blue color. For the preparation of methylene blue solutions, 20mg/L in distilled water solution was taken in a volumetric flask making in 100mL where 2mg of MB were added. The flask was then equipped with a magnetic stirrer at 300 rpm and left for mixing till the MB powder get dissolved. The beaker was placed inside an UV chamber of one 8W T5/

Backlight blue UV tube (NARVA). For the analysis, each time 5mL of the solution has been taken after filtering by 0.25 µm syringe filter. The naked eye's degradation rate can be observed with the decrease in intensity of the blue color with time.

2.3.14 Antibacterial Activity

Bacterial colony count:

Bacterial counts for prepared materials were determined by colony growth count using plate count agar (PCA), (supplied by HIMEDIA) media. 23.5g DI water solution was prepared in a 250 mL volumetric flask. The solution was properly mixed by sterilized by autoclaving at 120 °C for 20 min. These were cooled to 45-50°C and poured into sterile plastic petridishes and left for drying. Using 10 µL smooth surface disposable inoculation loops, streaking of the gel surface was done. Then 10 mg of prepared powder was dissolved in 1 ml sterile water using a vortex mixer. Each of the samples was diluted to a dilution factor of 10^6 to get a countable plate. Prepared plate samples were incubated at 35 °C for 72 h. After incubation, each plate was measured for bacterial counting.

Disc diffusion method:

The antimicrobial activity of prepared fabric layer was determined using disc diffusion method. Firstly, 100 µL, each for bacteria *E. coil* and *S. aureus*, comprising a cell content of (10^5 CFU/mL) was placed on sterile nutrient agar prepared in deionized water according to the standard procedure on petri disc and spread by a 10 µL inoculation loops. Then samples of antibiotic (Gentamicin) and prepared fabric were cut in disc shape (0.5 cm in diameter) and then cultured at 37°C for 24 h. Followed by optical images and inhibition zone measurement of bacterial cells by measuring the diameters of the inhibition zones of the plates were taken. Indeed, inhibition zone have shown the antibacterial effect of the prepared powder against both *E. coli* and *S. aureus*, (examples of gram-negative and gram-positive bacteria) respectively. The effectiveness of

antimicrobial activities can be seen by naked eye by the large diameter of the inhibitory zone.

2.3.15 Virus reduction study

The velogenic NDV strain Bareilly, Baby Hamster Kidney fibroblast cells (BHK-21) was used in this study [64]. ZL coated nanofabric samples with varying concentration was then incubated with virus dilution (10-16) for 10 min. Viral dilution extracted was added to the seeded BHK-21 cells. The infection was allowed to proceed for 72 h in presence of Dulbecco's modified Eagle's medium (DMEM) supplemented with Methyl cellulose and 2 % fetal bovine serum (FBS). After 72 h post-treatment was performed with methanol for removing the death cell that was stained with 0.5% crystal blue stain. All the virus reduction studies were performed after post-infection of NDV and imaging of the sterilized 12-well plate was done by ChemiDoc.

2.3.16 Cell culture and seeding

Baby Hamster Kidney Fibroblast cells (BHK-21) (at passage-82) were cultured in a T75 culture flask containing Dulbecco's Modified Eagle's Medium (DMEM) (Gibco™) along with 10% fetal bovine serum (FBS) and 1% Antibiotic-Antimycotic cocktail maintaining at 37°C in a humidified atmosphere with 5% CO_2. Countess® II FL Automated Cell Counter (Thermo Fisher Scientific) and trypan blue stain (SRL) were used for cell counting. Cells (5×10^3/well) were seeded (100µl/well) in a fresh 96- well plate 1-day before the addition of test samples to the cells.

2.3.17 MTT assay

Working samples of 10% (v/v) concentration and further lower concentrations were prepared in 2% DMEM from given samples (you can put sample names here) using serial dilution. Standard culture media used for seeding is removed and working samples (Test) and 2% DMEM (Control) were added to the plate wells in four replicates (100µl each) to

find out the non-toxic concentration. Plate incubated at 37°C in a humidified atmosphere with 5% CO_2 for 48 hrs. To view the cell growth of BHK-21 cells grown in the presence of different concentrations (in % v/v) of given samples and control, Evos XL Core cell imaging system (Invitrogen) was used. MTT stock solution of 5mg/ml was prepared in PBS and stored at 4°C. After incubation period of plate, all the samples were removed and MTT solution diluted to 0.5mg/ml in plain DMEM (Standard culture media without serum) was added (100µl/well). Plate incubated at 37°C in a humidified atmosphere with 5% CO_2 for 3 hrs. Discarded everything and 100µl of DMSO added in each well and plate incubated at 37°C in a humidified atmosphere with 5% CO_2 for 10 minutes to dissolve the formazan crystals. Absorbance was measured at 570 nm using a Multiscan GO UV-visible spectrophotometer. Graphs were plotted using the closest absorbance values of three replicates out of the four replicates for each sample.

2.3.18 Nanofiber fabrication Technique using Electrospinning Technique

A perfect way to describe this technique where there involves an electrohydrodynamic process. Here the liquid droplet out from the syringe is electrified to generate a jet of fibers. The laboratory-scale electrospinning setup although simple yet is accessible with important components including a spinneret in the form of a hypodermic needle with a tip, a pump, a collector, high voltage supply. The extruded charged liquid solution comes out of the spinneret depending on the surface tension of the liquid giving Taylor cone formation. Further under electrification, deformations of the droplet into a Taylor cone take place causing electrostatic repulsion among the surface charges and there is the ejection of a jet. First, the jet travels in a straight way followed by vigorous whipping motions due to bending instabilities and then stretched into finer diameters after quick solidification and get collected[65, 66]. The laboratory-available E-spin electrospinning instrument is procured from Nanotech, India. Electrospun nanofibers are usually

deposited on a grounded solid collector (e.g., a piece of aluminum foil) to form a nonwoven mat as shown in **Figure 16**. To better control the deposition of the nanofibers, various types of conductive solid collectors have been reported. Conductive solid collectors can be stationary or movable mode. For a stationary collector two different ways were mentioned:

(i) Patterning the surface of a conductive substrate with specific structures

(ii) Combining different substrates with distinct conductivities to form the pattern.

Moreover, metal stencil plates framed into various configurations, such as woven wire fabric, stainless-steel mesh, and copper grid, can be used to direct the deposited nanofibers toward the conductive regions, enabling the fabrication of a nanofibre-based mat that replicates the pattern on the original collector [67].

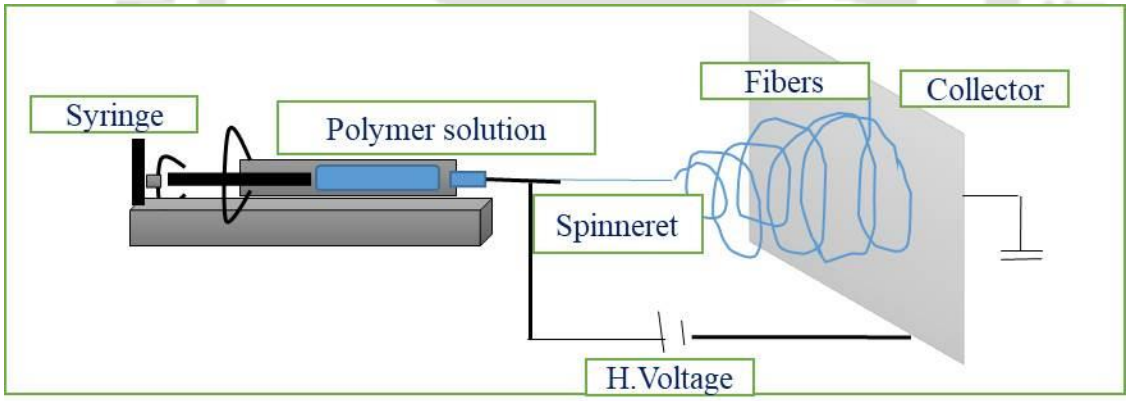

Figure 16: Schematic diagram of electrospinning technique.

****

CHAPTER 3

FABRICATION OF IN SITU *POLYMERIZATION OF PLLA/TCS NANOFABRIC*

Abstract: This study endeavored to explore and fabricate antiviral and antibacterial facemask using zinc (oligo-lactate) (ZL), developed through microwave synthesis technique. The prepared nano-fabric layer has excellent antiviral and antibacterial properties against Newcastle Disease Virus (NDV) and *E.coli, S.aureus* respectively. Thermogravimetric analysis (TGA) of ZL shows two steps thermal degradation, which confirms formation of low molecular weight end group lactyl units with zinc ions. Another investigation using varying ZL concentration and silk nanocrystal (SNC) with poly(lactic acid) (PLA) and electrospinning them into nanofibers, led to the fabrication of a facile and sustainable nanofabric that can be utilized as a protective layer for facemasks. Morphological analysis revealed a successful preparation of nanofabric with proper distribution and uniformity in fibre diameter. Hydrophobicity of the prepared nanofabric confirmed excellent protection from water droplets that may transfer during coughing or sneezing from an infected individual. Breathability and reusability test confirmed that prepared facemask could be reused by ethanol washing without compromising its surface properties till 4 cycles. The PLA/ZL nanofabric layer demonstrated 97% antiviral efficacy against NDV in 10 minutes. In conclusion, the electrospun nanofabric layered can be used as facemask having high hydrophobicity, good breathability, antibacterial and antiviral properties to control spread of contagious diseases.

Publications: Hazarika, D., Kumar, A., & Katiyar, V. Structural Evolution of in situ Polymerized Poly(L-lactic acid) Nanocomposite for Smart Textile Application. ***Scientific Reports***. **(Accepted 2021)**

3.1 Introduction

Rapid urbanization, industrialization, and fast population growth have resulted in enormous consumption of plastics for packaging, construction, and different household activities. These plastics are fossil fuel derived products and cannot be disposed easily after their end-of-life, as they are non-biodegradable; giving rise to serious environmental troubles by contaminating land, water as well as air. Biodegradable plastics are being looked upon as an alternative to these synthetic plastics due to their environmentally benign properties attained because of the presence of hydrolysable ester bonds that gets decomposed by microbial activity, thereby evading the use of thermal treatment techniques like incineration, which cause a lot of pollution[68].

Poly(lactic acid) (PLA), a linear aliphatic thermoplastic polyester, derived from 100% renewable resources, has been hailed by many researchers as one of the most promising bioplastic, owing to its eco-friendly nature, biocompatibility, biodegradability, and processability easiness [69, 70]. PLA is synthesized on a large scale either by direct condensation of lactic acid or by ring-opening polymerization (ROP) of cyclic lactide, with the later approach being more favorable due its solvent-free characteristic, resulting in no harmful byproduct formation [71]. PLA can be processed by film casting, extrusion, blow molding, or fiber spinning due to its greater thermal processability in comparison to other biomaterials such as poly(ethylene glycol), poly(hydroxyalkanoates), and poly(ε-caprolactone), leading to its widespread application in industries like textiles, biomedical and food packaging [72]. However, a few limitations of PLA such as low glass transition temperature, low melt strength, slow crystallization rate, low toughness, high brittleness, and low heat deflection temperature has made its use limited in broad scale engineering purposes [73]. Recent researches focus on using biofillers derived from plants and animals in the PLA matrix to improve its properties [74]. A recent study showed the

effect of silk nanomaterial hydrolyzed from muga silk cocoons as a biofiller for the improvement of crystallinity and thermal stability of PLA. These silk nanofillers originated from silk fibroin (SF) having repetitive and well-ordered β-sheets in their protein amorphous structure, displaying highly crystalline and hydrophobic properties [75]. These properties make them useful as a stiffening material in textile industries due to the presence of strong hydrogen bonding. Another study showed the application of magnetized silk nano-discs prepared by the co-precipitation technique and melt blended with PLA for tissue engineering purposes. Various studies have reported that doping of inorganic materials into organic nanomaterials can tune various properties of a polymer when incorporated into its matrix. Titanium dioxide (TiO_2), a metal oxide, also known as titania, has excellent chemical, structure, and thermal stability, and is also biocompatible and non-toxic, having high catalytic activity and low cost. Titania also possesses a unique self-cleaning property and can also function as a UV blocking agent. Anatase (ana), one of the three crystallographic polymorphs of titania, is highly photoactive in nature and had been used for the degradation of organic pollutants[76–78].

Commercialization of the application of PLA in textile commodities has been limited as PLA is prone to UV damage when exposed to sunlight for a long time, thereby restricting its usefulness as an environment-friendly material. The current study depicts the use of a biofiller supported with a metal oxide in the matrix of the biodegradable polymer, poly(L-lactic acid) (PLLA) to improve the crystallinity, thermal stability, and hydrophobicity of the prepared fabric. A facile sol-gel method was applied for the synthesis of polycrystalline ana-TCS, wherein SNC was used as the template. This anatase TiO_2 doped SNC nanohybrid acted as a nucleating agent and was incorporated into the PLLA matrix, resulting in the fabrication of a nanocomposite via a green synthesis route, i.e., in situ polymerization technique, which is essentially a solvent-free method. This is the first

study describing the in situ fabrication of a biodegradable and compostable PLLA/ana-TCS nanocomposite, spun into a nanofabric, behaving as a smart textile.

3.2 Results and Discussion

3.2.1 Molecular weight analysis

Molecular weight analysis reveals the chain distribution, which strongly depends on the synthesis parameters. The weight average molecular weight, $M_{w,}$ and number average molecular weight, M_n of the prepared nanocomposite were found to be 83 kDa and 150 kDa, respectively. A shoulder peak was seen near a high molecular weight position, signifying higher molecular weight grafted chains due to short and long branch formations [79]. The peak at elution time around 19.2 min appeared due to the mobile phase, chloroform, and other moisture traces if any.

3.2.2 Structural analysis

FTIR spectrum depicting the interfacial interaction of the lab-prepared ana-TCS, and PLLA/ana-TCS nanocomposite has been shown in **Figure 17**. The amorphous dried TCS powder gave broad peaks at 3340 cm^{-1} and 3017 cm^{-1}, which were assigned to stretching O–H groups adsorbed on the surface of TiO_2. After calcination, a band at 3274 cm^{-1} was observed due to the presence of unbonded N-H group of SNC, which was absent in as-prepared TCS due to the removal of adsorbed water molecules. The intense peaks found at 1695 cm^{-1}, 1634 cm^{-1}, and 705 cm^{-1} represented amide I due to their better arranged β structure in SNC after the removal of the amorphous part. Peak at 1534 cm^{-1} was for amide II (C-N) and peak at 1229 cm^{-1} was for amide III (C–N-H) [80, 81]. For nanohybrid, the peak for NH- shifted to 1530 cm^{-1} and was found to be highly intensified, suggesting bond formation between NH and OH- of TiO_2. Another slight shifting of the peak from 1632 cm^{-1} to 1629 cm^{-1} indicated bond formation between Ti-OH of titania and – C = O from the peptide bonds of SNC. It had been reported that the signals within

the range of 1000–400 cm^{-1} occurred due to the Ti–O, O–Ti–O, and Ti–OH bending vibration bonds, however observation of new peaks around 806 cm^{-1} was assigned to O–Ti–O bond [82]. In case of PLLA/ana-TCS, a band around 2916 cm^{-1} was assigned to aliphatic C–H vibrations. A decrease in intensity of C=O peak and appearance of a little hump due to –OH group of ana-TCS led to observation of bands at 1754 cm^{-1} and 1613 cm^{-1}, respectively. For neat PLLA, ester bond (C=O) was observed at 1752 cm^{-1}, asymmetric and symmetric C-O vibration bands were seen at 1182 and 1083 cm^{-1}, respectively, whereas the symmetric and asymmetric vibrations of C-H were observed at 1452 and 1361 cm^{-1}, respectively. The functional groups to confirm the grafting of ana-TCS with PLLA chains were established by shifting of PLLA chain groups assigned to C=O and C-O bonds, with a decrease in peak intensity at 1180 cm^{-1} and 1080 cm^{-1}, respectively [83]. Moreover, PLLA/ana-TCS nanocomposite showed a little broad peak at 3396 cm^{-1} due to the presence of few free –OH groups. A shoulder peak was observed at 734 cm^{-1} due to vibration of anatase phase Ti–O–Ti bond grafted with end group of PLLA chains [84–86]. An intensified peak assigned to the crystalline phase of PLA chains was found at 758 cm^{-1} due to its incorporation in nanohybrid. All these bonds confirmed the evolution of the structure in the prepared nanohybrid and nanocomposite.

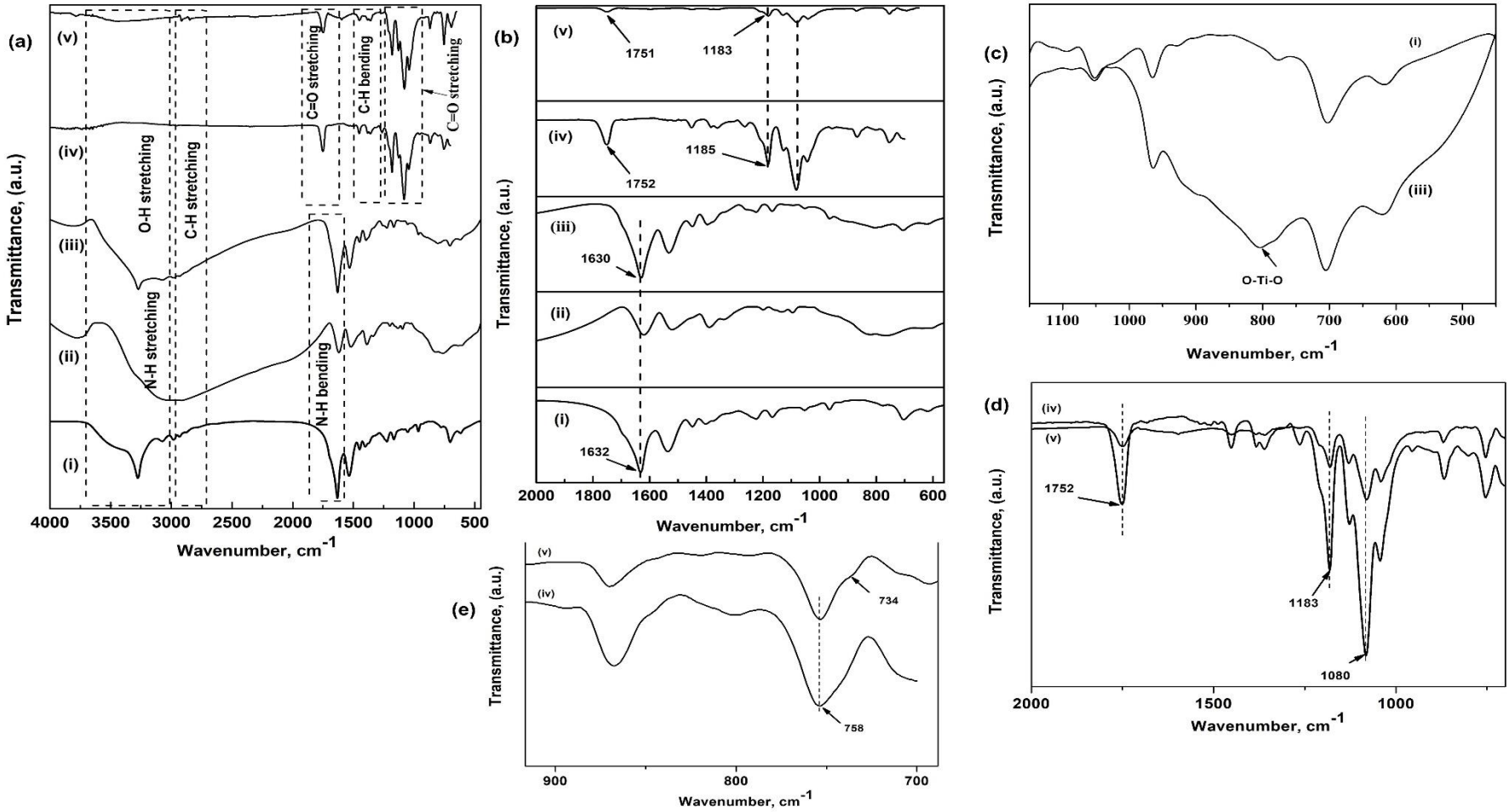

Figure 17: (a) FTIR spectra for (i) SNC; (ii) TCS; (iii) ana-TCS; (iv) PLLA (synthesized in lab for reference); (v) PLLA/ana-TCS, (b) Magnified FTIR spectra of the samples within the range of 2000-620 cm^{-1}, (c) Formation of O-Ti-O linkage in ana-TCS, (d) FTIR spectra of PLLA/ana-TCS within range 2000-700 cm^{-1}, and (e) magnified spectra showing presence of O-Ti-O bond in PLLA/ana-TCS.

The chemical shifts observed in the ^{1}H proton NMR spectra have a strong dependence on the intermolecular interactions of chains. $CDCl_3$ showed a resonance peak at 7.3 ppm and a little hump peak at 7.1 ppm was seen due to the –NH group of SNC nanoparticles. The -OH end groups of as-TCS played a major role in ring-opening of lactide monomers for their modification. The fabricated PLLA nanocomposite harbored –OH and –COOH functional groups at the two ends of PLLA chains. The resonance signal for the proton of CH_3 group and CH groups at δ = 1.6 and δ = 5.2 were assigned to the repetitive units in PLLA. The end group of PLLA chains showed a resonance signal at δ = 5, corresponding to the presence of methine group nearby the end -OH group [87, 88]. The ^{1}H NMR chemical shifts of CH- of Gly, –CH of Ala, and $–CH_3$ of Ala were seen at 4.1 ppm, 4.48 ppm, and 1.47 ppm, respectively [89]. Thus, the NMR characterization demonstrated fine structure of PLLA chains obtained by grafting its end group chains of –COOH with the TiOH- end groups, giving a resonance peak at 2 ppm. Moreover, another resonance peak at 3.73 ppm with five dips suggested the presence of four hydrogen atoms nearby, signifying the formation of a bond between Ti-OH and C=O of the Gly part of SNC. **Figure 18** shows the ^{1}H spectra of the prepared PLLA/ana- TCS. which is similar as discussed regarding the grafting of poly(D-lactic acid) and n-HAP [90].

XRD plots were used to confirm the crystallographic structure of the core nanomaterial (SNC) and the nanohybrid obtained after calcination, where area of crystalline peaks/ total area of peaks give crystallinity percentage (%). SNC showed diffraction peaks at 16.9° (002), 20.3° (201), 24.1° (003), 31° (300), 34.05° (004), 40.0°, and 43.45°, which were attributed to the conformational change from the structure of silk I to silk II, revealing the crystallographic structure of SNC [80, 81]. Considering the crystalline peak formula, the crystallinity % of SNC was calculated to be ~90% using the Origin Pro 8.5 software. **Figure 19** showed the plot of the as-prepared uncalcined TCS with less intense

characteristic peaks observed at 16.8°, 20.4°, 25.4°, 30°, 37.6°, 48°, 54°, and 62.8°, displaying that the amorphous nature of anatase TiO_2 had covered up the crystalline nature of SNC by engulfing SNC nanoparticles. These peaks became intense after calcination at 300 °C for 3 h. Ana-TCS showed a wide height at 2θ = 25.4°, confirming the formation of the TiO_2 anatase structure. The other noticeable shifts in the diffraction

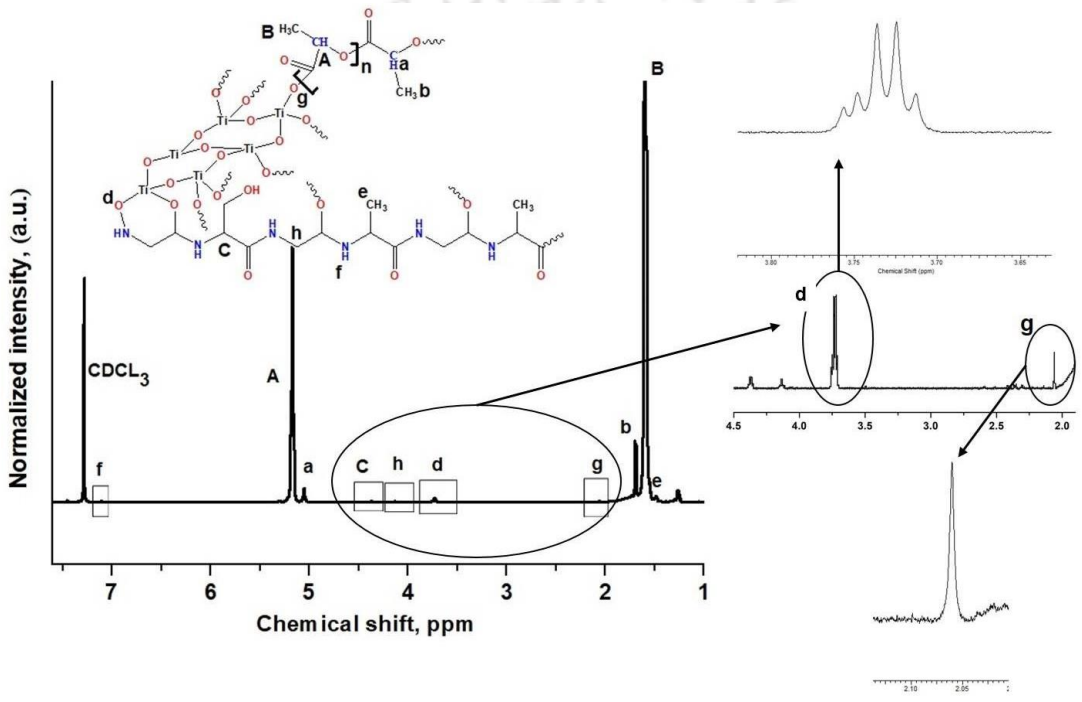

Figure 18: 1H NMR spectrum of PLLA-g-ana TCS, showing a magnified area within the range of 4.5-1.9 ppm.

peaks were observed at 38.08°, 48.0°, 54.35°, 62.8°, 69.7°, and 75.2°, corresponding to different planes, i.e., (101), (104), (200), (105), (204), (116), and (215), respectively, for the calcined anatase phase of TiO_2 supported over SNC. The ana-TCS had a crystallinity percentage of ~94% [91]. The PLLA chains showed diffraction peaks at 14.7°, 16.5°, and 18.9°, which were attributed to (010), (200/110), and (203) crystal planes[92]. The PLLA/ana-TCS had an increased crystallinity percentage of ~64% higher than the neat

PLLA 30% as reported[93], due to the formation of a grafted chain with PLLA end groups, confirmed by the overlapping peaks seen in **Figure 20**. Eventually, an intense diffraction peak at 16.64° reflected the highly crystalline nature of PLLA nanocomposite, with other peaks being observed at 14.72°, 19.0°, 22.27°, 29.1°, 31.39°, 35.44°, 41.61°, and 48.57°. The less intense, broad diffraction peaks at 22.27°, 31.39°, 35.44°, 41.61°, and 48.57° indicated very small-sized crystallite formations. The magnified image within the range of 35° to 55° as shown in **Figure 21** confirmed bond formation by broadening of the peaks between peptide chains and Ti-OH groups.

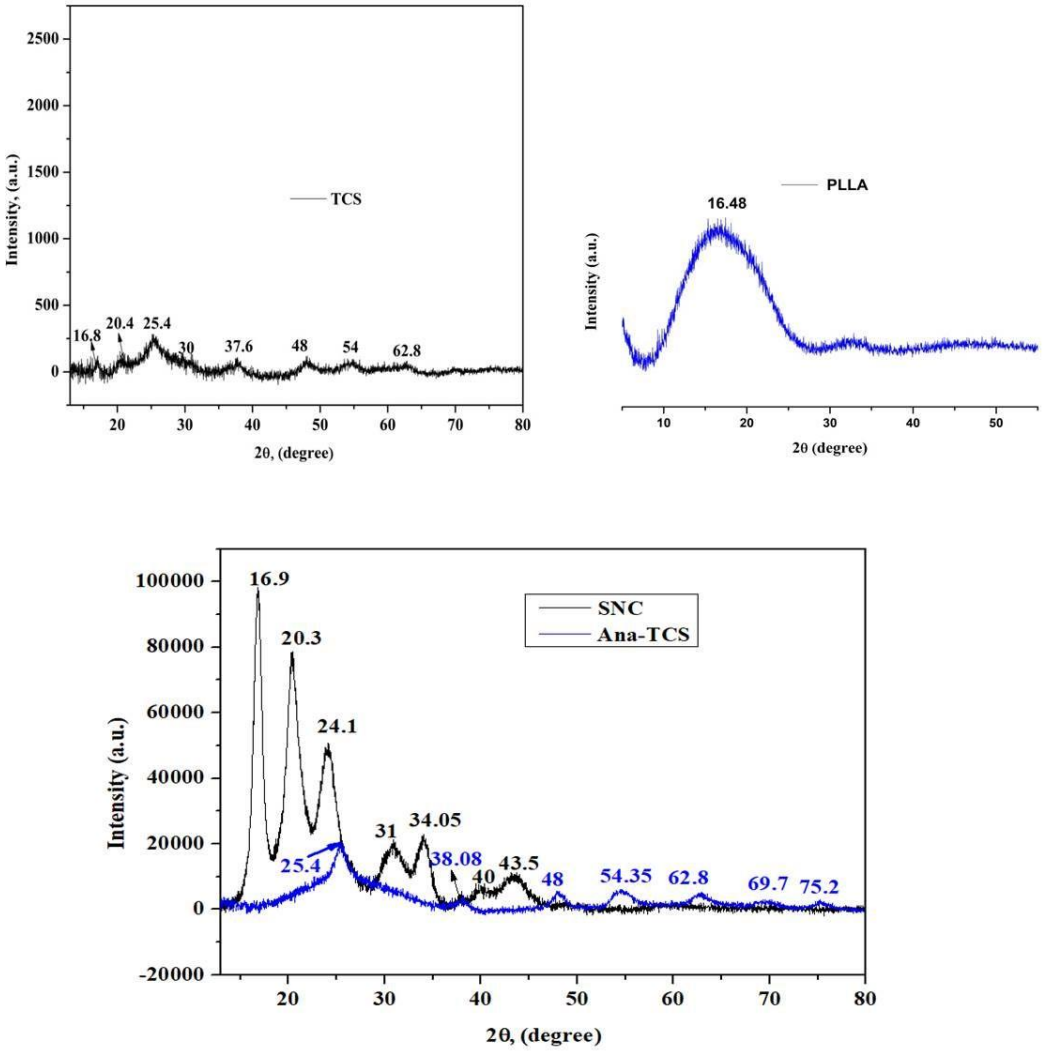

Figure 19: XRD spectra of the prepared TCS, PLLA, SNC, and ana-TCS (calcined at 300 °C).

The average crystal size estimation was done by calculating the full width at half maximum (FWHM) values using the Origin Pro 8.5 software, by selecting the peaks in the XRD plot and applying Debye-Scherer's formulae "Equation (1)". Whereas, the Bragg's law "Equation (2)" helped to interpret the interplanar d-spacing between the planes as follows[94].

$$D = \frac{0.9\lambda}{\beta Cos\theta} \quad \text{..... (xvii)}$$

$$2dSin\theta = n\lambda \quad \text{..... (xviii)}$$

Where λ = X-ray wavelength (0.154 nm), β = FWHM, Θ = Bragg's diffraction angle, D = Particle average diameter, and d = d-spacing.

The bulk anatase TiO_2 had the following lattice parameters: a=3.784 Å, c= 9.514 Å, α=β=γ=90°. The anatase form had a d-spacing of 0.352 nm for the (101) plane, which got shifted to a little higher d-spacing of 0.39 nm, with the 2Θ value shifting from 25° to 22.27°, confirming chain grafting in PLLA [95].

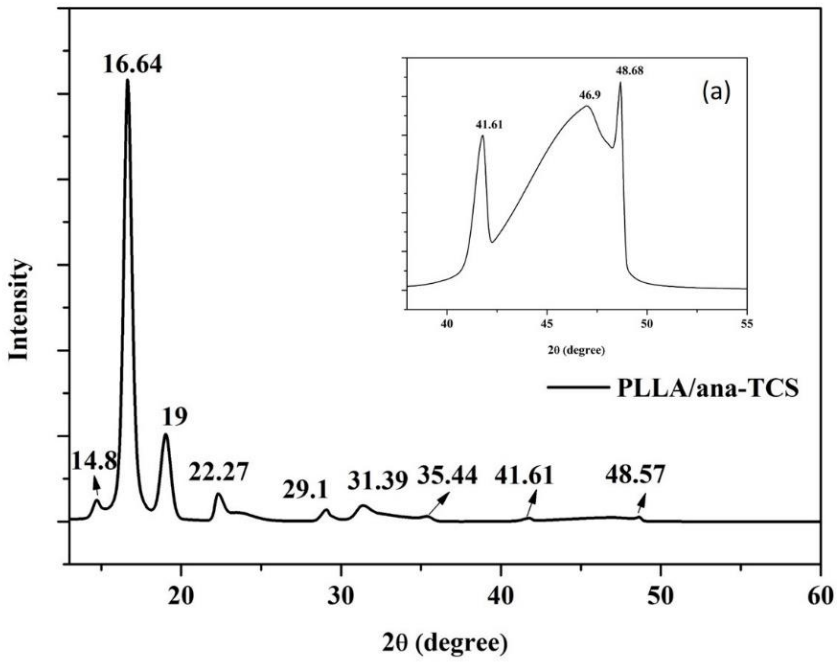

Figure 20: Structural evolution analysis using the XRD spectra of PLLA/ana-TCS, (a) inset: the magnified area between the range of 40-50° to show the peak at 48° clearly.

Raman spectroscopic technique was also used for determining the phase of prepared TCS. **Figure 21(a)** shows the characteristic shifted Raman peaks observed for ana-TCS nanohybrid. The peaks for SNC were reported to be present at 905 cm^{-1} and 965 cm^{-1}, corresponding to the -CN stretching and -CH_3 rocking, respectively [81], whereas in case of ana-TCS, the peaks showed a blue shift to 858.6 cm^{-1} and 950.29 cm^{-1}, respectively, suggesting formation of the nanohybrid. Anatase TiO_2 was found to be Raman active in the range of 100-900 cm^{-1}. The bands obtained at 162 cm^{-1}, 206 cm^{-1}, 396.7 cm^{-1}, 479 cm^{-1}, and 683 cm^{-1}belonged to the well-crystallized anatase form. A red shift of the peaks was observed due to a decrease in the particle size and bond formation between titania and SNC. The peaks at 162 cm^{-1} and 206 cm^{-1} were consistent with the Ti-Ti bonding [96]. Moreover, in the case of PLLA/ana-TCS nanocomposite, a sharp peak was

seen at 873.6 cm^{-1}, which was assigned to the –C=O stretching peak of the PLLA. The Raman plot of the in situ prepared PLLA/ana-TCS showed peak shifting to 160 cm^{-1}, 206.5 cm^{-1}, 398.4 cm^{-1}, 481 cm^{-1}, and 668 cm^{-1} due to bond formation between Ti-O-Ti and the C=O bond of PLLA chain end groups as shown in **Figure 21(b)**[97].

3.2.3 Water contact angle (WCA) analysis

The WCA measurement was performed without any irradiation on a solid surface. The WCA of the nanohybrid taken at 10 s was found to decrease to some extent when TiO_2 was supported over SNC, i.e., a reduction from 86˚ to 75.8˚ was seen due to the presence of –OH end groups on the surface of a complex network formed over titania nanoparticles. But when it was incorporated into the lactide during in situ polymerization, the WCA improved to 105.3˚ as shown in **Figure 21(c)**, signifying its good hydrophobic nature. PLA has a contact angle of ~78˚ generally, and an increase in the contact angle value for the PLLA nanocomposite was due to the formation of chain linkages between the end groups of PLLA and the surface hydroxyl groups of the ana-TCS as shown by NMR (decrease in open ended chains).

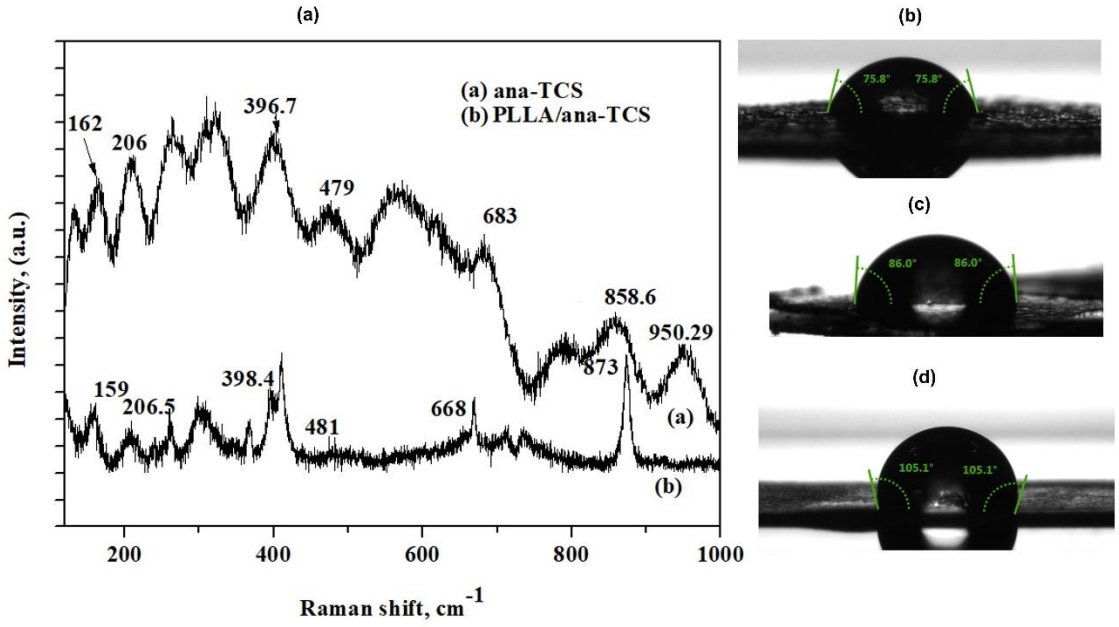

Figure 21: Raman spectra of (a) ana-TCS, PLLA/ana-TCS, (c) WCA meaasurement of (b) ana-TCS, (c) SNC and (d) PLLA/ana-TCS.

3.2.4 Morphological analysis

Figures 22 (a), (b), (c) and (d) shows the morphology of the fabricated nanoparticles, nanohybrid, and their elemental distribution. **Figure 22(a)** represents FESEM images of the structural shape of ana-TCS, which revealed a decrease in size of the anatase titania over the surface of SNC as compared to neat SNC on the same scale **Figure 23(a,b)**. **Figure 22(e)** shows the PLLA/ana-TCS, depicting bond formation between the carboxylic groups in PLLA with TiO_2 in a bridging bidentate, wherein the spherical titania nanoparticle supported SNC was incorporated in the PLLA matrix.

The composition of the calcined nanohybrid was observed by EDX analysis as depicted in **Figure 22(b)**, which demonstrated the formation of a well grown nanohybrid composed of titanium and oxygen layers. This analysis also showed the presence of 12.7 wt.% Ti. Additionally, elemental mapping analysis helps to investigate the distribution of the specific elements.

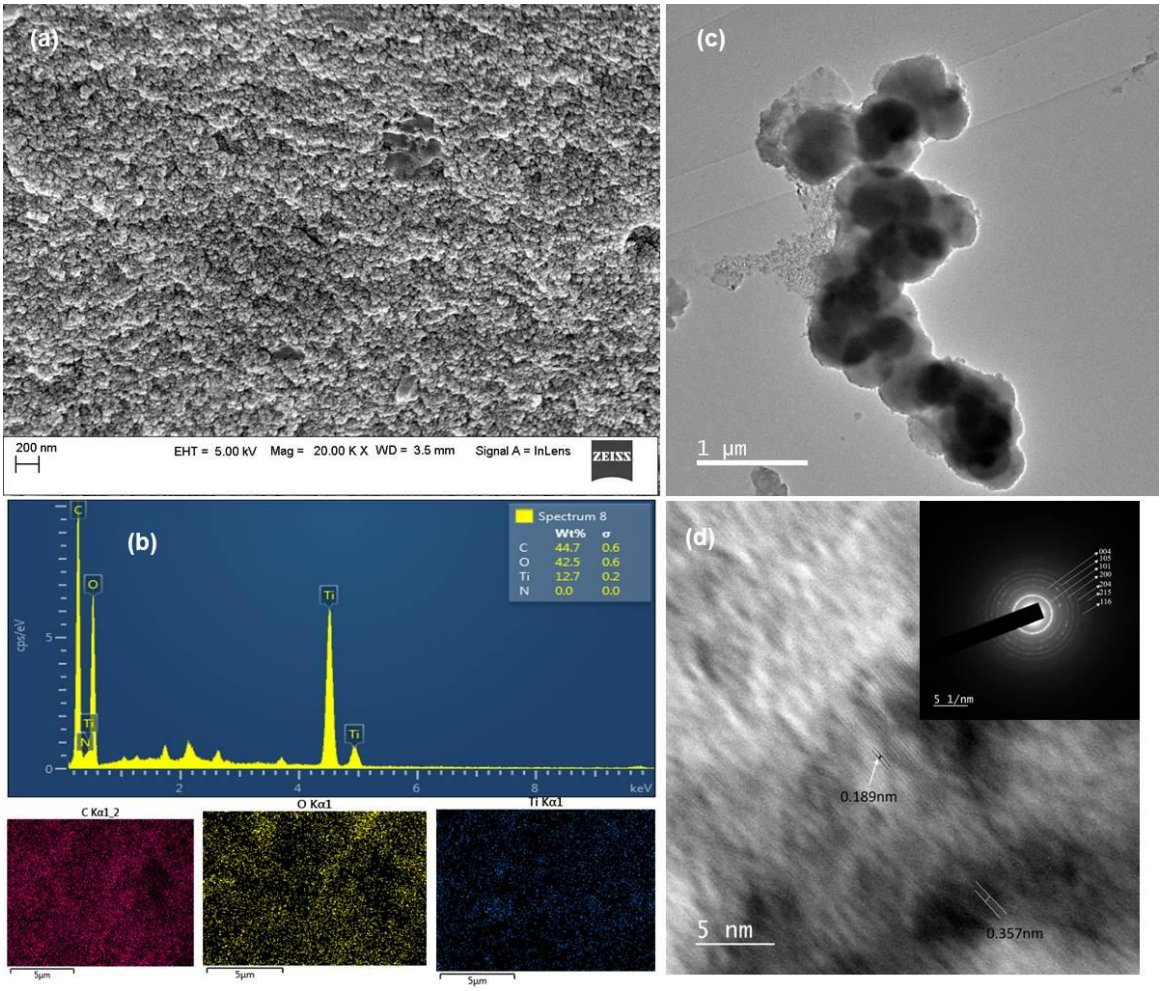

Figure 22: (a) FESEM micrograph showing SNC nanoparticles, (b) EDX analysis of ana-TCS (inset: mapping for Ti, O, N content with wt. % composition), (c) FETEM micrograph of the fabricated ana-TCS, (d) HRTEM image elaborating the d- spacing corresponding.

The absence of SNC wt.% indicated the creation of nanohybrid wherein the SNC nanoparticles were engulfed by Ti-OH bond from all sides. The anatase TiO_2 nanoparticles with a diameter of 7.5±1.4 nm was found to be doped all over the highly crystalline disc shaped SNC substrate (32±9 nm diameter and 4.2±1.2 nm width) in a well-ordered manner as unveiled by the FETEM images **Figure 22(c)**. A network formation was observed due to the polycondensation reaction of TiO_2 nanomaterials over SNC by the sol-gel process. In **Figure 22(d),** the HRTEM image shows two orthogonal lattice spacings of ~ 0.19 nm, corresponding to the characteristic d_{200} and d_{020} planes of

anatase titania, and 0.35 nm for the d_{101} plane [98]. On the other hand, SAED patterns revealed the visibility of highly polycrystalline circular rings for (101), (004), (200), (105), (204), (116), and (215) planes, corresponding to the anatase phase of titania. The calculated d-spacing value was matched with the value for anatase TiO_2 e phase having the same lattice planes. Incorporation of nanohybrid during the in situ polymerization of PLLA resulted in its network kind of distribution in the polymer matrix, as seen clearly in **Figure 23(e)**. From **Figure 23(f), (g)**, it was observed that the electrospun fibers formed a rough surface, having an average diameter of 178 ±30 nm. This surface property further enhanced the hydrophobicity of the prepared nanofabric with a WCA of 122°. The average dimensional calculations were done using Image J® software.

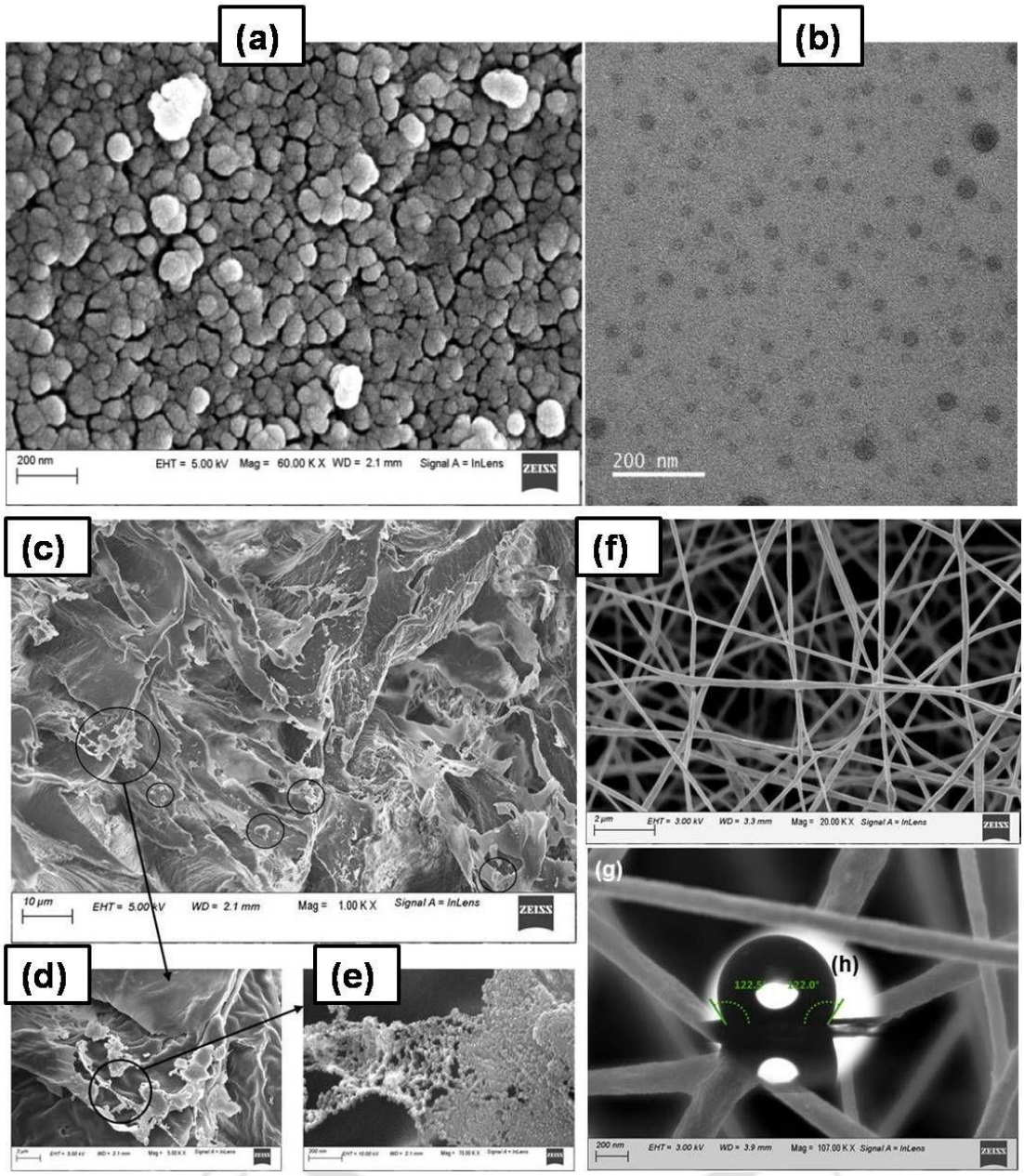

Figure 23: (a) FESEM and (b) FETEM images of SNC distribution at 200 nm scale, (c) FESEM micrographs of the PLLA/ana-TCS Nanocomposite, (d), (e) distribution of ana-TCS with network formation of TiO_2 over SNC nanoparticles in a magnified way, (f) PLA/ana-TCS electrospun nanofibre, (g) magnified smooth surface of the electrospun fabric, (h) WCA of the nanofabric material depicting surface morphology.

3.2.5 Thermal analysis

The thermal behavior of the degummed SF, SNC, TCS, ana-TCS, PLLA/ana-TCS are shown in **Figure 24 (a)**. In the case of nanomaterials and nanohybrid, peaks observed below 120 °C were due to the elimination of adsorbed water. The char residue enhanced

from 3.9% to 54% at 700 °C in case of ana-TCS, which might be ascribed to the presence of inorganic anatase TiO_2 doped over SNC, suggesting no further dissociation of carbonaceous material with an enhancement in thermal stability. The TGA thermogram of the nanocomposite showed maximum degradation at 320 °C for the PLLA chains and left back a char residue of 0.37% due to the incorporation of 0.5 wt. % of ana-TCS. This little change in the char value even upon incorporation was because of the grafting of the chains with PLLA end groups wherein the grafting % was found to be 26%. The TGA plot also suggested the successful synthesis of PLLA nanocomposite via in situ polymerization technique.

The PLLA chains crystallized in α form when T_c> 120 ˚C, wherein the melting and crystallization behavior was mostly related to chain entanglement. **Figure 24 (b)** shows the 2nd heating plot of DSC, which gave the values of T_g as 60 ˚C, T_{cc} as 125 ˚C, ΔH_{cc} as 165.2 J/g, endothermic peak with melting temperature as 173 ˚C and ΔH_m as -199.2 J/g.

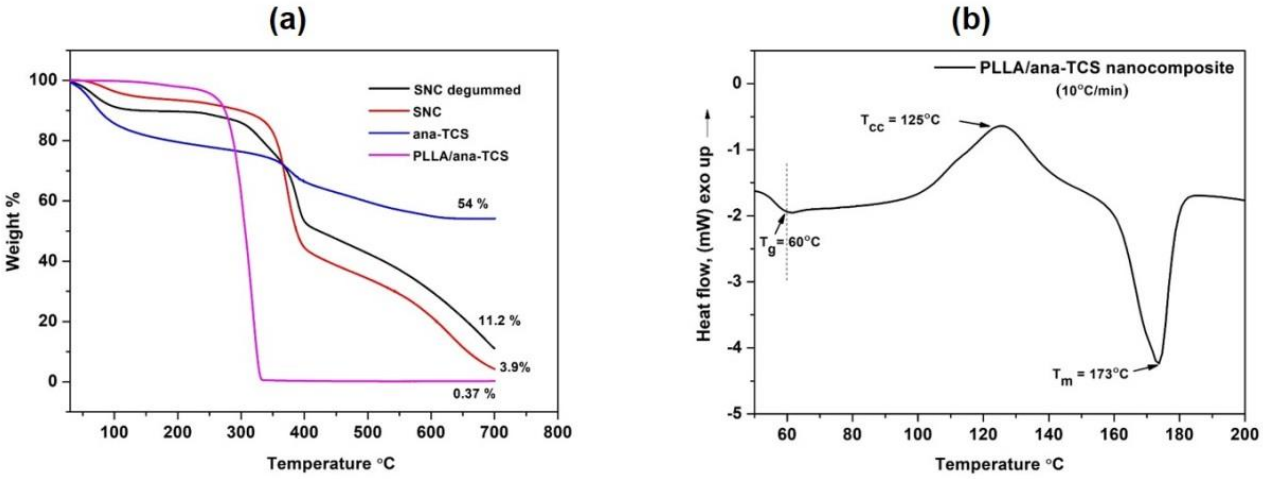

Figure 24: (a) TGA plot of SNC, ana-TCS, and PLLA/ana-TCS nanocomposite, (b) DSC thermograms showing T_g, $T_{cc,}$ and T_m of PLLA/ana-TCS nanocomposite.

3.2.6 Sperulite growth analysis

PLLA showed a characteristic slow crystallization behavior, and therefore the presence of nucleating agents might induce the growth of crystals. The presence of long grafted

compatible nanofillers throughout the polymer matrix regulated the rate of nucleation and the density of spherulites, by accelerating the crystallization process. POM images of the isothermally crystallized PLLA/ana-TCS nanocomposite showed a maltese cross pattern **Figure 25(a)**. As time escalated, there was an increase in the size of the spherulites very quickly, covering the whole area in only 275 s. It might be due to the presence of grafted chains which induced crystallinity, filling up the free volume, thereby overlapping the nearby spherurites, suggesting high crystallinity of the nanocomposite. **Figure 25(b)** shows the POM micrographs of the PLA-based ana-TCS nanocomposite at different time intervals. The average diameter of the full-grown spherulites were found to be 160±15 μm in 220 s and covered the whole area in 275s.

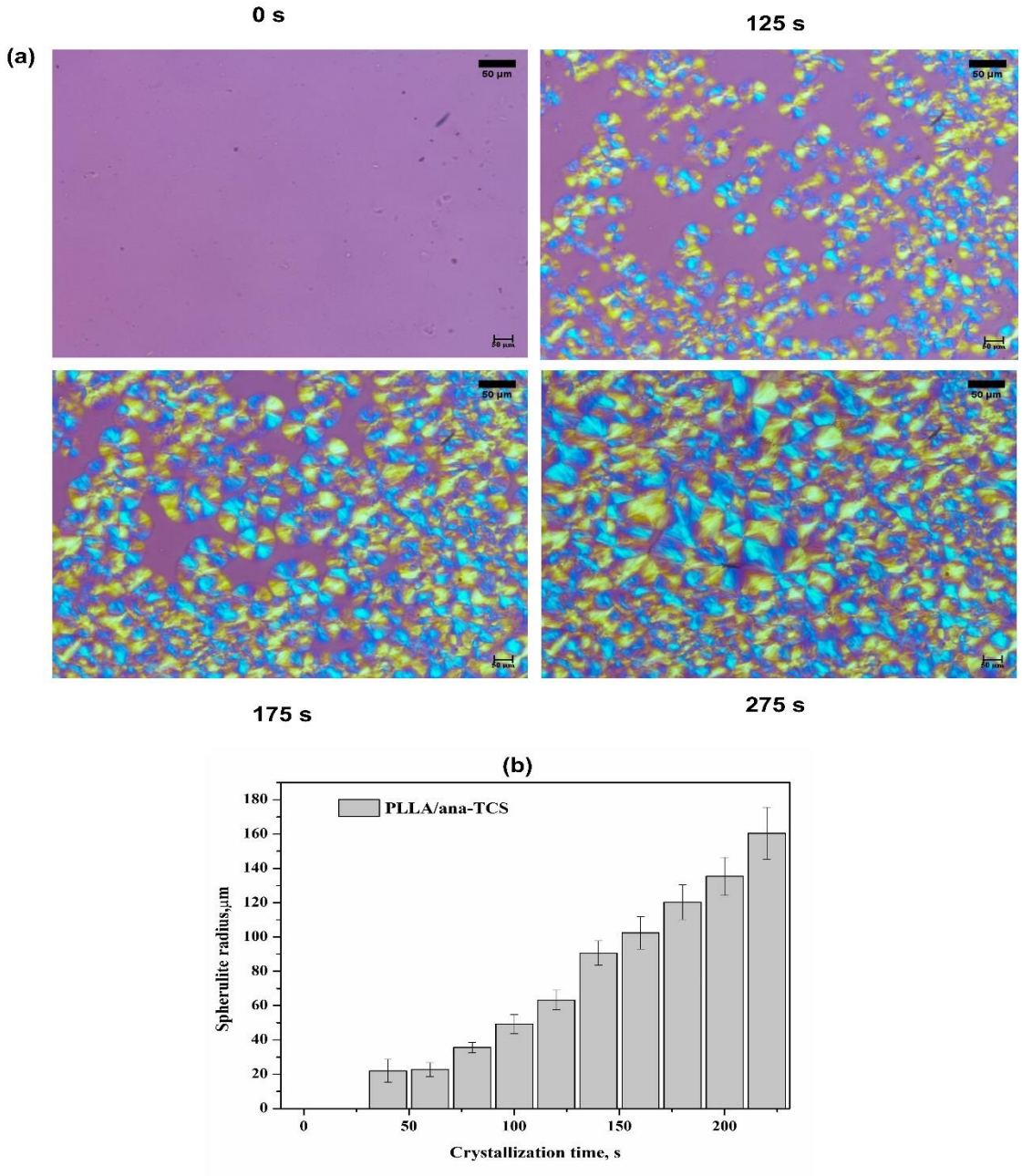

Figure 25: (a) POM images showing spherulite growth formation in the nanocomposite at isothermal condition of 120 °C, (b) Histogram plot showing spherulite growth rate in the nanocomposite with increasing crystallization time.

3.2.7 Photocatalytic activity analysis

To evaluate the experimental parameters obtained due to catalytic photodegradation, UV-vis spectroscopy was used to determine the decrease in band intensity at wavelength peaks of 245, 292, and 610 nm, and at a maximum peak of 664 nm with an increase in

time. **Figures 26 (a)(b)** shows that when anatase TiO_2 nanoparticles were doped over SNC nanoparticles, the dye started to decompose MB at a quick rate. This could happen due to the vigorous oxidizing activity of the photo-generated holes or due to OH· groups [99]. The reason behind this was the position of the conduction band such that it either reduced the oxygen molecules present or got adsorbed on the surface of MB. Therefore, due to the adsorption of MB over metal oxide, the blue coloration of the solution faded away after 15 days of time under UV illumination. The chromophores present in MB were mainly responsible for the discoloration of the solution [100]. The mechanism that took place due to the degradation of MB dye resulted in the generation of conduction band (e^-) electrons and valence band (h^+) holes when ana-TCS was irradiated with light energy greater than or equal to its band gap energy. These holes and electrons mediated the oxidation of organic compounds to (OH•) radicals and (O2•-) superoxide radicals. The ($OH^•$) oxides then degraded most of the MB colorant into non-toxic products [101].

A parallel study was done for the in situ synthesis of PLLA using nanohybrid so that the PLLA nanocomposite could act as a catalyst for dye removal when exposed to UV irradiation **Figure 27(a), (b)**.

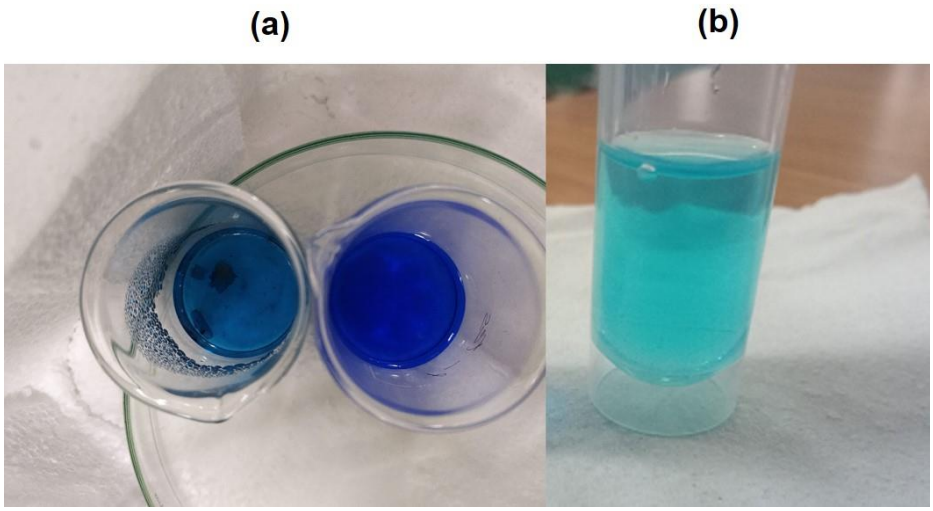

Figure 26: Digital images showing photocatalytic degradation of MB by (a) PLLA/ana-TCS as compared to crude MB and (b) ana-TCS nanohybrid.

For calculating the percentage degradation under UV irradiation, the ana-TCS values were taken and absorbance was calculated for all the humps, following the modified equation “Equation (3)” of Beer-Lambert Law.

$$\% \text{ Degradation} = \left(1-\frac{A_t}{A_o}\right) \times 100 \quad \text{.....(xix)}$$

Where A_0 = initial absorbance of dye at time 0 min, and A_t = absorbance of dye after time t min. Similarly, the kinetics of the photodegradation rates of most of the organic contaminants followed pseudo-first-order kinetics as given by the following equation “Equation (4)”.

$$-dA/dt = k_{obs}\, A \quad \text{..... (xx)}$$

Where A = absorbance of MB, k_{obs} = observed value for pseudo first-order kinetics after integrating it from A_o to A_t. The R^2 value was found to be almost equal to 1 for the peaks observed at 610 and 664 nm other. **Figure 27(c**) depicts the best fitted equation. Thereby, the peak at 664 nm was considered for calcultions as it had R^2 = 0.995, using which the dye degradation of MB was found to be 43%.

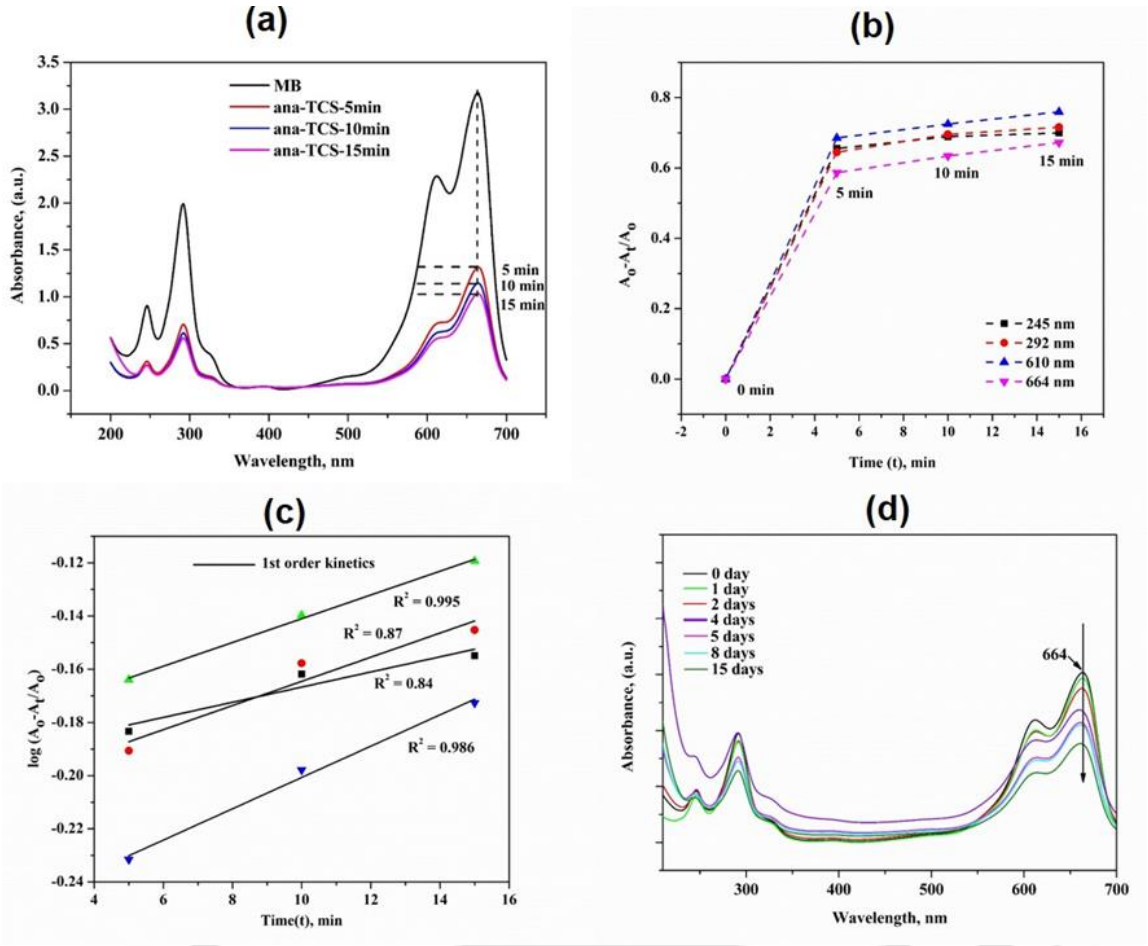

Figure 27: (a)Photocatalytic activity of ana-TCS in organic dye (MB), (b) Discoloration plot showing absorbance change with time, (c) Pseudo-first order kinetics for the 664 nm peak wherein R^2~1, (d) MB discoloration plot for the PLLA/ana-TCS nanocomposite with time for the peaks 610 nm and 664 nm.

3.2.8 Effect of MB adsorption under neutral pH

To evaluate the adsorption of MB cations on the surface of the prepared nanocomposite, the change in weight of the material, and molecular weight change after the 15th day was noted, by dipping the piece into MB solution under UV light (pH=7). For reference, the degradation of neat PLLA was also checked under neutral pH.

Neat PLLA degradation was studied by dipping the polymer in DI water for 15 days and noting down the readings. It could be seen from **Figure 28(a-d))** that there was very less change in the weight of neat PLLA at pH 7. The change in molecular weight for neat PLLA was calculated and it was found that almost 25% polymer had been degraded. But,

when PLLA/ana-TCS nanocomposite was treated with MB for its discoloration under UV irradiation, 3% of adsorbate was adsorbed on the surface of PLLA/ana-TCS due to the presence of Ti-OH group which reinforced its self-cleaning property **Figure 28(c)**. Moreover, the molecular weight value of the nanocomposite was found to be decreased by 50%, suggesting increased degradation rate for the prepared PLLA nanocomposite in comparison to the neat PLLA, which would further lead to the development of a sustainable environment.

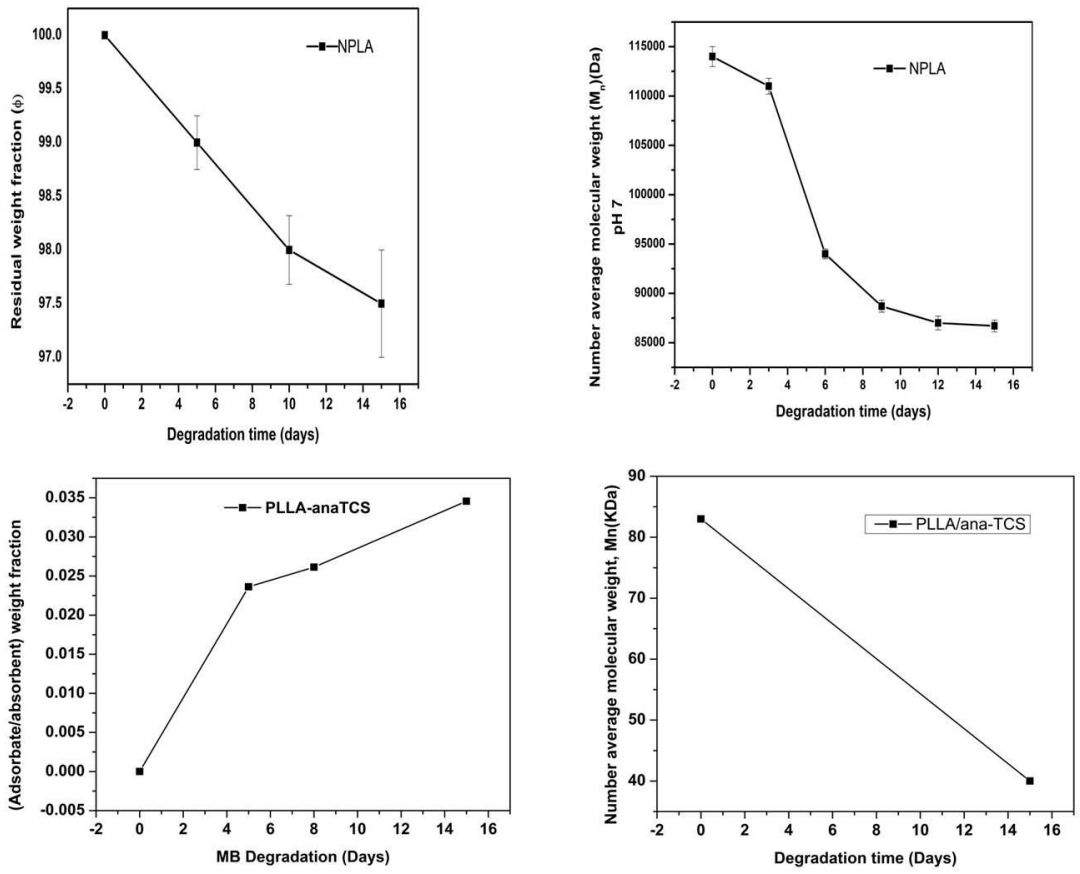

Figure 28: (a) Change in residual weight fraction of PLLA kept in water for 15 days for degradation, (b) Number average molecular weight vs. Degradation time of PLA, (c) Adsorbate/Adsorbent vs. MB degradation plot, (d) Number average molecular weight vs. degradation time of PLLA/ana-TCS nanocomposite.

3.3 Conclusion

In the present study, a single-phase SNC templated anatase TiO_2 (ana-TCS) nanohybrid was successfully prepared by a novel sol-gel process in an aqueous media, followed by aging at room temperature to promote crystallization. A crystalline anatase phase network-like structure of TiO_2 engulfing SNC was found to form after post-treatment at high temperature, resulting in the formation of ana-TCS nanohybrid. Furthermore, incorporation of this nanohybrid as a co-initiator during ring-opening polymerization of lactide rings via an in situ polymerization process, subsequently led to the fabrication of high molecular weight PLLA grafted ana-TCS nanocomposite. As a result of the inclusion of ana-TCS into the PLLA matrix, the crystallinity, as well as the thermal stability of the nanocomposite, increased. The prepared PLLA-g-ana-TCS nanocomposite presented a highly hydrophobic surface to remove dye and acted as a self-cleaning material. XRD and POM analysis showed that the prepared nanocomposite was a crystalline material, showing fast spherulite growth. The work also showed that the prepared nanohybrid could act as a nucleating agent under isothermal conditions. The fabricated ana-TCS/PLLA nanocomposite also promoted significant photocatalytic tendency within 15 days of time by degrading 43% of the organic dye, MB under UV irradiation at neutral pH. Additionally, the PLLA component in the nanocomposite underwent no significant hydrolytic degradation when dipped in an aqeous solution for 1 h. Thus, the developed nanofabric could be promoted as a degradable, self-cleaning cloth material which could be a way forward to tackle the serious environmental problems of discard of textiles in both landfills as well as in marine regions by industries, and which could also be used for waste water treatment.

****

CHAPTER 4

FUNCTIONALIZED POLY(LACTIC ACID) BASED NANO-FABRIC FOR FACE MASK AND FILTER APPLICATIONS

Abstract: This chapter endeavored to explore and fabricate antiviral and antibacterial facemask using zinc (oligo-lactate) (ZL), developed through microwave synthesis technique. The prepared nano-fabric layer has excellent antiviral and antibacterial properties against Newcastle Disease Virus (NDV) and *E.coli*, *S. aureus* respectively. Thermogravimetric analysis (TGA) of ZL shows two steps of thermal degradation, which confirms formation of low molecular weight end group lactyl units with zinc ions. Another investigation using varying ZL concentration and silk nanocrystal (SNC) with poly(lactic acid) (PLA) and electrospinning them into nanofibers, led to the fabrication of a facile and sustainable nanofabric that can be utilized as a protective layer for facemasks. Morphological analysis revealed a successful preparation of nanofabric with proper distribution and uniformity in fiber diameter. Hydrophobicity of the prepared nanofabric confirmed excellent protection from water droplets that may transpire during coughing or sneezing by an infected individual. Breathability and reusability test confirmed that prepared facemask could be reused by ethanol washing without compromising its surface properties upto 4 cycles. The PLA/ZL nanofabric layer demonstrated 97% antiviral efficacy against NDV in 10 minutes.

Publication: Hazarika, D., Kalita, N. K., Kumar, A., & Katiyar, V. (2021). Functionalized poly (lactic acid) based nano-fabric for anti-viral applications. RSC Advances, 11(52), 32884-32897.

4.1 Introduction

The aggressive necessity and application of facemasks, personal protective equipment (PPE) is now a new normal commodity. World Health Organization (WHO) dictated standard safety procedures to make them wearable for every human being that may diminish the ongoing infection risks of novel coronavirus (COVID-19). Facemasks with and without filter has been mostly used. Most commonly used facemasks are surgical facemasks and respirator masks like P2 and N95. Moreover, depending on the demand and supply of conventional polymers will give rise to new polluted episodes in near future [69, 102]. For facemasks with addition to filtering capacity, other factors are also important such as user comfort and breathability. For instance, although the tight-fitted N95 respirators without any functional features are having superior filter capacity than the surgical masks it lowers the breathability, sweating, causing discomfort after wearing for hours [70]. Furthermore, strengthening the thinking in research to provide eco-friendly alternatives and enhancing effective waste management systems can assist in finding a sustainable solution to plastic pollution that may arise from PPE equipment and accessories. However, utilization of sustainable and biodegradable based protective masks can lead us to overcome such problems [71]. Most of the single-time usable masks are made of polypropylene, polyethylene, polyester, polyurethane, polyacrylonitrile, polystyrene, or polycarbonate [103]. Mainly consists of an inner layer as soft fibers, middle layer by melt-blown filter, and outer layer made with nonwoven fibers, which are water-resistant. In general, fibrous materials were used to create particulate matter filters (PM), which can be planned accordingly to PM particular size. PM thereby classified by PM 0.1 as ultrafine (< 0.1 μm), PM 2.5, fine (0.1–2.5 μm size) and PM 10, course (2.5–10 μm) [73, 104]. There are particles just between the range of micro and nano in a tune of ~ 300 nm for such cases electrospun nanofibers are proven more efficient and address

two competing demands i.e. air filterability and air breathability. Focussing on nanoscale sized virus, non-woven filters are better when compared to natural fiber cotton, petroleum-based polyester polymers, and some woven filters of advanced nature [105]. These nonwoven filter media can be manufactured by using Electrospinning technique, a very efficient, lowcost technique to produce nanofibers mat for several applications having distinct features like higher surface area to functionalize for uniform morphology, structural consistency properties, and desired property [106].

Disinfection of mask is another parameter that needs to be addressed. Since reusability of mask would determine its economic viability as well as value addition in comparison to one-time use face masks. Cloth masks are generally disinfected by washing with detergents and bleach. Similarly, N95 masks and surgical masks are either heat-treated or UV treated and these processes are discrete and don't always guarantee contamination removal before reuse and get contaminated during reuse very easily. Therefore, masks with antimicrobial activity can automatically kill contaminations during their service life. These antimicrobial masks when made with hydrophobic materials can guarantee self-disinfection capacity and protect from moisture that is accumulated on the masks while speaking in the form of saliva droplets or sneeze droplets. Hydrophilic or the hydrophobic nature of the filter surface also plays an important role in providing favorable or unfavorable environments to different types of bacteria and viruses [107].

Zinc is a metal that has been purported to have antimicrobial properties. Zinc lactate, a salt obtained from reacted zinc and lactic acid (by bacterial fermentation). Various mechanisms are reported that show antimicrobial properties of lactic acid and their salts as in acidic environment, they act as ionophores and decrease the intracellular pH in bacteria[27, 28, 108]. Zn lactate may possess a protective effect and adjuvant therapy of COVID- 19 infection for the whole world. From the report zinc is considered as a

potential supportive treatment in the therapy of COVID-19 infection due to its antiviral effect and immune-modulatory effect [29]. Hence, Silk is harvested from silkworms made by silk moth caterpillars, like (domesticated silk moth namely Eri, Muga, Tassar silk), *Bombyx mori*, and Robin moth, *Hyalophora cecropia.* This silk fiber produced from their cocoons has been historically acting as "queen of textile'. Silk generally contains natural antimicrobial, antibacterial properties which traits their potentiality to ward off microbes, bacteria, viruses [109]. Due to good biocompatibility, controllable biodegradability, and easy fabrication into different forms, such as fibers, films, gels, and three-dimensional scaffolds silk fibroin has been used in biomedical material for long a time [110]. Silk due to its hydrophobic nature has been extensively reported for its use as fabric and as protective respirators. A study has been performed on crystallinity, hydrophobicity improvement by tuning molecular structure into nano-level through various routes like alkali treatment, enzymatic hydrolysis, partial acid-hydrolysis [81]

Different fabrication techniques have been utilized for making polymeric fabric. Among them, electrospinning technique is basically for nanofibers preparation acting as the best replacement for microfibers and thin films. Thus, nanofiber filters can be gradually utilized for masks applications globally. Collectors used during electrospinning of fibers may consist of several materials. Nanofibers produced during this technique are collected in different collectors. Most commonly collectors used are aluminum foils while others such as conductive cloth/paper, rotating wheel or rod, parallel bar, wire mesh, etc. [66, 111].

Among the various biodegradable polymers [112], PLA has its applications in many manufacturing industries, such as in fibers, textiles, plasticulture, packaging industries, and service ware [113, 114]. Furthermore, PLA exhibits excellent properties such as

nontoxic, strong mechanical strength, and good fiber-forming ability. This made PLA a strong candidate for fabrication of nanofabric.

Literature have reported that Zn powder, a cheap and easily available catalyst with microwave technique was used to produce moderate molecular weight PLA with high purity [57]. Another study was reported on PLA and lactic acid-grafted-Gum Arabic by polycondensation reaction in a microwave reactor without using any catalyst which was further solution cast with PLA for packaging application [115]. Studies demonstrated the preparation of antimicrobial hybrid materials using PLA as nonwoven fabrics, where phosphoro-organic compound-fosfomycin was used as a coating and modifying agent [24]. Nonwoven mats are made of a PLA/chitosan (PLA/CS) blend and PLA/CS blend containing silver (Ag) nanoparticles (Ag/PLA/CS) by electrospinning technique. The Ag blended nanocomposite had better antibacterial activity against the E. coli and S. aureus bacteria [58]. Another study was performed using electrospinning to prepare PLA/TiO_2 nanofibers where it was found that the antibacterial activity improved under UV-A irradiation, and 0.75 wt.% TiO_2 content nanofibers and films exhibited inhibition zones for *E. coli*, 4.86 ± 0.50 and3.69 ±0.40 mm and for *S. aureus*, 4.63±0.45 and 5.98 ± 0.77 mm [59]. Another study prepared activated charcoal (A.C.) reinforced polylactic acid (PLA) nanofiber membranes produced by electrospinning technique. It was found that Bacterial Filtration Efficiency (BFE) (% and Submicron Particle Filtration Efficiency (%) is ≥98%, which may act as personal protective equipment [116]. Few reports

This work focuses on easily available materials that would be beneficial for making face coverings, according to guidelines of current public health, so that they can be worn during shortage of standard PPE. Currently, various studies have been associated with different materials, from natural fiber spinning to synthetic fabrics for preparing and making them commercially available or do-it-yourself face coverings. Even to block

droplets and micro/nanoparticles, as well as identifying perfect facilitates for comfort, wearability, and reusability, face coverings are now gaining full attention to get relief from such situation. Therefore, in our current study, we have conducted an efficient strategy to prepare a material zinc oligo-lactate by microwave synthesis to act like a warrior during this situation. The prepared material with silk nanocrystal has been spunned with compostable PLA into a nanofabric form for constructing face coverings. Silk nanocrystal, in their level of hydrophobicity acts as a preventer for penetration and absorption of droplets, whereas ZL acts as an antiviral agent to prevent transmission of the virus. In addition, the prepared fabric was tested for cleaning by its reusability test and porosity.

4.2 Results and Discussions

4.2.1 Reaction Mechanism

Microwave-assisted single pot polymerization route is more favourable than the polycondensation and ring-opening polymerization to synthesize a low molecular weight polymer. Microwave synthesis is environment-friendly, less toxic in terms of performing at high temperature and for a long time, no use of toxic catalyst and initiator. Initially, the reaction takes place between lactic acid (water-soluble) and Zn powder (insoluble in water) and the system water absorbs microwave energy and dielectric heating generates ion radicals. These ion radicals then react with water and form free hydroxyl radicals. The free radicals of lactic acid then attach with the electropositive ions Zn^{2+} to functional groups i.e. OH from OLLA chains as shown in **Figure 29(a),(b)**.

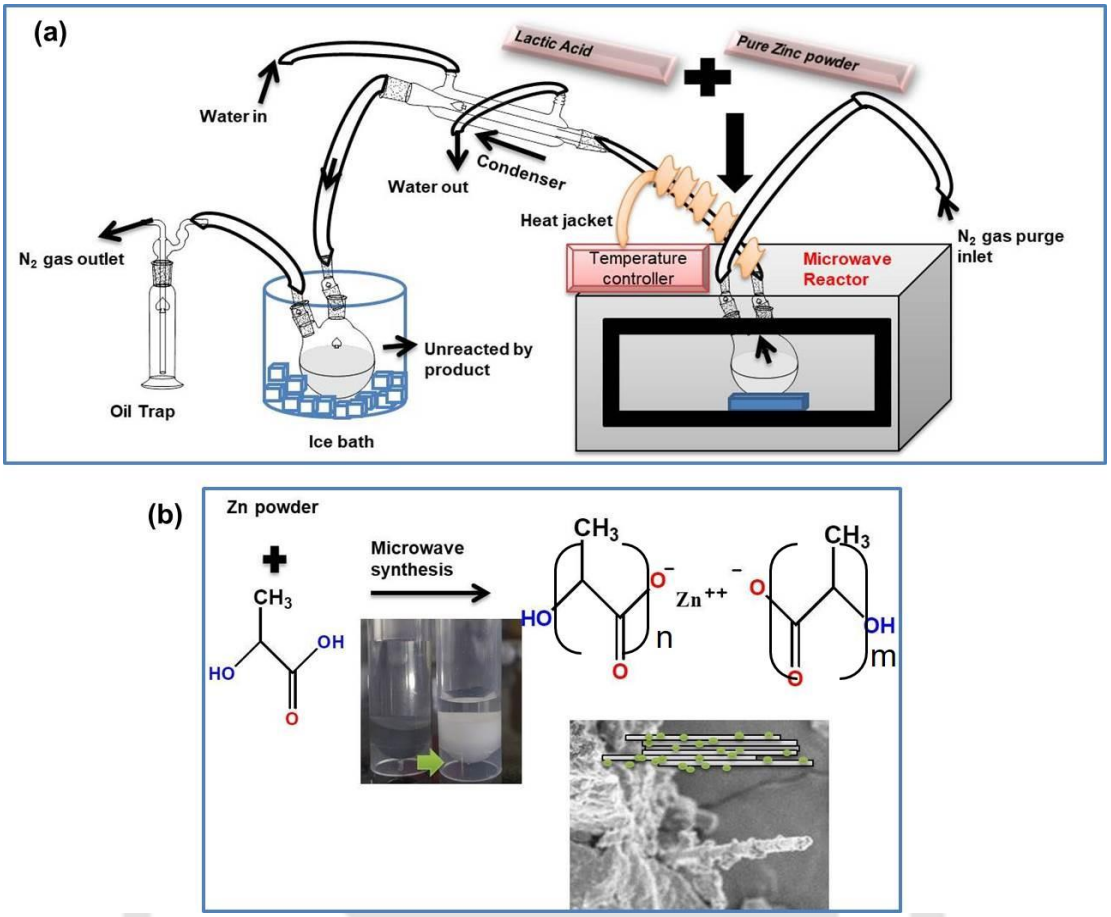

Figure 29: (a) Microwave-assisted synthesis setup for ZL, (b) schematic reaction for ZL formation.

4.2.2 ^{1}H proton NMR

The structural details of LA and ZL were compared by their peaks position with their shifting as shown in **Figure 30.** As reported for only oligomers the peaks of OLLA are obtained at 5.13, 1.56, and 1.24 ppm, which represent –CH protons of OLLA, $-CH_3$ protons, and $-CH_3$ protons of hydroxylated OLLA respectively [117]. The extra new peaks observed at 5.05, near 4.26, 4.09, 1.24, and 1.19 ppm attributed to –CH protons of repeating lactyl units, terminal –CH adjacent to Zn^{2+} of repeating unit, terminal –CH protons of hydroxylated lactyl units, $-CH_3$ of lactyl units at terminal groups and $-CH_3$ protons of hydroxylated lactyl units at terminal groups respectively. The lactic acid proton NMR shows the peak at 4.02 and 1.06 attributing to the terminal –CH and $-CH_3$ proton. The magnified plot **(inset: Figure 30(c))** shows the presence of the repeat lactyl

units, which confirms the formation of oligomer chains with zinc^{2+} thereby leading to the synthesis of ZL.

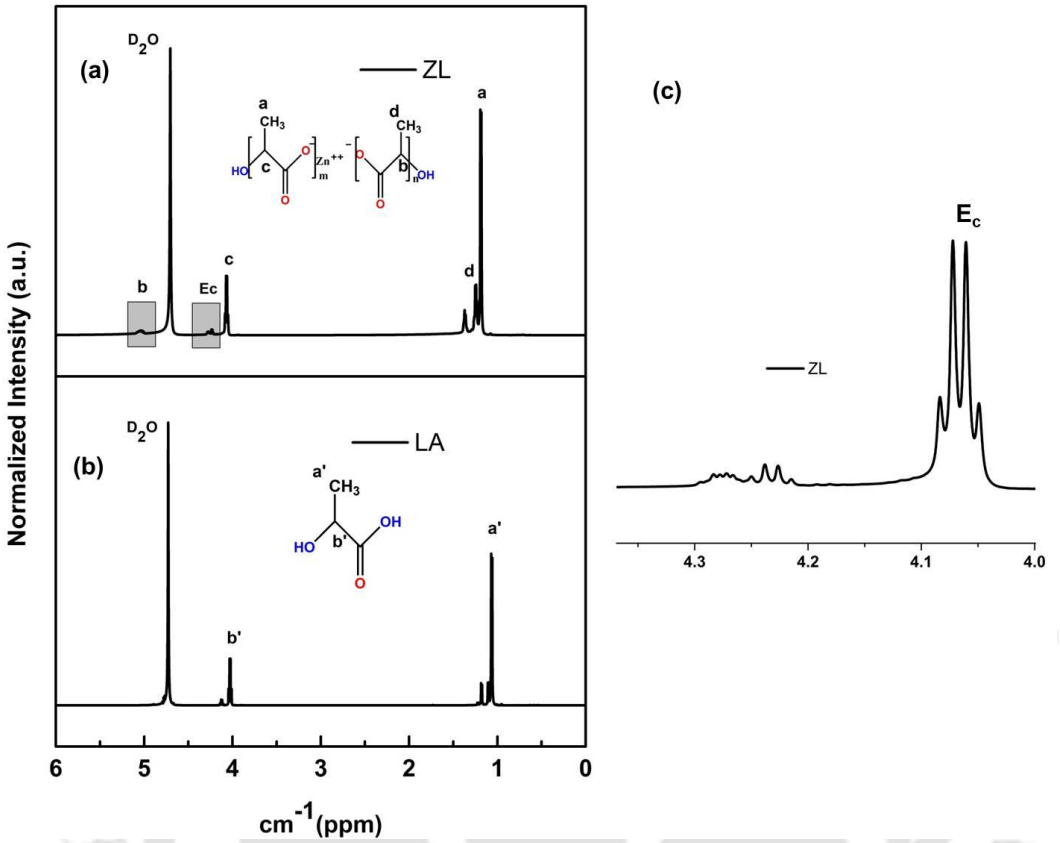

Figure 30: (a) 1H-NMR spectrum of ZL (b) Lactic acid, LA (c) magnified image of ZL spectra within range 4-4.3 ppm.

4.2.3 FTIR analysis

Figure 31(a-c) shows the FTIR spectra of LA, ZL, and PZL25 which was used to study the structural formation and chemical footprints. For lactic acid the band at 3430 cm-1 corresponds to O-H stretching vibration. Whereas for the case of ZL there is shifting of the OH group which signifies the formation of bond with –OH group of lactic acid. –C=O bond stretching vibration at 1745 cm^{-1} and the –C–O– bond at 1379 cm^{-1}, the asymmetric stretching vibration of the –COO– bond at 1589 cm^{-1} suggests formation of ZL. The band at 1666 cm^{-1} results from the bending mode of water absorbed by ZL.

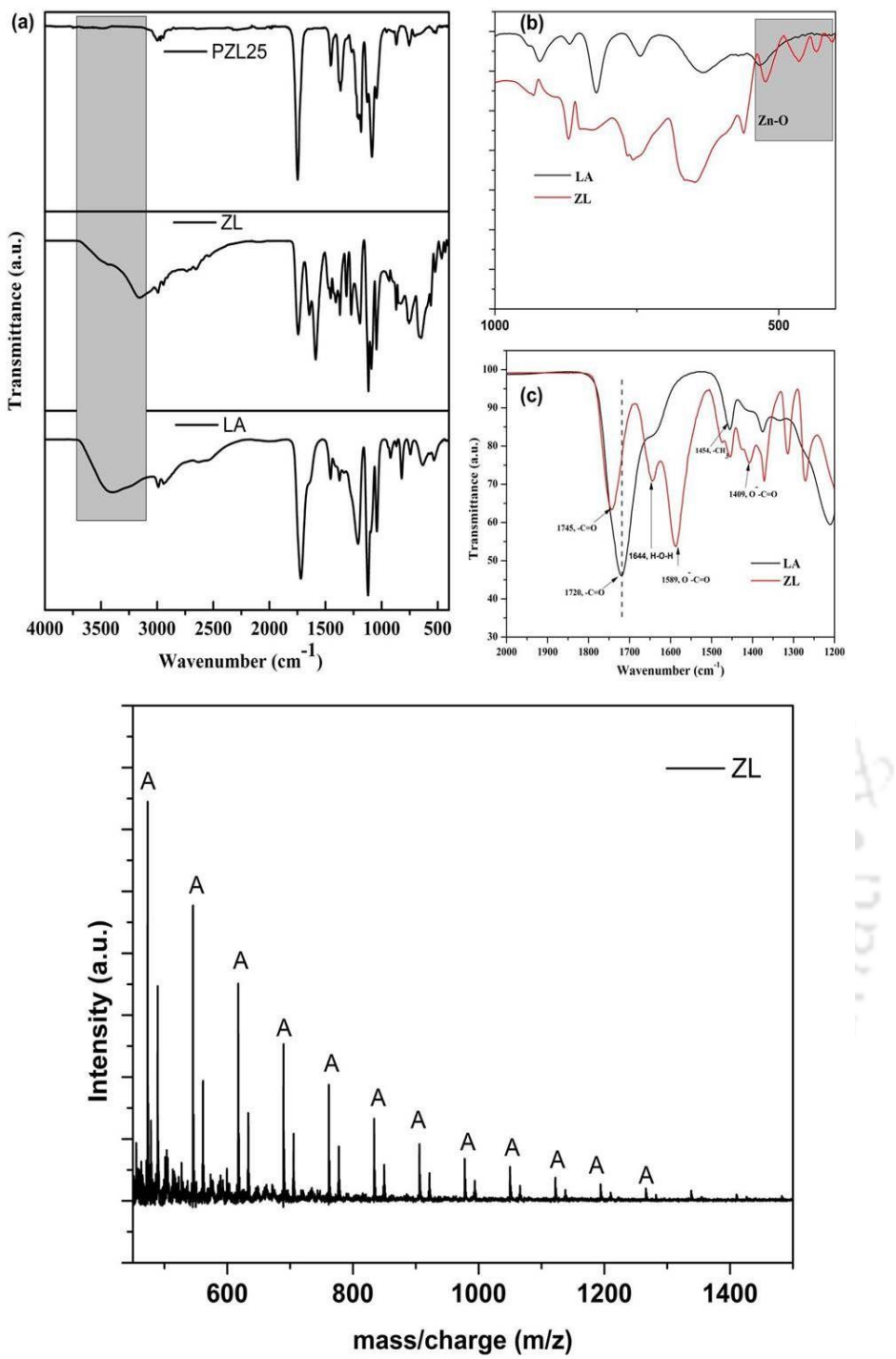

Figure 31: FTIR spectra of (a) LA, ZL, and PZL25, (b)magnified spectra of LA and ZL (c) spectral range of LA and ZL from 1200-2000 cm^{-1}. MALDI-TOF-MS spectrum of ZL synthesized by microwave-assisted technique with LiCl, NaCl, and KCl as cationizing agent's signals separated by 72 units.

Strong peaks at 1117 cm^{-1} with an intense hump at 1091 cm^{-1} is due to the linkage between Zn and C(O)–O–C stretching vibrations. Demonstration on oligomer synthesized

with lactic acid by the appearance of the –C–O–C– bond, characterized by signal at wavenumber 1174 cm^{-1} was reported [118]. The appearance of new peak around 460 cm^{-1} is due to linkage Zn–O that signifies successful preparation of ZL. The spectrum PLAZ25 shows characteristic peaks at 2938, 1380, and 898 cm-1 that can be attributed to stretching vibration of O-H, stretching, deformation, and rocking vibrations of C-H respectively. The PLAZ25 nanofabric was prepared by solution mixing of ZL and PLA under simple magnetic stirring conditions so no linkage between the ZL and PLA can be seen from the PLAZ25 spectrum. The sharp peaks at their particular position thereby suggest that the matrix (PLA) is chemically stable even after mixing a higher percentage of ZL.

4.2.4 MALDI-TOF-MS analysis

This analysis was performed for the synthesized ZL sample. The resultant spectra verified the investigation of the speciess (Zn) taking part in the synthesis of ZL.

$$A = 72x + M_{Zn}(63.5) + M_{K^+}(39) + M_{Li^+}(7) \quad \text{(xxi)}$$

$$B = 72x + M_{Zn}(63.5) + M_{Na^+}(23) + M_{Li^+}(7) \quad \text{(xxii)}$$

The term "x" is the number of lactyl repeat units with M_w value of 72 Da each, M_{Zn} (63.5), M_{Li^+} (7), M_{Na^+} (23), and M_{K^+} (39) are the molecular weights of Zinc powder, sodium ion, potassium ion, and lithium-ion, respectively, attached with the PLLA chains. Transesterification, may lead to redistribution of chain lengths and formation of polymers with odd numbes of lactyl units separated by a series appear, 72 units [119]. PLA with neutral C_4H_9O end group and with cationizing agents gives signals with *m*/*z* corresponding to n-mer + for corresponding cations (Li^+, Na^+, or K^+). This shows macromolecules are converted into ionic species in this case by intentionally attached cationizing agents. The MALSI-TOF spectra clearly show the intensity of the signals denoted as **A** values from m/z = 473.443 (for 5-mer unit) to m/z = 1266.136 (for

16-mer unit) following the same trend by difference of 72 units. Therefore, ZL synthesized by zinc contains single trend of chain obtained at masses, the equation (v), and hence confirm presence of terminal ended lactyl chains grafted in zinc surface shown by the schematic diagram **Figure 30(c).**

4.2.5 Thermal analysis

TGA is an effective method to study the thermal stability and amount of PLA chains grafted with Zn powder. The thermal performance of zinc powder has been studied and found that Zn powder is thermally stable until 438 °C. After that oxidation of Zn powder takes place which is obvious from the TGA spectra **Figure 32(a)** by weight gain [120]. Whereas for the case of ZL, two-step degradation occurred, where 1st step maximum degradation occurred around 270 °C due to short PLA chains grafted with Zn powder whereas 2nd step, maximum degradation step occurred at 425°C because of Zn powder. As Zn is thermally stable until 438°C for the case of ZL it can be seen from the carbon residue that the remaining 55% of Zn remains un-grafted thereby maintaining thermal stability upto 700 °C. TGA plot revealed in **Figure 32(a)** that short PLA chains are grafted with Zn powder, as generally PLA degradation starts around 270-400 °C [121]. ZL spectra concluded that there were around 25 % of grafted chains of PLA with Zn powder as PLA chains are thermally stable between 267-400 °C. From the spectra of PLA nanofabric the onset thermal decomposition temperature is above 270 °C but for the cases of PZ25 there is the decrease of ~44 °C in the onset temperature (T_{onset}). The thermal behavior is mostly evaluated based on maximum degradation temperature (T_{max}) where maximum weight loss takes place. From the DTG graph **Figure 32(b)** it can be seen that there is the decrease in the maximum temperature for PZ25 and $PZ15S_1$ than PLA due to the presence of short chains of ZL that may start degrading the long PLA chains lowering the temperature. When we consider the DTG spectra for $PZ15S_1$, T_{max} was found to be

308 °C, which was higher than PZ25 T_{max} i.e. 280 °C that was due to the presence of SNC, which had increased the temperature. Furthermore, percentage grafting and percentage conversion of ZL have been calculated by the following equations (i) and (ii). The results showed ZL percentage grafting and conversion was ~47% and ~150% percent conversion respectively.

$$\text{Percentage grafting (\%)} = \frac{\text{Final weight of ZL} - \text{Initial weight of Zn powder}}{\text{Initial weight of Zn powder}} \times 100 \ldots \text{(xxii)}$$

$$\text{Percentage conversion (\%)} = \frac{\text{Final weight of ZL}}{\text{Initial weight of Zn powder}} \times 100 \ldots\ldots\ldots\ldots\ldots \text{(xxiv)}$$

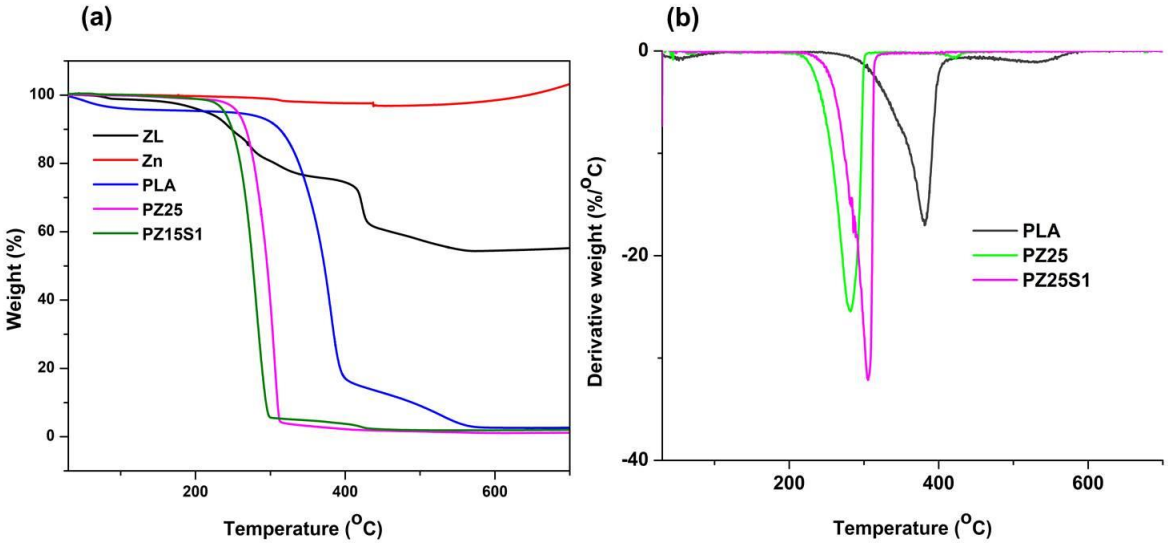

Figure 32: (a) Thermal gravimetric analysis of ZL, Zn, PLA, PZ25, PZ15S1 (b) derivative thermograms, DTG curve for PLA, PZ25, and PZ15S1.

4.2.6 Morphology of prepared fabric

Figure 33(a-d) represents FESEM and X-ray energy dispersive spectroscopy micrographs. It displayed the morphologies of ZL and elemental mapping of the prepared ZL and mat based on electrospinning of $PZ15S_1$ nanofibers to have a qualitative determination of the material distribution with the PLA. The FESEM micrograph of ZL

clearly shows surface roughness due to presence of short PLA chains. Moreover, the corresponding ZL mapping shows presence of Zn, C, O composition confirming the formation of ZL from Zn powder. The elemental composition in wt. % of Zn is ~33 wt. % which also satisfies the taken Zn powder amount in (wt. %) for the microwave synthesis of ZL i.e. ~29%. In addition, EDX analysis was also performed to study the elemental composition of electrospun fabrics (concentration of fillers in the nanofabric is at 15% ZL and 1% SNC) as shown in **Figure 34**. Here, **Figure 35(a-f)** displays several SEM micrographs associated with the final morphology of PLA and PLA/ZL/SNC nanofabric mat. The average fiber diameters had been calculated using Image J software from the SEM images, and the values were found to be 2.5±2 µm for the PLA nanofibers in **Figure 35(a),** 15%ZL over PLA, (For comparison commercially available PP fabric was FESEM image was taken that has an average diameter of 17±3 µm as shown in **Figure 35(b)**. Moreover, for the PZ15 nanofibre mat, the fiber diameter has decreased to 1.5±2 µm and few with 5.1±2 µm, which suggests the uneven formation of nanofibers after incorporation of ZL **in Figure 35 (c).** However, when there is the incorporation of SNC with PZ15 there is uniformity in the fiber diameter having average fiber diameter of 1.4±2 µm as shown in **Figure 35(e-f).**

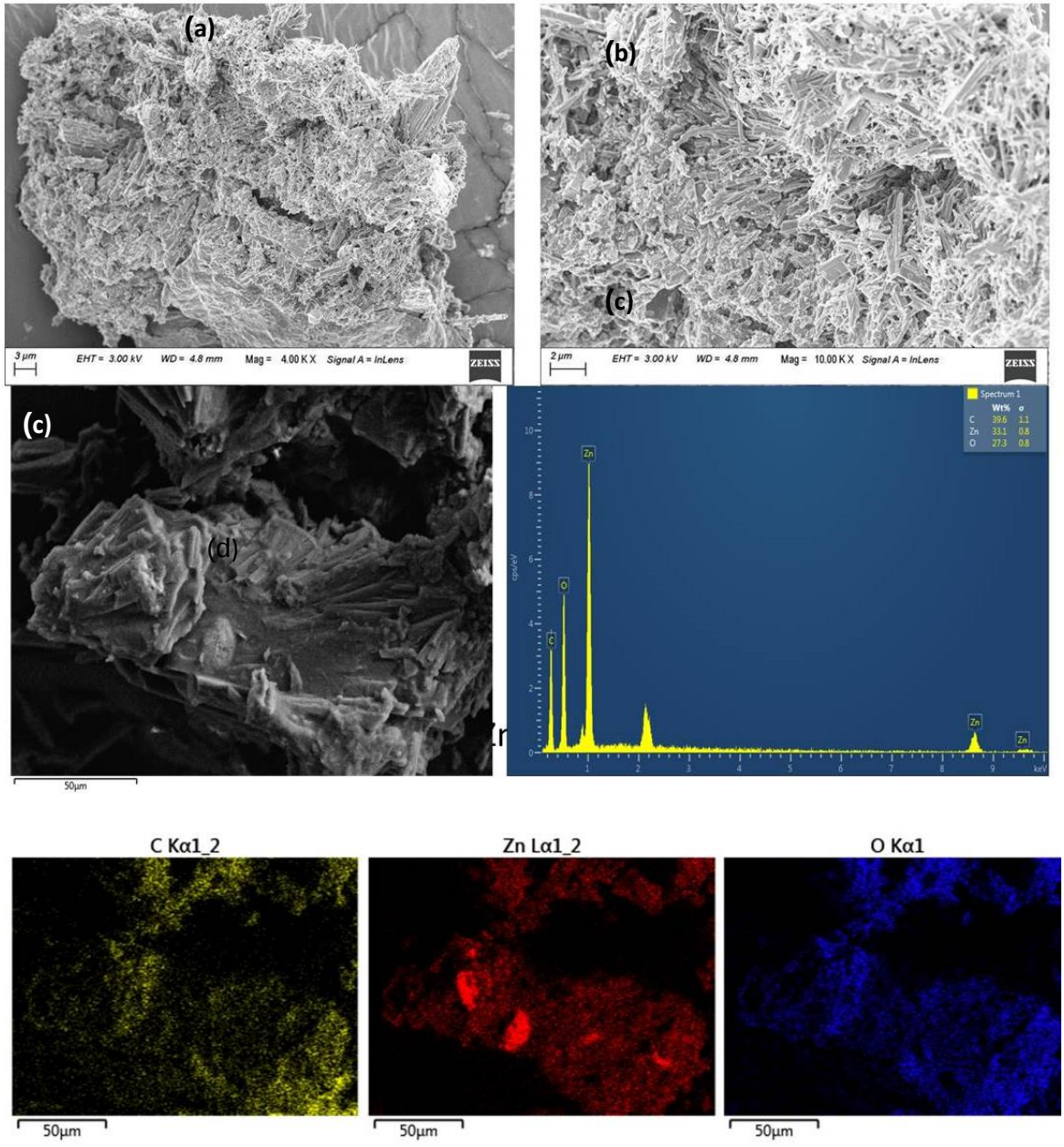

Figure 33: (a) FESEM image showing Zinc lactate powder on 3 µm scale, (b) magnified image showing ZL surface roughness due to presence of grafted PLA chains, (c) EDX analysis with its elemental composition (d) mapping for C, Zn, O content with wt. % composition

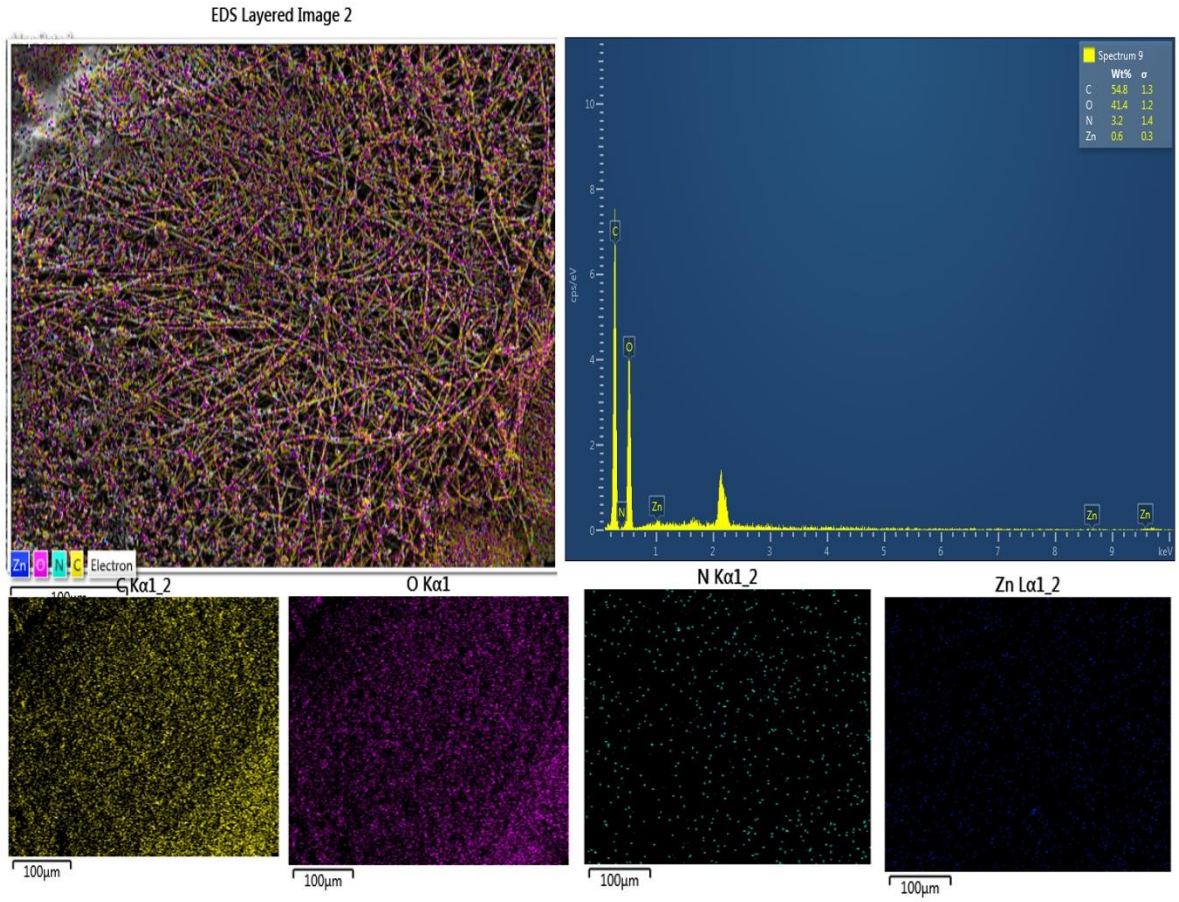

Figure 34: EDX image of fabricated $PZ15S_1$, with distribution of elements C, O, N, and Zn elements and its mapping.

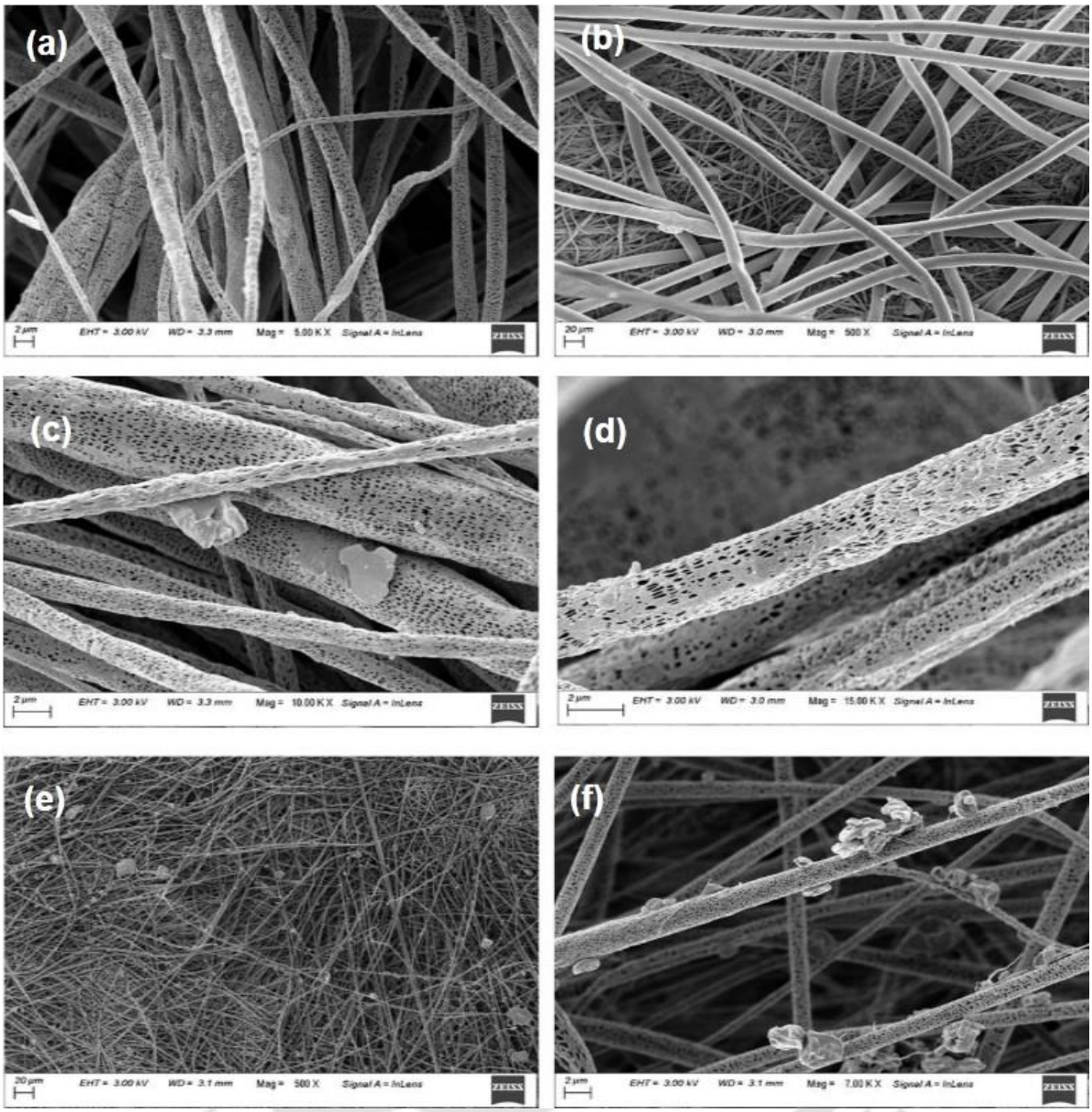

Figure 35: FESEM micrographs of (a) PLA nanofibers, (b) PZ15 electrospun nanofibers compared with non-woven PP micro fabric, (c) PZ15, (d) magnified surface of PZ15, (e) PZ15S1 nanofibers micrograph showing the distribution of filler (15% ZL and 1% SNC), (f) showing decorated distribution of ZL and SNC nanoparticles over PLA fibers via electrospinning method.

4.2.7 Mask wettability analysis

For nPLA, the static contact angle obtained is 126°±3°, which indicates hydrophobic nature of nanofabric as shown in **Figure 36**. The hydrophobicity of nanofabric mat can be attributed to fiber surface and texture. For PZ25 it is 112° ± 3°, less than neat PLA nanofabric which shows the effect of ZL, decrease in value on the wettability is due to the

presence of short chain ZL incorporated into PLA masks. But there is addition of ZL in PLA didn't change surface energy significantly although contact angle reduced from 126° ± 3° to112° ± 3°, promoting hydrophobicity**.** However, for modified nanofabric there is negligible change in WCA, even after 15 min in static condition. In addition, we found that using SNC in PLA/ZL nanofabric there was an enhancement in contact angle, which was similar to commercial PP nanofabric, used which is due to presence of hydrophobic domains in SNC. Therefore, the conclusion can be drawn that treatment of PLA nanofabric with 25% ZL and 1% SNC enhanced very good hydrophobic nature into the fabric. As an enhancement of fabric, surface hydrophobicity will also ensure that saliva or sneezing droplets will not easily pass through it.

Mostly, contact angle hysteresis has been raised due to surface roughness and chemical heterogeneity, between advancing contact angle and receding contact angle. Therefore, for real surfaces, the advancing θ_{adv} and receding θ_{rec} contact angles were considered to play an important role to obtain the state of wettability. In general, θ_{adv} indicates the maximum contact angle of solid surface whereas; θ_{rec} illustrates the minimum contact angle of the surface. In addition, contact angle hysteresis explains the degree of drop adhesion onto solid surface as higher contact angle hysteresis possesses stronger drop adhesion. **Figure 37** shows receding contact angle and hysteresis was calculated for the tested samples. Interestingly, for nanofabric surface compared to that of pristine PP surface, low contact angle hysteresis was observed that shows lower droplet adhesion, which is desirable in case of masks for protection from viral as well bacterial and dust particulates. The linear dynamic modeling for all the test samples has been evaluated to understand the effect of ZL over PLA nanofibers. The θ_{adv} and θ_{rec}values were calculated both experimentally and by linear model at 27 °C shown in **Figure 38**.

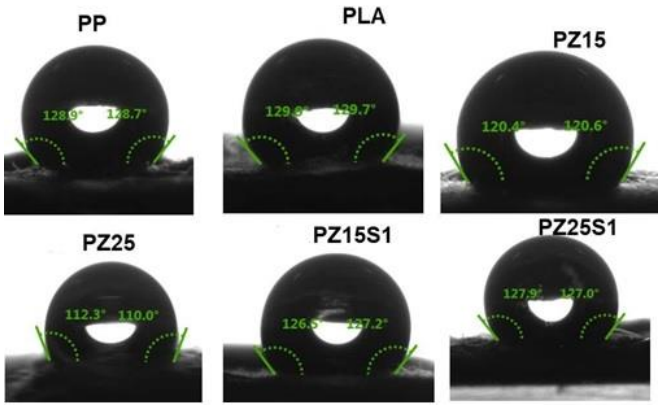

Figure 36: Water contact angles of the test samples.

Figure 37: Receding water contact angle of the tested samples.

The θ_{adv} andθ_{rec} strongly suggests the applicability of this model for the system PLAZL mask which might be due to the good porosity maintained on electrospunned nanofabric surface. The slope (k) values for the curves and hysteresis (H) values are shown in **Table 2**. When ZL and SNC are added there is no such significant effect on the θ_{adv} and θ_{rec} for fabricated electrospunned fabrics as calculated by Young's contact angle. Nevertheless, it can be observed that the hydrophobic nature of fabricated nanofabric is greatly determined by the surface topography, and due to incorporated nature of additives or fillers.

Table 2: Data representing contact angle hysteresis with surface free energy and slope. Regression represents the linear models' efficacy

Sample	C.A. Hysteresis	Advancing C.A. (θ_{adv})	Receding C.A. (θ_{rec})	Surface free energy for (θ_{adv}) (mN/m)	Surface free energy for (θ_{rec}) (mN/m)	Slope	Regression
PZ25	10	120.0±1.0	110.4±11.7	11.5	16.8	0.7	0.99
PZ25S$_1$	63	125.6 ±0.3	61.9±18.7	8.7	46.6	0.7	0.99
PZ15S$_1$	26	115.3±0.6	89.3 ±6.1	19.8	29.6	0.7	0.99
PLA	51	130.3±0.3	79.5 ±2.3	6.7	35.7	0.8	0.98
PP	22	117.1 ±1.0	95.0 ±8.1	13.5	25.0	0.7	0.98
PZ15	25	113.0 ±0.7	88.0 ±4.2	14.7	28.0	0.8	0.96

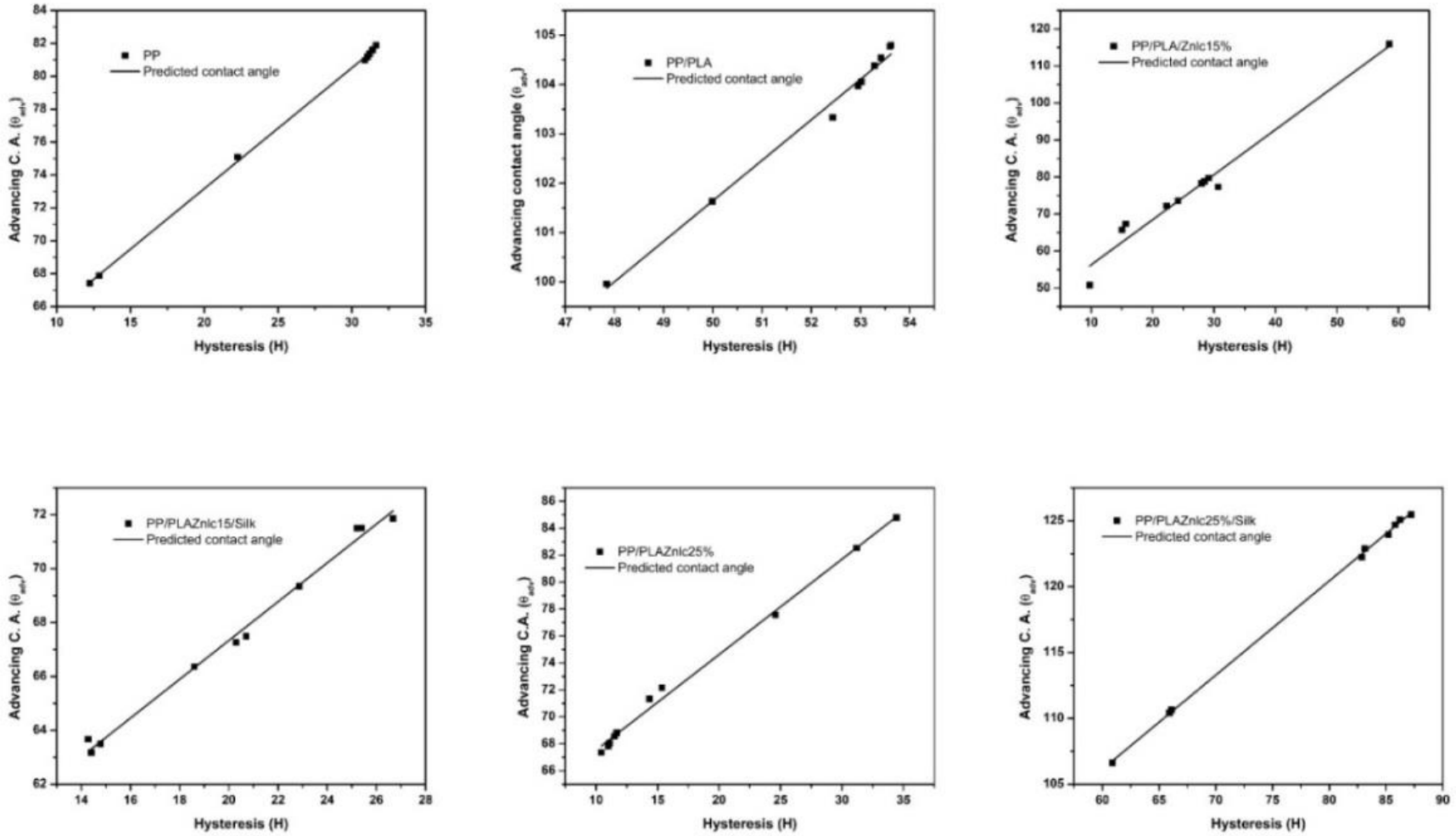

Figure 38: Linear plot representing contact angle hysteresis plot of the advancing contact angles of the test samples

4.2.8 Mask breathability, porosity, and reusability

For successfully demonstrated good breathability of the nanofabric over the substrate together while maintaining wettability of nanofabric surface. Our strategy of electrospinning of PLA based fibers and comparision with PP based fabric was successful which was evident from our **Figure 39(a,b),** breathability experiment. The silica gel over nanofabric surface has changed its color from blue to pink signifying its water vapor permeability.

Air permeability or airflow through a material area is influenced by its openness, which affects its porosity. **Figure 40** shows measured porosity of the samples. Interestingly, for the cases of PP fabric, high porosity value was observed i.e. 79.2% compared to that for the modified PLA nanofabric (76-46%)**.** The high porous structure in terms of porosity value indicates high air permeability efficiency. The decrease in porosity for modified fabric can be attributed to the utilization of fillers ZL and SNC that have reduced or mutilated the porous structure. Also, high concentration of ZL and SNC in PLA nanofibers decreases porosity of the fabric. Although PZ15 and $PZ15S_1$ showed good porosity percentage when compared to PP and can be further optimized and utilized for face masks preparation.

Figure 39: Silica gel placed over nanofabric changed its color from blue to pink signifying its breathability.

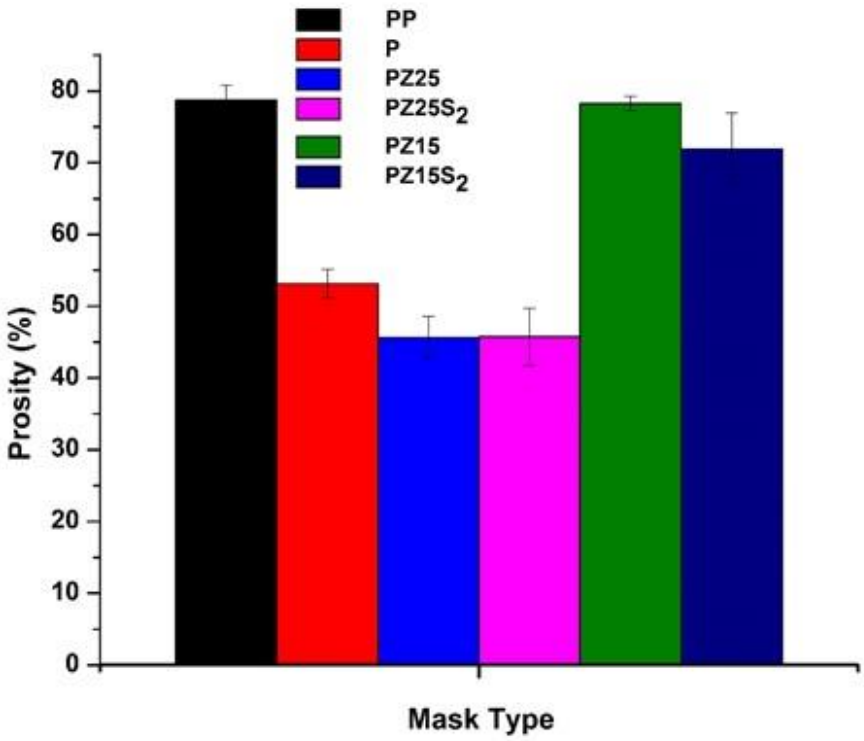

Figure 40: Porosity percentage of the prepared facemasks in order to understand its air

Figure 41: Water contact angle images after 5 min-24 hours of dipping treatment. This indicates reusability of the facemasks prepared.

For analyzing reusability of the masks static CA for the fabric were tested as shown in **Figure 41**, and WCA values were listed in **Table 3**. and morphological analysis was done in order to understand its morphology dipping the masks in 75 % ethanol for 5 min-24 hours in four cycles. After dipping treatment from SEM analysis, it was clear that the modified PP mat did not undergo any significant morphological changes. This test confirmed our prepared modified PP fabrics have good indicator in terms of reusability, consumer end-use, and commerciality.

Table 3: Comparative data for reusability test of facemasks dipped in ethanol solution from 5min-24 hours in four different cycles.

Sample	**1st R (5 min)**	**2nd R (30 min)**	**3rd R (12 hours)**	**4th R (24 hours)**
PZ25	125°±5	120±7	120±4	116±2
PZ25S1	125±4	123±2	119±3	119±2
PZ15S1	129±8	125±3	125±5	123±4
PLA	124±3	122±4	122±3	118±6
PP	132±2	125±3	118±3	112±9
PZ15	112±4	123±2	123±5	108±4

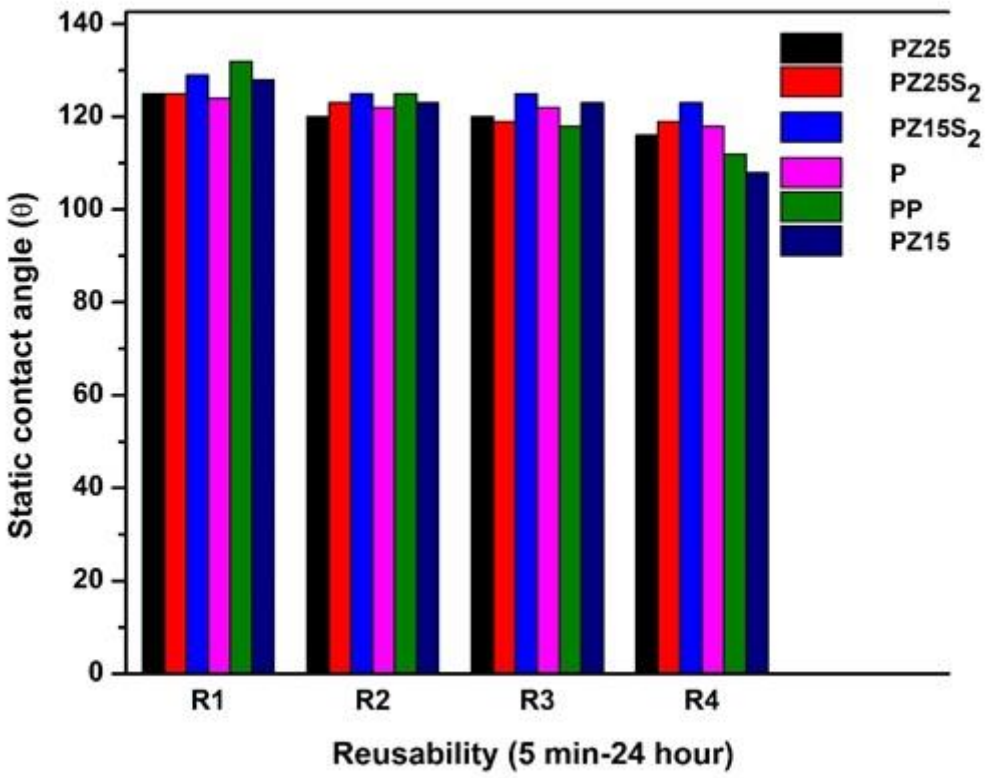

Figure 42: Calculated contact angle before and after dipping treatment for 5 min-24 hours. The measured contact angles represent hydrophobicity of the prepared facemasks.

From **Figure 42,** it was evident that there was no significant decrease in hydrophobicity of the samples even after 4th cycle of reuse. This parameter satisfies our prepared compostable fabric can be reused up to 4 times without compromising its surface properties like hydrophobicity and surface texture and can be used as facemasks. After 4th cycle, FESEM images showed negligible surface changes for the prepared fabric as shown in **Figure 43(a-c).** Similar characterization technique were used elsewhere [107] where they demonstrated reusability of the facemasks upto 10 times after ethanol dipping. Here we also proved its reusability using mentioned analysis without any morphological changes considering as a performance parameter of the prepared facemasks.

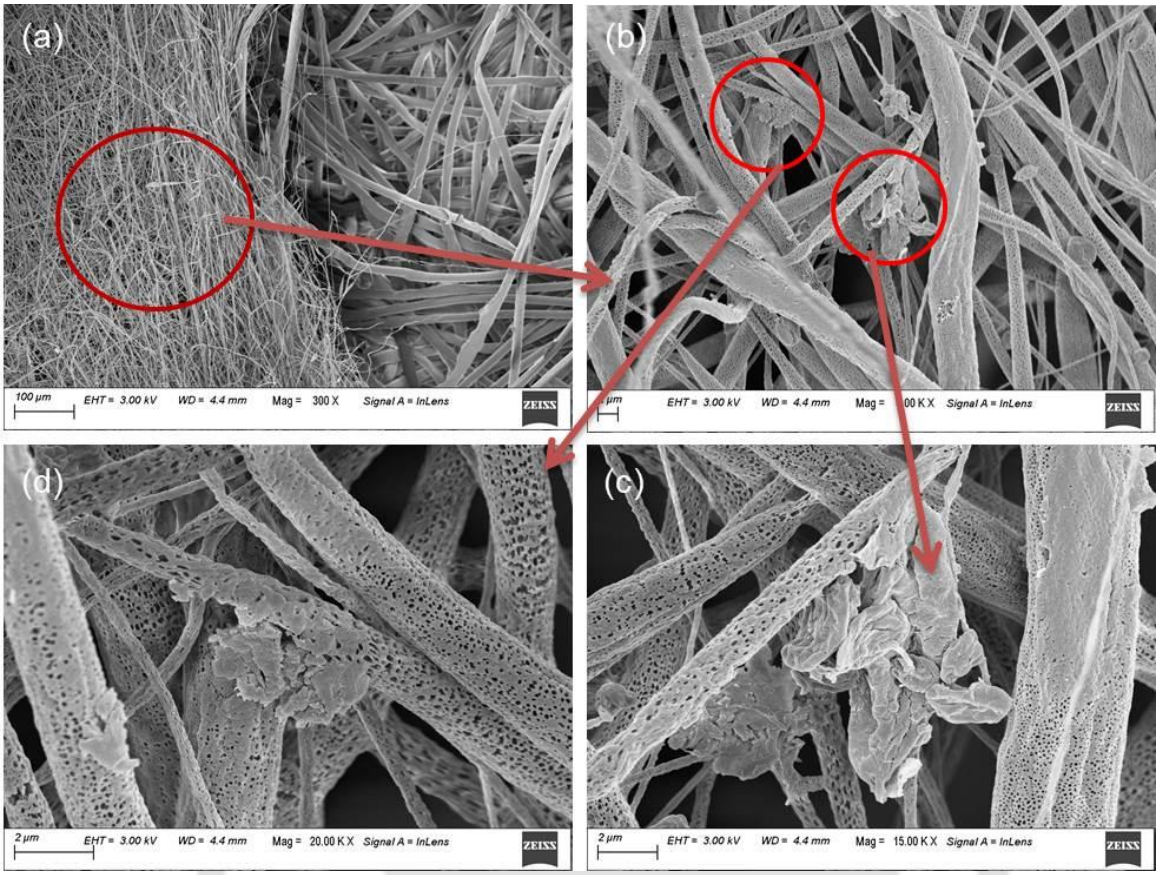

Figure 43: (a) SEM images of PZ15fabric over PP substrate (for comparing) after 24 hours of dipping in Ethanol (b) Distribution of ZL and SNC in the fabric, (c, d) magnified image of distributed ZL and SNC.

4.2.9 Antibacterial activity of ZL incorporate into PLA nano fabric

Firstly, antibacterial activity has been studied by disc diffusion assay then by bacterial growth count. **Figure 44** shows the nutrient agar plate cultured with *E. coli* and *S.aureus* treated with antibiotic (control), and prepared PLA/ZL fabric. Repetitive analysis was performed for the fabricated nanofabric layers. It was found that significant bactericidal activities against microorganisms can be seen when compared with antibiotics (10 mcg) after 24 h of incubation. Overall, the results indicate the killing of the bacteria by clearly visible inhibition zones which was due to the release of Zn^{2+} ions that damages the cell membrane and penetrate the intracellular contents. Compared to *S. aureus*, the nanofabric

showed a larger inhibition zone toward *E. coli* of nearly 1 cm depicted using blue-lined circles with arrow head.

The concentration of ZL was changed (10 µgmL^{-1}–200 µgmL^{-1}). It was found that 200 µg mL^{-1} concentrations give significant effective bactericidal activities against microorganisms. Whereas reported value for ZnO nanomaterial bacterial inhibition concentration is 500 µg mL^{-1}for *E.coli* [122]. Thereby ZL may act as a better material having superior antibacterial activity against both the gram-negative and gram-positive bacteria. This has been proved using viable bacteria counts by dilution method for ZL and SNC against *E.coli* bacteria and compared with control (no zinc or SNC added only *E.coli*). After 72 h of incubation, visual studies showed zinc significantly reduced the viability of *E.coli* compared to silk nanocrystal and controls shown in **(Figure 45)**. The reviewed studies have agreed that the antibacterial effectiveness of zinc was mostly concentration-dependent. As reported increase in the concentration of zinc can increase in antibacterial effectiveness [123].

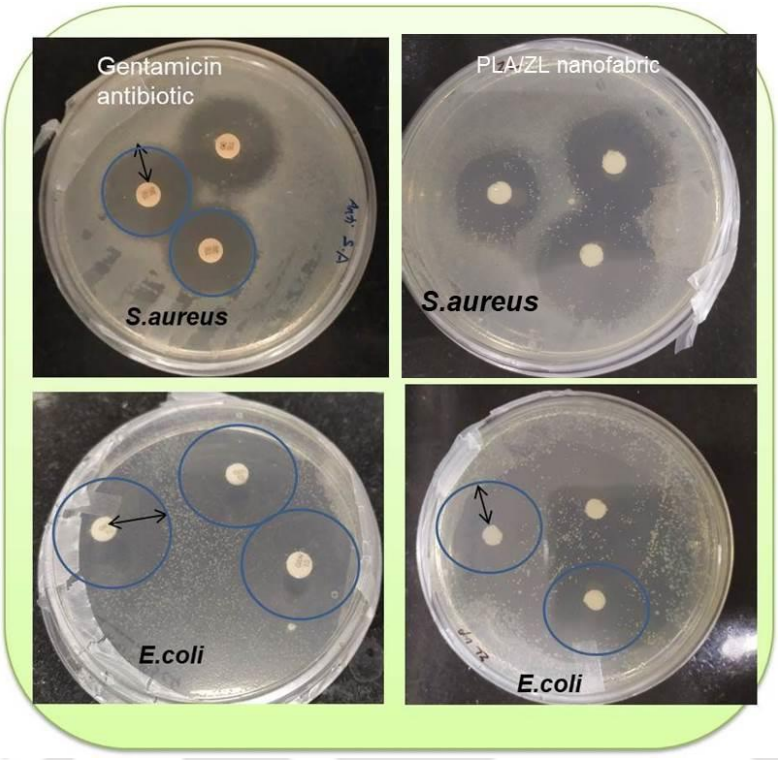

Figure 44: Visual images (smartphone camera) of inhibition zone by ZL showing similar trend of antibacterial activity against the taken bacteria as antibiotic Gentamicin.

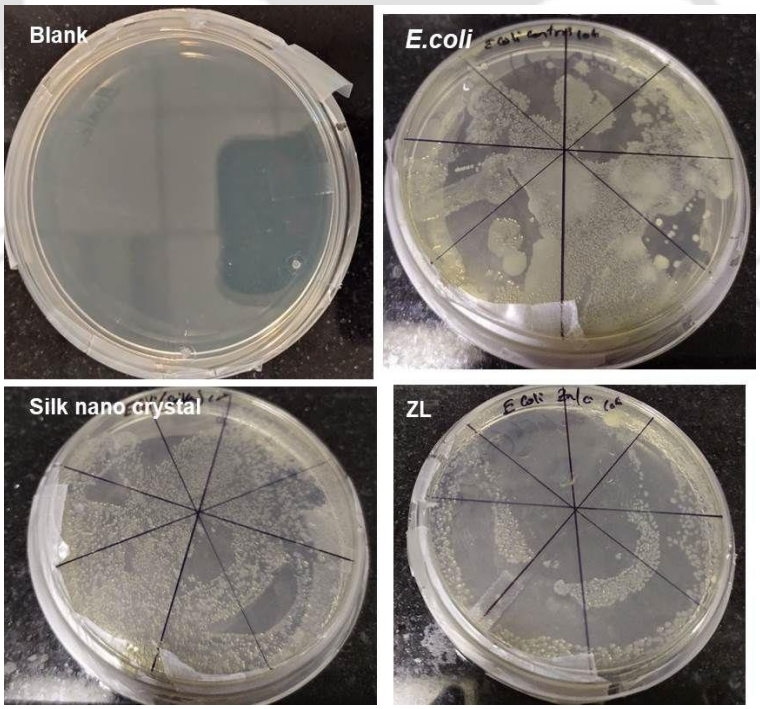

Figure 45: A comparative visual images (smart phone camera) of bacterial colony formation for the prepared ZL and SNC against *E.coli*.

4.2.10 Antiviral analysis

The diluted PP/PLA-ZL nanofabric was tested and observed that there is a significant reduction in a plague for the coated nanofabric in 10 min of time which is 97%. Thereby this revealed the antiviral potential against NDV by the inhibition of virus growth. Though at the beginning cell death was occurred later, this has been resolved after dilution. The mechanism lies behind the presence of the taken concentration of Zn^{2+} ions grafted L-lactate oligomer chains which can engulf the virus by inhibiting its growth as shown in **Figure 46.** When compared with the reported studies we found that here the antiviral efficacy is more than already reported prepared facemasks where CuS was used in 3-layered nylon masks (99.9% antiviral efficacy was found in 1 h) [124].

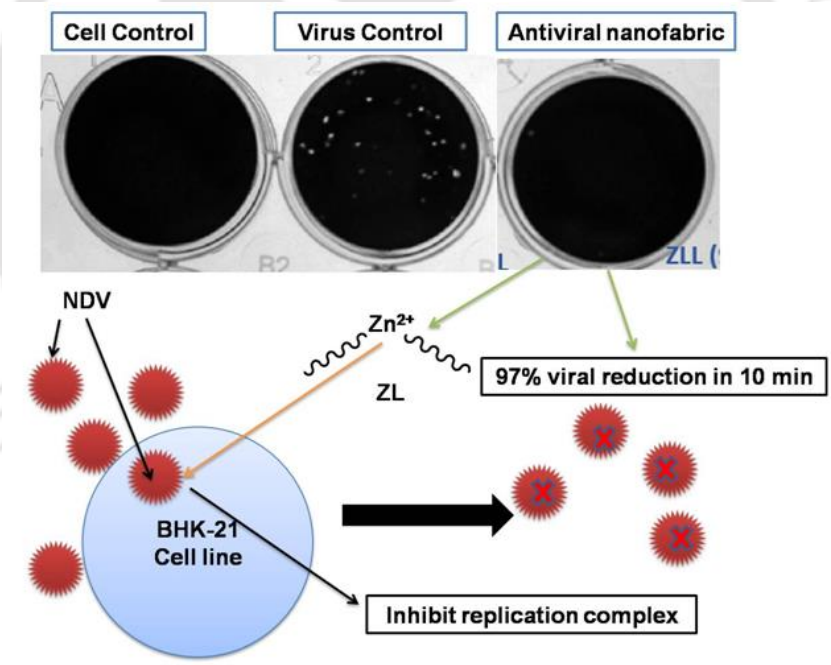

Figure 46: Schematic antiviral mechanism of the fabricated nanofabric showcasing 97% viral efficacy in 10 minutes of time.

4.3 Conclusion

In summary, a hydrophobic, antimicrobial, and antiviral nanofabric layer having viral efficacy of 97% in 10 minutes was fabricated comprising of PLA, ZL, and SNC. This antiviral layer was developed from polycondensation reaction of Zn with LA, forming ZL and PLA followed by electrospinning into nanofabric for property enhancement. This can be used as a protective layer in a conventional PP based mask. Prepared nanofabric had good breathability and promoted hydrophobicity which is the most essential property of a material for its application as face mask. The prepared SNC based PLA/ZL nanofabric exhibited water contact angle (125.69±0.35°) even higher than commercial PP fabric (117.7±1 °). This also indicated that use of ZL in PLA had no inverse effect on hydrophobicity. Reusability data of the prepared nanofabric demonstrated that can withstand upto 4 cycles by ethanol dipping/washing treatment without undergoing significant changes in its surface morphology. This suggests that the prepared nanofabric as a mask can be reused several times by treating it with ethanol. The prepared layer further exhibited excellent antibacterial properties against *E. coli* and *S. aureus* in presence of ZL. This novel facial mask preparing technique promotes sustainability, biodegradability, and reusability. Future works such as multiple layers of using hybrid materials with PLA can be studied in detail, focussing mainly on material processing and compostability without compromising its antiviral properties.

****

CHAPTER 5

NANOCHITOSAN/ZINC-OLIGO-LACTATE AS A NON-TOXIC SHIMMERY NANOFINISH FOR PLA BASED NANOFABRIC APPLICABLE IN PROTECTIVE WEARABLES

Abstract: The current chapter discusses the pandemic era that has made significant importance in developing a multifunctional electrospun nanofabric for advanced protective textile applications merging bio nanomaterial and engineering materials as a protective layer. Precisely different analytical methods like FTIR, XRD, TGA, FESEM, FETEM have been used to characterize the formation of nCS, ZL and their solution. Herein, we investigated the use of nanochitosan (nCS) as a non-leacher film for Zinc-oligolactate (ZL) rods showing significant properties for the PLA Poly(lactic Acid) nanocomposite nanofabric with average diameter of 190 nm. The electrospun PLA nanofabric was prepared by simply electrospinning technique and dipping into different concentrations of nCS/ZL in 1% (v/v) acetic acid solutions. The novel fabricated electrospun PLA based nanofabric shows excellent properties in terms of **(a)** hydrophilicity, **(b)** self-cleaning activity, **(c)** antimicrobial activity against bacteria, **(d)** antiviral activity is more than 97% for nCS-ZL (80:20) concentration and 92% for nanochitosan, **(e)** biocompatible nanofabric.

Publications: Hazarika, D., Ghosh,T., Sankhla, A., Bhonsale S., Kumar, S., Kumar, A., & Katiyar, V. Behaviour of Nanochitosan and Zinc-Oligo-Lactate as a Nanofinish for PLA Nanofabric for application of Protective Wearables **(to be submitted).**

5.1 Introduction

Chitosan, a natural biopolymer is derived from chitin and is the second most abundant natural polysaccharide. It has been reported that preparation of chitosan as nanoparticles revealed no toxicity at lower concentration (30 µg/ mL). CH has advantageous nature in terms of biodegradability, hydrophilicity, biocompatibility, non-toxic, antimicrobial activity, etc. It can be processed into distinct forms, such as solutions, blends, sponges, membrane, gels, paste, tablets, microspheres, or microgranules for different applications.

Nanoparticles with their ability to enhance their physical, chemical, mechanical, optical, and magnetic properties are in great demand. It has a vast area of application that can be used in commercial products like polymers, cosmetics, smart textile, and packaging and transformed into various forms. Nanochitosan has been used as green finishing in cotton textile for improvement in UV resistance, dyeability, thermal stability, antibacterial activity [15]. Textile finishes using nanomaterials as the coating has gained much importance these days that provides multifunctional options. Research works on PLA spinning into fibers and coated with nanofinishes are also in great demand owing to their biocompatible, biodegradable, compostable nature. In textile industries, chitosan has been used as eco-friendly finishing agent to develop a functional fabric. Finishing with chitosan is a convenient and effective way to improve the antibacterial, antiwrinkle, textile dyeing performance of the fabric. Antiviral is not an inherent property of textile material which is susceptible to microbial growth due to high moisture retained tendency. The sun emits electromagnetic radiation as Ultraviolet radiation and is divided into UV_A range within 320–400 nm, UV_B range 290–320 nm, and UV_C region below 290 nm. As long term exposure to UV radiation causes serious human skin inflammation, reddish skin, skin tanning, cell damage, premature aging, cataract problem, photokeratitis, and even skin cancer[125].

The report has been made on fabrication of electrospun chitosan-coated PLA nanofabrics as immobilization support for saccharification of gelatinized CFW. Modified chitosan (amphiphilic) has been used with hydrophobic PLA for better dispersion of hydrophilic chitosan and electrospinning into nanofibers [121, 126]. Thereby, present study, the concept of using hydrophilic nanochitosan as a shimmery nanofinish in the form of film-coated over electrospun PLA nanofabric.

Textiles are the carriers of micro and nano organisms (bacteria, virus, and fungus) that can damage the quality, texture, discoloration leading to skin diseases. Thereby functional finishes can maintain hygiene and enable to avoid infection from one person to another of from the environment. Hydrophilicity is another mode for microbial attack and natural fibers surface are prone to microbial attack acting as a supplier of nutrients for them. Literature has reported on leaching and non-leaching agents by control and release mechanism from the surface or interior of the fabric. Among the non-leaching agents includes chitosan, poly-hexamethyl biguanide, octadecyl aminodimethyl trimethoxy silylpropyl ammonium chloride, etc. Guneet et al. has discussed the antimicrobial finishes of cotton finished with triclosan, silver, and chitosan [127]. PLA has been reported to have spinning capabilities and fiber forming abilities.

5.2 Results and Discussion

5.2.1 Structural analysis

The X-ray diffractogram of chitosan **(Figure 47(a)**) had a semi crystalline nature with two main diffraction peaks at around 2θ=10° and 20°. The semi crystalline nature of pure chitosan was confirmed from the appearance of the diffraction peak centered at diffraction angle 2θ=9.06° and sharp diffraction peak at 20° which are indicative of high degree of crystalline morphology. The chitosan molecule easily forms crystalline regions and regions and this may be due to the presence of plenty of -OH and -NH_2 groups in the

chitosan structure, which could form stronger inter and intramolecular hydrogen bonds [40].

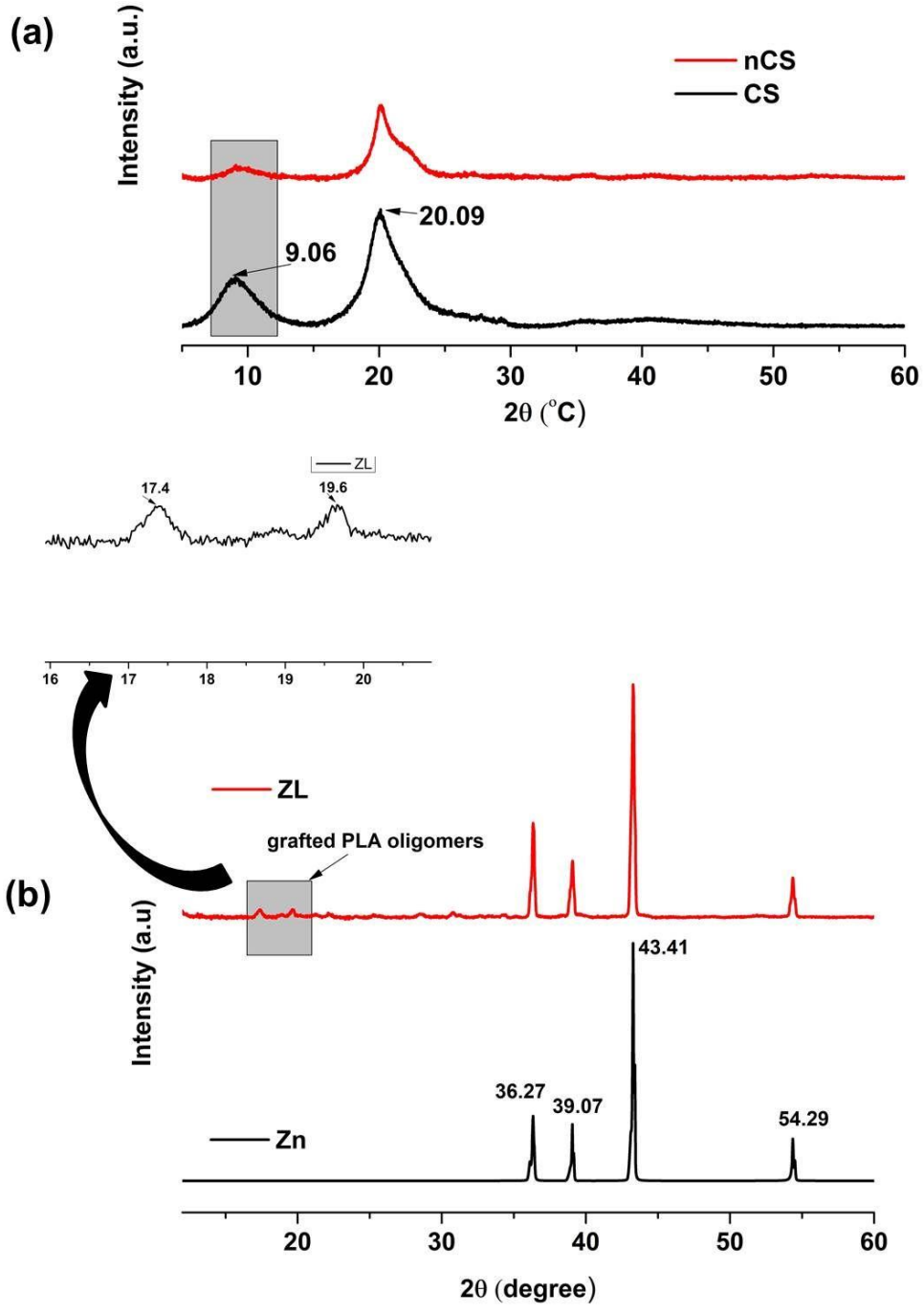

Figure 47: X-ray diffraction patterns of (a) nCS powder, and (b) ZL material (inset grafted short PLA oligo chains).

The X-ray diffraction pattern of nanochitosan was obtained using ionic gelation technique. The X-ray diffractogram of nanochitosan shows a broad peak at around 2=28°. The broadening of the peaks is due to the deformation of the crystalline regions by the increased packing of chitosan chains by ionic crosslinking. As shown in **Figure 47(b)**. Zn powder for reference show characteristics peak at 36.27, 39.07, and 43.41. But for the ZL spectra, there is the appearance of another two characteristic diffraction peaks at 2θ = 17.37° and 19.67 which is attributed to the formation of the grafted oligomer lactate chains.

The FTIR spectra for nCS, ZL, PLA, PLA/nCS and PLA/nCS-ZL are represented in **Figure 48(a).** The FTIR spectral details of crosslinked chitosan i.e. nanochitosan using ionic gelation method is shown. The FTIR spectra of ZL and nCS, it confirms their formation. The broad peak in the range 3682-2260 cm^{-1} is for –OH and –COOH end groups short chains which confirms the formation of oligo-PLA chains with Zn^{2+} ions. The absorption band at 3385.92 cm^{-1} is attributed to –NH, and –OH groups in chitosan which has been broadened by physical interactions with sodium tripolyphosphate, STPP. Strong peaks obtained at 2920.57 cm^{-1}, 2908.57 cm^{-1}, 1635.23 cm^{-1}, 1510.05 cm^{-1}, 1376.80 cm^{-1}, and 1219.00 cm^{-1} indicate the presence of asymmetrical and symmetrical stretching in CH_2 group, NH_3^+ stretching, C=O stretching in amides, N–H bending vibration of amide group, O–H in-plane bending in alcohols and P=O stretching. The characteristic peaks appear between 1,000 and 1,250 cm^{-1} for glycosidic linkage and C–N of C–NH_2 of nanochitosan. The peak obtained at 1163.38 cm^{-1} indicated the overlapping peak of C–O stretching in polysaccharide and formation of chitosan nanoparticles due to the interaction of ammonium ion and phosphate ion in chitosan nanoparticle molecules.

The characteristic band at 1747.23 cm^{-1} is due to the ester group present in neat as well as the composite fiber. The prepared PLA/nCS composites fibers are characterized by the

presence of very less broad peak around 3100–3500 cm^{-1} than neat nCS due to –OH and –NH stretching. There is a small shift in wavenumber from 1578 cm^{-1} to 1589 cm^{-1} which satisfies the presence of ZL has some effect on the N–H band of nCS. Further another peak at 1027 cm^{-1} was found for C–O stretching vibration concerning primary alcohol for nCS. Whereas for the PLA/nCS and PLA/nCS-ZL there is shifting of peaks from 1083 cm^{-1} to 1090 cm^{-1} with more intensity which confirms the presence of nCS and ZL linkage with –C-O band of PLA with possible hydrogen bond interaction. Further decrease in the peak intensity carbonyl group also suggests the interactions between the PLA and the nCS-ZL hybrid film formation over the PLA nanofabric.

Figure 48(b) shows the UV-Vis absorption spectra of nCS, ZL and their hybrid solution. The concentration of nCS was taken according to its functional property. Although the peaks are not much reached in case of nCS but there is a broad absorption band for nanochitosan showing the characteristic broad absorption band around 282 nm that might be ascribed to C=O group in chitosan. The particle size also influences the UV-vis absorption edges. The red shift of peak around 265 nm also suggests the presence of the ZL particles in the nCS solution has attributed to the existence and formation of the hybrid solution. The electrospun modified PLA nanofabrics are fabricated to develop a UV protective textile. Hence, it can be seen that the hybrid solution tends to act as a UV protective layer when utilized for PLA nanofabric. Oh et al. reported that the absorption peak wavelength was at 320 nm in the UV region for CSNPs and 363 nm as reported by Yasmine [128][129].

5.2.2 Thermal analysis

The thermogravimetric curves of CS, nCS, PLA, PLA/nCS, PLA/ZL and PLA/nCS-ZL were recorded as shown in **Figure 48(c-d)**. The TGA of CS and nCS shows mainly two stages of mass loss. The first stage occurs from 65 to 160 °C and reaches a maximum

degradation at 95 °C with 12.74 % due to the dehydration process as the polysaccharides usually have a strong affinity towards water. The second occurred from 236 to 385°C due to the degradation and decomposition of the backbone chain of volatile fraction of chitosan and shows remained 27.72% of the sample as residue. The TGA thermogram for nanochitosan indicates the first thermal event occurs at temperature 50 to 150 °C with a weight loss of 8.3 % which may be due to the loss of residual water. The water content has been decreased by the cross-linker STPP as the phosphate groups present strongly interact with NH^{3+} and thereby also decreased the different interaction like hydrogen-bond, dipole-dipole, and ion-dipole between the water molecules and nCS chains. The maximum weight loss takes place after 150°C as there is decomposition of polymer matrix. It was evident from the plot that for the nanochitosan there is 22.26% from 202 to 275 °C owing to degradation of the backbone chain. Thereby, we can see from the TGA thermogram when considered the range in 400 °C that there is 45.79% mass loss for chitosan, and for nCSs 35.10% of the sample gets disintegrated. At the residual temperature (700 °C) nearly 45.40% of the nanochitosan sample remained as residue showing the higher thermal stability of nanochitosan. The enhanced thermal stability indicates formation of a stronger and stiffer hydrogel kind network due to crosslinked structure. The higher the amount of residue is the indication of the highly stable thermal behavior of nanochitosan.

The PLA-ZL shows lower thermal stability than PLA maybe due to poor compatibility of ZL or the presence of short chains of oligomer in ZL that has been disintegrated first. Further, the stability of PLA-nCS nanofinished nanofabric has been decreased due to the presence of nCS with lower thermal stability. The plot shows three steps of degradation for PLA/nCS nanofabric. The first step arises due to disintegration of moisture present, second step shows maximum degradation at 292°C due to presence of nCS. Another

degradation step occurred at 411°C due to the intensive destruction of nCS nanofilm formed over PLA nanofabric. Similarly, for the PLA/nCS-ZL nanofinised nanofabric there is also three-step degradation where maximum degradation occurs at 288 °C due to the main chain scission, abstraction of side groups, and the meaningful difference is caused by the difference in weight residue which is higher (12.10%) than PLA/nCS (2.23 %) in case of PLA/nCS-ZL due to the presence of ZL which attributes its higher thermal stability. The derivative thermograms of the prepared materials and nanofabrics are shown in **Figure 49 (a),(b).**

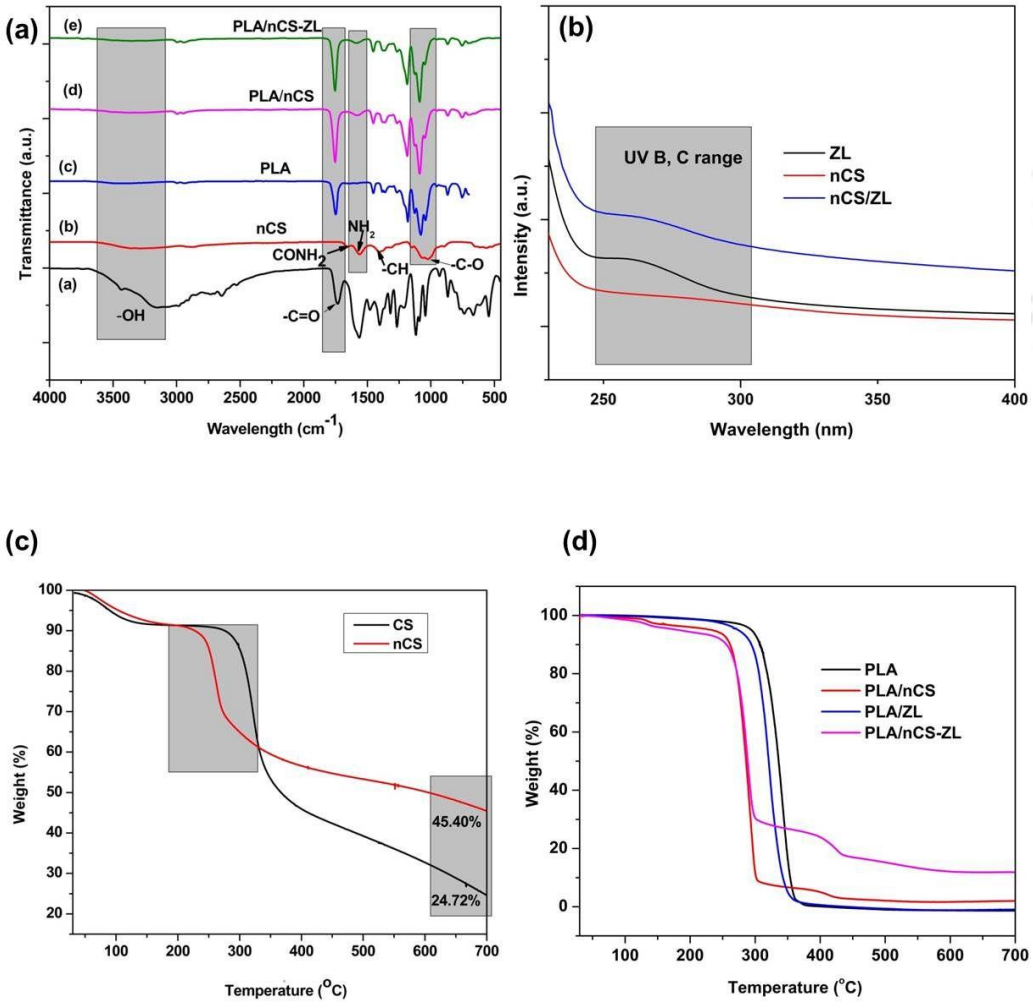

Figure 48: The FTIR spectra (a) ZL, nCS, PLA, PLA/nCS, PLA/nCS-ZL, (b) UV-vis absorbance spectra of ZL, nCS, and nCS-ZL hybrid solution, (c) TGA thermogram ranging from 30-700 °C for CS and nCS, (d) TGA curves of PLA, PLA/nCS, PLA/ZL, and PLA/nCS-ZL

5.2.3 Tunable hydropilicity for the finished PLA nanofabric

The WCA as shown in **Figure 49 (e)-(f)** has been used to evaluate surface tunable hydrophilicity of nanofinished PLA nanofabric. Chitosan, a hydrophilic polymer, has an amphiphilic character that can significantly improve the hydrophilicity of the nanocomposite that will be beneficial for cell adhesion as well as growth[130].

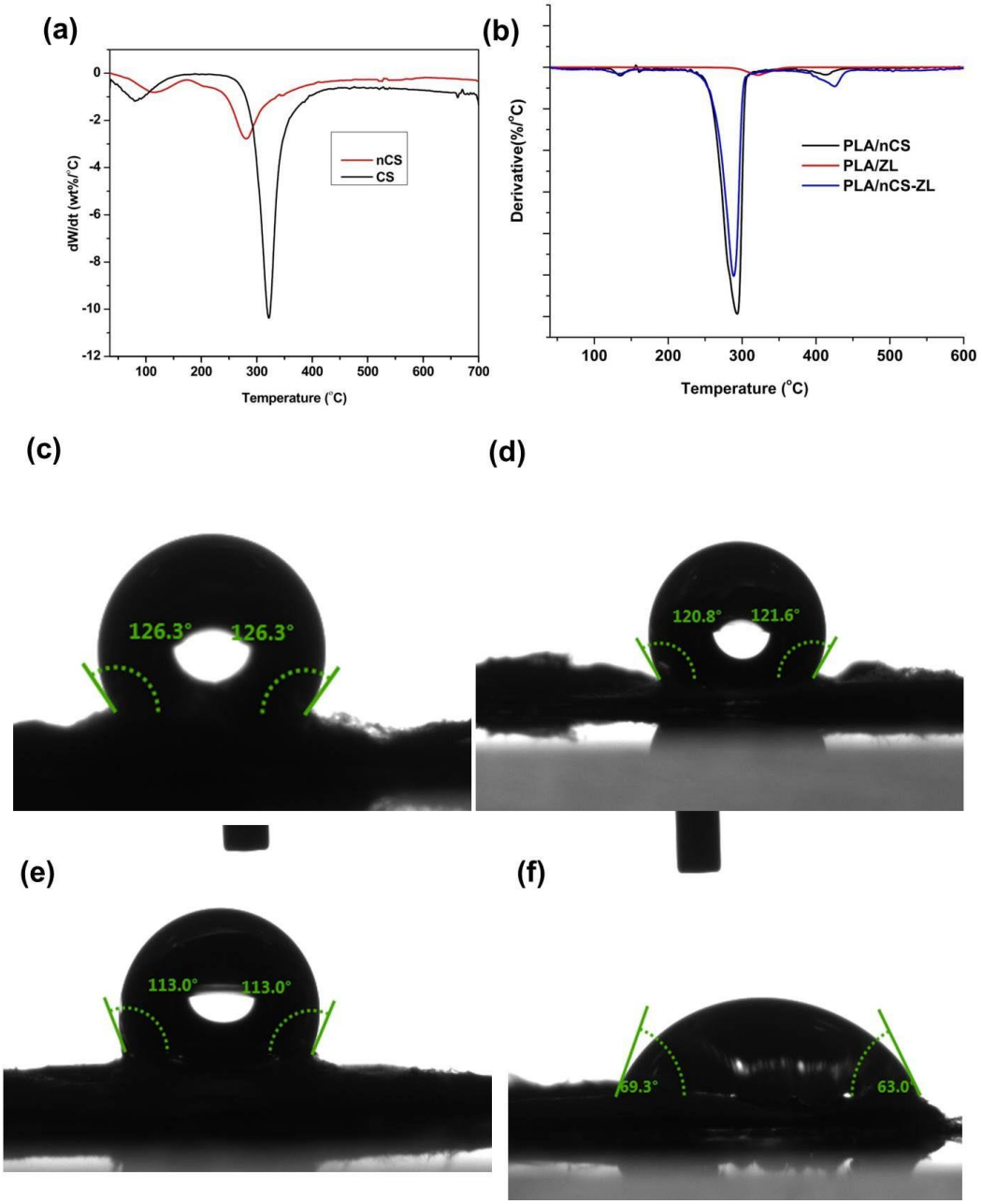

Figure 49: Differential thermogravimetry, DTG curve of (a) CS, nCS, (b) PLA nCS, PLA/ZL, and PLA/nCS-ZL.

As expected the prepared nanofabrics can decrease the WCA values after giving a finish with ZL, nCS, and nCS-ZL as shown in **Table 4**. The WCA of pure PLA nanofabric is 126 °, PLA-ZL is 120.8°, PLA-nCS is 113°and PLA/nCS-ZL is 69.3°. The decrease in contact angle is due to the presence of hdyophobic nature of nanochitosan which in addition in the form of a nanofinish has decreased the WCA drastically. Because, the hydrophilic −OH and $-NH_2$ groups in nCS were transferred to the surface of the PLA nanofabric, which has reduced the WCA. For the other two cases, there is not an obvious change in the WCA which also suggests the hydrophobic behavior of ZL.

The gloss value has been calculated as it is an important esthetic factor that enhances general appearance as well as consumer acceptance. The main reason is the formation of a smoother nanofilm surface of nCS enhancing the regularity of coated film surface which has led to an increase in the gloss value. From the **Table 4**, we can see that the gloss value has been increased to 97.40 for PLA/nCS-ZL nanofabric at geometry angle 20° which is even higher than unfinished PLA. Thereby it can be concluded that a shimmery nanofabric can be obtained by the presence of nCS nanofilm as a nanofinish over PLA nanofabric for enhancing its appearance also.

Table 4: Comparative datas for PLA and nanofinished PLA nanofabric

Sample	WCA (°)	Gloss value (20°)
PLA	126.3±1.1	96±.22
PLA-ZL	120.8±0.84	96.96±0.7
PLA/nCS	113±0.40	96.48±0.41
PLA/nCS-ZL	69.3±0.24	97.40±0.89

5.2.4 Morphological analysis

It can be observed in higher magnification using FESEM, micrographs of lyophilized nCS are having smallest particle size of average 48± 12.4 nm and are presented in a certain isolated form; it can be appreciated the formation of very fine spherical particles with uniform distributions as shown in **Figure 50(a)**.

EDX analysis has been performed to characterize the elemental composition of the synthesized nanochitosan represented by the observed spectra. Elements such as carbon (C), oxygen (O), nitrogen (N), and phosphorus (P) are presented in the spectra whereas sodium as an added element is present in it. The presence of phosphorus confirmed the formation of chitosan nanoparticles cross-linked with STPP and no evidence of the presence of any impurity has been also confirmed [131]. The values of the elements for nCS are as shown: carbon 47.1%; nitrogen 7.1% oxygen 39.50%, phosphorus 0.4 % and sodium 6% respectively as depicted in **Figure 50(b)**. The pH under acidic conditions of pH $\leq$ 6 could also increase the number of protonated amines and increase cross-linking [132]. Sodium tripolyphosphate (STPP) a major ingredient for cross-linking has a pronounced effect on the properties of chitosan dispersion.

In **Figure 51(a), (b)** the schematic representation of nCS and ZL deposition and film formation nanofinished PLA nanofabric and synthesized ZL has been shown. The figure shows the FETEM image of nCS-ZL solution nanofilm formation morphology to check the distribution of ZL into the nCS nanofilm. **Figure 51(c),(d),(e)** shows the aggregates of ZL sitting into the PLA nanofabric pores which are evident from the micrographs after dipping into the ZL solution. The other micrographs show nanofabrics that are dipped into the solutions of nCS and nCS-ZL solutions. The morphological structure and an average diameter of PLA nanofabric is 340±20 nm. The formation of nanofinish/nanofilm over PLA electrospun nanofabric can be seen whereas for the case of nCS-ZL hybrid

solution form nanofilm with agglomerated ZL distribution over PLA nanofabric as marked with blue circles. Few reports have been made on the nanochitosan coated cotton fibers in the form of film for coloration [133]. Thereby the surface of PLA nanofabric treated with nCS and ZL is dramatically different due to formation of a thin film which enhanced the shimmery behaviour.

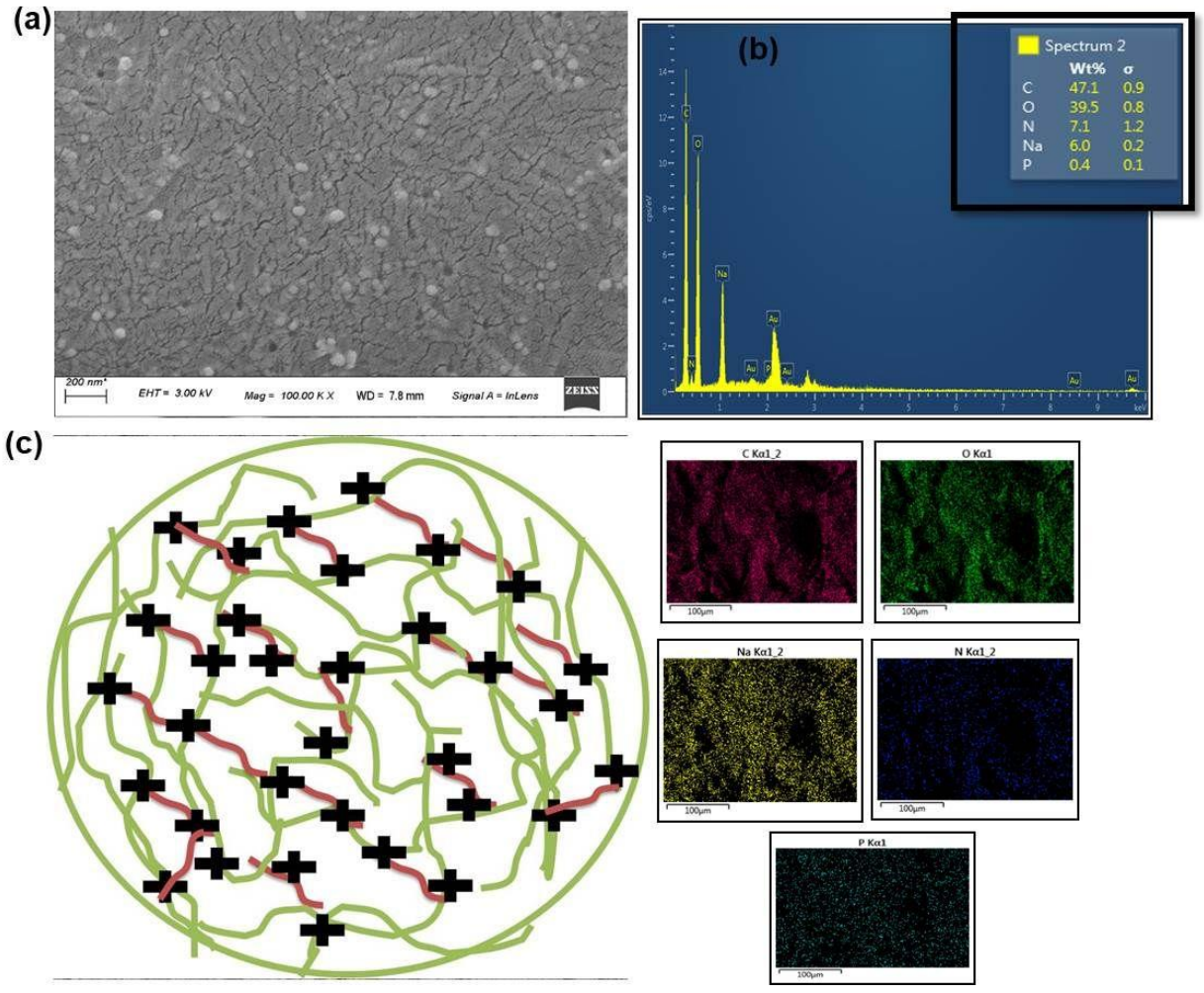

Figure 50: (a) FESEM micrographs of nCS at 100 kX magnification 200 nm scale, (b) EDX spectra of crosslinked nCS showing with elemental analysis, and (c) CS-STPP complex by ionic gelation.

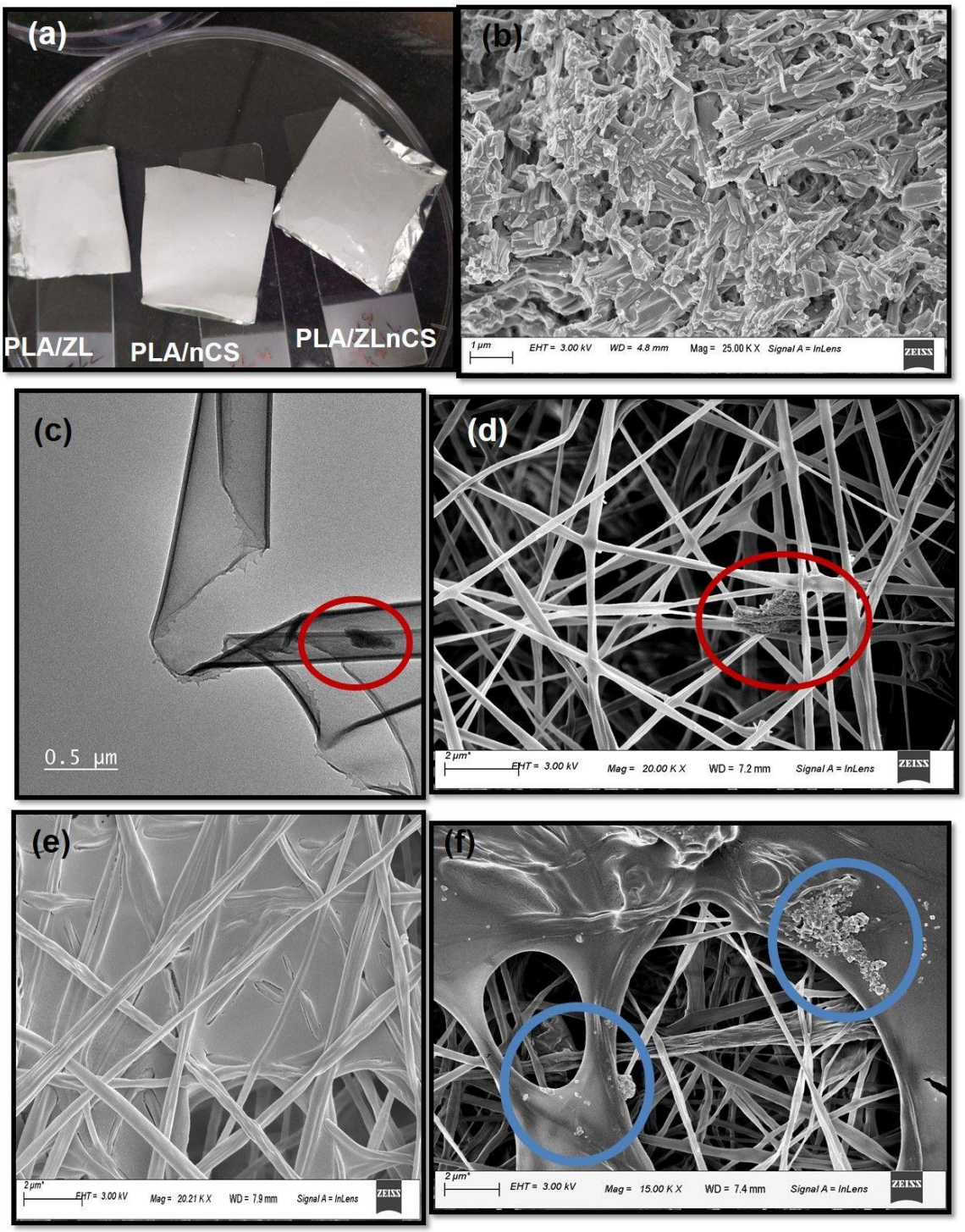

Figure 51: (a) Digital images on functionalized finishing over PLA nanofabric, (b) FESEM image of ZL, (c) FETEM micrograph of nCS-ZL nanofilm after solution drop cast over grid, (d), (e), and (f) FESEM images of PLA/ZL, PLA/nCS and PLA/ZL-nCS respectively.

5.2.5 Determination of Color strength of PLA nanofinished fabric

Here curcumin, a natural dye has been used for coloration by dipping into the three different solutions. The electrostatic interaction and hydrogen bonding were considered to contribute greatly to the absorption of dye on the fiber. It can be seen that the unfinished PLA nanofabric has shown a yellowish colour. But after giving an nCS nanofinish the intensity of the yellow color has been increased and changes to a higher. K/S value of a dyed material has a close relationship to the amount of dye absorbed by the fabric due to the presence of the primary amino groups. K/S values show the colorimetric data (L*, a*, and b*) with chroma and hue values for the different fiber samples dyed with their color shades are shown in **Table 5.**

Table 5: Color parameters of PLA/ nCS-ZL nanofabric after dyeing with curcumin color as represented herewith.

Sample Name	L^*	a^*	b*	Chroma	Hue angle
PLA	95.05±.2	-0.43±0.12	1.11±0.19	1.19±.28	111.38±1.9
PLA_{dyed}	89.49±1.1	-7.09±0.5	77.65±0.71	78.03±1.4	95.66±0.39
PLA/nCS_{dyed}	64.17±0.5	31.69±0.28	59.90±0.6	67.77±0.84	62.12±1.5
PLA/ZL_{dyed}	85.54±0.4	3.15±0.67	32.63±1.3	32.78±73	84.49±0.71
$PLA/nCS\text{-}ZL_{dyed}$	85.39±0.67	3.43±0.78	22.66±0.5	22.92±2.11	81.38±.74

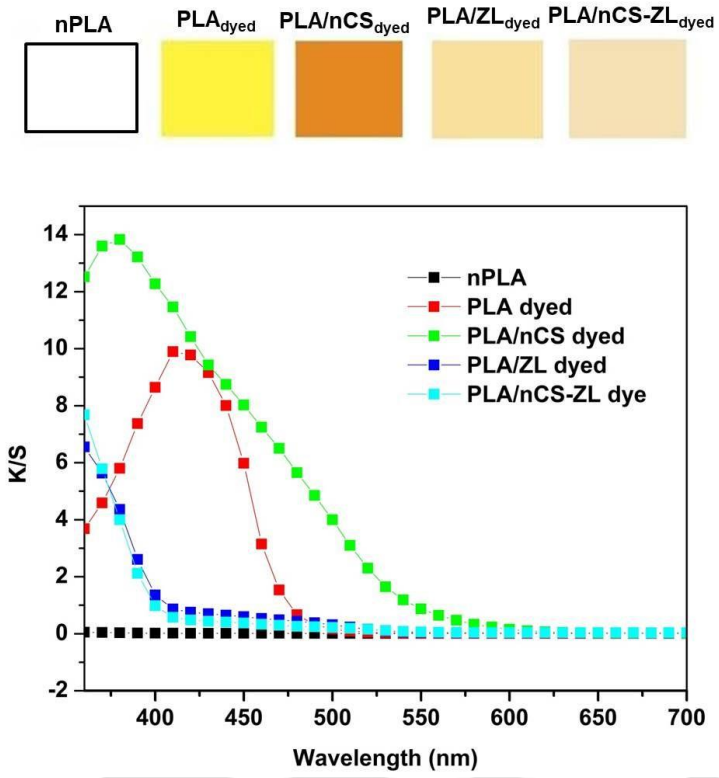

Figure 52: Change in color differences of untreated PLA, dyed PLA and functionalized dyed PLA nanofabric.

Figure 52 shows the K/S values of nCS treated dyed PLA fabrics are higher than that of untreated PLA showing the incremental value. As shown for PLA curcumin dyed fabric has the finest yellowish color The addition of nCS has decreased the hue value upto 62.12 which indicates the more yellow color and similar kind of decrease in hue value obtained after treating with nanochitosan[134]. The decrease in the L^* value indicates the contrast of the nanofabric between dark and light. The sudden raise in the more brownish color indicates the increase in the value of a^* for the case of PLA/nCS and an increase in the yellowish color of the nanofabric is indicated by the increase in the b^*values in the positive direction. The chroma values show the intensity of the color when it changes from neutral to dull whereas chroma values are more in the case of untreated dyed PLA nanofabric.

5.2.6 Antibacterial actions of the prepared nanofabric

The antibacterial activity of the prepared treated nanofabric was tested against *S.aureus* and compared with the commercial antibiotics as shown in **Figure 53**. The inhibition zone diameter of the nanofabric against the growth of the bacteria was measured as shown in the figure. PLA/ZL nanofabric shows inhibition zone of 9.2 ± 0.9 mm and is compared with the commercial antibiotic. Depending on the concentration of the nCS used negative charge present in the microbial cell which is taken for achieving antibacterial activity. But for the PLA/nCS nanofabric the antibacterial activity has shown inhibition zone of (3.1 mm) whereas for the other two multiple samples we can see that slight inhibition zone, maybe nCS nanofinish has not distributed properly leaving some voids after evaporation. Noted that for the case of PLA-nCZS-ZL, inhibition zone is 5.3 ± 0.23 mm which shows the hybrid nanofinish is having antibacterial activity towards *S.Aureus*.The presence of antibacterial activity is in correlation with the NH^{3+}groups that interact with the physical characteristics of the nanoparticle size and the surface charge of the activities of the microorganisms are predicted from the image in mm[135]. This property has been enhanced by the addition of ZL, another highly antibacterial material that depends on the correlation with the chemical characteristics due to the presence of the Zn^{2+} ions as well as high surface area.

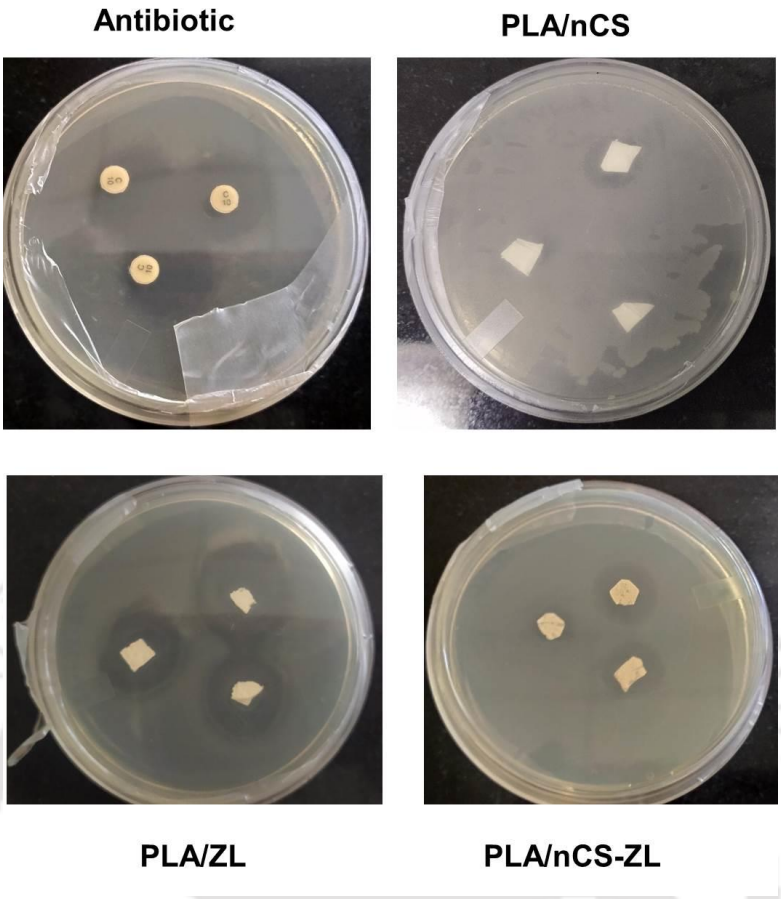

Figure 53: Growth inhibition by fabricated nanofabric against *S.aureus.*

5.2.7 Antiviral Activity

The known term "safer-by-design" has to be ensured while designing a polymeric nanofabric so that they won't create any adverse effect on human health. As textiles can also play a part in spreading pathogens and regular contact with hands has been proven to contribute in virus spreading. Further report has been made on using polyester fabric treated with metal salts like copper, CuCl, although they have a high antiviral activity they cause skin irritation after long-term use. Moreover, non-biodegradable polyester fabrics have the disposable problem causing global pollution.

Thereby a novel antiviral nanofabric has also been proposed after surfing through the literature. Mostly this invention prefers a low-temperature microwave synthesized technique to produce a metal-based oligomeric lactate (no high-temperature calcination step is required) that has not been reported earlier which is having significant antiviral

activity. Thereby our main motive was synthesizing an antiviral solution for fabricating a sustainable and biodegradable PLA antiviral nanofabric with more rapid virus deactivation (more than 97% in 10 min) and without any UV treatment as shown in **Figure 54**. The presence of the nanofilm over PLA nanofabric can act as a supportive layer as well as biocompatible nanofilm thereby acting as an excellent antiviral nanofabric for its applications in medical towels, gloves, caps, shoes cover as PPE.

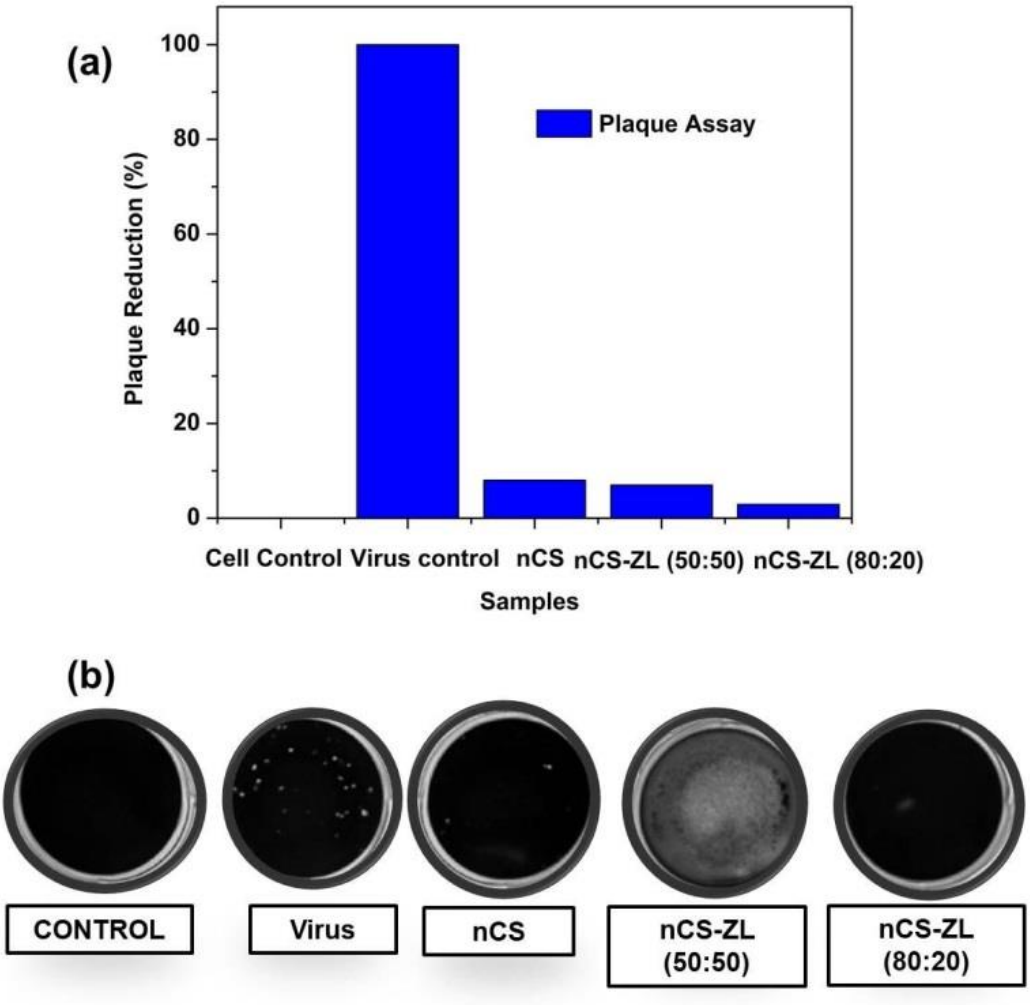

Figure 54: Plague reduction values and images showing antiviral efficacy against NCDV infection by nCS-ZL.

Table 6: Database of antiviral activities of various materials against different infections

Literature review	Results	Disadvantages	Reference
Copper polymers inside the spinning fibers	Antiviral and antimicrobial material for use in fabrics or sheet	Since it is in powder form can get removed after repeated washes, a limitation not to be used more than 1%. As high concentration has its adverse effect.	[136]
CuS treatment was carried out in nylon making three-layer mask design	SARS-CoV-2 was inactivated by 99.9% in 1 h	After, 1h and 2 h exposure, near-complete elimination of virus, 80% efficacy for longer exposure times of 5–10 min	[124]
Cuprous oxide (Cu_2O) particles bound with polyurethane, on stainless steel or glass	SARS-CoV-2, inactivates 99.9% of in 1 h	PU is non-biodegradable, presence of toxic isocyanantes	[137]
CuO film	SARS-CoV-2, was reduced by 99.8% in 30 min	Used for communal objects	[138]
Polyester fabric was treated with copper pigments in mild acidic, high-temperature exhaust process, padded with a polymer binder and cured	Tested against the bacteriophage MS2	90% of the virus concentration was reduced in cloth	[139]

Literature review	Results	Disadvantages	Reference
Hydroxyl group rich ZNPs (H-ZNPs), oleic acid modified ZNPs (OA-ZNPs) and chitosan-Zinc nanoparticles (C-ZNPs)	completely inactivated the virus within a period of 24 h, for H-ZNPs and C-ZNPs when Incubating Herpes simplex virus type-1 (HSV-1)	peptide (growth hormone) gH-(626- 644) which is rich in hydrophobic residues and to reduce viral ability by compromising hydrophobic part	[140]
Powdered oxide or hydroxide of calcium and magnesium. Fibers with core made of propypropylene and hollow fiber with polyethylene and powder	Potency of virus was mentioned from $10^{7.8}$ to $10^{2.3}$ against New castle disease virus	High temperature calcination step required, No exact duration has been mentioned properly	[141]
Curcumin chitosan (CuCs) nanocomposite	Hepatitis C virus genotype 4a (HCV-4a)	High antiviral activities against entry of HCV-4a into Huh7 cells by almost 100% reduction in viral titer, and curcumin inhibited viral entry by almost 95%.	[142]

5.2.8 Study of cytotoxicity:

Currently, toxicity studies are considered as the mandatory factor for demonstrating its use. The research result of toxicity testing was done where toxicity parameter in BHK-21 cell culture monitored based on the number of living cells/cell viability shown as optical density (absorbent), can be shown in **Figure 55**. The cytotoxic effect of various concentrations of ZL, and nCS-were taken and it has been detected that non-toxicity concentrations are 0.5 (v/v %) for ZL when considered for 48 hours of cell exposure. But the utilization of nCS as nanofinsh layer with ZL has enhanced the non-toxicity up to concentration 1.25 (v/v %). BHK-21 cell growth is monitored using a number of cell viability by optical density (absorbent), as shown in **Figure 56** where optic density values are decreasing as the concentration is increasing. It can be concluded that nCS/ZL with concentration 0.25% to 1.25 % does not have a toxic effect on BHK-21 cell culture since they do not have any "toxic cluster" structure which can cause a toxic reaction. A reduction in the concentration of suspensions thereby increases cell survival. The microscopic fibroblasts images hence signify mixed species of suspended and adherent cells thereby showing cell growth patterns without any cytotoxicity for the mentioned concentration.

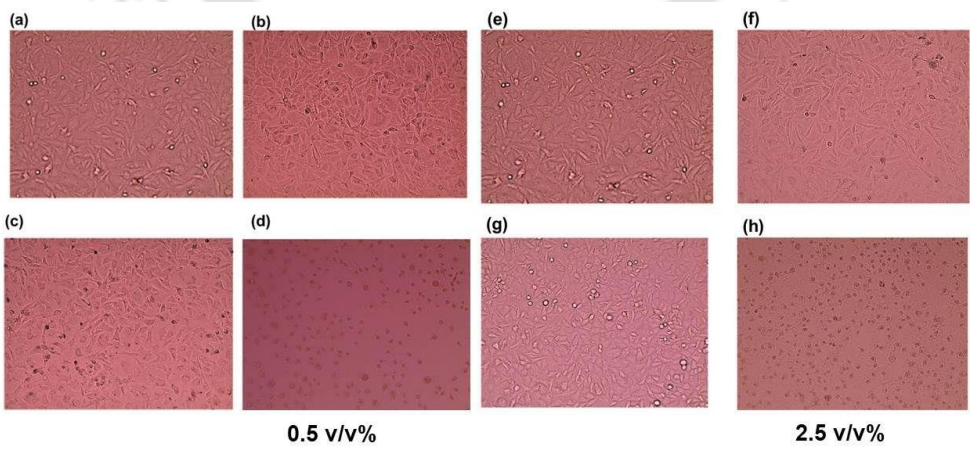

Figure 55: Microscopic images of BHK-21 fibroblasts grown in presence of ZL and nCS-ZL different concentrated solutions showing both suspended and adherent cells.

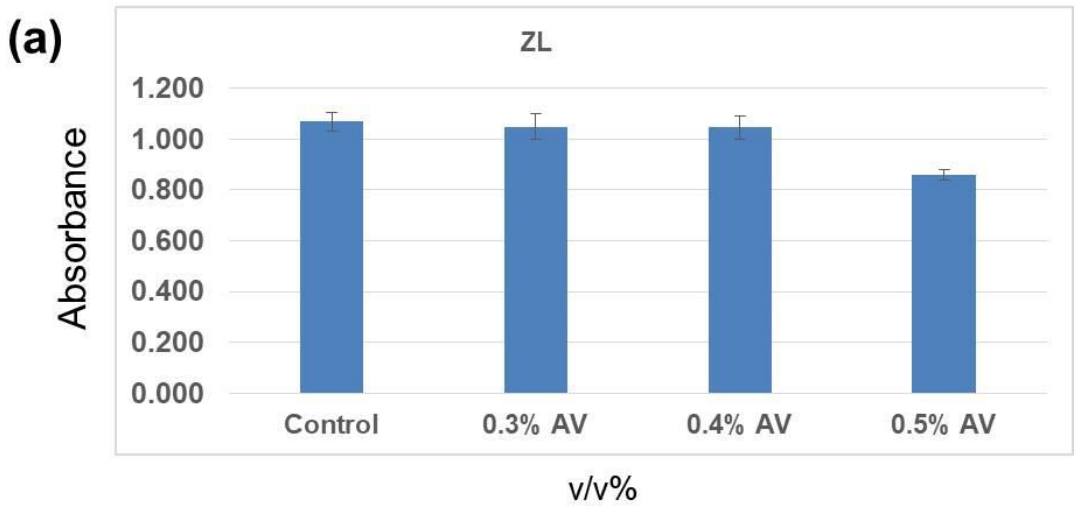

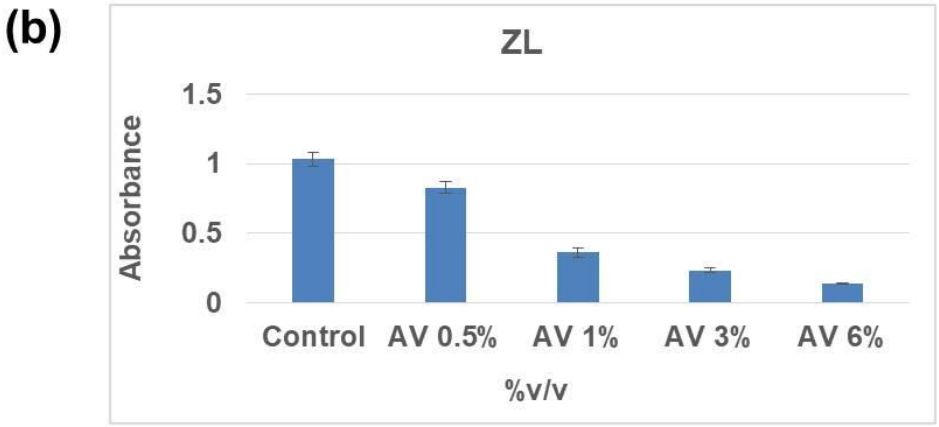

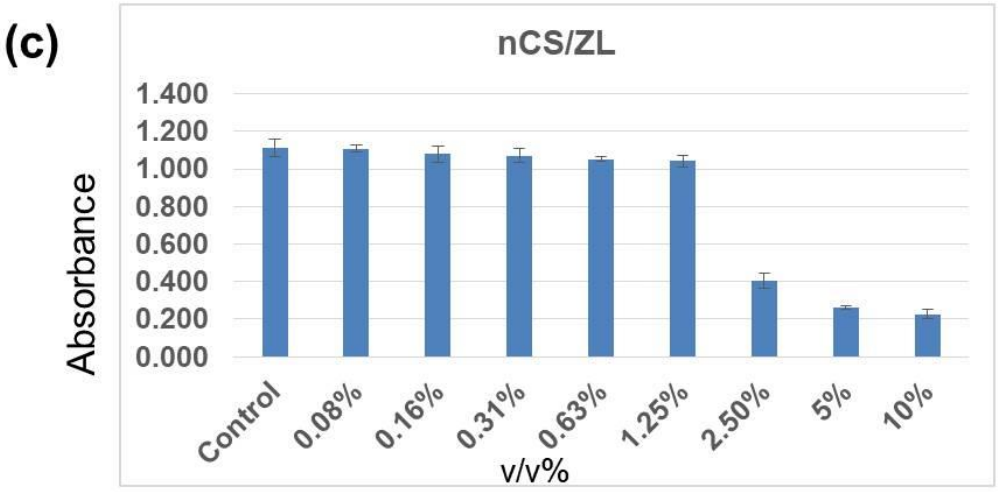

Figure 56: Cytotoxicity graphs from typical MTT assay showing the effect of ZL and nCS-ZL on the viability of BHK-21 cells.

5.3 Conclusion

In this chapter, the effectiveness of biocompatible biopolymer and ionic gelation synthesized nanochitosan has been studied as a shimmery nanofinish when treated over PLA electrospun nanofabric. The multifunctional PLA nanofabric has been fabricated using the dipping method. For better property enhancement the dipping solution has been prepared using antiviral zinc-oligo lactate and nanochitosan in an acetic acid solution. Even there is improvent in the antibacterial activity for the hybrid solution against *S.aureus* than the individual nanochitosan as zinc ions into/onto the nCS increase positive charge density of nCS. We have also found that the utilization of nanochitosan as nanofilm can help ZL distribute properly and suppress the toxic cluster behavior. In addition, the use of yellow dye proves the dye ability shows PLA/nCS has better dying ability than the PLA/nnCS-ZL. The nCS nanofinished PLA nanoabric shows 86% antiviral activity that has been enhanced to 97% for the hybrid solution. All such multifunctional attributes presented in this study results in promising applications for PPE as medical towel, shoe cover, and hair cap to protect one from viruses.

****

भारतीय प्रौद्योगिकी संस्थान गुवाहाटी
Indian Institute of Technology Guwahati

CHAPTER 6

FABRICATION OF HIGHLY HYDROPHOBIC, ANTIBACTERIAL PLA/SNC-ZNO ELECTROSPUN MAT MIMICKING A WOVEN PATTERN AND ITS ACCELERATED CRYSTALLIZATION KINETICS STUDY

Abstract: This chapter deals with a successful synthesis of bud and magnificent flower-shaped ZnO nanoparticles that have been possible to develop over SNC as a biosubstrate due to the presence of reactive sites. The nanohybrid prepared by in situ precipitation method were identified and characterized by FTIR, XRD, UV, PL, FESEM, FETEM, EDX analysis. The functionalized PLA composite nanofibers are produced by electrospinning using PLA and decorated with SNC-ZnO nanohybrid (concentration 1%, 3%, and 5%). The morphological analysis gives an average diameter of nanofibers 154±0.053 nm where nanohybrid tends to adhere on the surface of the PLA nanofabric with high hydrophobicity having WCA 135.3 ±0.25° for 5% nanohybrid incorporation. The nanofabric has significant antibacterial activity against *E.coli* and *S.aureus* bacteria. Further, an extensive study has been made on thermally stipulated processes using DSC on non-isothermal crystallization kinetics using various models like Avrami, Ozawa, Mo, Tobin plots. The results revealed sites for heterogeneous nucleation and improvement in crystallinity, $t_{1/2,}$ and nucleation effect due to the incorporation of nanohybrid with PLA. Further, both primary and secondary crystallization process is taking place can be analyzed using Avrami plot which confirms that the crystallization mechanism and crystal structure of PLA remained unchanged even after the incorporation.

Publications: Hazarika, D., Chakraborty G., Kumar, A., & Katiyar, V. Non-Isothermal Crystallization Kinetics Studies on Fabrication of Highly Hydrophobic Poly(Lactic Acid)/Silk Nanocrystal-ZnO Nanofiber Composite **(to be submitted)**

6.1 Introduction

Silk fibroin has been extensively utilized in the production of fabrics in the textile industry, in biomedicine as catalysis due to its biocompatible nature, biodegradability and mechanical properties. Silk-based textile manufacturing is among those industries where the demand for water usage is high and can have a significantly adverse impact on the environment due to large volumes of wastewater produced. Because of the defined primary structure, the silk nanoparticles may offer various possibilities for surface modification. The versatile nature of the compound has made its utilization in the form of macro, micro, nano like nanoparticles, nanofibers, hydrogels, etc[143]. And due to the outstanding properties of silk fibroin in the form of nanocrystals as nanofiller for polymer composites have gained increasing interest for both in academic and industrial research. Moreover, the introduction of inorganic particles that have interesting properties for tuning the properties than bulk materials in terms of antibacterial, crystallization, structural modification typically using metals, oxides, etc. Zinc oxide (ZnO) is an important nanomaterial aside from titanium oxide, silver, and copper oxide used as antibacterial, biosensing, catalysis agents[144]. Moreover, the shape of ZnO nanoparticles also plays an important role in influencing on the properties. Using various efforts morphology modification has been done like comb-like ZnO nanoferns, tetrapod nanocrystals, rod-like with possible utilization in unique applications [55]. Several reports have been made on modification of the surface of ZnO physically or chemically in order to reach super-hydrophobicity in the manufacture of self-cleaning[145].

Despite the important desirable properties of PLA its crystallization properties are very low compared with other thermoplastics. The utilization of foreign materials such as in the form of nanomaterial has opened the enhancement in crystallization process by increment in the nucleation probability. For such cases, various nanofillers have been

reported to provide nucleating effect for PLA nanocomposites using nano-$BaSO_4$, silica nanoparticles, multiwall carbon nanotubes (MWCNT), organically modified silica, expanded graphite, halloysite nanotubes (HNT) etc. Further to have applications in highly aided value as PLA is currently focusing on the applications of packaging materials and textile fibers using finely dispersed nanomaterials. Although incorporation of a few nanomaterials such as calcium carbonate, calcium oxide, ZnO has enhanced the antibacterial properties even in low filler amounts. Further studies have been made on modification of ZnO surface using triethoxy caprylylsilane for designing films and fibers for functional properties like antibacterial and UV as well as enhancement in nucleation activity[146–148]. Work has been mentioned using silk nano-discs (CSNs) as biofiller to study the non-isothermal crystallization kinetics reinforced with PLA where it was found acting as a heterogeneous nucleating agent. The hybrid materials formed by organic/inorganic materials result in synergetic effect irrespective of their components in nanometre-scale leading to better mechanical, thermal, and gas-barrier properties [149].An increase in interfacial area by creating a volume fraction of interfacial polymer due to their small size even at lower loadings like less than 5wt% also improves the nucleation efficiency of the fillers for the PLA nanocomposites[150]. Thereby, the idea of incorporating using a surface modification of ZnO with biofiller will be another tunable area of interest to study the crystallization kinetics of PLA.Electrospinning is regarded as a facile method to design with integration of architecture and characteristics of materials for achieving multifunctional that includes nanofibrous structures, with woven/nonwoven/ random and aligned structures. For such desirable designs, the selection of different patterned architectures can be achieved by using corresponding metal mesh-shaped collectors that enhance the accumulation effect between the charged nanofibers and the collector [151].

6.2 Results and Discussion

6.2.1 Structural analysis using FTIR

Figure 57 shows the compared FTIR spectra for the ZnO, SNC, and nanohybrid (under neutral and basic pH). The characteristic crystallized bands observed at 1625 cm^{-1}, 1235cm^{-1}, 698 $cm^{-1}$and 1512 cm-1 are attributed to amide I (C–O stretching), II ((N–H deformation and C–N stretching), III (C–N stretching and N–H deformation), V band formed due to the presence of β-conformation of the crystalline region of the SNC. The peak within the spectral range of 400 and 600 cm^{-1} is attributed to Zn–O which indicates high purity zinc nanoparticles due to inter-atomic vibration. The band at 643 cm-1 is due to random coil/silk I conformation which has been disappeared after changing the pH to 10 for the hybrid SNC-ZnO. The presence of broad characteristic peak around 3250.23 cm^{-1} is due to the stretching vibration of the hydroxyl group (O–H) present in SNC. This has been changed to a less broad peak due to the electrostatic interaction formed between SNC (–C=O and Zn^{2+}) and ZnO. Further, the intense peak around 480 cm^{-1} as seen in the spectra of SNC-ZnO (SZn-pH10) also confirms the formation of ZnO on the amide surface of SNC. The rotational vibration peak at 980 cm^{-1}, (−CH_2, A_n) as found in SNC and SNC-ZnO (SZn-pH7) has increased in broadness and intensity due to the charge transfer between the metal ions and the random coil structure of SNC.

FTIR analysis was also performed to investigate the functional groups of electrospun nanofibers of different compositions as shown in Figure 3. The peak at 1748 cm-1 (–C= O) is attributed to the PLA, where peak at 2989 cm^{-1} and 2954 cm^{-1} for (−C−C) band that were caused by asymmetric and symmetric stretching vibrations respectively by the presence of –CH_3 group of saturated hydrocarbons which can be seen clearly after incorporating nanohybrid within. For the case of 5% PLA/SNC-ZnO nanofabric the peak intensity around 1600 cm^{-1} has been enhanced which also suggests formation of chemical

interaction corresponding to the presence of Zn–O stretching.Whereas the − C=O peak at 1748 cm^{-1} has been changed in intensity due to the presence of SNC-ZnO also there is changing of the positions of the peaks and shape at1455 cm^{-1}, 1382 cm^{-1}, 1182 $cm^{-1,}$ and 1076 cm^{-1}respectively. They also attribute presence of SNC-ZnO in varying concentrations to have affected the vibrations of the fingerprint. Moreover, the peak at 1121 cm^{-1} for (−C−O) stretching has become more prominent due to the presence of the higher concentration of SNC-ZnO. The increase in the peak intensity is due to the addition of nanohybrid which has increased the nucleation rate and density of PLA. It also destroys the macromolecular chains to generate low molecular weight chains, which causes accumulation of lactide molecules, oligomers and acetaldehyde groups [152]. For the nanofabric where the addition of 5% SNC-ZnO to PLA has made, the peak at 3499 cm^{-1} has broadened the region due to presence of the amide group as well as free –OH groups present in the hybrid, attributed to bending and stretching vibrations of surface hydroxyl groups related to the formation of hydrogen bonds between SNC-ZnO and PLA.

The XRD pattern of precursor ZnO was taken as the representative sample while the other prepared SNC-ZnO nanohybrid samples with different pH are used for the discussion as depicted in **Figure 58 (a).** The XRD spectrum, as shown in **Figure 58(b),** reveals the prominent peaks of hexagonal ZnO belonging to (1 0 0), (0 0 2), (1 0 1), (2 0 1) phases along with the weak phases of (1 0 2), (1 1 0), (1 0 3), (1 1 2) and (2 0 2). The peaks are matched well with Bragg reflections of the standard hexagonal wurtzite structure of ZnO (PDF Card No.: 00-003-0888). The peak broadening indicates that small nanocrystals are present in the samples with presence of other peaks of less intensified which is a resemblance of the major peaks of SNC nanoparticles indicated by the peaks at 16.7° (002), 20.2° (201), and 23.8° (003). Moreover, the sharp diffraction peaks indicate the

high crystallinity of the prepared material which is increased from 90% ZnO to 94% for SnZnO-pH10.

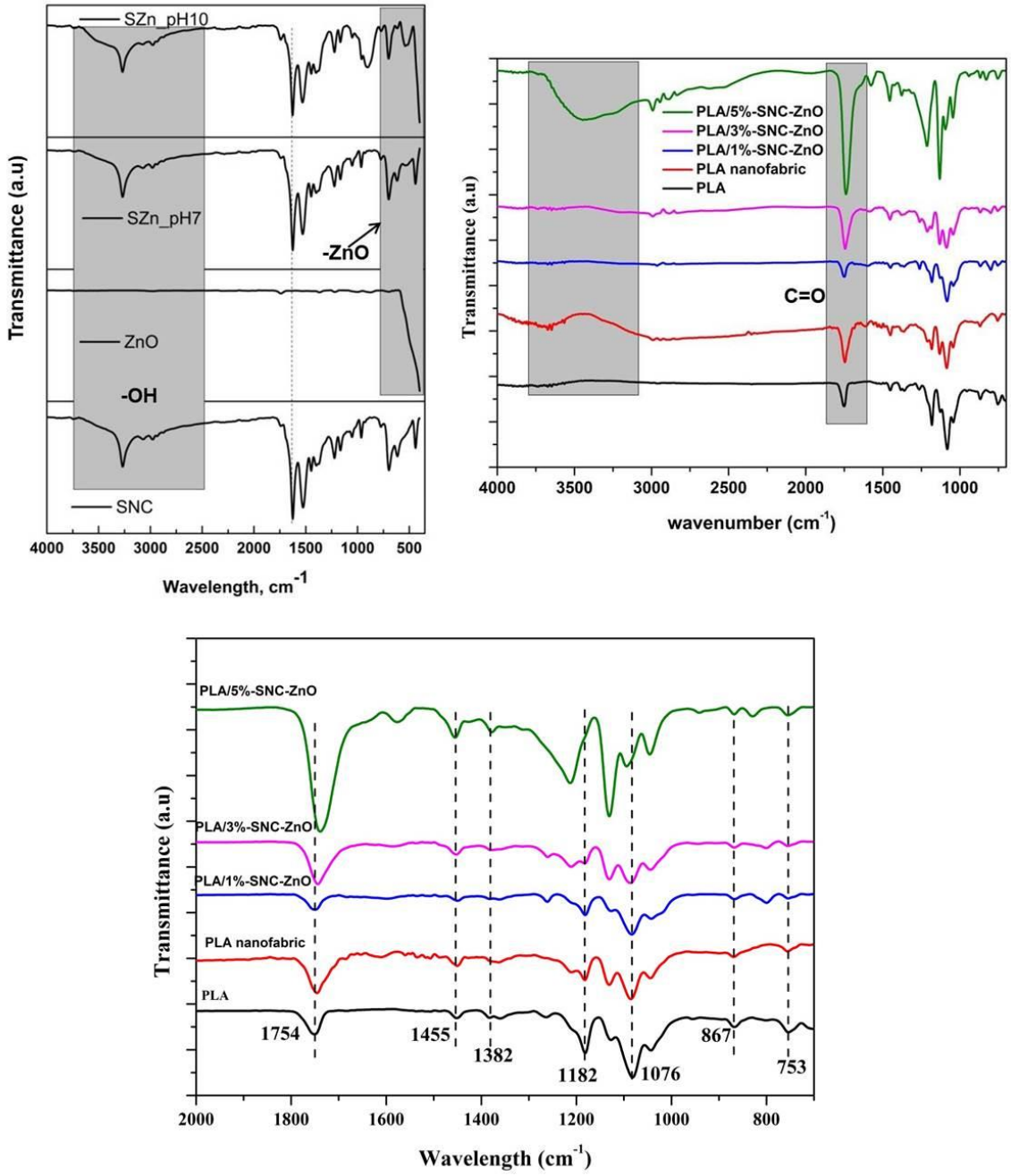

Figure 57: FTIR spectra of ZnO, SNC, SNC-ZnO nanohybrid at pH 7 and 10, PLA/SNC-ZnO (1%, 3%, and 5%) electrospun nanofabric with magnified spectra ranging from 800-2000 cm^{-1}.

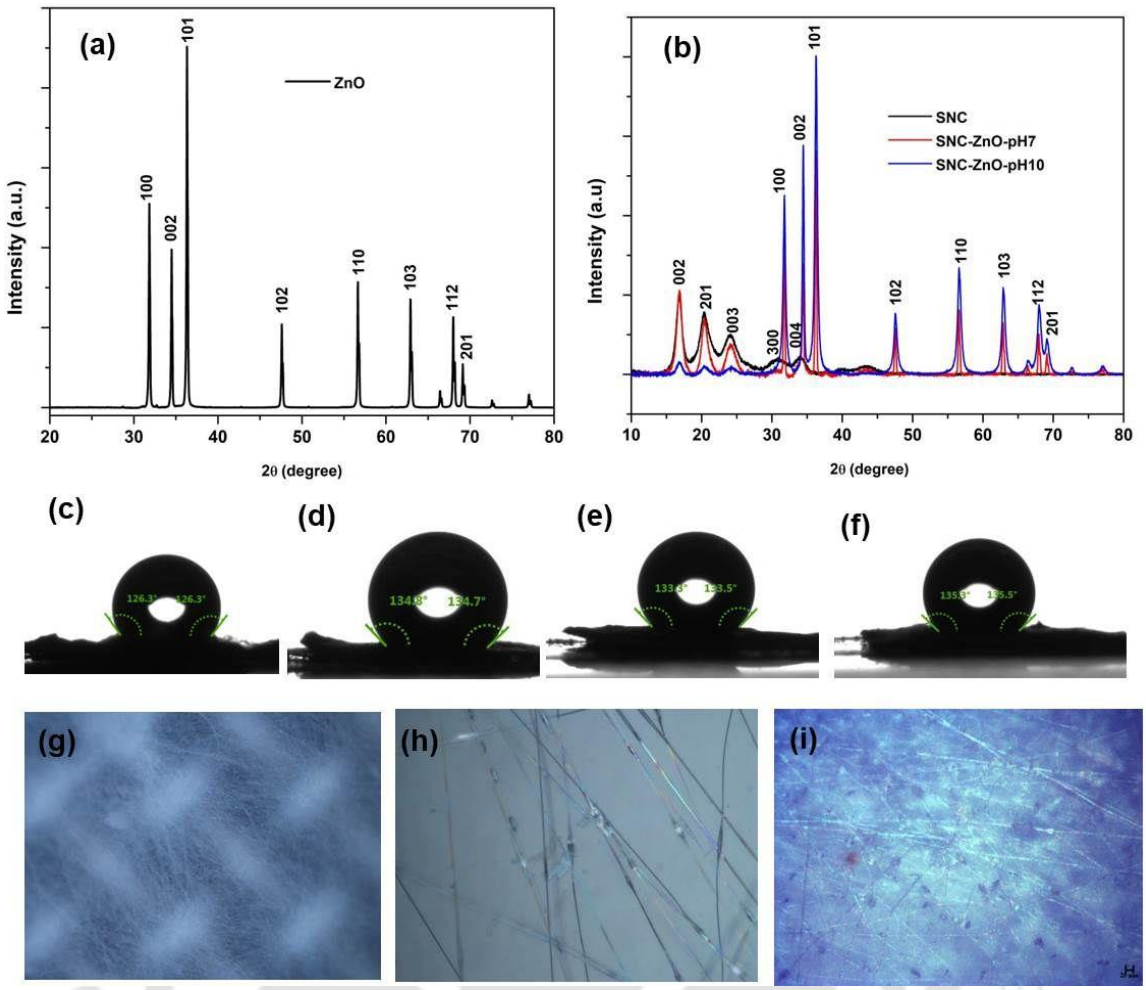

Figure 58: XRD spectra of (a) ZnO, (b) SNC, SNC-ZnO-pH7, pH10, (c) the pictures of water drop contact angle test on: (c) PLA mat (d) PLA/1%SNC-ZnO mat,(e) PLA/3%SNC-ZnO,(f) PLA/5%SNC-ZnO, (g),(h),(i) Optical microscope image at magnification 10x to obtain a pattered nanofabric mimicking as a woven nanofabric, Polarized light microscopy

6.2.2 Self cleaning ability

The most demanding condition to have self-cleaning effect owes to behave like a super-hydrophobic surface. Generally, due to the polar facet of ZnO that attracts the water molecules, there should be changes in the ZnO surface by increasing the non-polar ends which are done by incorporation of hydrophobic SNC [81]. The water contact angle (WCA) for prepared electrospun fibers has higher WCA than the pristine electrospun PLA. It was found that the surface roughness has been increased by incorporating

nanohybrid into the matrix. The PLA nanocomposites are having lower surface energy than PLA nanofabric. The WCA has been increased from PLA fabric 127° to 135° with in creasing concentration for PLA/SNC-ZnO electrospun nanofabric as shown in **Figure (c-d)**. The reason for fabricating thin nanofibers with a higher density of beads can also lead to a high value of hydrophobicity. Thereby the visual value as shown in **Figure 58(e-f)** suggests that the hydrophobicity has been reached to nearby the superhydrophobic value (~150°) for the PLA nanocomposite nanofibers, which can be attributed for the application of non-wettable textile.

Patterned architectures can be seen in **Figure 58(g-i)** under electrostatic attraction of collectors, and the charged nanofibers that are being collected to form into a cellular nanofibrous structure mimicking the woven like nanofabrics showing zones like node, corner, and screen. The POM leads to the formation of intermittent shiny birefringent segments distributed over the PLA nanofibers due presence of nanohybrid. Even in some places, there is the distribution of reflective iridescent nanohybrid beads formation along with the PLA nanofabric. Finally, under polarized light, at room temperature shining overlaid birefringence could be visualized due to randomly distributed nanohybrid along with the PLA nanofibers.

6.2.3 Morphological analysis

The morphology of the as-synthesized ZnO was examined by FESEM and the images at different magnifications are shown in Figure 19. From **Figure 59 (a)** it can be seen that the ZnO has few hexagonal prisms, rod-shaped and quasi-spherical. Even the hexagonal prism-shaped ZnO also has inhomogeneous aggregated nanoparticles as shown in the histogram of unmodified ZnO from the magnified image. Also, the FESEM image of SNC and SNC-ZnO nanohybrids is shown in **Figure 59 (d-e)**. It can be observed that the SNC have disc-shaped morphology which after modification by precipitation reaction

between SNCs and Zn^{2+} ions, well-dispersed ZnO nanoparticles are found to be obtained in the form of controlled flowers and bud kind of morphology with average basal diameter 86±5 nm and average length 170± 12nm calculated from Image J, for the sample pH 10 and some portion with irregular flower-like structure ZnO where each of them are having a tip and a cap. It can be seen that due to the presence of SNCs the regular magnificent flower has been formed tulip type bud acting as substrate for the buds.

Whereas in the EDX spectrum of the synthesized nanohybrid as seen in **Figure 59 (f,g)**, the nanohybrid sample consists of zinc (Zn), nitrogen (N) carbon (C) and oxygen (O). The two primary elements in a ZnO nanoparticle are zinc and oxygen and in SNC are nitrogen and oxygen. Meanwhile, the weight percentages of carbon, oxygen, zinc, and nitrogen are 36.5 %, 32.9%, 19.3%, and 11.2 % respectively. The EDX analysis thereby indicates that SNC-ZnO nanohybrid has been successfully formed.

The lattice images **Figure 60(c)** shows long-range crystalline order and attachment of nanoparticles having (101) planes corresponding to d-spacing values of 0.25 nm of ZnO nanoparticles present in the nanohybrid. The FETEM image also reveals the average length of the nanohybrid as 110 nm with an average diameter of 42.6 nm (cap) calculated using image j software. From the SAED pattern as shown in **Figure 60(d**) we can identify the d-spacing value 0.28 nm for plane (101) by calculating in image J (drawing a perpendicular line from the point to the lattice fringe and taking the distance between the two peaks from a line plot of "Gray Value" and "Distance") for ZnO nanoflowers. Meanwhile, the HRTEM image shows the overlapping of lattice plane (002) due to superimposing of SNC and ZnO at 34.55˚ (related to XRD spectra) which also attributes the formation of the nanohybrid. The presence of amino and carboxylic groups in SNC that are electron-donating groups gives the surface a substrate for the plenty of Zn ions for deposition during the treatment in basic conditions. The ZnO form fine crystal grains

of flower-like morphology by the excess of alkali treatment by etching the hexagonal structure also inducing surface defects and bestrew on the SNC surface.

Scanning electron microscopy (SEM) was also used to examine the morphology of electrospun mats, i.e., those obtained by electrospinning of PLA with nanohybrid loading have affected the fiber diameter and bead morphology. The FETEM image in **Figure 60 (e-f)** reveals the diameter of the fiber as 142.5±26.7 nm. Also, deformed fiber morphology can be seen in figure 21(c) due to the trapped nanohybrid in PLA polymeric chains.

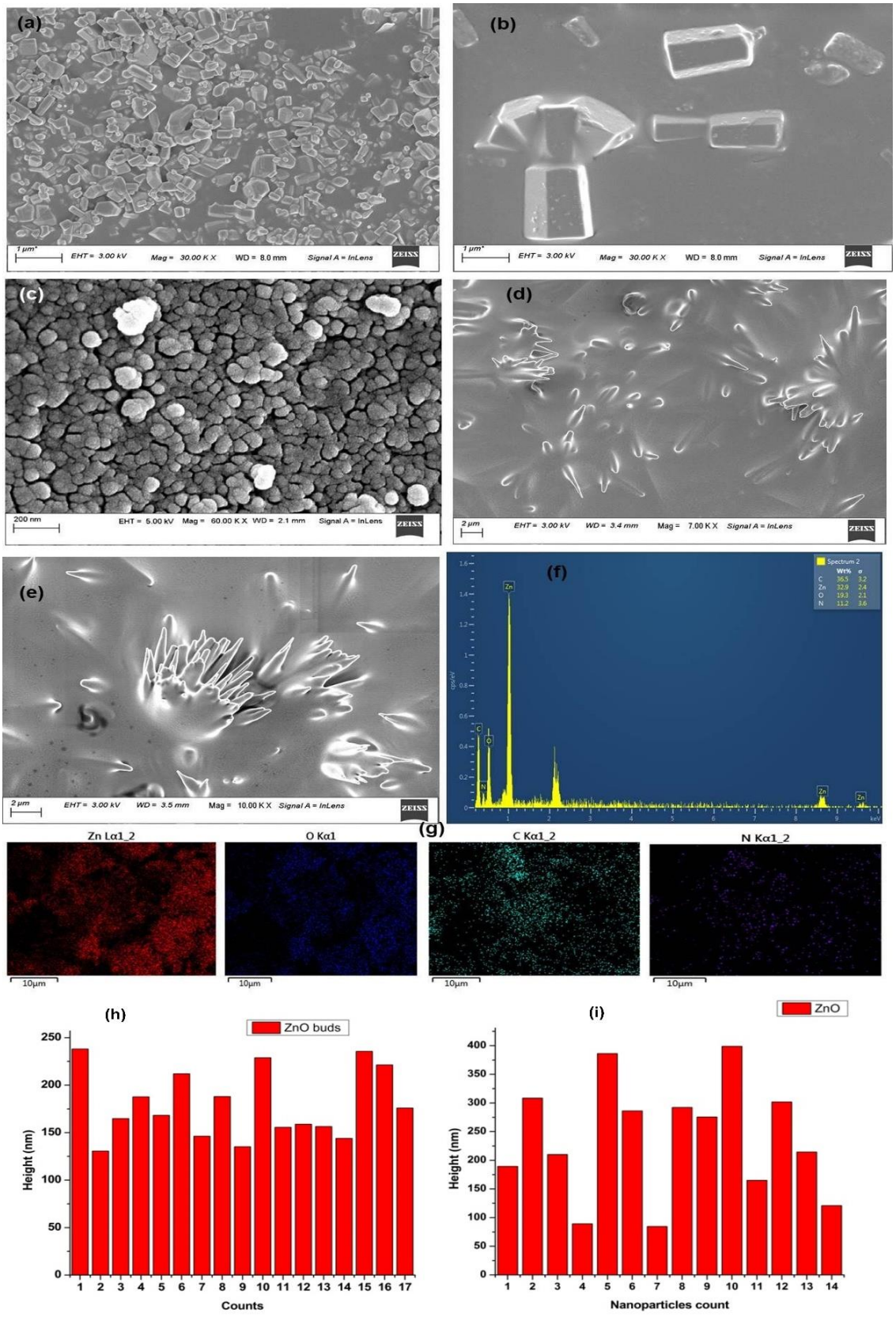

Figure 59: FESEM micrograph of (a) ZnO, (b) highly magnified ZnO with aggregation, (c) SNC, (d) irregular flower morphology, (e) aggregates of the flower bud with SNC distribution, (f) EDX for elemental analysis of SnZnO-pH10 (g) mapping for Zn, O, C, N content.

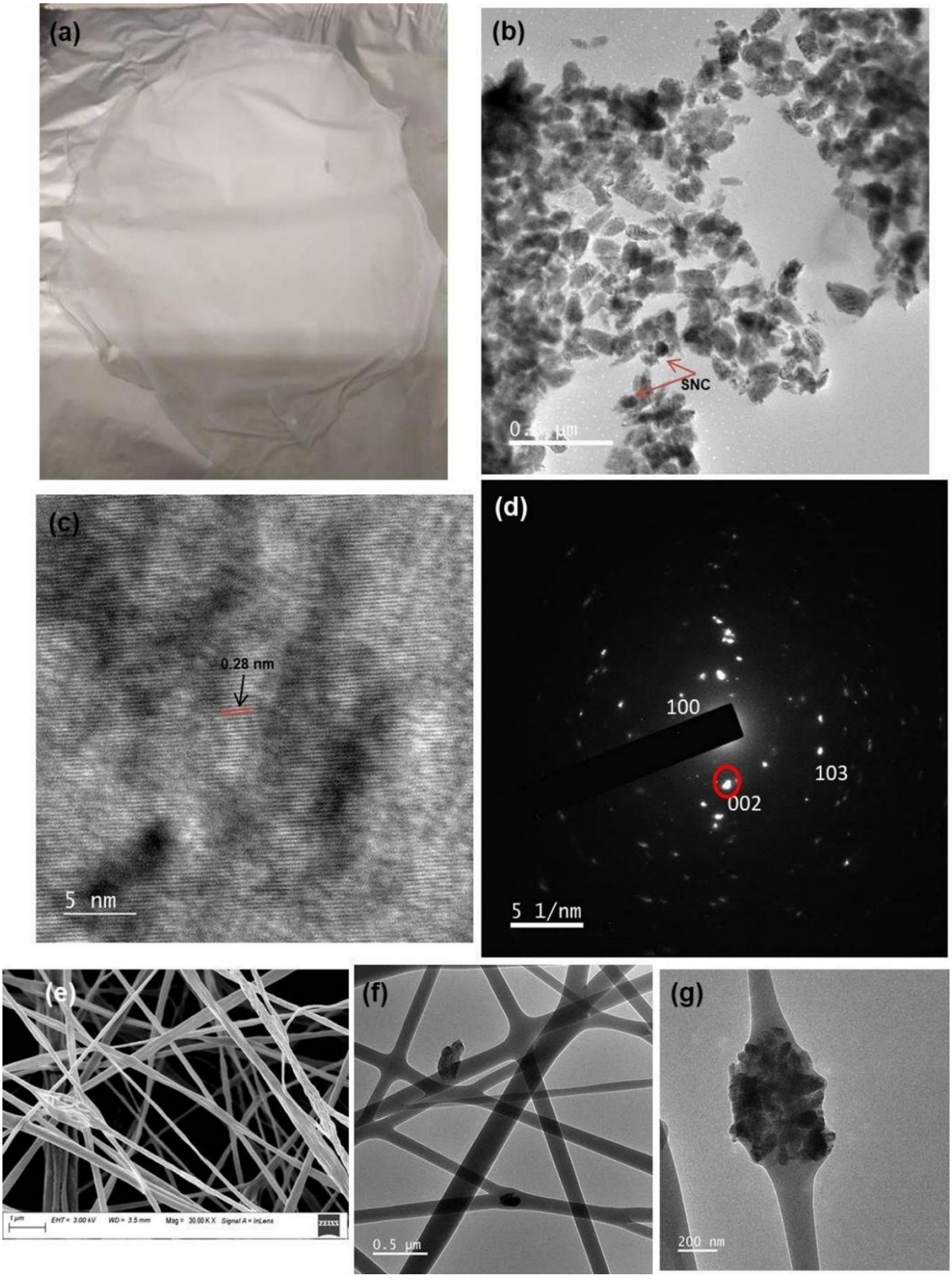

Figure 60: (a) Digital image of electropun nanofabric, (b) FETEM images of nanohybrid nanostructures (c) HRTEM image of SnZnO_pH10 FESEM micrographs of electrospun at high magnification for d-spacing (d) SAED pattern to show lattice planes with overlapped (002) lattice plane, (e),(f) and (g) highly magnified surface of the nanofiber showing the distribution of distributed over and trapped nanohybrid.

6.2.4 Antimicrobial activity

The antibacterial activity of SNC-ZnO nanoflowers was evaluated by measuring the zone of inhibition against the test organisms. The results for the synthesized nanoflowers were comparable to the results obtained for gentamicin (commercial) as per its excellent antibacterial activity. The activity of prepared SNC-ZnO nanoflowers at two different pH values (7, and 10) and the antibacterial inhibition zone has been calculated. A report has been made on the utilization of silk fibroin in chitosan/silk fibroin blend where it was found that silk fibroin has an adverse effect on the antibacterial activity of chitosan against Gram-negative or Gram-positive bacteria[130]. But here in this study, we can find that the nanoflowers form has significant antibacterial activity as shown in **Figure 61 (a-h)** showing the zone of inhibition forming a clear area around the discs. The most possible mechanism explains the antibacterial activity based on the zinc ions released from the ZnO nanoparticles, which strongly bind to thiol groups on the cellular surface of bacteria, leading to cell death for making them suitable for applications in biomedical applications, special textile, etc.

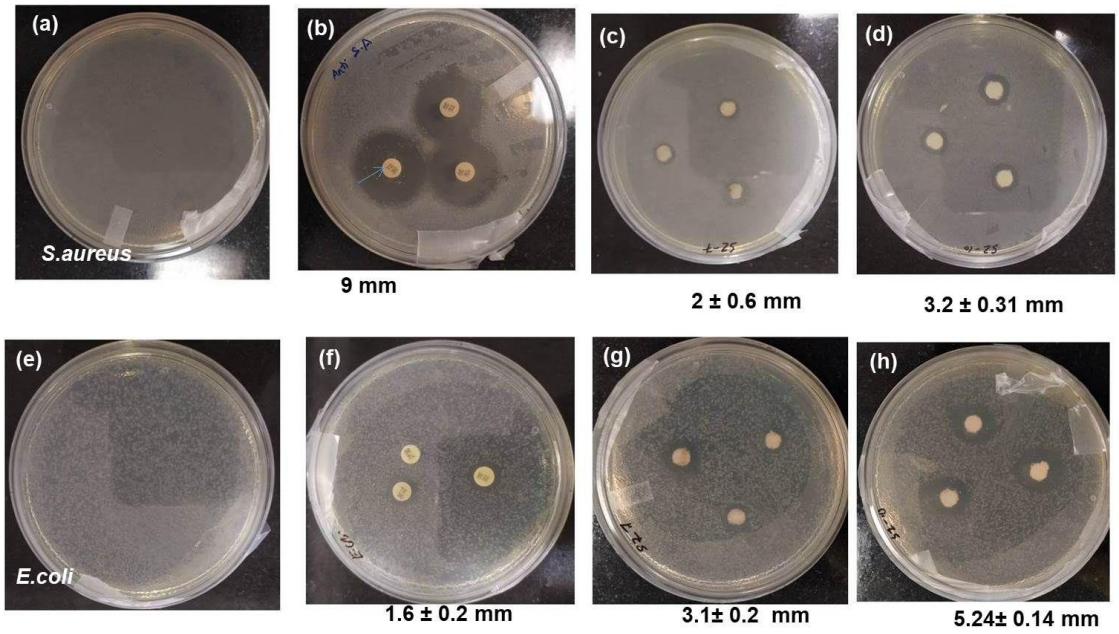

Figure 61: (a-h) Representative photographs of the antimicrobial activity of Gentamicin, PLA/3%SNC-ZnO for pH 7 and pH 10 respectively against Staphylococcus Aureus (left) and Escherichia coli (right)

6.3.5 Non-isothermal crystallization (NIC) behavior of PLAnanofabric due to incorporation of SNC-ZnO nanoflowers

Several kinetic models like Avrami's, Ozawa's, Tobin's, and Mo's approaches have been studied to describe the NIC behavior of the fabricated nanofabrics. This section includes all the approaches to determine the most appropriate one to relate the crystallization mechanism of PLA nanofabric.

As shown in **Figure 62,** where the DSC spectra exhibit the successive thermal events: $T_g$around 64 °C, an exothermal effect ascribed to the $T_{cc}$and endothermic peaks attributed to the T_m of PLA. As found from the 2nd heating plots the non-isothermal cold-crystallization peaks shifted towards lower temperatures when the nanohybrid, SNC-ZnO content increases, and changes are shown in the Table. But no major changes in the T_g value occur at a lower heating rate signifies no formation of short chains on the addition of nanoflowers. The results as shown in **Table 7** clearly shows that the addition of SNC-ZnO accelerated the non-crystallization along with narrower peaks has been observed

which suggests ease cold-crystallization of PLAacting as a nucleating agent at lower heating rates. This supports the explanation that a slower heating rate provides more sufficient time to activate nucleation at a lower temperature, and this change was seen much prominent with a higher amount of nanofiller. The report has been made on ZnO nanoparticles with silane treated surface with evidence of playing a retardant role for the crystallization process to higher values on increased in heating rate[148]. The percentage crystallinity of PLA and PLA/SNC-ZnO electrospun nanofibers were enhanced from 11.1% and 19.36% at the higher heating rate and from 35% to 64% at the lower heating rate respectively. It is interesting noticed that the presence of nanohybrid and annealing above the T_g causes an increase in the crystallization percentage to a higher value. It was also observed that the increase in SNC-ZnO contents produced an effect of bimodal melting process. This double melting peak for PLA has increased its visibility more at lower heating rate. This has been occurred due to formation and reorganization of crystal during heating just before the completion of melting of crystals in PLA due to detection of endothermic event at lower temperature that can be caused by the melting of ά-crystals, superimposed by an exothermic formation of α-crystals melt at a higher temperature. Patwa et al. has reported on crystalline silk nanodisc acting as nucleating sites for PLA crystallization with a unimodal melting peak[153].

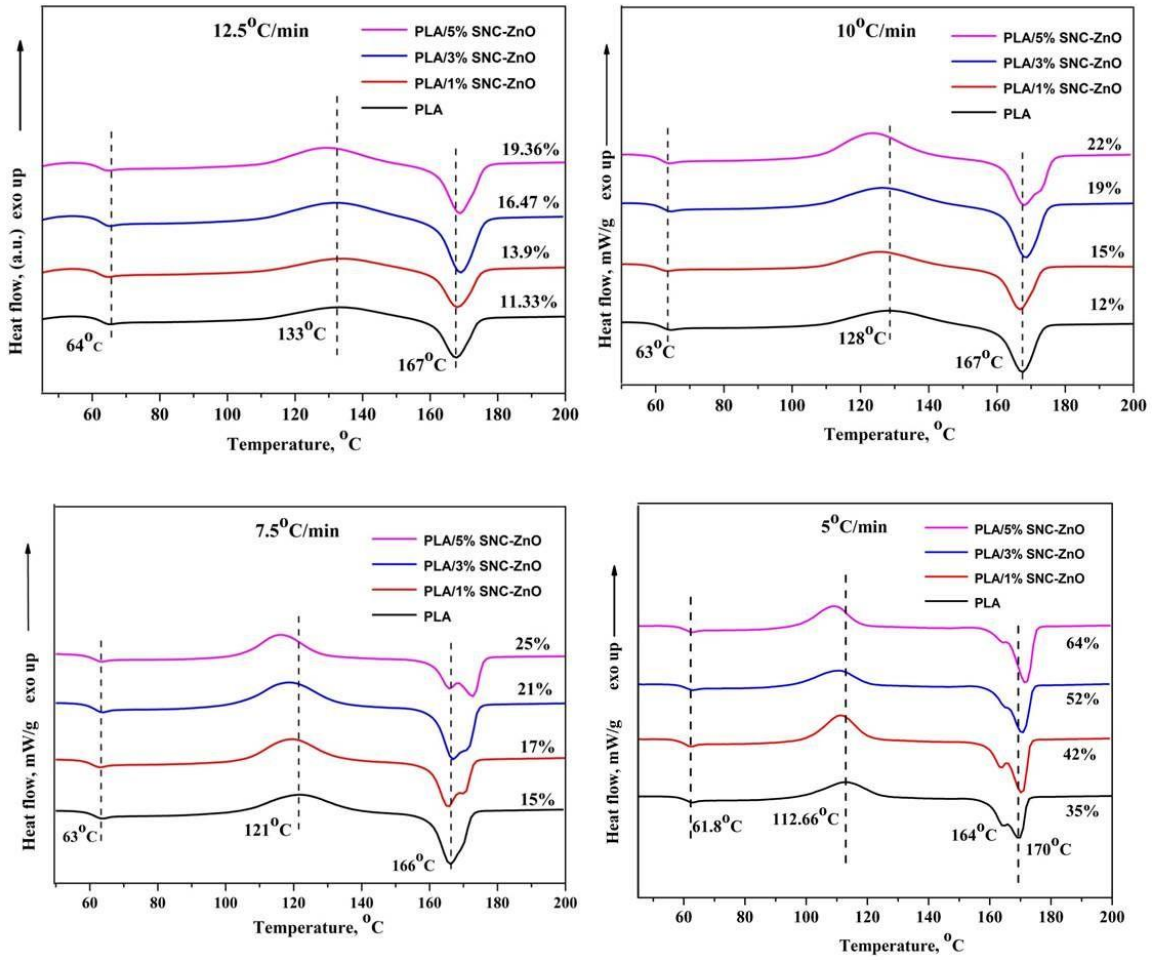

Figure 62: DSC curves of crystalline region showing percentage crystallinity for as-spun nanofibers measured at various heating rates for the different compositions.

Table 7: Comparative thermal properties datas on PLA and PLA/SNC-ZnO electrospun nanofabric at different heating rates

Sample	Temperature rate	T_g(ºC)	T_c(ºC)	ΔH_{CC}(J/g)	T_m(ºC)	ΔH_m (J/g)	X_c(%)
PLA 4032D	12.5ºC/min	62	133.2	120.8	167.6	-95.5	11.33
	10ºC/min	63.5	128.7	120.8	167.4	-131.7	11.58
	7.5 ºC/min	63.1	121.5	114.5	166.2	-120	15.43
	5ºC/min	62.3	112.7	92.15	169.4	-127.3	34.94
PLA/1%SNC-ZnO	12.5ºC/min	62.9	133.1	112.4	168	-99.87	13.9
	10ºC/min	62.89	125.3	112.4	166.8	-126.3	14.89
	7.5 ºC/min	62.6	119.5	119.1	165.5	-134.7	16.60
	5ºC/min	61.8	111.2	108	170.6	-147.7	42.32
PLA/3%SNC-ZnO	12.5ºC/min	61.5	132	140.7	169	-139.6	16.47
	10ºC/min	62	126.6	140.7	168.4	-158.2	18.7
	7.5 ºC/min	63.3	118.5	128.4	167	-148.4	21.34
	5ºC/min	62.6	110.4	82.03	170	-131	52.12
PLA/5%SNC-ZnO	12.5ºC/min	62.4	129.5	161.2	168.8	-131.9	19.36
	10ºC/min	61.5	122.7	161.2	168	-181.7	21.89
	7.5 ºC/min	62.5	116.2	95.65	170	-119	24.93
	5ºC/min	62.4	109.4	92.31	171.7	-148.2	63.76

The representative **Figure 63** shows the relative crystallinity curves of X_t(%) vs t, a time where we have seen that the overall crystallization is less for the PLA/SNC-ZnO nanofabrics which is 5.63 min compared to PLA nanofabric i.e. 7.28 min at higher concentration of nanofiller and lower heating rate. In case of lower heating rate of $t_{0.5}$ for PLA it is 3.96 min which has been decreased to 2.93 min showing faster crystallization.

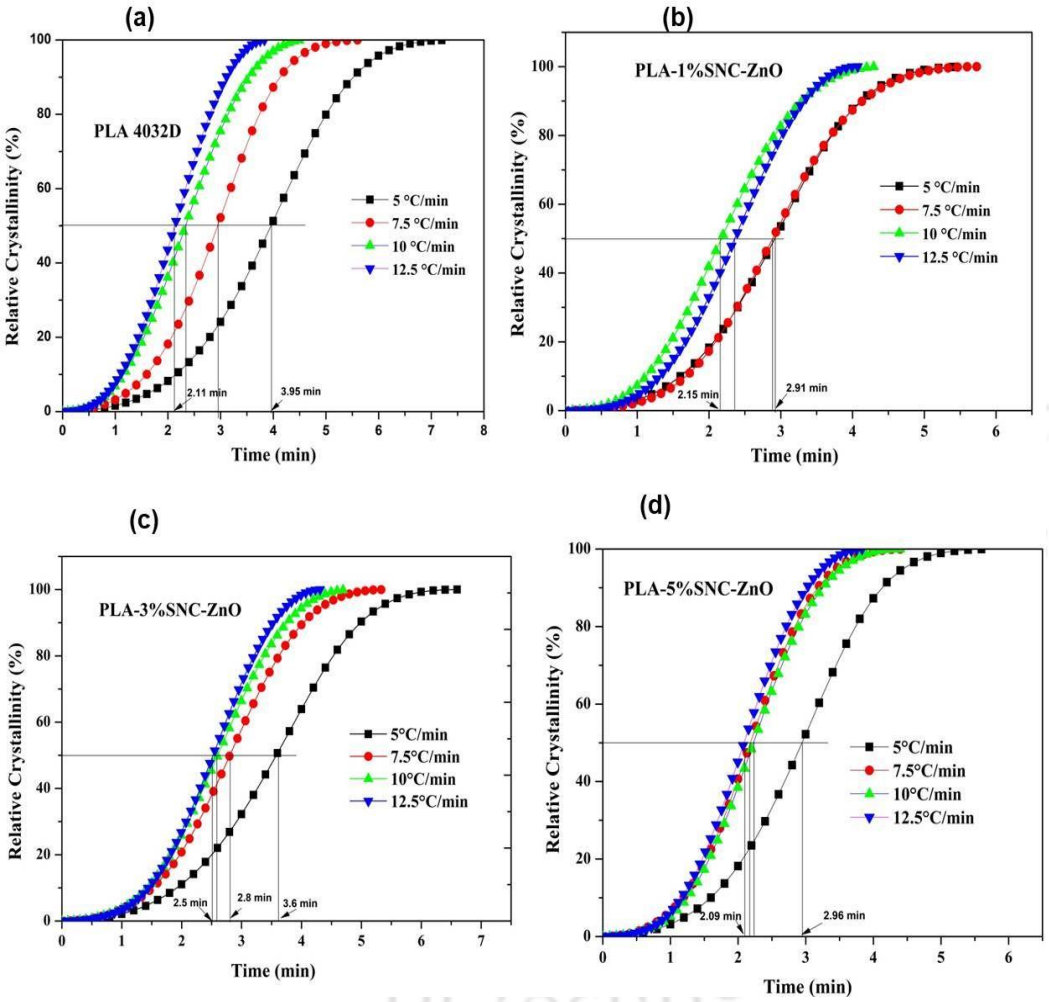

Figure 63: Relative crystallinity vs. time plots of PLA and its nanohybrid composite electrospun PLA nanofabric.

From the results shown in **Table 8** it was found that as SNC-ZnO content increases the $t_{0.5}$ decreases with decrease in the heating rate and acted as a nucleating agent in the PLA nanofabric thereby facilitating the crystallization rate. Both the heating and cooling rate

(β) is generally got neglected in Avrami equations for isothermal crystallization kinetics and so to make it suitable to adapt crystallization rate constant, modified Avrami equations have been used. The plots shown in **Figure 64** are then compared and found identical sigmoidal curves with two stages of crystallizations. The initial part shows a linear relationship and Z and n can be calculated. And the second stage shows deviation from linearity suggesting secondary crystallization with spherulite impingement. Thereby the curves signify increasing rates and increase in the nanofillers content the sigmoidal curves shift progressively towards shorter times. The values of log [− ln (1 − *X*t)] vs log t curves are plotted to determine the Avrami exponent (*n*) and rate parameters (*k*/*Z*c) from the slope and intercept respectively as listed in the Table. The average value of n for polylactic acid is 2.68, while that for PLA/SNC-ZnO nanofabrics was found ~ 2.79, suggesting that imperfect or faster spherulite growth was taken place due to heterogeneous nucleation phenomenon with mixtures of 2D,3D, and circular disc-like crystal growth[154]. The values of *Z* and *Z*c for both PLA and PLA/SNC-ZnO nanofabrics shows an increasing trend as heating rate is increased, but interestingly, *Z*c values are higher for higher nanofiller content that agreed the faster crystallization rate than neat PLA as related to the decrease in $t_{0..5}$ values as discussed earlier.

The Ozawa plot of log[-ln(1-X(T))] vs logβ for non-isothermal sold crystallization of samples is shown in **Figure 65** where the plots were made at a different range of crystallization temperature for each peak of crystallization. The plot shows poor linear correlations in some cases of temperature plots for PLA but as the nanohybrid content increases the linearity has been improved. The values of m are not constant with temperature during the primary crystallization process which gets increased after higher nanofiller content. For the case of PLA there are more non-linear curves for different crystallization temperatures. The reasons for the invalidity are probably due to the strong

secondary crystallization of PLA and/or the dependence of lamellar thickness on crystallization temperature as well as a heating function over the entire crystallization process. But the nonlinearity of the curves decreases on an increase in nanofiller content which may be due to the early crystallization process taking place. Although there are still non-linear plots which suggest that Ozawa's model has not been properly explained to some extent.

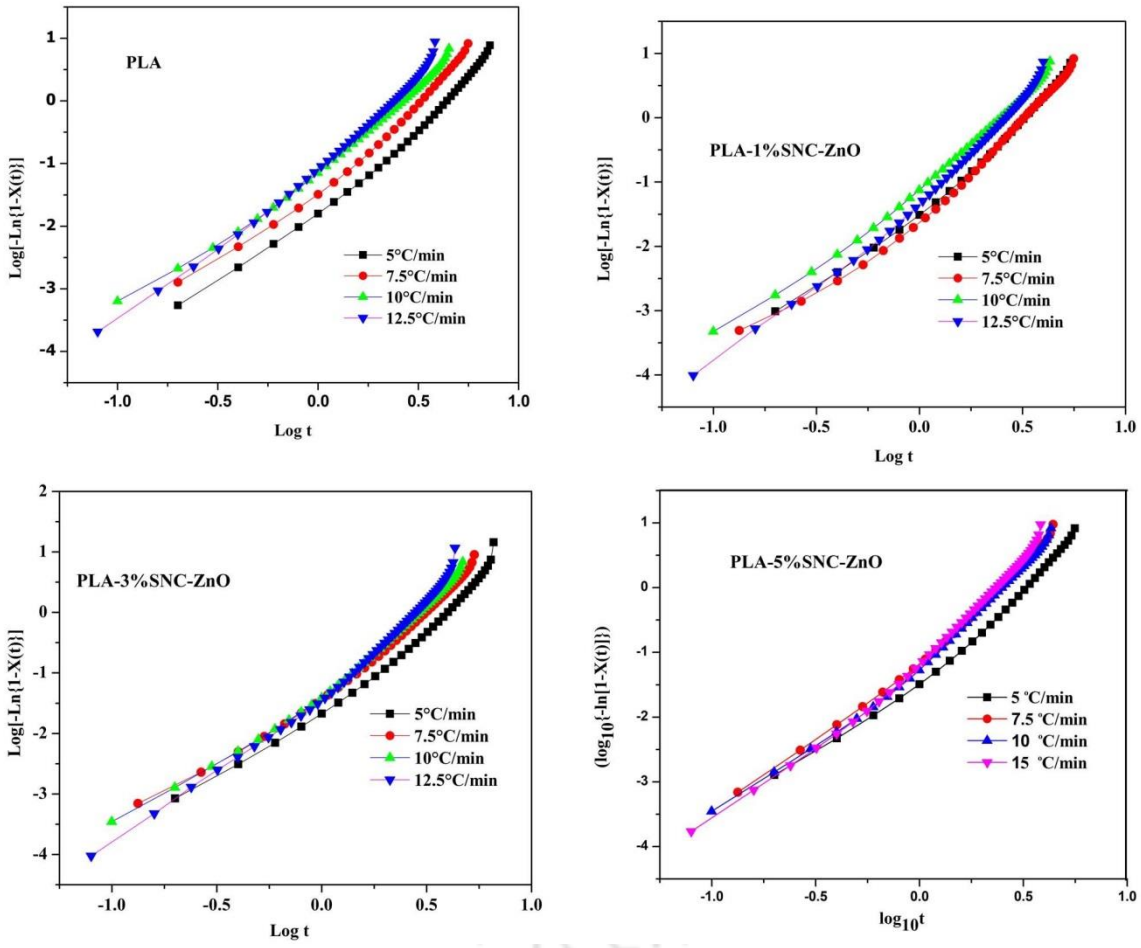

Figure 64: Avrami Log plots for non-isothermal cold crystallization of a PLA and PLA nanohybrid elecropun nanofabrics.

Table 8: Crystallization kinetics Parameters from Avrami, Jeziorny, Ozawa's analysis

Sample	Heating rate (°C /min)	$t_{0.5}$(min)	n	Z	Z_c ($\times 10^{-3}$)	Total time	T (°C)	m	K(T)	R^2
PLA	5	3.96	2.75	0.0182	3.64	7.28	108	5.49	19.49	0.996
	7.5	2.95	2.74	0.0426	8.52	5.64	116	3.29	15.33	0.958
	10	2.12	2.52	0.089	8.9	4.59	120	2.97	11.24	0.9448
	12.5	2.34	2.73	0.098	7.84	3.87	128	2.85	16.37	0.858
PLA/1%-SNC-ZnO	5	2.92	2.79	0.039	7.8	5.44	108	4.79	18.35	0.936
	7.5	2.89	2.87	0.036	4.8	5.77	116	3.87	20.47	0.996
	10	2.15	2.69	0.095	9.5	4.35	120	3.68	10.27	0.998
	12.5	2.35	2.9	0.061	7.6	4.11	128	2.33	8.07	0.999
PLA/3%-SNC-ZnO	5	3.57	2.75	0.025	5	6.64	108	4.13	13.68	0.971
	7.5	2.8	2.66	0.051	6.8	5.37	116	3.68	18.63	0.996
	10	2.59	2.68	0.057	5.7	4.76	128	3.68	22.42	0.999
	12.5	2.53	2.88	0.053	4.24	4.35	132	3.10	26.54	0.992
PLA/5%-SNC-ZnO	5	2.93	2.73	0.042	8.4	5.63	108	5.35	51.17	0.995
	7.5	2.17	2.76	0.089	11.8	4.43	116	4.23	33.78	0.993
	10	2.22	2.79	0.079	7.9	4.43	128	3.91	48.51	0.995
	12.5	2.08	2.88	0.089	7.12	3.87	132	4.53	134.39	0.992

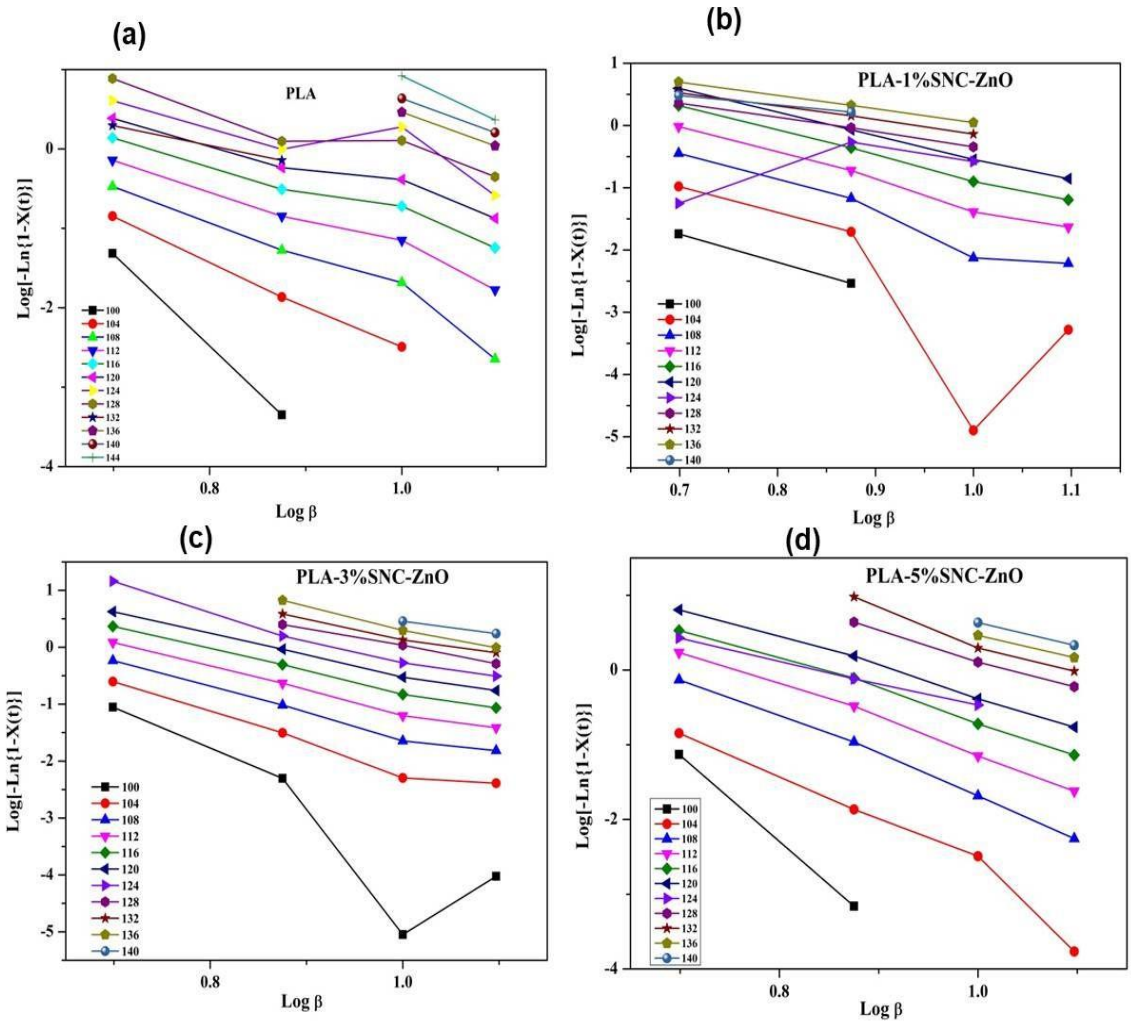

Figure 65: (a-d) Ozawa's Plots of Log{-ln[1 - X(T)]} vs. log β for PLA and its composites.

Avrami model is not appropriate to study the early phase of the crystallization process as it does not describe growth site impingement and secondary crystallization process. For such reason, Tobin's Model has been utilized. Tobin method describes the crystallization with growth site impingement. The value of n_T and K_T are calculated from Tobin's plots and summarized in **Table 8.** The n_T values are found in a range of ~3.53–~4.52. The range observed is ~3.5–~3.9 for nPLA, ~3.56–~3.85 for PLA/1%SNC-ZnO, ~3.460–~4.1 for PLA/3%SNC-ZnO, and ~3.78–~4.35 for PLA/5%SNC-ZnO respectively. It gets decreases concerning heating rate and for all the cases of PLA and PLA/ SNC-ZnO

nanofabrics. Tobin exponent (n_T) is also following Avrami exponent "n but n_T value is higher than "n" value of Avrami at same cooling rates. The slight deviation from linearity indicates the presence of both primary and secondary crystallization as shown in **Figure 66**.

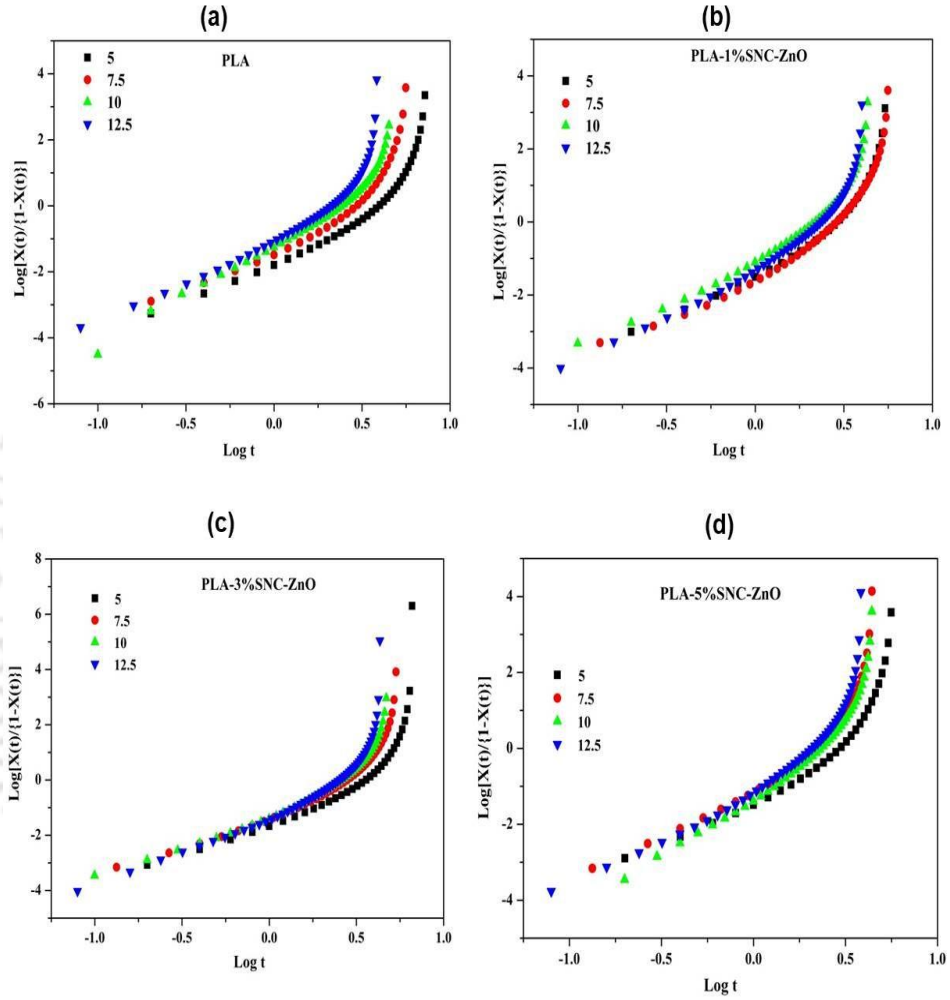

Figure 66: (a-d) Tobin's Plots for non-isothermal crystallization of PLA and PLA-nanohybrid nanofabrics blend and its composites.

According to Ozawa equation there is the weak linear relationship among the plots which suggests using Mo's plot for non-isothermal crystallization kinetics. This Mo's model is a combined form of Avrami and Ozawa. **Figure 67** suggests "α" values from Mo's plot within the range of 1.35-1.57 respectively for 20%, 40%, 60% and 80% relative

crystallinity for PLA which is found to be higher in the case of PLA/SNC-ZnO nanofabrics within the range of 2.3-3.3 for 20%, 40%, 60%, and 80% relative crystallinity indicates the faster change of crystallization mechanism. Moreover, an increase of "F(t)" values with increasing crystallization implies higher heating rate is required to achieve higher crystallinity. The curves obtained are nonlinear which also suggests the primary and secondary crystallization and is following the previous methods. Hence the values of a and F(t), for 20%, 40%, 60%, and 80% relative crystallinity are summarized in **Table 9**.

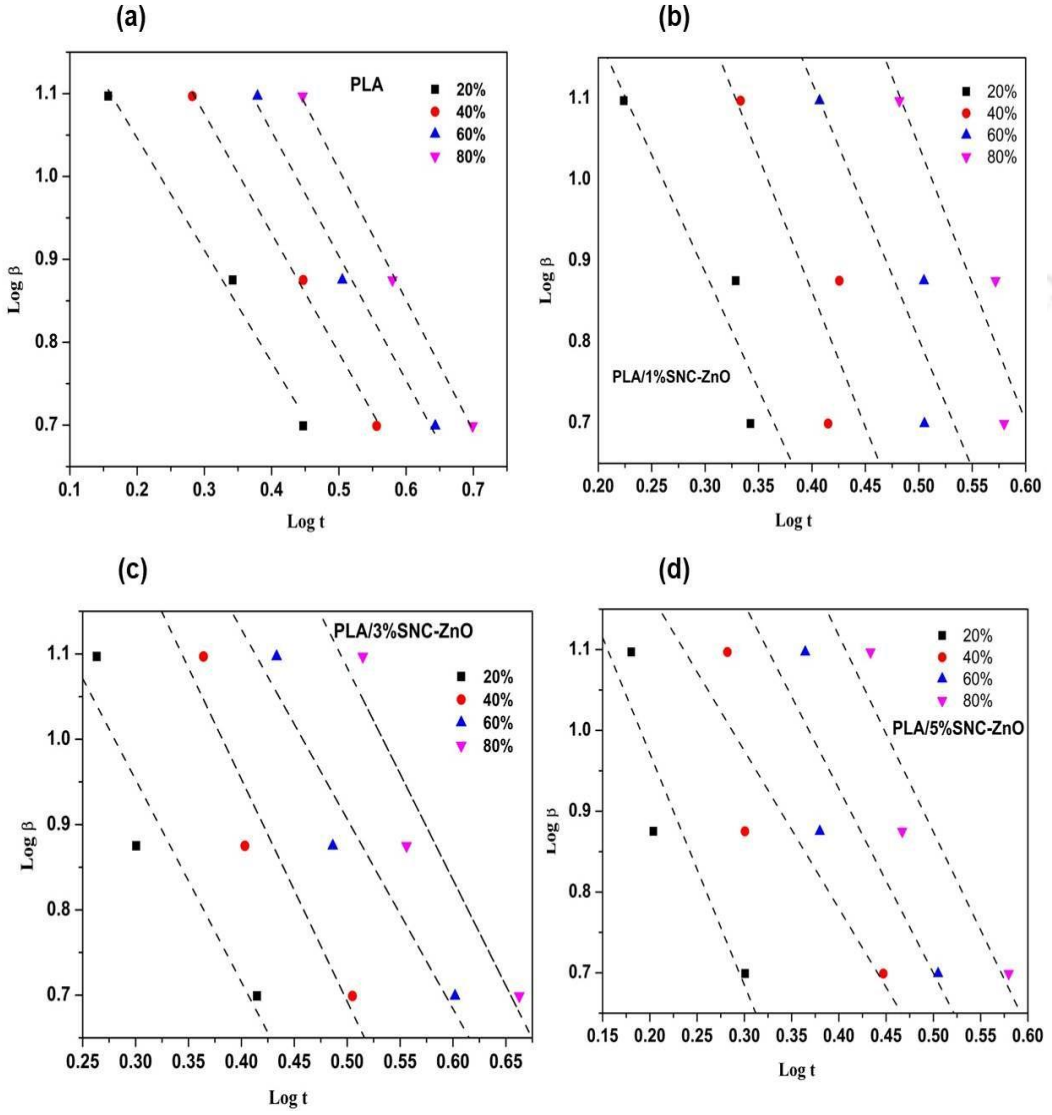

Figure 67: (a-d) Plots of Logβ vs. Log t from Mo's method for non-isothermal crystallization of PLA and PLA/SNC-ZnO its composites.

Table 9: Crystallization kinetics parameters from Mo's and Tobin's plots

Sample	Mo Model			Tobin Model		
	X(t)(%)	a	F(t)	Cooling rate (°C/min)	K_T	n_T
PLA	20	1.35	3.70	5	0	3.73
	40	1.44	4.48	7.5	0	3.91
	60	1.50	5.20	10	0	3.64
	80	1.57	5.98	12.5	0	3.54
PLA/1%-SNC-ZnO	20	2.89	5.75	5	0	3.56
	40	3.33	8.93	7.5	0	3.81
	60	3.17	10.80	10	0	3.85
	80	3.37	15.48	12.5	0	3.62
PLA/3%-SNC-ZnO	20	2.37	5.25	5	0	3.73
	40	2.60	7.31	7.5	0	3.46
	60	2.22	7.46	10	0	3.69
	80	2.48	10.27	12.5	0	4.10
PLA/5%-SNC-ZnO	20	2.86	4.71	5	0	3.78
	40	1.95	4.75	7.5	0	4.35
	60	1.84	6.29	10	0	3.98
	80	2.42	8.07	12.5	0	3.78

6.3 Conclusion

SNC/ZnO Magnificient flowed shaped nanohybrid was fabricated using precipitation method. The obtained powder has been analyzed using XRD, FTIR, UV to confirm the formation of the nanohybrid. This nanohybrid has been used as nanofiller for fabricating different compositions of PLA electrospun patterned mimic nanofibers. The EDX analysis gives mostly the elemental composition of the fibers, which also confirms the

presence of the SNC and ZnO. The FETEM image also reveals the average length of the nanohybrid as 110 nm with an average diameter of 42.6 nm (cap). The FETEM image for the electrospun fiber of 1%SNC/ZnO PLA reveals the diameter of the fiber as 142.5±26.7 nm with a uniform diameter. The visual of contact angle over the film was measured and found to be highly hydrophobic (135°) which can have an excellent potential to apply as a non-wettable textile. The incorporation of nanohybrid not only increased the initial crystallization temperature but also enhances the enthalpy, indicating acceleration in crystallization rate and leading to more complete crystallization. The analysis of Jeziorny and Mo's methods indicated that incorporation of nanohybrid exerted a nucleating effect on the PLA matrix and therefore enhanced the overall crystallization rate and depended upon the loading level.

****

CHAPTER 7

FABRICATION OF SUPERHYDROPHILIC STEREOCOMPLEX PLA/N-TIO$_2$ NANOFABRIC FOR MULTIFUNCTIONAL ATTRIBUTES

Abstract: This chapter involves the fabrication of a superhydrophilic fabric with a nanofibrous architect to develop a multifunctional textile. This environmentally friendly non-woven nanotextile has been prepared using enantiomeric pairs of poly (lactic acid) PLA by electrospinning technique. Solution blending of synthesized high molecular weight (~10^5 Da) poly (L-lactic acid) PLLA and poly (D-lactic acid), PDLA for prolonged time stirring produce solely stereocystallites (sc). The high crosslinking effect of sc-PLA has played an important role, with multifunctional behavior on the addition of anatase-TiO_2 (a-TiO_2) in three different ways (Case- I-III). The high crystallinity of a-TiO_2 (~7.14 nm), has been confirmed from XRD and TEM studies as 98%. The nanofinish as studied in (Case -III) by dipping and drying has decreased the water contact angle for the electrospun sc-PLA nanotextile from highly hydrophobic (132°) to superhydrophilicity after 8 min. An easy demonstration of high temperature treated nanofabric (at 100 °C) has proven to obtain an anti-shrinkage sc-PLA nanofabric. Even, the presence of a-TiO_2 has improved the color strength ability of sc-PLA as a dark dyed nanofabric. The loading of as-synthesized a-TiO_2 nanoparticle has enhanced adsorbent dosages for $5T_{dip}$scPLA upto 1.44mg/g of MB dosage, at contact time (8h), and 68% methylene blue (MB) removal efficiency under UV irradiation. Thereby, this a-TiO_2 impregnated sc-PLA nanofabric has the tendency for dye removal.

Publications: Hazarika, D., Kalita, N. K., Kumar, A., & Katiyar, V. (2022). Crystalline titanium-dioxide nanofinish impregnated on electrospun stereocomplex poly (lactic acid) as non-woven nanotextile with superhydrophilic, anti-shrinkage, dark dyeing and waste dye removal ability for sustainable application. *International Journal of Biological Macromolecules*.

7.1 Introduction

Polyester fibers are driving human attention and leading almost all textile industries. Out of which polyester clothing obtained from polyester polyethylene terephthalate (PET), the petroleum-derived polymer has taken about 75% of the global synthetic fiber market. But due to their contribution in depleting the resources, non-biodegradability with ecosystem destroy, endanger human health increase the challenges to sustainability [155]. Among the various biodegradable polymers, poly(lactic acid) (PLA) is more preferable in terms of higher barrier, thermal, and mechanical and can replace the petroleum-based polymers for a sustainable environment [47]. Limitations of PLA can be overcome by two stereoregular enantiomers, namely PLLA and PDLA, allowing the formation of stereocomplex PLA, with melting temperature higher upto 50°C with better properties than its pure component [156]. Studies on the interactions ($CH_3\cdots O{=}C$) hydrogen bond formation was made during crystallization with an increase in chain packing, where hydrogen bond formation occurs due to the alignment of the C–O–C backbone during stereocomplexation [157, 158]. The stereocomplex crystallites (sc) have better thermal stability and mechanical properties when compared with different form crystalline forms (an α, β, and γ during processing) of PLLA and PDLA[159]. Here PLLA and PDLA chains are packed into the crystal lattice of sc crystallites having 3_1 helical conformations with tight chain packing than homocrystallites (PLLA or PDLA) with 10_3 helical conformations contribute to the improvement of melting temperature upto 50 °C than homocrystallites. But when the molecular weight of each PLLA or PDLA goes beyond 10^5 g/mole then subsists the formation of homocrystallites and prevails stereocomplex crystallites. Thereby, the authors here have studied the repeated casting of this blend in various solutions, increasing the duration to enhance stereocomplexation [160]. Electrospinning (continuous fibre) and electrospraying techniques are mostly used for

nanofibre formation [161]. Functionalized textiles are prepared using various inorganic metal oxide nanoparticles like TiO_2, ZnO, SiO_2, Fe_3O_4, etc.,with their inherent properties, can be used with polymeric non-woven fibers trending to be the most promising applications as protective fabric[162]. The authors have demonstrated an antibacterial filter fabricated using chlorogenic acid (CA)-contained sc nanofibers[163]. Researchers presented electrospun nanofibers and suggested an adsorption method as a choice employing adsorbents to treat polluted dyes (such as MB) as textile industry effluent from wastewater [164]. Conventionally polyester fabric dyeing is carried out above 120 ° that causes problems like shrinkages, wrinkle or tear distort, and mechanical properties [74, 165]. Therefore, scPLA can be a better idea of utilizing as an adsorbent for such situations as sc mesophase was obtained by annealing of PLLA/PDLA (50/50) blends [166]. Another study demonstrated the solvent-induced sc crystallization of PLLA/PDLA blends and stereocomplex microparticles was prepared in a solution with their improvement in heat resistance and mechanical properties [167][168][169]. Membranes with self-cleaning were prepared using gallic acid (GA) and tetrabutyl titanate ($Ti(OBu)_4$) in aqueous solution, to prepare a superhydrophilic scPLA membranes for oil/water separation [170].

Here in this investigation, we synthesized a pure form of anatase TiO_2 by sol-gel method followed by fabrication of an electrospunned scPLA nanofabric. An equimolar blend of PDLA/PLLA with almost similar molecular weight, optimized stirring temperature, and time for enhancing the stereocomplexation were used. The material formed by dipping scPLA nanofabric into the TiO_2/ ethanol solution has superhydrophilic nature, acting as a self-cleaning fabric under optimized conditions. In this study, enhancement in dyeability of scPLA can be seen when treated at elevated temperature without any shrinkage of the fabric. Moreover, the photocatalytic activity of the scPLA/a-TiO_2 nanofabric can give a

better pathway for water purification application with the removal of a textile dye from industrial eluent in near future. This study also advances knowledge in adsorption phenomena through the deployment of biodegradable polymeric nanofabric.

7.2 Results and Discussions

7.2.1 Molecular and structural characterization of as-synthesized a- TiO_2

A successful synthesis of a-TiO_2 was done using sol-gel method and high-temperature calcination as reported. The in situ polymerization of L-lactide and D-lactide using melt state condensation followed by solid-state condensation that gives high molecular weight PLLA and PDLA. The molecular weight of synthesized polymers, PLLA and PDLA were presented in **Table 10**. **Figure (a)** shows FTIR spectra for uncalcined and calcined TiO_2. FTIR spectrum of TiO_2 shows a broad band at ~3200 cm^{-1} (fundamental stretching vibration of O–H hydroxyl groups) for the uncalcined TiO_2 but the broadness was decreased for the calcined a-TiO_2. The band~1600 cm^{-1}originates from the surface-adsorbed water, which indicates H_2O bending present on the surface of TiO_2, which is very less after calcination. The shoulder observed at 650 cm-1 may have been due to O–Ti–O bond vibration. In this curve, peaks at 485 cm^{-1} and 740 cm^{-1} are for Ti–O stretching bands bonding in anatase form.

7.2.2 X-ray Diffractometer (XRD)

The X-ray diffractogram obtained for the calcined (500 °C) TiO_2 catalyst as prepared using the sol-gel route is presented in **Figure 2(b)**. The peak at 25.4° is marked as anatase (1 0 1). Thereby having tetragonal structure with characteristic peaks 2θ = 25.46 (101), 37.92 (004), 48.18(200), 55.86(105), 62.86 (211), 69.18 (220) from the data base ICDD (International Centre for Diffraction Data) found in JCPDS library, similar kind as reported [171, 172].

The average crystallite size of a-TiO_2nanocrystallites was estimated based on Scherrer's equation

$$D = \frac{K\lambda}{\beta \cos \theta} \quad \ldots\ldots\ldots\ldots\ldots\ldots\ldots\ldots\ldots\ldots\ldots\ldots\ldots\ldots\ldots\ldots(xxv)$$

Where, parameters like K is a constant which depends on crystallite shape with value (0.9), x-ray wavelength, λ taken as 0.154 nm, β is the full width at half maxima (FWHM) correlated to XRD patterns, Θ is the Bragg's angle, the unit cell volume. Results were shown in **Table 10**. Using Scherrer's equation average crystalline size of a-TiO_2 was calculated as ~7.14 nm. Further XRD confirmed the formation scPLA and scPLA/a-TiO_2 nanofibers. The first spectrum **Figure 68(b)** shows peak at 2Θ= 23° with no clear formation of stereocomplex and homocrystal crystallites for the unannealed samples. Here, scPLA nanofabric and for case-1 scPLA nanofibers nano without any peak of a-TiO_2. We have taken case- II and Case- III higher concentrations for analysis as referred to in the method section. No detection a-TiO_2 peak for the $5T_{spray}$scPLA samples, due to spraying hydrophilic solution over a hydrophobic nanofabric. **Figure 68(c)** shows annealed samples at 100°C, the diffraction spectra of neat PLLA that has major characteristic diffractions at 2θ of about 14.5°, 16.8°, 19.1°, and 22.5°, assigned to (010), (200/110), (203) crystal planes for α crystal of PLA in agreement with reported peaks of higher molecular weight [158]. Meanwhile, for the case- of scPLA, 2θ around 11.8°, 20.5°, and 23.9° is agreement as reported [92]. For case- III, an extra peak at 24.5° suggests the presence of a- TiO_2 on the scPLA nanofabric without any chemical bond. Furthermore, absence of homocrystal (hc) reason lies in electrospinning and the rapid solidification process inhibits polymer crystallization regularly with an increase in molecular weights and concentration for solution mixing that has reached higher values, where higher viscosity causes a restriction in molecular chain rearrangement. The

intensified peak observed at 20.39° diminished the scPLA peaks suggests the hindrance in the crystal formation due to the presence of a-TiO_2 **(Figure 68(c))**.

Table 10: Detailed calculations of crystallinity percentage and average crystal size for the synthesized a-TiO_2 nanoparticle.

2Θ (degree)	**Area (nm^2)**	**FWHM (radian)**	**Crystal size (nm)**
25.46	45872.72	1.14	7.11
37.92	17373.73	1.45	5.77
48.18	15631.54	1.15	7.5
54.86	19903.47	2.03	4.4
62.86	10341.19	1.31	7.05
69.18	5907.68	1.13	8.48
75.42	5976.50	1.04	9.65
	Crystalline area* = 118940.83 Total area = 21824.53		Average diameter (nm) = ~7.1
	Crystallinity %, $\chi_{c,sc}(\%)$= 98%		

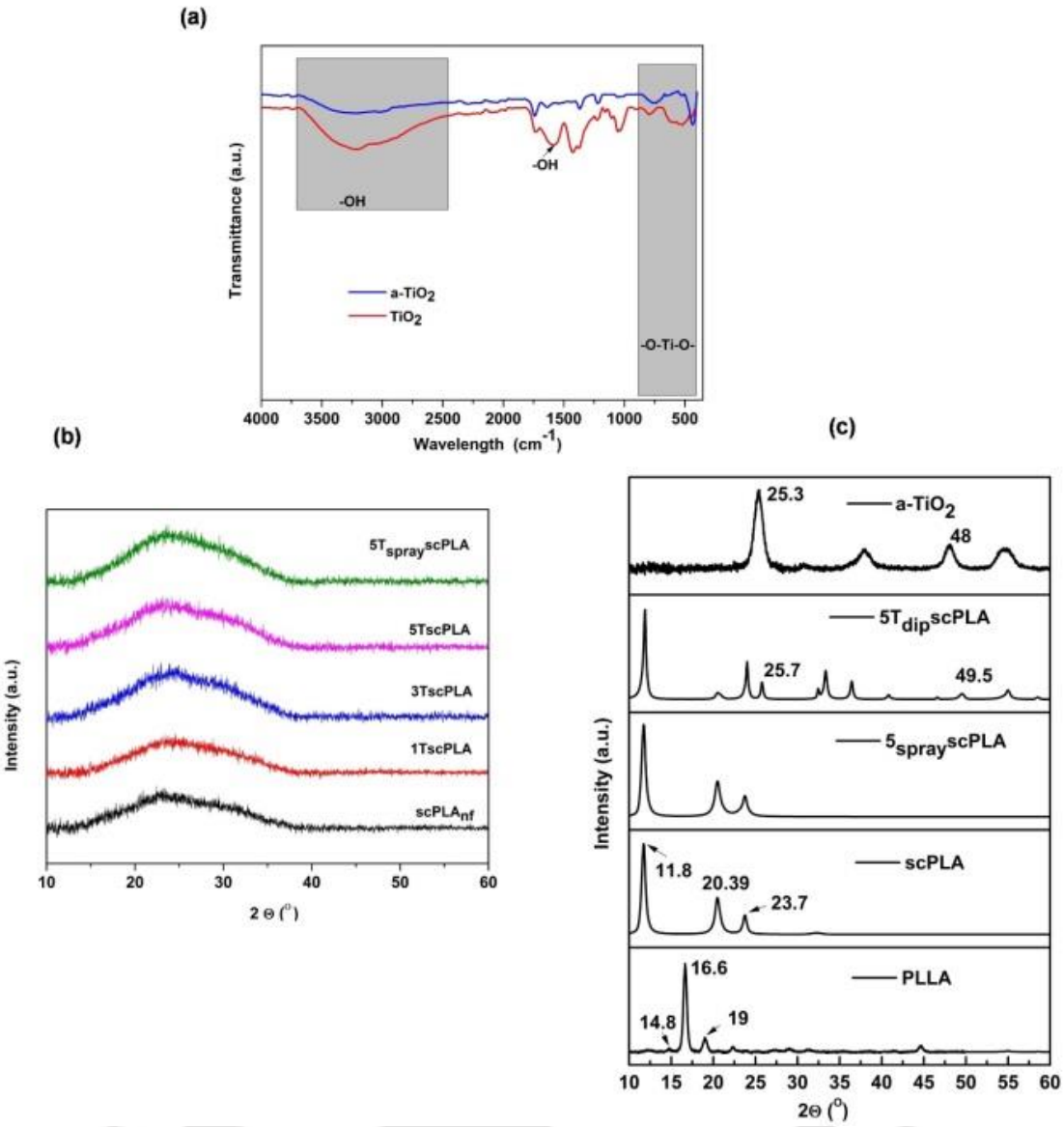

Figure 68: FTIR spectra for the as prepared TiO_2 and a-TiO_2, (b) Un-annealed XRD spectra fabricated nanofabric, (c) XRD spectra for synthesized a-TiO_2 at 400°C, and annealed scPLA/a-TiO_2 nanofabric at 100 °C, (inset: PLA as reference).

7.2.3 Optical purity of TiO_2 structures

The absorption spectrum of a-TiO2 nanoparticle has a peak at wavelength 250 nm and the absorption range continues within the range 250-450nm (UV range 100-400 nm) **(Figure 69(a))** with ultraviolet light active compound and some visible light absorbance activity.

For the E_g calculation, UV-vis spectra can be considered using Tauc plot of $(\alpha h\nu)^2$ versus (E_g) and extrapolating linear portions of the curve to the energy- axis accordingly mentioned elsewhere [173]:

$$\alpha\ (h\nu) = B(h\nu - E_g)^m \text{.....(xxvi)}$$

$$E_g = \frac{hc}{\lambda}$$

$$\text{or } \frac{1240}{\lambda} \text{.....(xxvii)}$$

Here, E_g = band gap (eV), h = Planck's constant (J.s), B = absorption constant, ν = light frequency (s^{-1}) and (α) = extinction coefficient. The exponent m depends on the type of transition between bands, here we considered direct transition for a-TiO_2, where m = 1/2 for our estimations.

Drawing an extrapolating tangent from the curve to the x-axis which was found E_g value as 2.98 eV for a-TiO_2 (**Figure S2(b))** nearby values as reported [171].

7.2.4 Raman spectroscopy

Anatase has six raman active modes ($1A_{1g}$, $2B_{1g}$, $3E_g$). The spectrum of TiO_2 as shown in **(Figure 69(c))** had the anatase vibration modes at 152 cm^{-1}, 200 cm-1 (assigned to E_g modes), 400 cm-1 (designated as B_{1g}), 519 cm-1 (A_{1g}/B_{1g}), and 641 cm^{-1}(A_{1g}) which were similar to reported results [174].

7.2.5 Differential Scanning Calorimeter (DSC)

The peaks of cold crystallization temperature (T_{cc}), and melting temperature of stereocomplex crystallites ($T_{m,sc}$) were observed using DSC. High molecular weight PDLA or PLLA has a single sharp peak which corresponds to the melting point of homocrystal (hc) of PLLA or PDLA (**Figure 70(a)**). In the first heating cycle **(Figure 70(b))**, no cold crystallization peak was observed for scPLA in 2nd heating, because it was cooled at a slow rate i.e. 10 °C/min. The polymer chains had more time to get relax and

integrate into an ordered crystalline structure, facilitating the crystallization process. Tuning the molecular weight by dissolving scPLA in a solvent, first in chloroform and then in a binary solvent may hinder homocrystal formation which can be seen from the spectra. For unprocessed scPLA($scPLA_p$), the 2nd heating curve showed endothermic peak at a much higher temperature of melting points at 216 °C higher than hc, whereas, no endothermic peaks related to hc have been observed, indicating solely formation of sc. Sc was a dominant crystal phase for the nanofibers, which induced improvement in thermal resistance properties. For the cooling curve of $scPLA_p$ there is formation of two humps and a broad area around 140-160 °C which may be due to two different crystal growth formations in a disoriented manner with slow crystallization behavior. Here, we have used case III for all the analyses as they are showing better distribution after treatment.

Higher T_{cc} suggests 50% PDLA facilitated crystal nucleation process resulting in a higher crystallization temperature due to longer PDLA chains and retarding the crystallization of PLA matrices due to its low chain mobility. The electrospun scPLA nanofibers and scPLA/a-TiO_2 nanofibers the melting temperature increases from 207 °C to 214 °C due to presence of metal oxide. The melting temperature for the 2nd heating DSC curve for all samples had decreased (**Figure 71(a),(b)**) due to the removal of the thermal/processing history of the samples. In addition, for case-III of $5T_{dip}$scPLA there occurred a broadening in peak area for T_{CC} causing hindrance in crystal formation due to difficulty in molecular chain movement with a higher concentration of a-TiO_2 in scPLA. Similar cases can be obtained on the addition of a higher percentage of grafted CMC- scPLA nanocomposites using a twin screw extruder [92].

Furthermore, electrospinning of PLLA/PDLA blend solution causes high shear force induced by electric field leaving no hc[175].

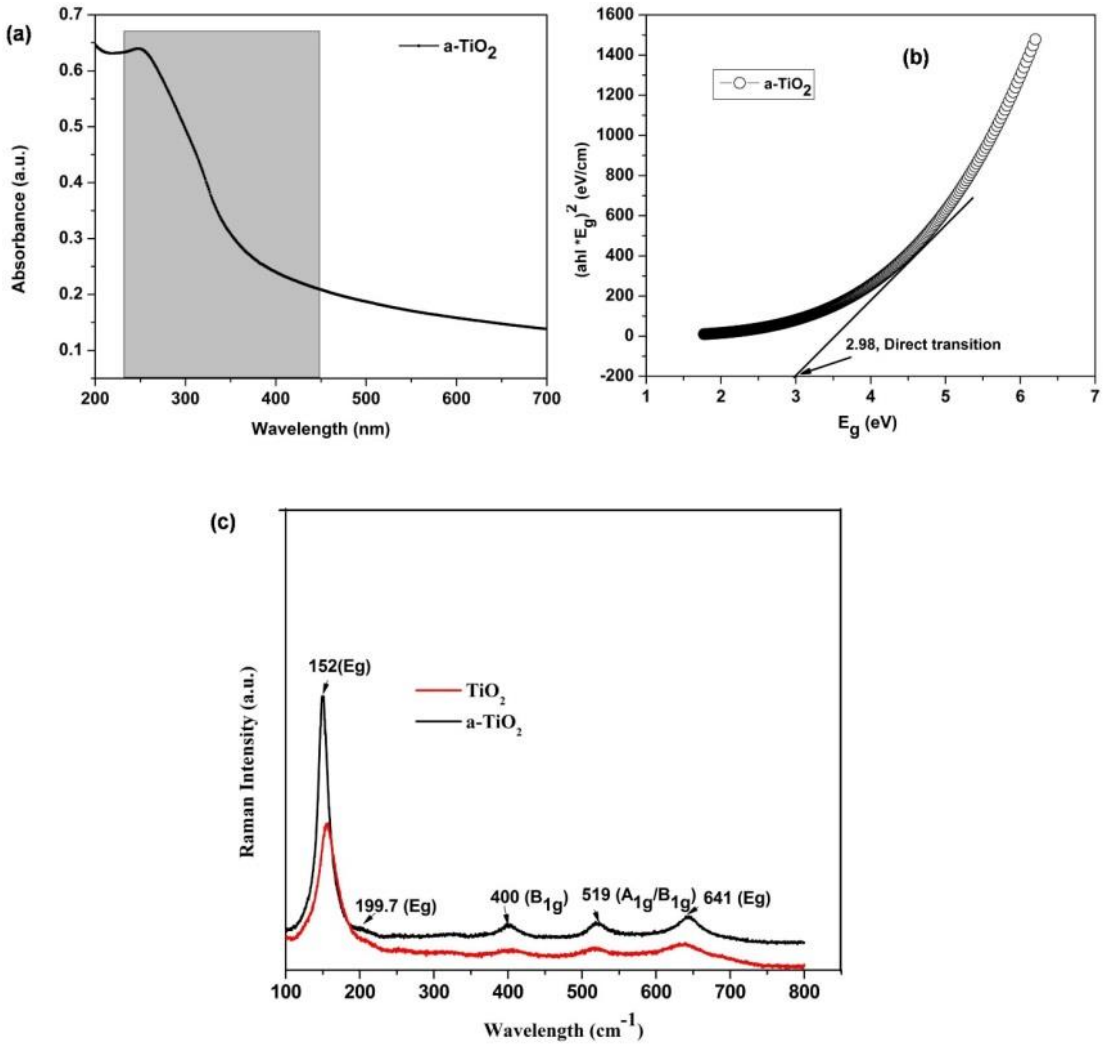

Figure 69: (a) Uv-vis spectra and Band gap energy calculation by Tauc plot, (b) $(\alpha (h\nu))^2$ versus E_α(eV) plots for direct transition band gap E_g obtained by extrapolation to a = 0 (c) Raman spectra for uncalcined as-prepared and (calcined TiO_2).

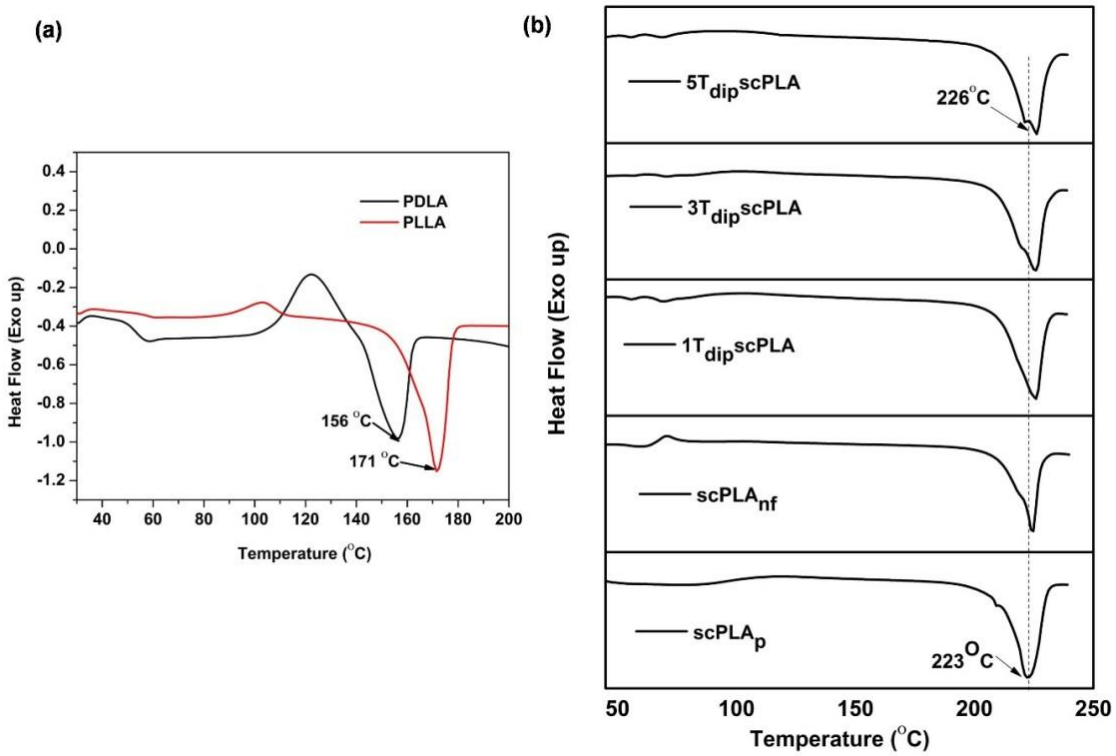

Figure 70: DSC thermograms (a)First heating of lab-synthesized PLLA and PDLA, (b) prepared nanofibrous fabric.

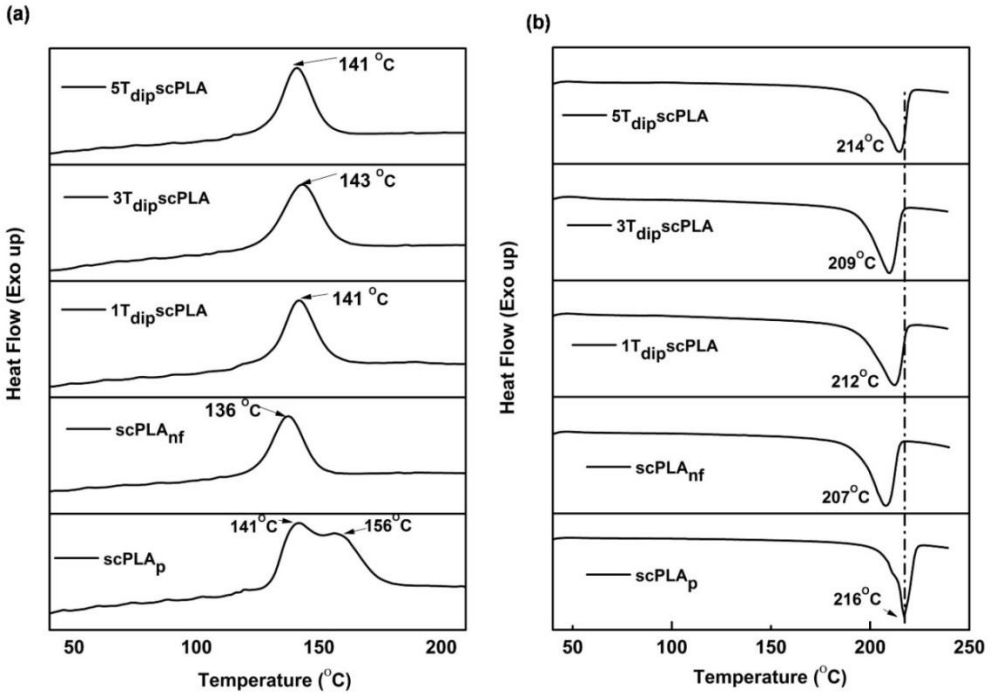

Figure 71: Thermal transition properties (a) Cooling DSC thermogram showing T_{cc}, (b) 2nd heating DSC thermogram showing T_m for all the samples.

7.2.6 Morphological analysis

FESEM and FETEM for a-TiO_2 nanoparticles revealed its spherical nature with SAED pattern, crystal lattice fringes with d-spacing of 0.35 nm corresponding to the (101) plane of anatase TiO_2 **(Figure 72(a-d))**. **Figure 73(a-c)** shows an image of fabricated electrospun nanofabric surface morphology. For **(case- I)** a-TiO_2 cored inside the scPLA nanofibers as shown in **Figure 73(d-f). Figure 74(a)** explains the FESEM micrographs of nanofibers with nanoparticles **Figure 74(b)** EDX spectrum shows the presence of Ti, C, and O atoms distribution of the synthesized a-TiO_2. In **Figure 74(c),** for sample T_{spray}scPLA, dispersion of a-TiO_2 nanoparticles can be seen adhered into the porous network of nanofibers without any rough surface. From the micrographs **(Figure 74(b-f))** the average diameter of the nanofibers was measured and found that for 5TscPLAthe average nanofabric diameter was (680 ± 0.172) nm, $5T_{spray}$scPLAis having 412± 0.124 µm diameter, $5T_{dip}$scPLA was having (427 ± 0.065 nm). From the micrographs it can be understood that the effect of nanoparticles was more in case- III when dipped into the solution than comparing it with case- I-II and observing the presence of a-TiO_2 over the scPLA nanofabric. Agglomeration is generally more pronounced for the aqueous dispersion of hydrophilic nanoparticles. Here, it can be seen in the case of $5T_{dip}$sc-PLA that the nanoparticles are weakly or strongly in an agglomerated form which could be due to drying a liquid dispersion over the nanofabric without any application of deagglomeration step to prevent scissioning of electrospun nanofibers.

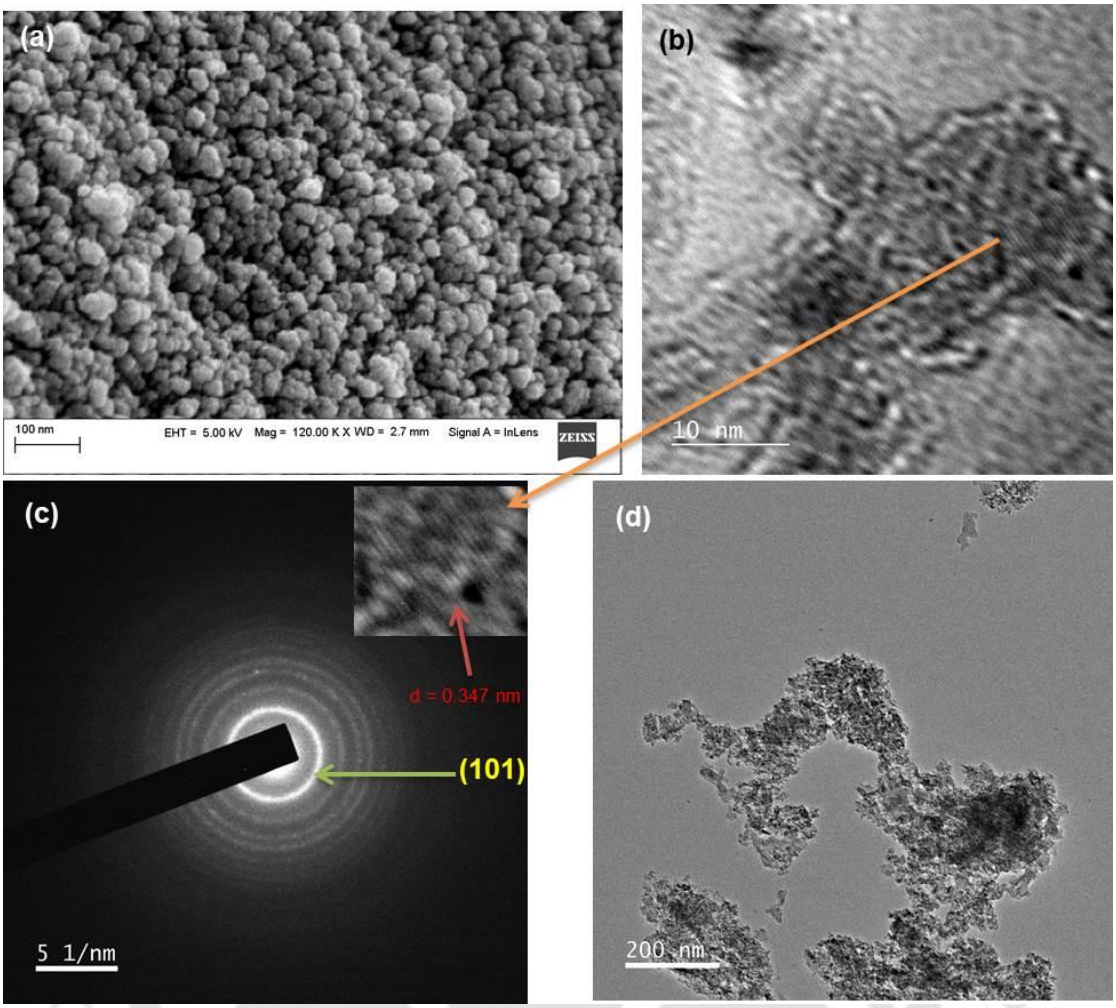

Figure 72: (a) FESEM image of a-TiO_2, (b) HRTEM image of a-TiO_2,(c) SAED pattern showing (101) plane for d-spacing 0.35nm (d) FETEM image of a-TiO_2.

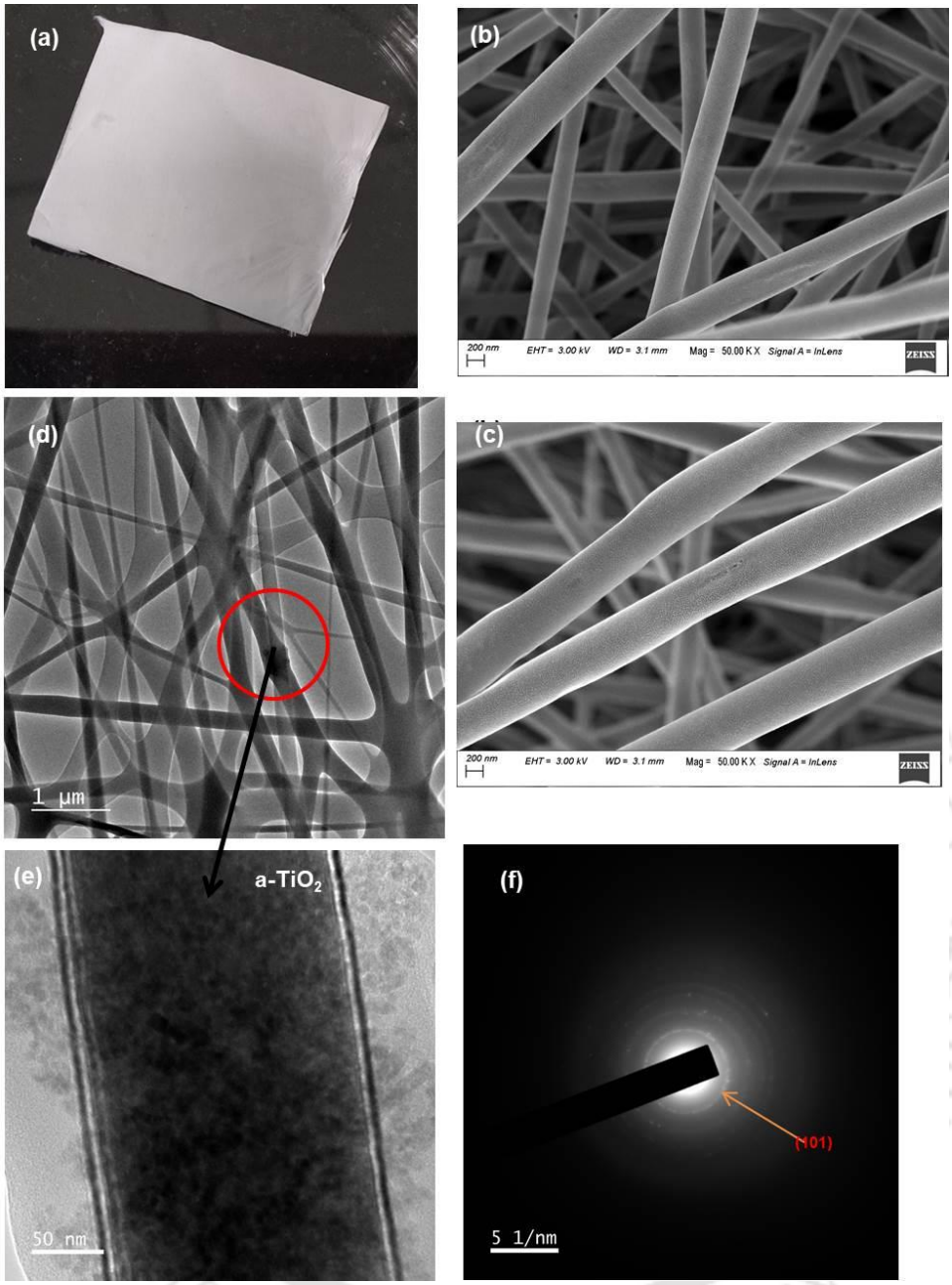

Figure 73: Fabricated 1TscPLA electrospun fabric (digital picture clicked by a mobile camera),(b) FESEM image of the surface of scPLA with scale bar 200nm.(c) magnified surface image scPLA, (d) High-resolution transmission electron microscopy image of 1TscPLA(e) magnified image of the circled portion to show TiO_2 distribution (f) a typical selected-area electron diffraction pattern for the nanofabric showing at bar, 5/nm, the lattice spacing of 0.352 nm was attributed to the (101) reflections from the anatase TiO_2 phase**.**

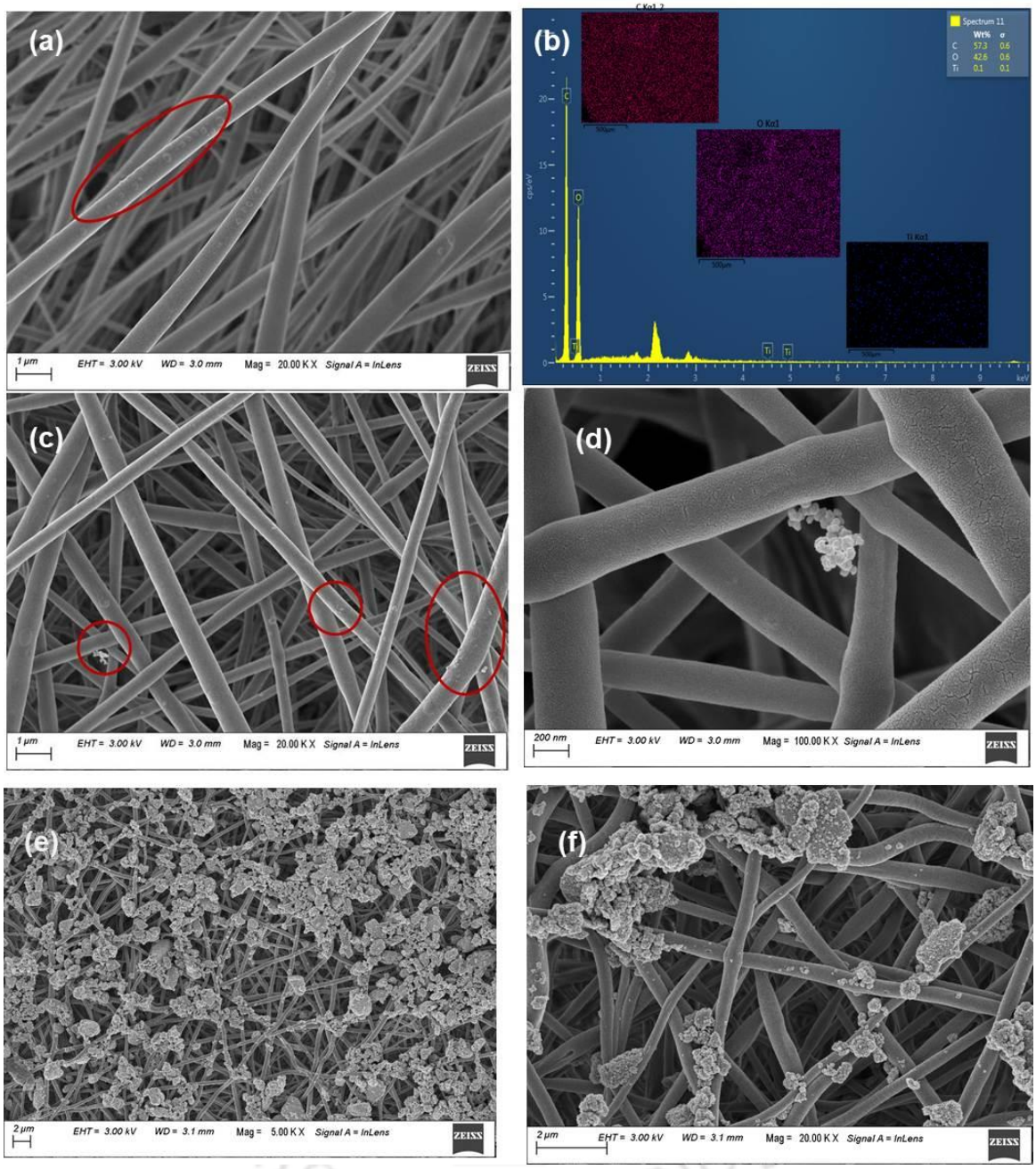

Figure 74: (a) FESEM image of 1TscPLA showing cored a-TiO_2 inside the nanofibers, (b) EDX spectrum of 5TscPLA showing the very less content of a-TiO_2 due to improper dissolution with scPLA solution, (inset: mapping of area distribution of C,H, and O content), (c) FESEM image of $5T_{spray}$scPLA showing a-TiO_2 in the pores of nanofibers, (d) magnified image in 200 nm bar scale, (e) FESEM image of $5T_{dip}$scPLA showing a-TiO_2 over the surface of nanofibers turning into a rough surface, (f) magnified scale image showing the distribution of a-TiO_2.

7.2.7 Wettability analysis by water contact angle (WCA) and self-cleaning studies

Figure 75(a-b) under normal day light, where we can find that the contact angle of synthesized a- TiO_2 has a contact angle of 53° (a hydrophilic) when snapped at 10 s and decreased to 40° (highly hydrophilic) after 3 min and remain stable even after. From **Figure 75(c-g)** it was observed that the scPLA nanofabric have WCA 132°, with a decrease in WCA for the case- I up to 121° and case- II for $5T_{spray}$ scPLA nanofabric has WCA of 114°. From **Figure 75(h-k)** for case- III, WCA was 127° at 10s. It gradually got decreased with time and reached to angle nearby 0° that satisfies the transformation to superhydrophilic nature thereby promoting self-cleaning properties under optimized conditions.

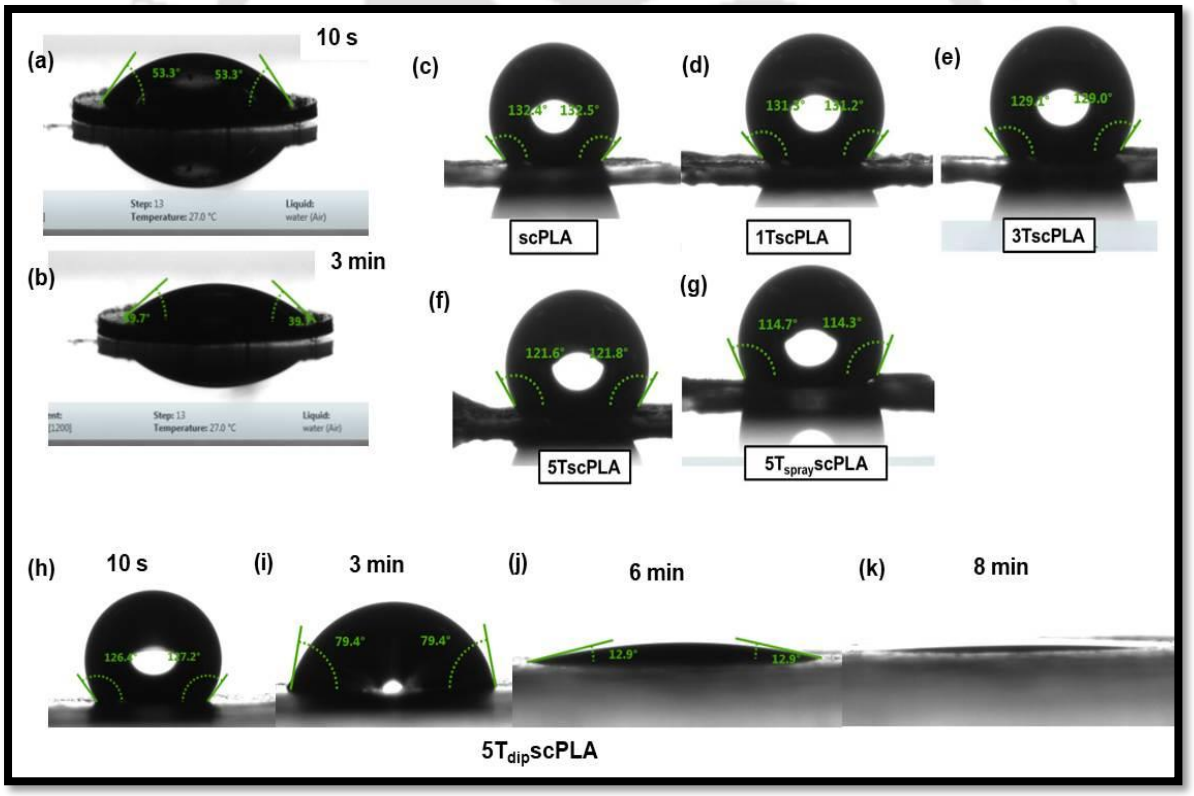

Figure 75: Surface wettability images of the static water droplets of (a) a- TiO_2 at 10s, (b) a-TiO_2 at 3 min, (c)scPLA at 10s, (d-f) treated scPLA matrix for case-I at 10s, (g) $5T_{spray}$scPLA at 10 s, (h-k) $5T_{dip}$scPLA from 10s to 8 min.

7.2.8 Effect of dye on treated nanofabric

Adsorption of dyes onto surface of neat PLA and scPLA/ a-TiO_2 nanofabric material depends upon the conditions of dye solution (pH, temperature), nature of nanofibers fabric (morphology, functional groups, porosity, surface area), and dye types and its concentration (cationic form, anionic form, molecular size) [176]. The bonding type between the surface coated a-TiO_2 nanoparticles and scPLA nanofabric may be electrostatic interaction, π -π interaction, and hydrogen bonding interaction. The images for dye adsorption on the various nanofabric were shown in Figure 7 (a). The increase in adsorption capacity of the prepared fabric increases with temperature at 100 °C (temperature mostly use for dyeing PLA fabric) was attributed to higher mobility of the dye molecules and strong interaction between the dye ions and a-TiO_2 sites adhered on the nanofabric surface. Distortion of the neat PLA fabric was observed, but for scPLA, there was no change in structure, reflecting its better shrinkage resistance than neat PLA on elevated temperature treatment. For PLA, the TCC starts around 90 °C but for *scPLA*, it starts around 120 *°C* which may cause no shrinkage of the chains while treating at 100 °C. As the more robust interaction with amorphous polymer leads to higher T_{CC} whereas, weaker interaction with crystalline polymer results in lower T_{CC} as observed from the thermal transition graphs **(Figure 2).** Further**,** a-TiO_2 nanoparticles demonstrate agglomeration nature in aqueous suspension because the TiO_2 nanoparticles get relatively stable tend to join from their unstable state during nanoparticle formation. The color strength (K/S) and RGBY plot values of the dyed fabric were shown in (**Figure 76(b-c))** and is represented by K/S value. The results were measured from the reflectance (%). $5T_{dip}$scPLA showed a high K/S value suggesting higher dye adsorption capacity, which signifies its color strength. This shows that the used dye has good distribution on the $5T_{dip}$scPLA fabric. scPLAdye also showed good color strength as compared to other

tested samples but less than $5T_{dip}$scPLA. ΔE_{ab} values suggest color adsorption of the dye on the fabric which was visible through the naked eye. Color difference values i.e., ΔE_{ab} values of $5T_{dip}$scPLA was much higher **(Figure 76(d))** than other samples. ΔE_{ab} values of test samples and their color difference with PLA fabric without dyeing show the trend as follows PLA<PLA_{dye}<$5T_{scPLA}$<$5T_{spray}$scPLA<$scPLA_{dye}$<$5T_{dip}$scPLA. For the case-s of $5T_{scPLA}$, $5T_{spray}$scPLA the ΔE_{ab} value was less than even scPLA dye fabric which may be due to less a-TiO_2 engulfed inside scPLA nanofibre and blocking porous network of nanofibers by a-TiO_2.

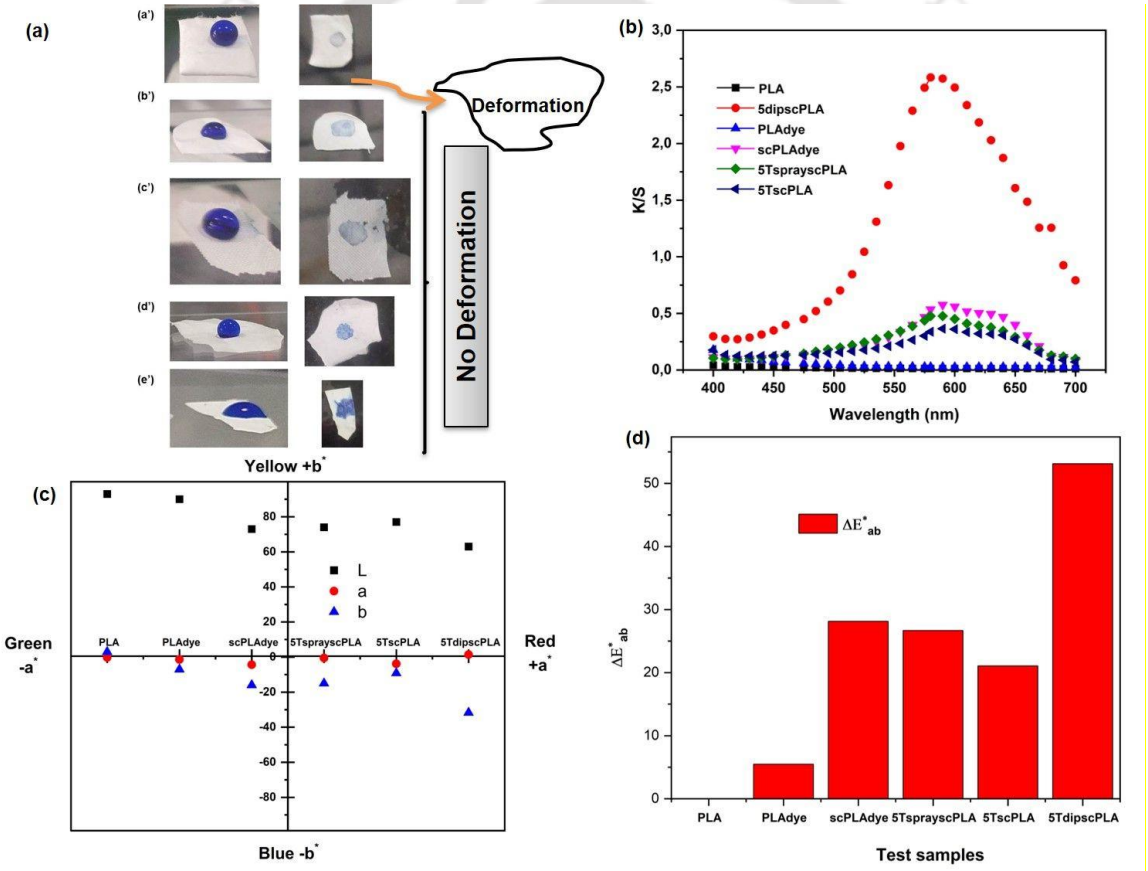

Figure 76: Dye adsorption digital images on (a) drop dyed fabric PLA_{dye}, scPLAdye, 5TscPLA, $5T_{spray}$scPLA, 5TdipscPLA, (b) K/S color strength, (c) RGBY plot representing L,a, b values, (d)$\Delta \mathbf{E}^*_{\mathbf{ab}}$ values obtained from L,a,b datas.

7.2.9 Photocatalytic disintegration activity of a-TiO_2 and scPLA/a-TiO_2 nanofabric towards methylene blue (MB)

From **Figure 77(a-d)** it was noticed that on diluting the MB solution with the photocatalyst to 10 mL higher than the initial (20D to 30D) the main absorbance peak at 664 nm decreased in its intensity of the blue color as well as blue shift of the absorbance peak for a-TiO_2. The discoloration of MB dyes is due to presence of the catalyst. The photocatalytic ability of the fabricated neat scPLA and scPLA/a-TiO_2 nanofabric was scrutinized by degrading basic dye MB under underexposure to UV light. The representative plot as shown in **Figure 78(a-d)** gives optical absorbance of dye solution against wavelength for the test samples which was recorded at different time intervals and concentrations during the photodegradation process. The results demonstrated the significant degradation of dye by the nanocomposite in the presence of UV light with the decrease in the intensity of the peak at 664 nm after 8h.

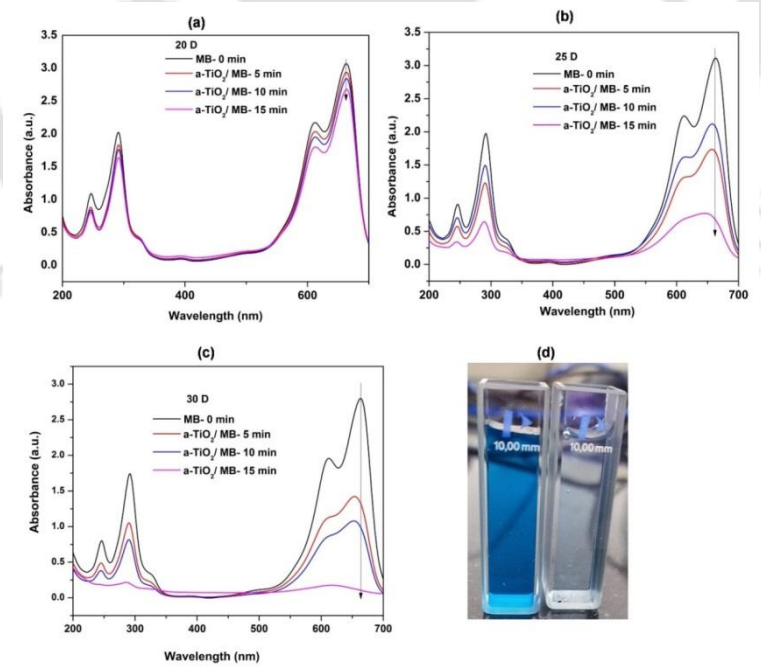

Figure 77: Photocatalytic activity of TiO_2 nanoparticle in neutral condition under UV treatment with varying dilution, (a) (20 mL dilution), (b) 25 mL dilution, (c) 30 mL dilution, (d) Digital image of dye discoloration placed inside a cuvette.

.

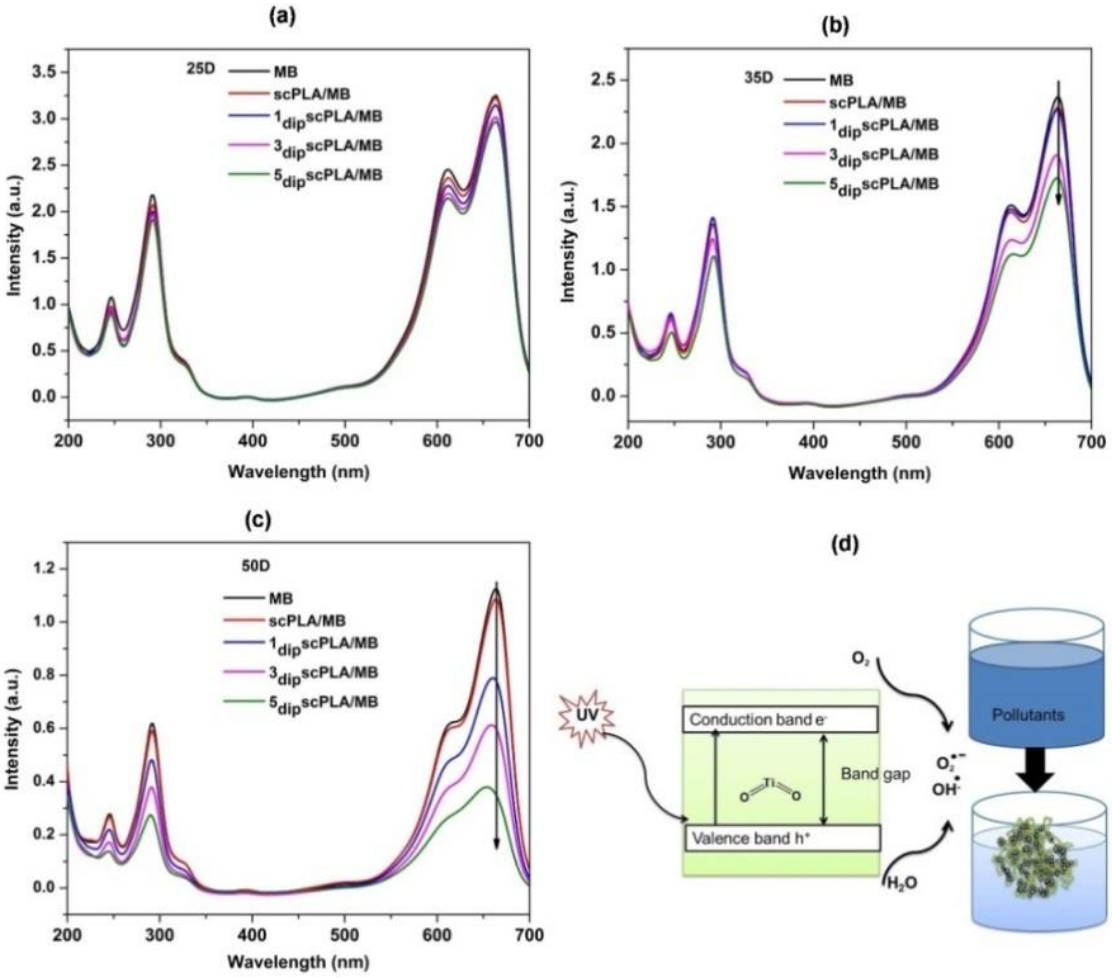

Figure 78: Photocatalytic activity of scPLA/a-TiO_2 electrospun nanofabricfabric in neutral condition under UV treatment with varying dilution (a) 25 mL dilution (20D), (b) 35 mL dilution (30D), (c) 50 mL dilution (50D), (d) dye degradation mechanism for the fabric (used case- III).

7.2.10 Effect of initial dye concentration and contact time

In general, only fixed amount of adsorbate was adsorbed by a given amount of adsorbent. In **Figure 79(a-d)** adsorption % and graph was plotted between the amount of dye adsorbed (q_t) versus time, t, at different initial dye concentrations after diluting the solution has been showing after UV treatment. The MB dye adsorption was found to be 100% for TiO_2 nanoparticles and 65 % for the nanofabric after dilution of MB solution.

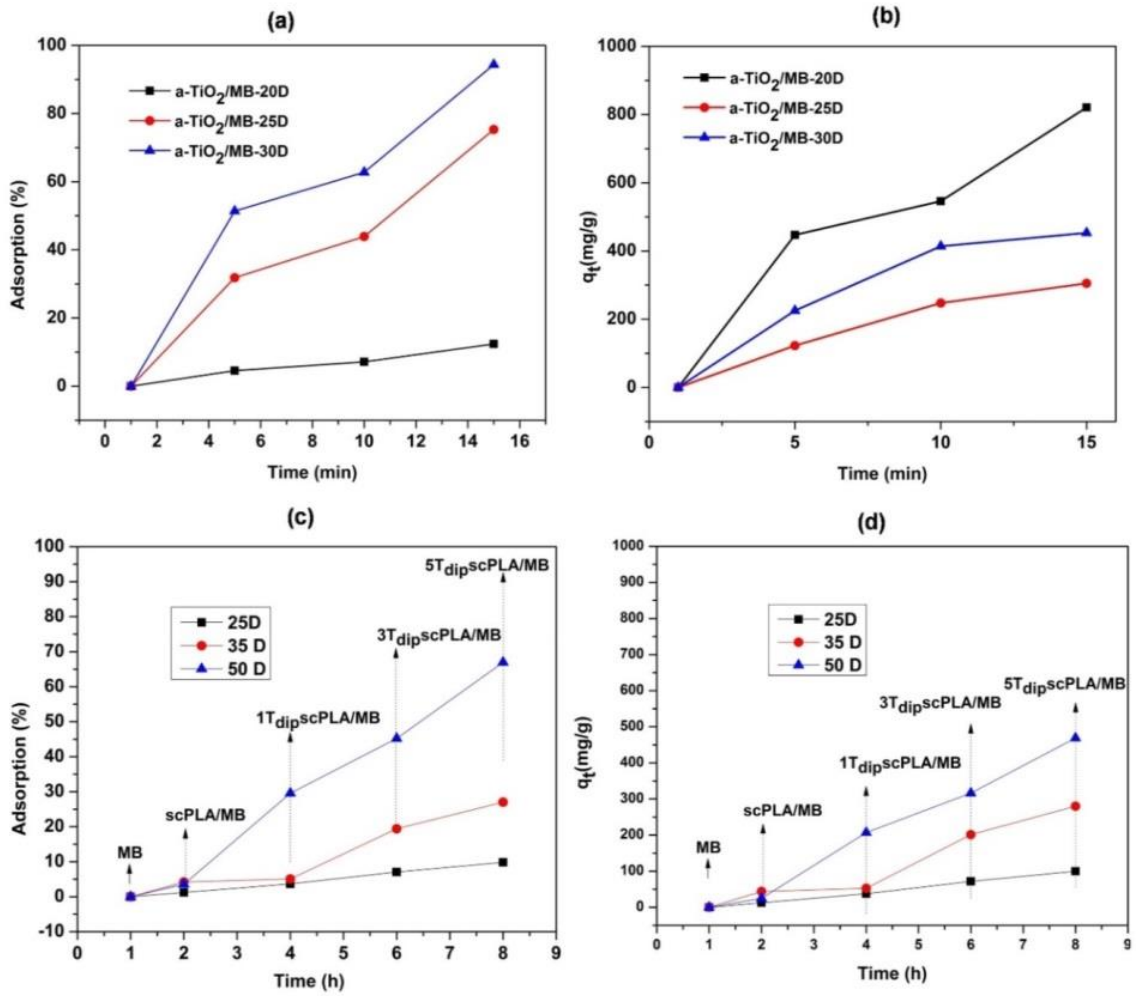

Figure 79: Effect of adsorbent dosage on MB adsorption showing adsorption % (a) (20D, 25D, 30D) for a-TiO_2 and (c) (25D, 35D, 50D) scPLA/a-TiO_2 (case 3) for, and (b, d) their amount of dye adsorbed (mg/g) vs. time.

It can be seen that there is a slow dye degradation approach for nanofibrous initially, but it gradually increases as dilution increases with time and remains constant. There were vacant surface sites at the prelim stage, but with time, a state comes where all the sites get occupied. This generates a repulsive force between a-TiO_2 on the adsorbent surface. Thereby after attaining equilibrium, there was not much appreciable dye removal change with time. Here batch adsorption was carried out where the rate of dye removal was controlled mainly by the transport of MB molecules from the surrounding sites to the interior sites of the a-TiO_2 nanoparticles and nanofibrous. From the plot, we can observe

that amount of dye adsorbed (mg/g) by a-TiO_2 and nanofibrous varies with varying initial dye concentration and increases with increase in initial dye concentration which after equilibrium reaches a constant value after 8h due to the driving force offered by increase in the concentration of solute. This was sufficient enough to overcome the resistance for having mass transfer between the solid and liquid phases. Hence, the adsorption will enhance by decreasing the initial dye solution from 2mg/100mL to 0.3/100mL for a-TiO_2 and 0.5 mg/100mL for nanofibers at 25 °C. Out of which 20 mL MB solution was considered for checking the dye removal characteristics of a-TiO_2. The sorption capacity increased from 0.186 to 1.44 mg/g. The increase in adsorption of dyes with adsorbent dosage can be attributed to increased surface area and the availability of more adsorption sites. We can see the amount of adsorbate adsorbed onto the surface of the adsorbent due to varying dosages. Further, as the SEM micrographs show re-structured nanosized particles over scPLA nanofibrous with special architecture advanced the photocatalytic activity. This fabulous ability has been described by researchers that might be due to the nanoparticle component and the pore structure between the nanoparticles reported elsewhere.

7.2.11 Adsorption behavior of a-TiO_2 and scPLA-TiO_2

The kinetics of an adsorption process provides clear information regarding the mechanism of adsorption by the catalyst and its nanofibrous. The pseudo-first-order kinetic equation given by the Langmuir-Hinshelwood model at various concentrations was tested.

$$r = - dC/dT = k_{obs}\, C \quad \text{..... (xxviii)}$$

Integrating the equation w.r.t C=Co from time t=0 to C= C_t to degradation time t gives the followed reaction

$$\mathrm{Log}(C_0/C) = k_{obs} C \times t \quad \text{.....(xxix)}$$

where k_{obs} is the apparent pseudo-first-order rate constant affected by the concentration of MB dye.

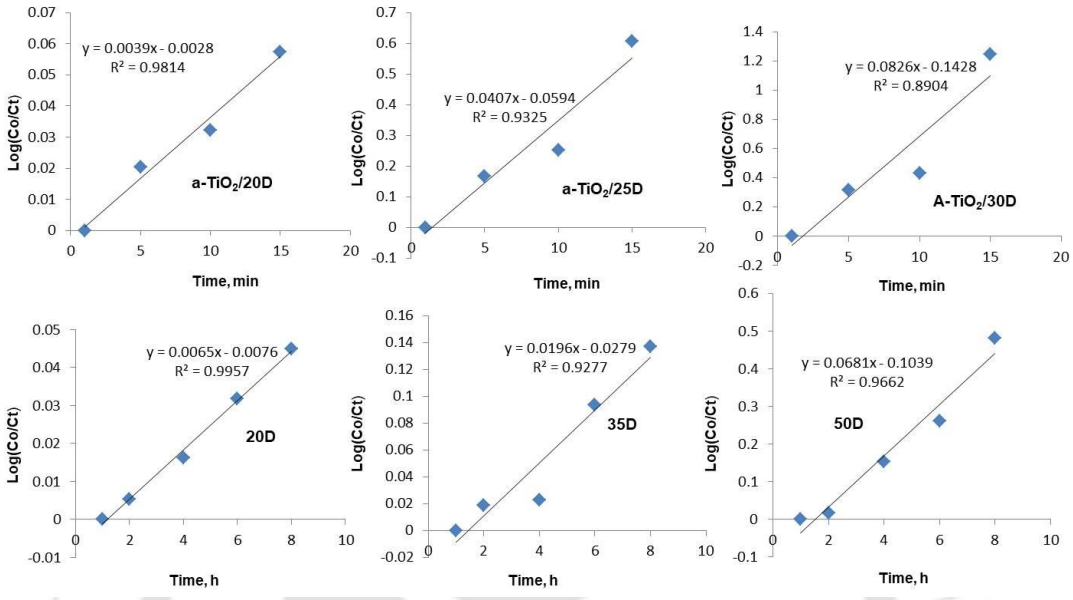

Figure 80: Plot of $\ln(C_0/C_t)$ versus irradiation time. C_0 and C_t are the concentrations of MB at time = 0 and t, (b) the kinetics of the degradation all the samples under UV light using the a-TiO_2 photocatalyst.

The graphs were obtained by plotting Log (C_0/C) vs. t, from the absorption data's, where a straight line was obtained. Graphs (**Figure 80)** demonstrated both the nanoparticle as well as nanofabric for MB dyes degradation, following first order-kinetics under the diluted condition. Thereby, it is an assumption based on that the adsorption is physical adsorption. Here, the correlation constant for the fitted line gives a good correlation to the first-order reaction kinetics where (R^2 = 0.90 for a- TiO_2 which is due to a sudden increase in dye discoloration with time and R^2 = 0.97 for a scPLA/a-TiO_2) was found. The calculated pseudo-first-order rate constants of a-TiO_2 and nanofibers were tabulated **(Table 11)**. The results further demonstrated that prepared a-TiO_2 and scPLA nanofibers can act as a good candidate for photocatalyst and thereby corroborate its corresponding degradation efficiency.

Table 11: First order straight line fitted kinetics values.

Sample	Rate constant k (min^{-1})	R^2
a-TiO_2/20D	0.0039	0.98
a-TiO_2/25D	0.041	0.93
a-TiO_2/30D	0.083	0.89
25D scPLA/a-TiO_2	0.0065	0.99
35D scPLA/a-TiO_2	0.019	0.93
50D scPLA/a-TiO_2	0.068	0.97

7.3 Conclusion

In summary, scPLA based non-woven fabrics were successfully fabricated by electrospinning technique, with no bead formation. The high T_m at 216 ˚C and high T_{cc} at 141 ˚C satisfy the successful preparation of scPLA which was different from the homo PLLA and PDLA. The high contact angle of scPLA fabric has been decreased to 0° in 8 min under the static condition at room temperature and was attributed to its self- cleaning behavior which is influenced by the addition of optimized concentration of a-TiO_2. Furthermore, the cross-linking network and stable sc form have inhibited the shrinkage problem of PLA fabric when dyed above elevated temperature without and with a-TiO_2. Presence of a-TiO_2 nano structure significantly influencesscPLA nanofabrics as photocatalyst for dye degradation. The photocatalytic degradation reactions obeyed the pseudo-first-order reaction model as studied. The nano-TiO_2 is having an even dispersion problem with scPLA matrix due to its unstable nature though it has the efficiency was of 68% in 8h to remove dye from solution when irradiated with UV-light. Thus, these intelligent properties can widen up its application for multifunctional textiles.

CHAPTER 8

INVESTIGATIONS ON ZINC-OLIGO LACTATE AS A CATALYST FOR POLYMERIZATION OF CYCLIC ESTERS AND DEPOLYMERISATION OF HIGH MOLECULAR WEIGHT PLA FOR RECYCLING

Abstract: This chapter includes an investigation on microwave synthesized scalable zinc-oligo-lactate, (ZL) catalyst for use in ring-opening polymerization of ester rings and often in conjugation with degradation of PLA by alcoholysis under mild conditions. The polymerization was carried out at a higher temperature of 180°C for 30 min to achieve a maximum upto 13kDa number average molecular weight. Here tuning the molar ratio of monomer: catalyst: initiator we can obtain the linear polymer homopolymer chain. The different characterization techniques such as GPC, MALDI-TOF, NMR, FTIR spectra support the above statement. Whereas the temperature, time, and concentration-dependent degradation process have led to degrading high molecular weight PLA from 130kDa to 3kDa for 4% catalyst concentration at 50 °C for 3h reaction time. Here High molecular weight PLA and medium molecular weight outdoor stored waste PLA can be degraded by green solvent THF and methanol as protic solvent through extensive transesterification reactions. It has been possible to obtain oligo- methyl-lactate with the optimized conditions which has been proved by the earlier mentioned analytical methods. The catalyst can be reused thrice where its stability has been checked by NMR and found that no significant loss in molecular weight has been found. Further molecular weight distribution and chain scission studies have been performed by GPC analysis

Publications: Hazarika, D., Kalita, N. K., Kumar, A., & Katiyar, V. Investigations on Zinc-oligo Lactate as a Catalyst for polymerization of Cyclic Esters and depolymerization of High Molecular Weight PLA for recycling **(to be submitted).**

8.1 Introduction

The intensive demand has increased the annual production of plastics as in back to 1950s it was only 1.5 million tons that have been increased tremendously and have approached to 400 million tons in 2018. Such data has projected that global plastic production thereby will reach 1800 million tons per year by 2050[177]. Another problem arises from global warming caused by the excessive emission of greenhouse gas. Thus, biobased polymers such as PCL; PLA can be a sustainable alternative to petrochemical-based polymers. Non-degradable polymers, owing to their longevity and demand result in creating plastic pollution which is harmful to human, land, and marine animals.

PLA polymerization has been conducted since 1932 by either direct poly-condensation step of lactic acid or by ring-opening polymerization, ROP of the cyclic dimer of lactic acid. During the direct polycondensation process lactic acid dehydrates into oligomers and is polymerized to PLA which arises difficulty by trapping residual moisture and starts degradation limiting the achievable molecular weight[178]. The industrially more preferable method to obtain high molecular weight is ROP which is carried out in melt, solution, suspension, or in presence of a catalyst. Another polyester, PCL has the potentiality to utilize as an alternative to the various non-biodegradable polymers via tunable molecular weight synthesized by ROP of ε-caprolactone rings using a list of metal alkoxide catalysts[179, 180]. Many metal complexes such as. Al, Li, Zr, Mg, Fe, Sn, and complexation of zinc with β-diketiminato ligands has been reported and used as initiator/catalyst for the ring-opening polymerization of lactides and ε-caprolactone[181]. Further, the drastic demand for PLA in recent years and similar properties to polystyrene and PET has led to producing a wide range of products. For the polymerization transition metal compounds and Brønsted acids are mostly used catalysts for the polycondensation reaction of PLA. But the disadvantage of using metal catalysts can be sometimes unsafe

for food and biomedical applications. Various reports have been made on using various catalysts at different long polymerization times to achieve the required molecular weight for their application [182]. However, its high-cost production hinders its widespread application, and cost reduction can be achieved by chemical recycling. As literature provides knowledge on different methods of chemical degradation such as hydrolysis, thermolysis, and alcoholysis but both the first cases involve high temperature increasing the operating cost. Whereas the latter presents economically and environmentally sustainable on an industrial scale[48]. Thereby, the formation of low molecular weight lactate esters is an alternative to hydrocarbon and has the potential to transform to lactide thereby allowing polymer reformation[183]. And as PLA doesn't dissolve in alcohol its alcoholysis required high temperature and high conventional acid/base catalyst concentration. Various researchers have reported on PLA chemical recycling to lactates using various acid/base catalysts, ionic liquids, alkali, and alkaline earth metals catalysts[184]. Dupont has worked on acid-base catalyst i.e. in presence of H_2SO_4 at a high-temperature range between 150-190°C[60]. Jones and co-workers used Zr(IV)/Hf(IV) salalen complexes used to prepare and degrade PLA at 25°C and 80°C with 75 % conversion to methyl lactate on degradation in 24 h. Binuclear Zn(II) N heterocyclic carbine, Organocatalysts such as 4-(dimethylamino)pyridine (DMAP) and 1,5,7-triazabicyclo[4.4.0]dec-5-ene (TBD). Also Zinc(II) complex is the facile catalyst reported to be used for transesterification reaction of industrial-grade PLA using controlled degradation pathway. The degradation was carried with different industrial grade PLA at operating conditions (0.05-0.2 g/mL, 40-130 °C, 4-16 wt.%) with possible high conversion of methyl lactate in 15 min[62]. During alcoholysis displacement of alcohol takes place by another alcohol where milder conditions can be applied compared to hydrolytic and thermal.

Further PCL synthesis can be carried out using condensation polymerization where 6-hydoxycaproic (6-hydroxyhexanoic) acid and ring-opening polymerization (ROP) of ε-caprolactone takes place. ROP is favourable and follows up four different categories of catalyst such as co-ordination insertion reaction anionic, cationic, and monomer activated mechanism. High molecular weight PCL has been obtained using tin octoate as catalyst in presence of ethylene glycol as co-initiator as reported [185].

Thus, this chapter is mainly focussed on upscaling of PLA production by studying the degradation of different molecular weight PLA by using an inorganic/organic hybrid catalyst by chemical means. Further, the hybrid has been used as a catalyst in polymerizing cyclic esters by a ring-opening polymerization reaction. Here, the role of operating conditions has been further understood by catalyst and polymer concentration which leads to the formation of moderate molecular weight repeated polymer chains. Here we have also synthesized PCL, PLA of weight average molecular weight (Mw) ranging upto 19.6 kDa, 21.6 kDa in 30 min at 180°C. The chapter discussed the ring-opening polymerization lactide and transesterification reaction using methanol of industrial-grade PLA and waste PLA to methyl oligo-lacate using ZL, a microwave synthesized catalyst.

8.2 Results and Discussion

8.2.1 Laboratory scale-up synthesis of linear polymers from cyclic polymers

The microwave synthesized ZL catalyst was characterized as discussed in **Chapter 3**. **Table 12** depicts the lactide and ε-caprolactone polymerization as investigated using ZL catalyst which showed the effect of polymerization time. The maximum weight average molecular weight was obtained upto 20kDa for PCL in1h of polymerization time at 150 °C and PLA 22kDa in 30 min at 180°C. Polymer PCL-1, and2 and PLA-1,2, and 3 showed comparative results of the catalytic activity of ZL respectively. The maximum yield

obtained was 93 % for [M]/[I] =2000/1. The results confirmed that the role of initiator in both the cases of ring-opening of cyclic esters is not much significant as their presence has not changed the molecular weight to a higher value. Further the role of [M]/[I] ratio, temperature, and time also plays a significant role during the reaction. All the molecular weights data corresponding to the polystyrene standards with RI detector prepared by using ZL as a catalyst with and without catalyst in a solvent-free environment. The increase in the PDI value denotes the increase in the number of short PLA chains

Table 12: Operating conditions and GPC results of ROP of L-lactide and ε-caprolactone using zinc-oligolactate catalyst.

Sample	[M]/[C]	Initiator (I)	Temperature (°C)	Time (min)	M_n	M_w	PDI	M_n [a]
PCL-1	1000:2	EG=1	150	60	10602	19565	1.84	10215
PCL-2	1100:2	EG=1	150	75	8209	19089	2.34	6981
PLA-1	1000:1	-	180	30	8160	18521	1.58	3516
PLA-2	2000:1	BA=2	180	30	12531	21615	1.72	6572
PLA-3	2500:1	-	180	30	11858	18993	1.60	6125

a= calculated from ^{1}H NMR spectra

8.2.2 Structural confirmation of prepared linear polymers

NMR analysis has been utilized as a useful tool for determining the number average molecular weight, M_n quantitatively. This technique also analyses end groups, as well as determination of residual lactic acid, or lactide that maybe formed due to unzipping of chain ends even the study in stereochemistry. As the polymerization of cyclic esters takes place with optimized parameters so the spectra showed in **Figure 81** give the ^{1}H NMR spectra for PLA and PCL end group confirmation. The NMR spectra moreover confirm PLA polymer containing zinc oligo lactide as chain end group at one end. Similarly, the

PDI values for PCL increases with an increase in the [M/C/I] as obtained from GPC analysis which also confirms the presence of a catalyst as an end group.

8.2.3 Spectroscopic data for repeating units' calculations:

- Further for PCL ^{1}H NMR spectra shows chemical shift at δ=1.42 ppm [2H, –$CH_2CH_2CH_2CH_2CH_2COO$–], 1.64 ppm [4H, –$CH_2CH_2CH_2CH_2CH_2COO$–), 2.33 ppm(2H,–$CH_2CH_2CH_2CH_2CH_2COO$–], 4.07 ppm [2H, t, –$CH_2CH_2CH_2CH_2CH_2OC(O)$–)] ppm and one triplet peak at δ=3.66 ppm assigned to α-methylene protons next to the hydroxyl group at the end of the chain suggests presence of the catalyst giving sites for the chain length increment.
- The ^{1}H NMR spectra for PLA show two sets of signals where the absorption peaks are at 1.58 and 5.14 ppm can be attributed to the proton of CH_3 group and CH group present in PLA chain. The lower intense peaks at 1.70 and 5.05 ppm signify end group –OH giving site for catalyst by co-ordination insertion reaction leading to the increase in the chain length.

The number average molecular weight has been determined by ^{1}H NMR from the magnified plots for both the polymer using the followed calculation from **Figure 81 (a), (b).**

Degree of polymerization of dihydroxyl terminated PCL, $DP_{PCL} = \frac{f}{g} + 2$

Degree of polymerization of dihydroxyl terminated PCL, $DP_{PCL} = \frac{d}{e} + 2$

The number average molecular weight of dihydroxyl terminated PCL,

$$\mathrm{M_{n,PCL}} = (M_{r,PCL} \times DP_{PCL} \times 2) + \mathrm{M_{ZL}}$$

$$= [114.14 \times \{(\frac{f}{g} + 2) \times 2\} + 1266]$$

The number average molecular weight of dihydroxyl terminated PLA,

$$M_{n,PLA} = (M_{r,PLA} \times DP_{PLA} \times 2) + M_{ZL}$$

$$= [72 \times \{(\frac{f}{g} + 2) \times 2\} + 1266]$$

where, M_r = repeating unit Molar mass, M_{ZL} = Molar mass of ZL

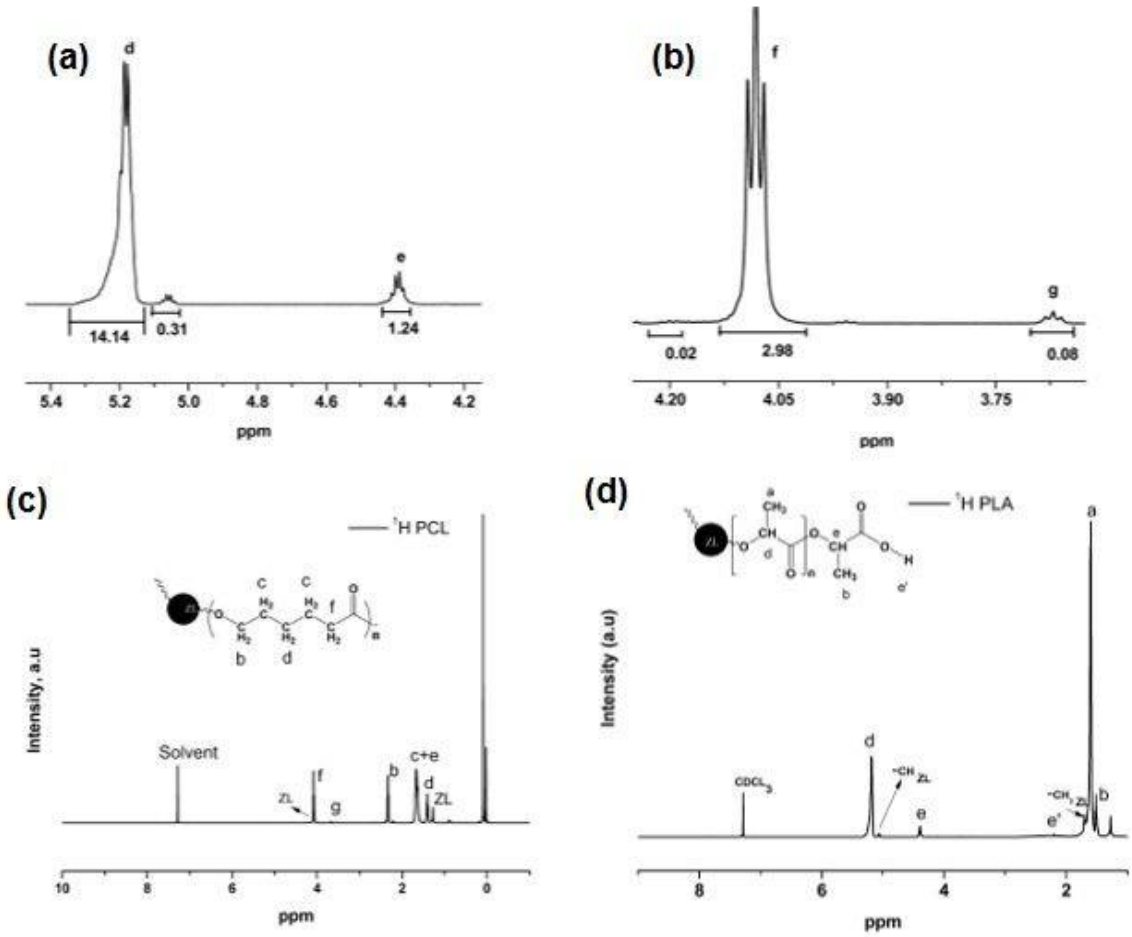

Figure 81: NMR spectra of **(**a, b) magnified range for calculating repeating unit, (c, d) structure showing polymerized PLA and PCL.

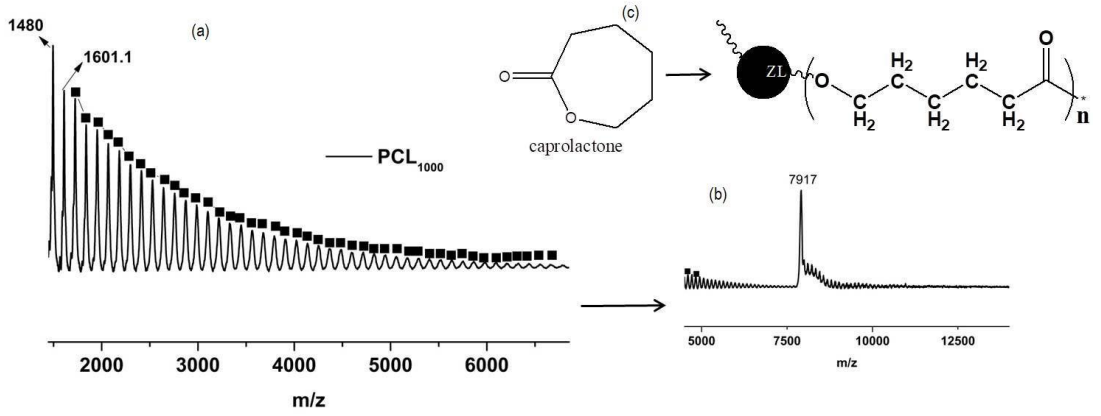

Figure 82: MALDI-TOF MS spectra of PCL synthesized using ZL as a catalyst in presence of an initiator.

- The series of peaks are characterized by a mass increment of 114 Da, which is equal to the mass of the repeating CL unit in the PCL. It can be assigned to PCL terminated with a hydroxyl group (residual mass: 23 Da, Na+ adduct; PCL cycle, Na+)
- The MALDI spectrum as shown in **Figure 82** is dominated by a series of intense peaks ranging from mass 1480 to 9982 Da corresponding to the following equation. The lower value series follows the direct equation
- Another intense peak was obtained for mass 7917 Da corresponding to the following equations

$$M_n = 114x$$

$$M_n = 114x + M_{ZL}(1266) + M_{K+}(39) + M_{Li+}(7)$$

$$M_n = 114x + M_{ZL}(1266) + EG(108) + M_{Na+}(23) + M_{H+}(1)$$

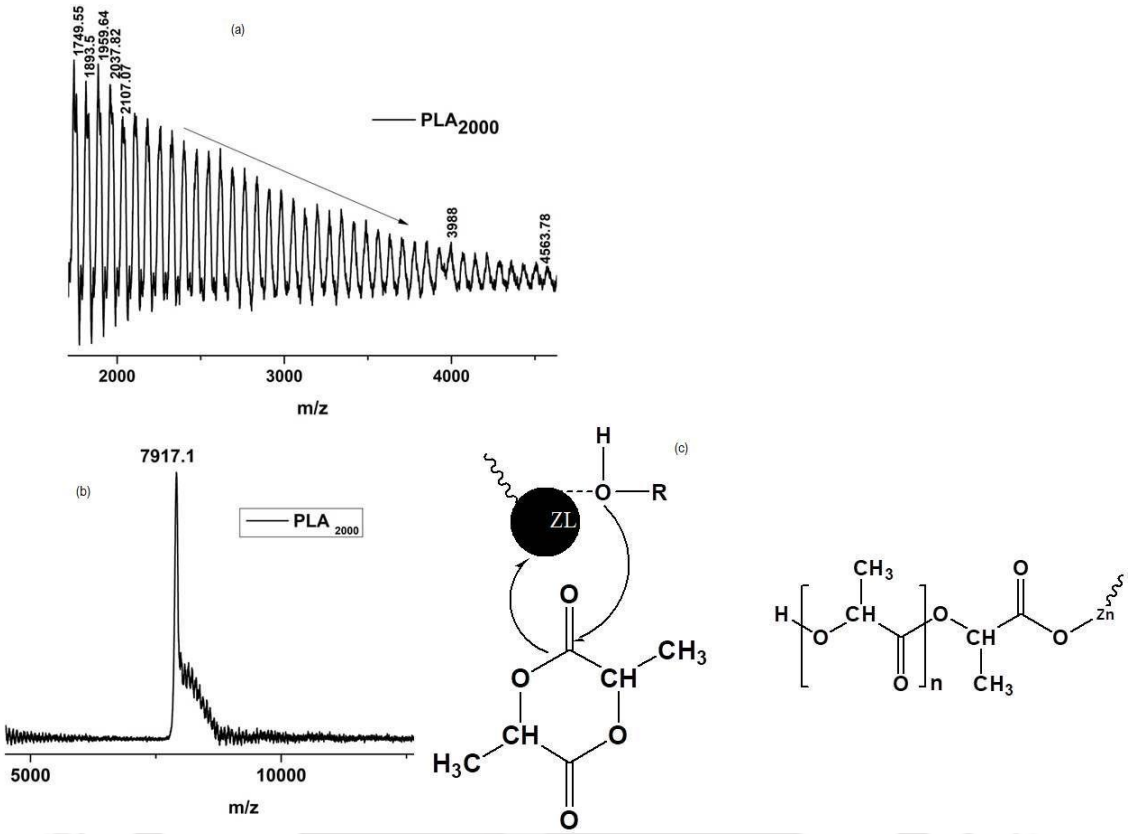

Figure 83: MALDI-TOF MS spectra of PLA synthesized using ZL as a catalyst in presence/absence of an initiator.

Further for different [M/C/I] the MALDI spectrum as shown in **Figure 83** is dominated by a series of intense peaks ranging from mass 1749.55 to 4563.76 Da corresponding

$$M_n = 72x + M_{ZL}(1266) + M_{K+}(39) + M_{Li+}(7)$$

$$M_n = 72x + M_{ZL}(1266) + M_{Na+}(23) + M_{H+}(1)$$

The term "x" denotes the number of lactyl repeat units having an Mw value of 72 Da each. The molecular weights of Zl, sodium ion, potassium ion, and lithium-ion, respectively, attached with the PLLA chains

The MALDI spectrum is dominated by a series of intense peaks ranging from mass 1375.29 to 4564 Da corresponding to the followed equations whereas the high intense peak at 7941Da corresponds to polymers doped with K+ and Li+ here the value of n is 92as shown in the enlarged figure.

$$M_n = 72x + M_{ZL}(1266) + M_{K+}(39) + M_{Li+} \quad (7)$$

$$M_n = 72x + M_{ZL}(1266) + BA(108) + M_{Na+}(23) + M_{H+}(1)$$

$$M_n = 72x + M_{ZL}(1266) + M_{Na+}(23) + M_{Li+} \quad (7)$$

A trace amount of presence of water in ZL catalyst may act as a chain transfer agent (CTA) in this protocol that can decrease the efficiency of the catalyst as well as the molecular weight of the PCL. The ZL in the presence or even in absence of the initiator can have the ability to induce ROP of ester rings.

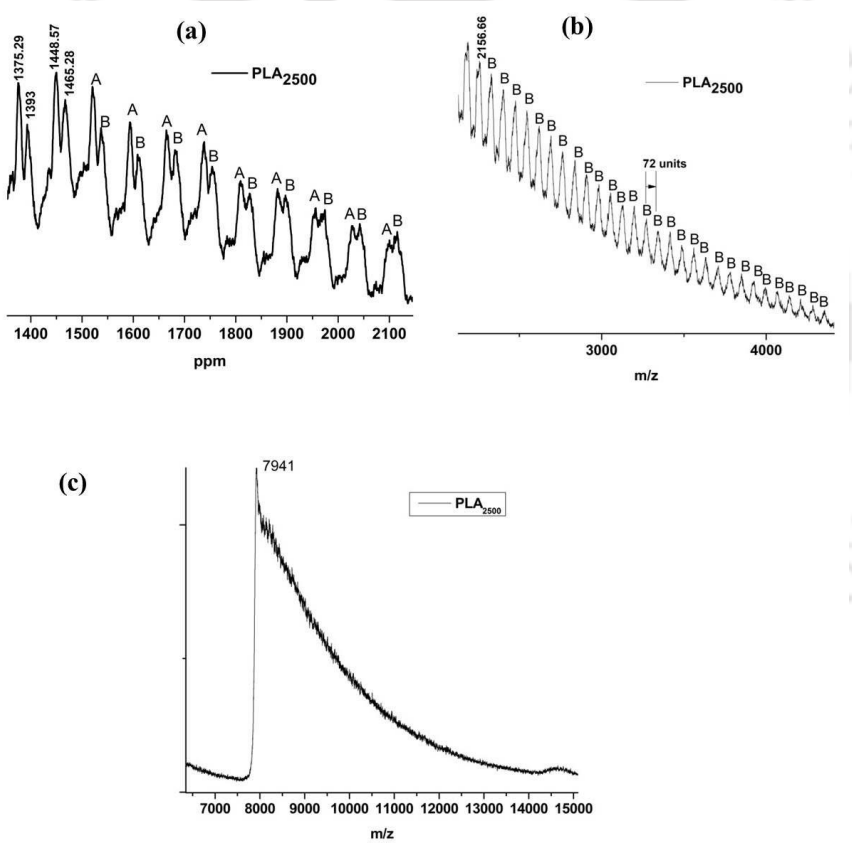

Figure 84: MALDI-TOF MS spectra of PLA synthesized using ZL as a catalyst using [M/C/I] = 2500.

Analysis of FTIR was performed to confirm the formation of the PCL and PLA polymer as shown in **Figure 85**. Both of them are of similar functional groups as they are all aliphatic polyesters. The C=O, C–O–C, and C–C peaks were visible at 1726, 1176, and

1240 cm^{-1}, for PCL and 1747, 1182, 1264cm^{-1} for PLA respectively, as shown in the IR spectra figure. As depicted in **Table 13**, each functional group has a characteristic peak and their peak position in the spectra. The presence of ZL at one end of the polymer chain can also be confirmed by the presence of the intense peak at 2942 and 2995 cm^{-1} in the case of PCL and PLA respectively. Further, the band for –OH should get decrease after the formation of the respective polymer due to polyesterification where –OH react with the acid groups to form the ester bond to reduce the number of –COOH and –OH. But broad appearance of peak was found which denotes the presence of short-chain polymers along with the presence of an attached catalyst at one end of the polymer chain.

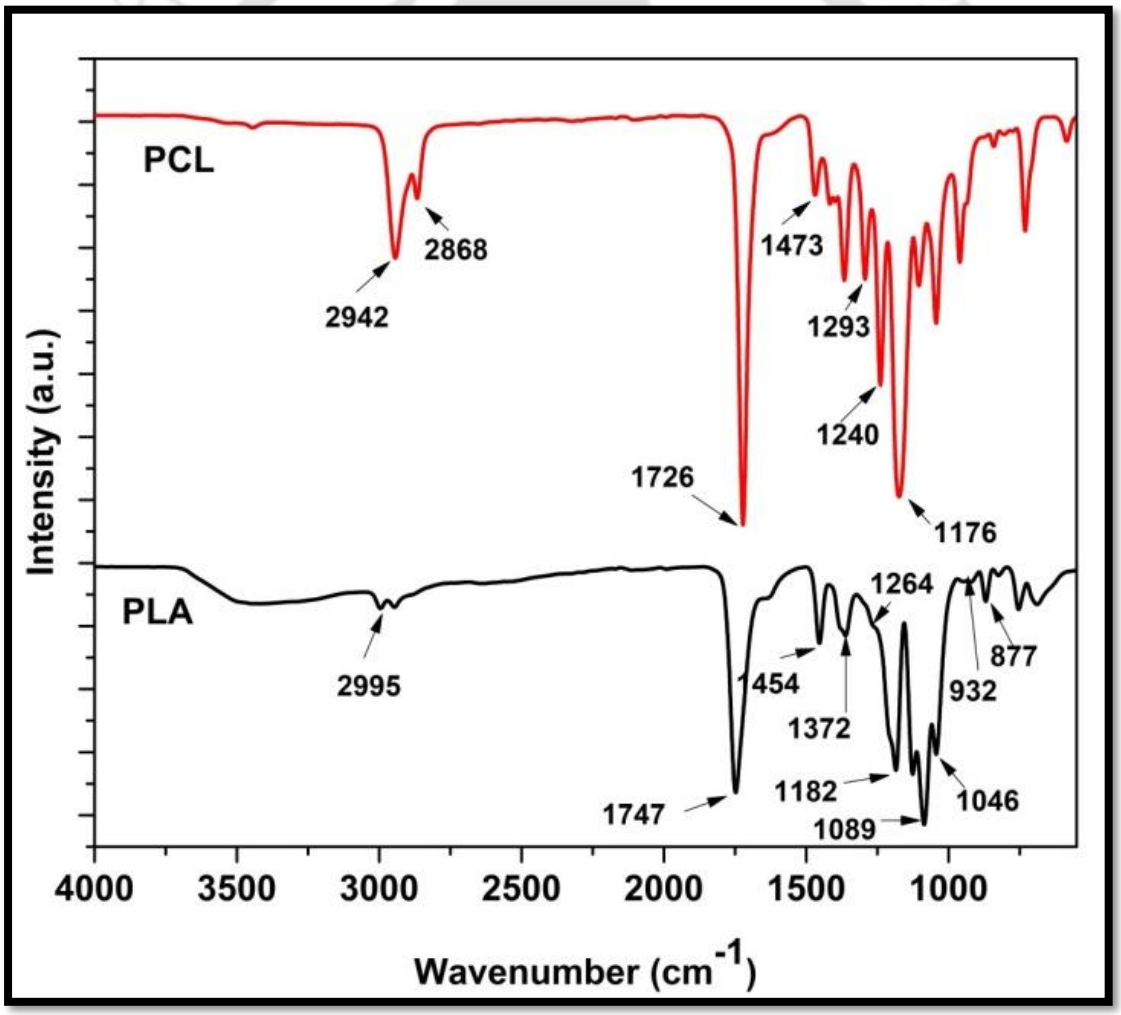

Figure 85: FTIR spectra of PCL and PLA showing the functional fingerprint.

Table 13: Wavenumber assignments of FTIR of PCL and PLA

PCL		PLA	
Wavenumber (cm^{-1})	**Assignments**	**Wavenumber (cm^{-1})**	**Assignments**
2942	CH_2 asymmetric stretching	3466	Terminal hydroxyl group
2868	CH_2 symmetric stretching	2993	CH_3 asymmetric stretching
1726	C–O stretching	2947	CH_3 symmetric stretching
1473	CH_2 bending	1747	C=O stretching
1293	C–O and C–C stretching in the crystalline phase	1454	CH_3 asymmetric bending
1240	C–O–C asymmetric stretching	1372	CH_3 symmetric bending
1176	O–C–O stretching	1181	C–O bending in esters
1165	C–O–C stretching	1089	C–O stretching in esters
1157	C–O and C–C stretching in the amorphous phase	877	C–C stretching Amorphous phase of PLA
		758	C–C stretching Crystalline phase of PLA

8.2.4 Depolymerization study of PLA

Table 14 shows the degradation of PLA into oligo methyl lactate in methanolic environment in solution showing the effect of reaction conditions on the methanolysis at 40°C and 50 °C. In general, significant catalyst activity was observed under mild conditions as compared with the various catalyst used in reported chemical degradation studies[50, 62, 186]. The catalyst performance was assessed according to the molecular weight of the obtained product. The ZL usually is not soluble in the methanol/THF system as seen from the figure. It has been reported that the methanolysis of PLA is a

transesterification reaction where ZL is chosen as a catalyst. The reaction temperature plays a significant role in the methanolysis consequences depolymerized by ZL catalyst. The lower temperature and lower time preferred reaction gives higher degradation of high and medium molecular weight PLA chains to small oligomer chains. In the absence of catalyst, no effect can be seen on the PLA solubility and swelling behavior. But after the addition of catalyst the more quickly PLA can get dissolved or swell in presence of adequate dosage of methanol and THF as too much methanol is unfavorable [61]. The heat and stirring (400 rpm) assisted dissolution of commercially available high molecular weight PLA and waste stored PLA composites after degrading produce methyl oligo lactate as determined by ^{1}H NMR analysis where the conversion is obtained from methine region. The alcoholytic depolymerization involves transesterification of ester linkage present in the repeat unit of the PLA macromolecule. The maximum coversions obtain from the parameters usig catalyst 4%, 50°C and 3h is 72% that has been enhanced to around 80% after 72h. Hence the table shows the reaction conditions and molecular weight values for degradation of PLA and waste stored PLA nanocomposites.

Table 14: Effect of reaction conditions with molecular weight values on degradation of PLA and waste PLA extruded nanocomposite were investigated and discussed as follows in the table.

Sl. No.	Sample	Catalyst (ZL) Concentration (wt. %)	Solvent	Temperature(°C)	Time (h)	M_n (kDa)	M_w (kDa)	PDI
1.	PLA 2003D grade	…….	…….	…….	…….	134	222	1.65
2.	PLA 2003D grade	2%	THF, Methanol	50	3.30h	7.7	21	2.75
3.	PLA 2003D grade	4%	THF, Methanol	40	3h	19	51	2.65
4.	PLA 2003D grade	Reused Catalyst, 4%	THF, Methanol	40	3h	23	49	2.06
5.	PLA 2003D grade	4%	THF, Methanol	50	3h	4.6	11	2.57
6.	PLA 2003D grade	4%	THF, Methanol	50	12h	3.4	8.6	2.48
7.	PLA 2003D grade	4%	THF, Methanol	50	24h	2.1	6.6	3.08
8.	PLA 2003D grade	4%	THF, Methanol	50	72h	1.9	6.4	3.22
9.	Extruded PLA nano composite waste	……	.....	.....	.....	39	111	2.76
10.	Extruded PLA nano composite waste	4%	THF, Methanol	50	3h	1.1	2.6	2.63

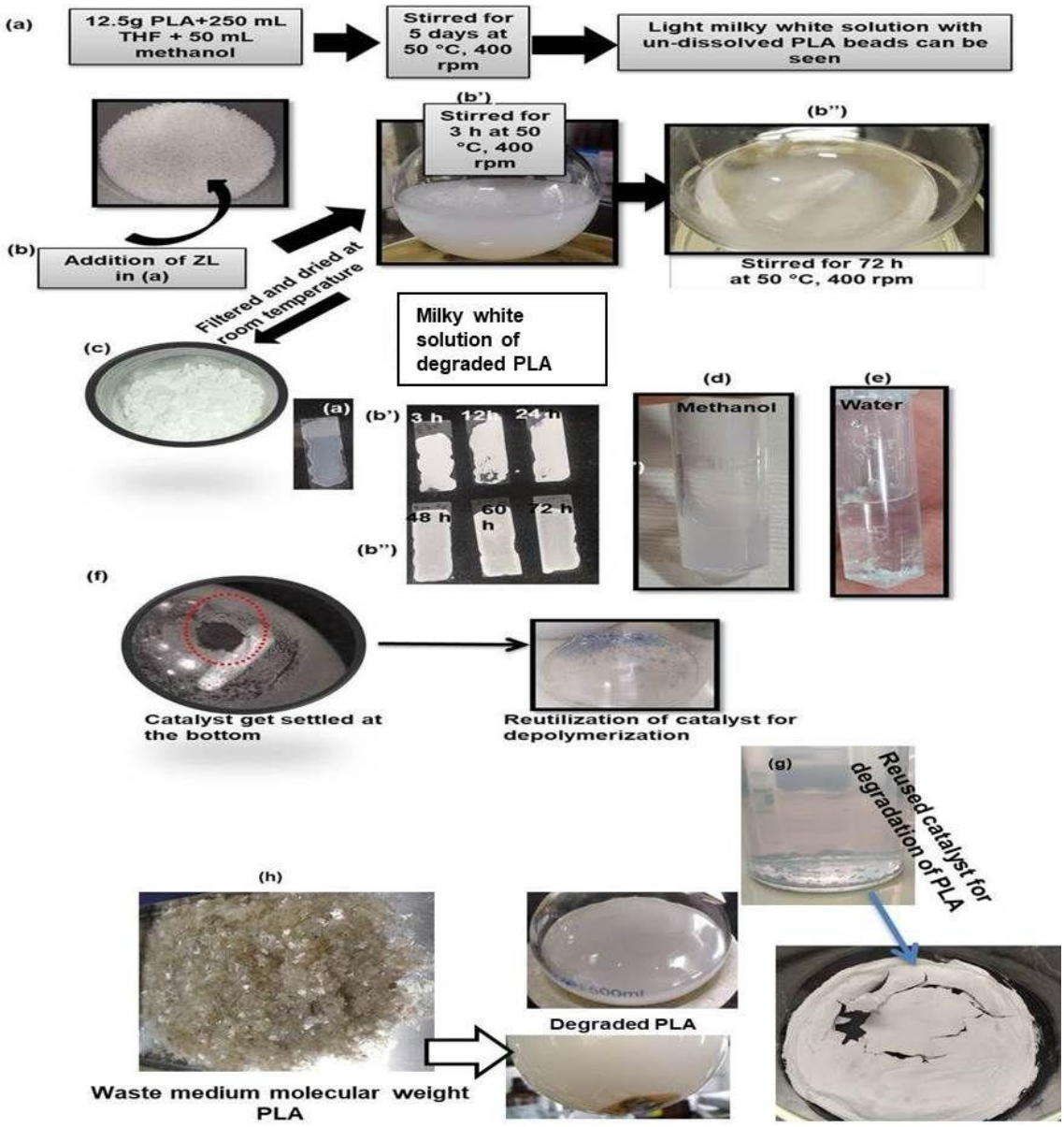

Figure 86: Flowchart showing digital pictures taken during the degradation reaction process over a time of 72 h for PLA system and PLA with catalyst system and another for waste extruded PLA nanocomposite.

Figure 86 shows the photo macrographic images of degraded PLA and waste stored extruded PLA nanocomposites clicked at different time intervals. It has been found that the reaction was not triggered without the addition of a catalyst. But after adding ZL the PLA in solution turns into milky white gel solution after 3h of time. The images show that on increasing the reaction time few portions get dissolved into the solution forming a clear solution whereas a small part of it remained gel kind of solution after 72h of time.

This may be due to the dissolution of short oligomer chains in the binary solution system. We have also found that catalysts remain settled below inside the reaction vessel considered. The utilization of catalyst was also performed to check its stability and degradation tendency. It has been found that a similar trend of change in molecular weight has been obtained therewith. The cracked and increase in opacity of the casted film from the solution also confirms its degradation. Moreover, when waste PLA nanocomposite was taken and optimized condition for the reaction was considered we have found that the nanofiller gets separated from the polymer chains and settled down right at the bottom. Hence the microwave synthesized ZL catalyst has presented an excellent role in the chemical degradation of PLA.

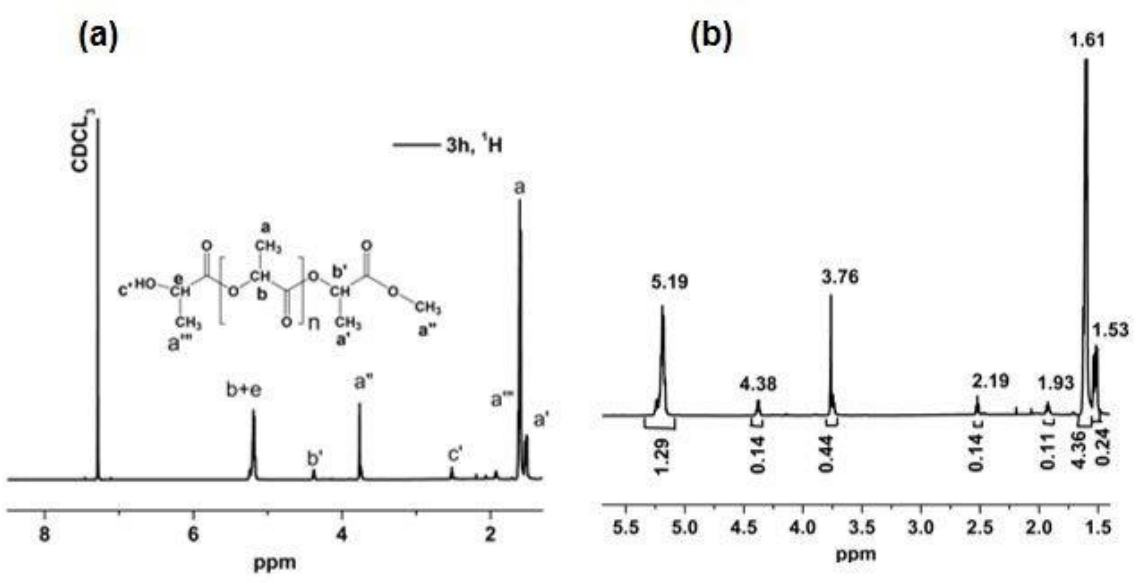

Figure 87: NMR spectra of degraded PLA after 3h of reaction (a) chemical structure of degraded PLA, and (b) spectra showing the multiplets and integrated peaks.

^{1}H NMR determined the presence of internal methine group, chain end methine group, and methyl oligo lactate methine group as shown in **Figure 87(a)**. For clarity, the chemical structure has been shown in **Figure 87(b)** with the integration values. The molecular weight of the sample (4%,50˚C, h) is calculated from the integrated values

obtained by considering the following equation. There were no peaks due to lactide in this polymer

8.2.5 Molecular Weight Distributions

- ***Cumulative Weight Fraction Distribution***

Molecular weight distributions or cumulative weight fraction distribution were calculated according to the given equation

$$W_i = 1 - \sum_{j=1}^{i} H_{N,j} = 1 - \sum_{j=1}^{i} H_j / \sum_{j=1}^{N} H_j \text{.....(xxx)}$$

Here, W_i = Cumulative weight fraction distribution, H_j = peak height and N = is equal to the number of data points obtained from the chromatogram between the average elution volume.

- ***Differential Molecular Weight Distribution***

Weight differential distribution functions $f_w(M)$ and $F_w(\log_{10}M)$ are defined as the weight population density or frequency distribution of molecular weights. The distribution function is defined as follows.

$$\mathrm{F_w\ (log_{10}M_i) = \ - H_{N,i}/(\frac{dlog_{10}M}{dV}}$$

The differential molecular weight distribution is determined using

$$\frac{\mathrm{dW}}{\mathrm{d(log_{10}M)}} = \mathrm{log_{10}M} \text{.....(xxxi)}$$

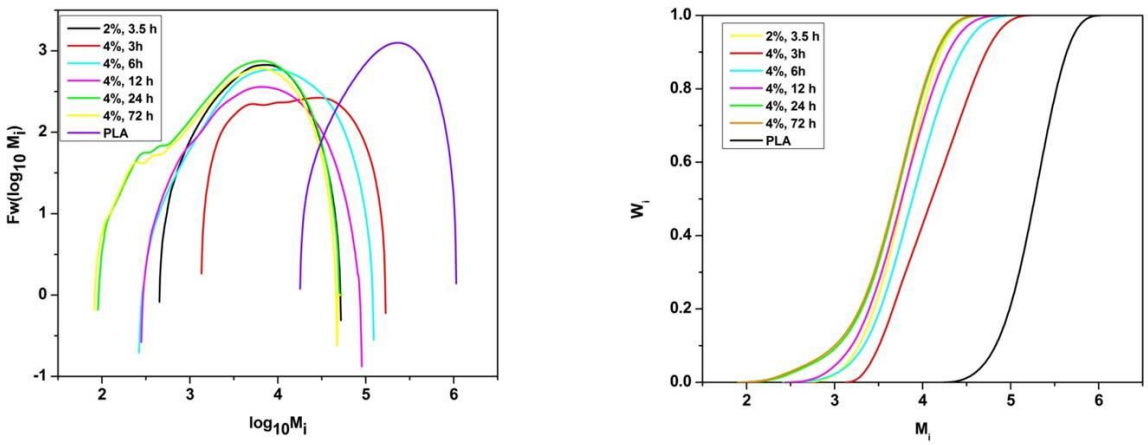

Figure 88: Cumulative and differential molecular weight distribution of degraded PLA from 3h to 72h.

Figure 88 shows cumulative plots that depict the dependence of the weight fraction as a function of the molecular weight. The change in molecular weight makes shifting of peaks and formation of bimodal is the most substantial evidence of degradation of a polymeric material. Broad peaks were observed due to chain fragmentation representing a higher polydispersity index (PDI). The formation and presence of newly formed peaks represent the short crystalline polymer chains left behind after the degradation of the amorphous portion. Molecular weight change confirms the chemical degradation of PLA and PLA waste under the different degradation times.

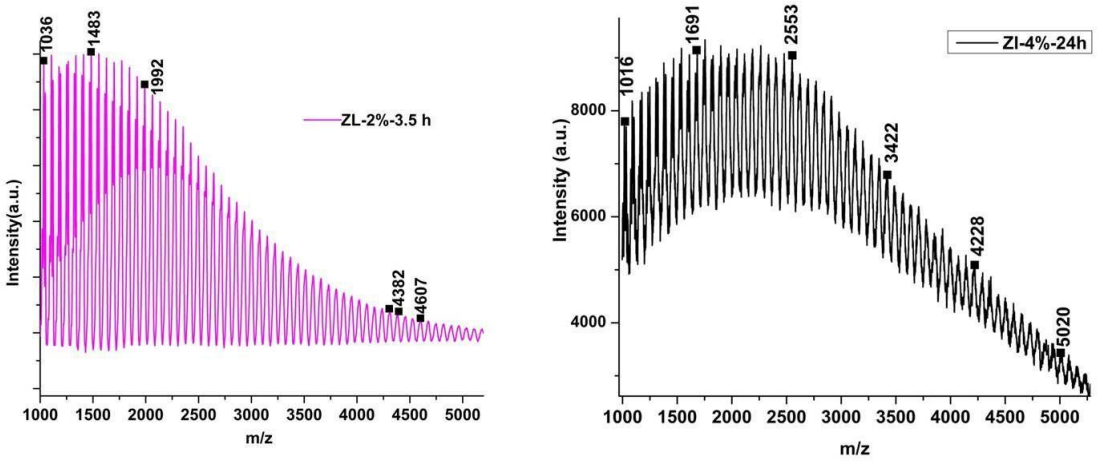

Figure 89: MALDI-TOF MS spectra of degraded PLA sample to oligo methyl lactate for 2% and 4% at 3.5h and 24h.

Generally, oligomer contained chains terminated by OH on one side and COOH on the other. MALDI-TOF was also used to demonstrate the presence of oligomers, which had the expected Methyl end groups due to transesterification. The oligomers follow the series as shown in the spectra having the main chain as H− [O− CH (CH_3)− CO−]O–CH_3. The oligomers doped with sodium ions overlap with the doped potassium ions peaks of the type H−[O−CH (CH_3)−CO−]OCH_3−Na^+, H−[O−CH (CH_3)−CO−]OCH_3−K^+, that is, linear polymer molecules with a methyl ester end group instead of carboxylic acid (again, mass 72n +34+23 and 39) respectively. Few oligomers with repetitive chain H−[O−CH (CH_3)−CO−]O–CH_3 are undoped with ions and follow the series with mass 72n+34.

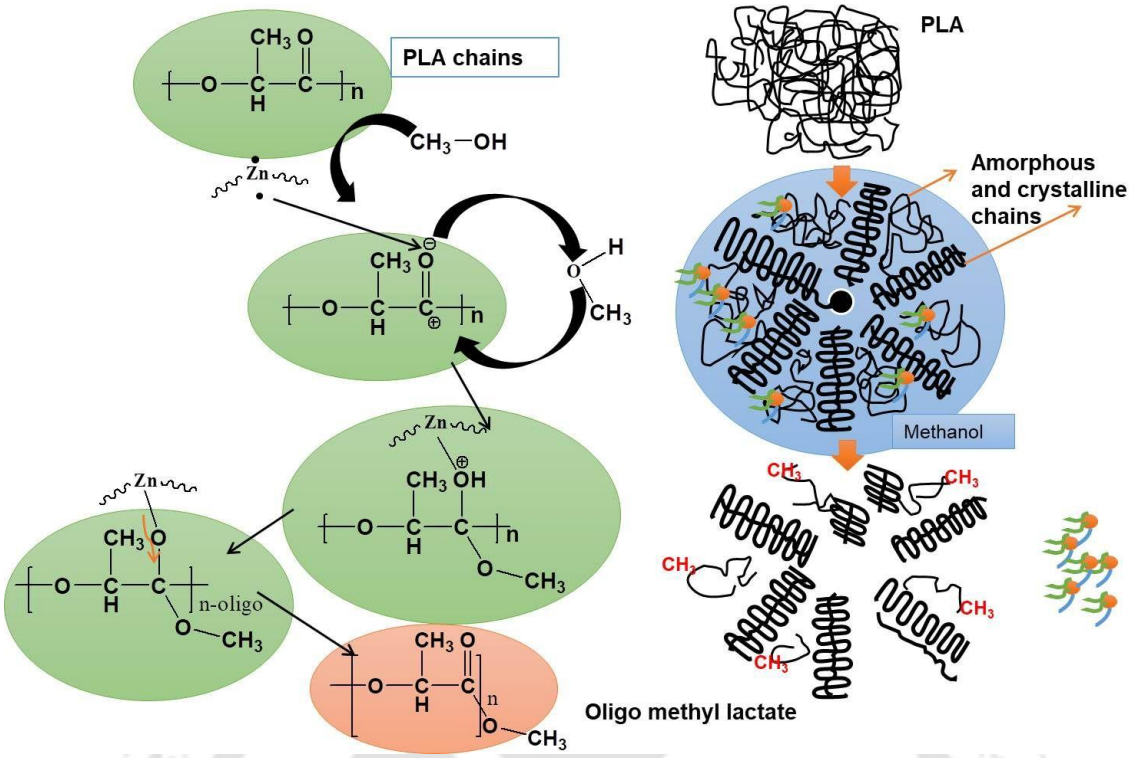

Figure 90: Schematic representation of the chemical. Long PLA chains are represented with black zigzag lines comprised of amorphous and crystalline regions a short PLA chains are in orange, and OLA is represented in green.

8.2.6 Mechanism of the methanolysis of PLA using ZL

The investigation has been performed to study the reaction mechanism of using GPC where the initial molecular weight and the molecular weight of the depolymerized PLA were characterized. The optimized catalyst content and reaction temperature, time shows the decrease in the drastic molecular weight of PLA after methanolysis in presence of a catalyst and solvent THF. Thereby, a probable mechanism for the methanolytic depolymerization in presence of a catalyst. As far, PLA was dissolved or swelled in the ZL, the hydrogen present in the cation of ZL interacts with the carbonyl oxygen (O=C) in the ester, forming a hydrogen bond and increasing the positive electricity of the O=C carbon. Also, the O-atom in CH_3OH attacked the C atom of the O=C group forming a tetrahedral intermediate and the two interactions result in the breakage of the C–O bond. This accelerates the decrease of average molecular weight PLA that further results into

the formation of oligomers reacted with methanol further to produce the main product, oligo methyl lactate. The proposed reaction scheme of ZL-catalyzed methanolytic depolymerization of PLA is depicted as shown in **Figure 90**. The degradation process can be divided into three steps. In the first step, the ZL broke the ester bond of the long polymeric chains in the amorphous phase (Stage I). Then, during the second week, a reorganization of the short-chain occurred, attributed to an increase in amorphous carboxyl peak (Stage II). Finally, in (Stage III) the polymeric chains showed a drastically chemical degradation due to the diffusion of catalyst within the degraded matrix, which makes the sample opaque, and thereof its crystallinity increases for all the samples. Further, the EDX analysis as shown in the figure also confirms the absence of the catalyst attached with the degraded polymer as no traces of weight % of Zn can be seen in the dried degraded sample as shown in **Figure 91**.

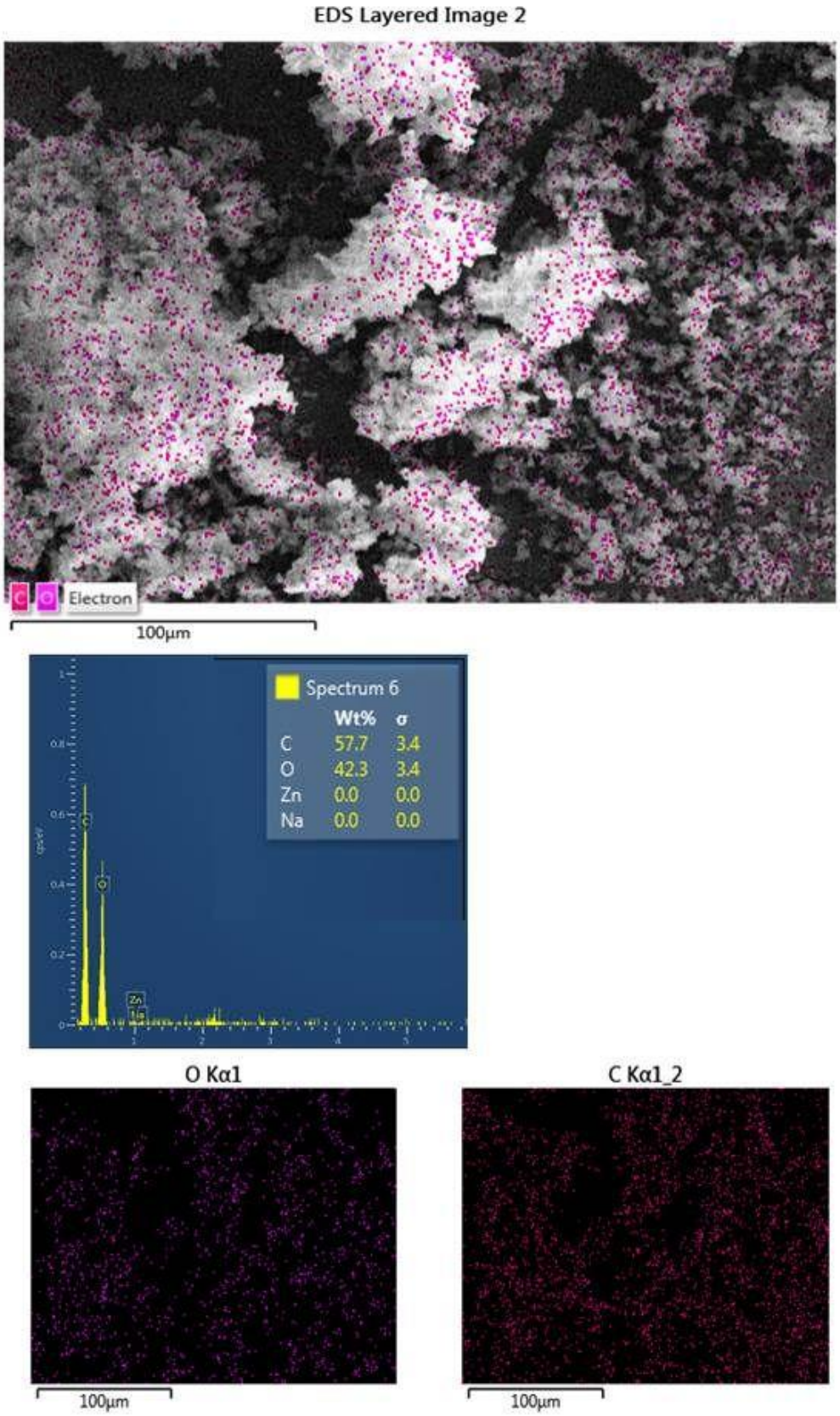

Figure 91: EDX analysis showing the distribution of Carbon and Oxygen constituents and absence of Zn.

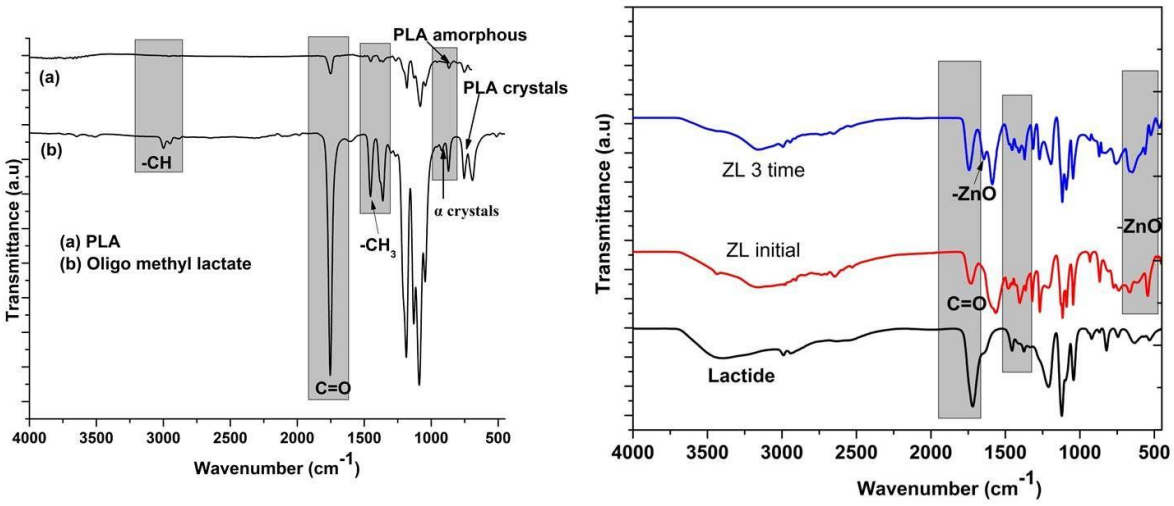

Figure 92: FTIR spectra of PLA and oligo methyl lactate, Lactide, ZL initial, and ZL reusing upto 3 times.

A comparison of FTIR spectra for neat PLA and degraded oligo PLA is shown in **Figure 92**. The FTIR spectrum showed intense and high transmittance peaks at 1751 cm^{-1}suggesting the formation of carboxylic groups, amides, and ketones due to the degradation process with a significant conformational change. The prominent appearance of intense IR bands at 2,999, 2,955, and 2,879 cm^{-1} are assigned to CH stretching region – CH_3 (asym), CH_3 (sym), and CH mode for the case of the degraded sample which attributes presence of short degraded PLA chains. Also, the deformation vibration absorption peak for $–CH_3$ at 1457cm^{-1} and 1360 cm^{-1} were gradually weakened, which also indicates that the PLA molecules were degraded. Peaks at 871 and 751 cm^{-1} are attributed to the amorphous and crystalline phases of PLA according to literature but a new intense peak appeared at 920.61 cm^{-1} is due to the formation of α crystals and highly intense peak around 870, 757 and 697 cm^{-1} are due to the presence of short degraded amorphous chains and appearance of highly crystalline peaks [187]. Thereby due to the degradation process higher mobility of the polymer chains in the amorphous phase occurs that tends to recrystallize increasing the crystal phase easily. The appearance of a peak at

1606 cm^{-1} and a highly intensified peak at 1040 cm^{-1}also signifies the existence of degraded chains having carboxylate and hydroxyl end groups.

8.2.7 Stability and reusability of ZL after the reaction

Environmental conservation is an important point and the reusability of catalysts is very important. To study the catalyst stability the neat ZL and reused dried ZL after the 3rd reaction (3^{rd} time) were considered for further analysis. The stability of this catalyst was therefore assessed by structural analysis like FTIR, ^{1}H NMR spectroscopy, and thermal analysis.

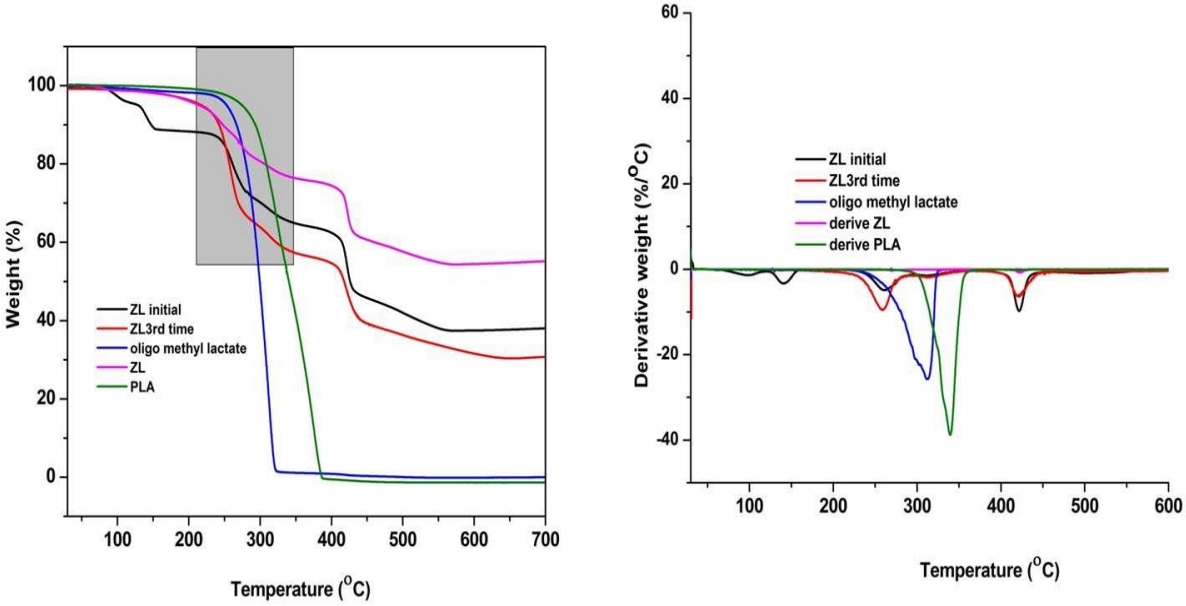

Figure 93: TGA thermogram of PLA, ZL, oligo methyl lactate, ZL initial and ZL reusing 3^{rd} time, DTG graph showing the maximum thermal degradation of the samples.

The maximum thermal stability (T_{onset}) of neat PLA is around 330 °C whereas ZL as mentioned earlier is highly thermally stable than PLA with a two-step degradation, where the first stage occurs around (T_{onset}) 315°C owing to the presence of degradation of short PLA chains and the second step occurred due to the presence of Zn metal presence with a residue of ~54% as an evidence around 415˚C due presence of free Zn^{2+} ions after

degradation of short oligo lactate grafted chains. This suggests formation of new sites which enhance degradation rate after reusing of catalyst. Further, it can be observed that for the case of degraded PLA the thermal stability has been decreased to 300°C (T_{onset}), shifted to a lower temperature with no carbon residue which suggests that there is no presence of a catalyst in the degraded sample after reaction terminates as shown in **Figure 93**.

The methyl oligo lactate can be separated using filter paper attached Buchner funnel under vacuum to filtrate the liquid whereas the catalyst remains settle at the bottom of the RB which can be dried for reuse. The TGA, FTIR, and MALDI-TOF analysis for the fresh one and the reused catalyst confirmed the reusability of the catalyst after using it 3 times. The TGA analysis shows few changes in thermal stability which maybe due to the presence of the oligo PLA grafted chains with Zn ions which itself may get depolymerized giving higher carbon residue.

.

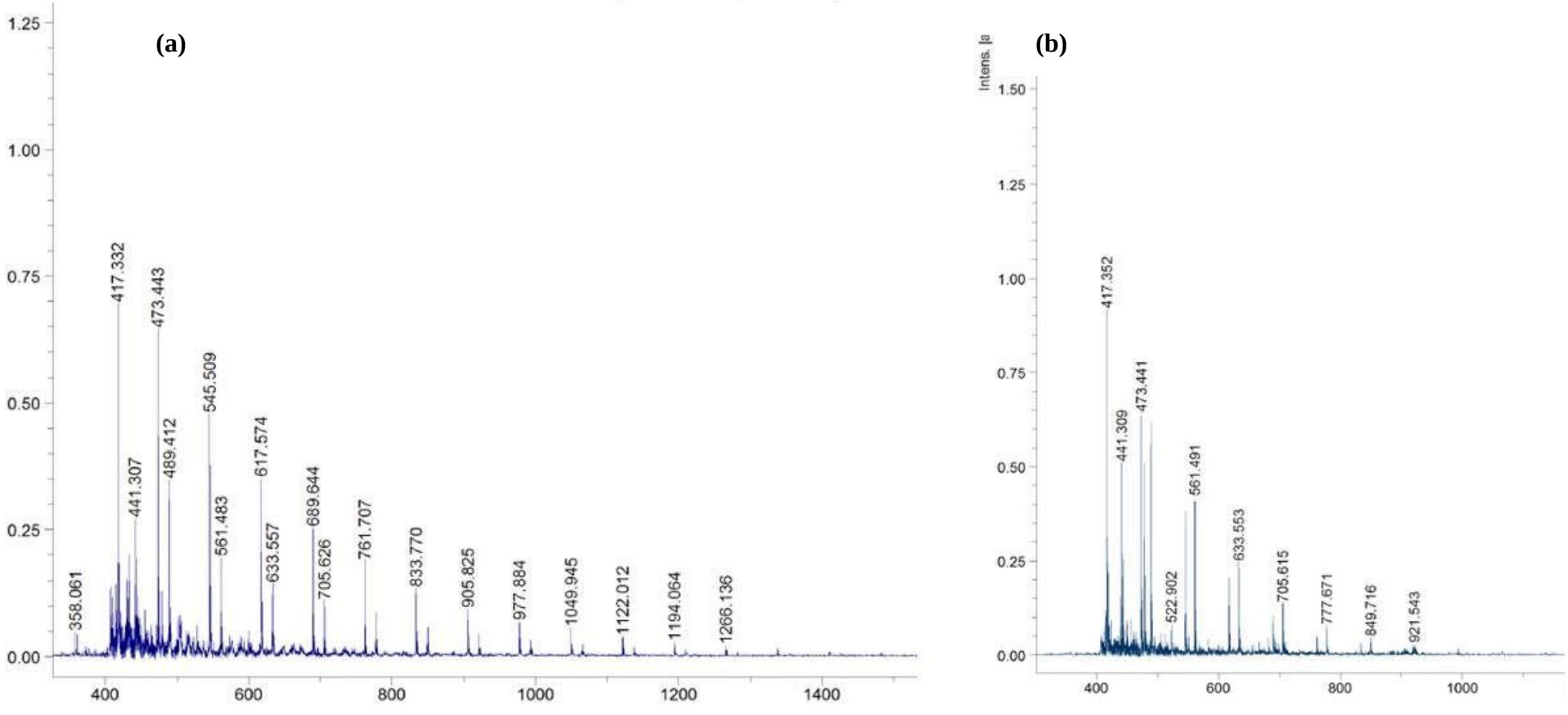

Figure 94: MALDI-TOF MS analysis of (a) ZL, and (b) ZL after reusing 3rd time.

Further, the MALDI-TOF analysis shows that there is a decrease in the repeat unit than the fresh one as shown in **Figure 94**. The stability of ZL after reusing 3 times was therefore found to be more air-/moisture, solvent sensitive, showing evidence via ^{1}H NMR spectroscopy of degradation after getting separated and dried. The MALDI-TOF mass spectrum of ZL and as expected the sample shows a series of intense molecular ion peaks that range from 417.32 to 1266.13 D separated by potassium ions of the type HO–(–CH(CH_3)COO)m–O–Zn–O(COCH(CH_3)n–OH–K^+ type that is linear polymer molecules with grafted Zn^{2+} ions where (m+n) values reach upto 16 monomer repeat units as mentioned earlier. But after recycling, there is a change in the number of repeat units for the ZL as shown in **Figure 94(b).**

After using thrice the molecular weight of ZL has decreased from 1266 to 921 Da where the peaks ranging from 417.351 to 921 Da (n varies from 8 to 13) corresponding to a new structural formula, HO–[CH(CH_3)CO–]$_{m-1}$–O–Zn–O–(OCOCH–CH_3)$_{n-1}$–OH where there is a decrease in mer units values than the original can be found which follows the corresponding equation. This result confirmed that a small amount of catalyst dissociates duringde polymerization reaction as it is in the system, due to the short PLA oligomer linear region. The doped potassium ions that appear in the same region are also of the cyclic oligomers.

8.3 Conclusion:

The first study includes polymerization of cyclic esters using catalyst ZL in presence and absence of catalyst. The GPC analysis shows a higher molecular weight of around 20kDa after polymerization with one end ZL and another end as –OH group. The NMR and FTIRspectra confirm the formation of the PCL and PLA polymers. Further, depolymerisation of PLA using methanolysis in the present of ZL catalyst has been preceded easily under relatively lower temperature, and 400 rpm stirring speed in

presence of THF as a solvent. The GPC chromatograph shows a shifting of the broad peaks with the formation of small peaks indicating the breaking of long coiled chains. The EDX analysis shows the ease of removal of ZL due to its insolubility nature in THF. An attractive case is that the ZL obtained can be reused upto 3 times where few changes in the repeat units take place that gets decreased from 1266 to 921 Da as analyzed by MALDI-TOF.

****

CHAPTER 9

CONCLUSION AND FUTURE SCOPE

'Our imagination is the only limit to what we can hope to have in the future.'

Charles F. Kettering

Composite materials have been always a preferable solution in setting up performing structures to make them applicable in all sectors of industries. The unique properties of nanomaterials have attracted researchers, especially in textile to increase the durability and performance beyond that of normal fibers. Furthermore, the electrospinning technique can give apparition, special nonwoven micro and nano textiles that can lead to a new revolution for the textile industry. Two different methodologies have been applied here in these studies one is by in situ polymer nanocomposite method and another is providing efficient multifunctional finishing to the fabrics either by electrospraying or dip-coating process. Tunable properties like hydrophobicity, hydrophilicity, antiviral, antibacterial, self-cleaning, dyeing ability, shrinkage-free, shimmery finishing have been achieved. The nontoxicity and the chemical stability of UV blockers like TiO_2 and ZnO make them preferable over other organic blockers. Tunable in the hydrophobicity of PLA nanofabric to highly hydrophobic, superhydrophilic, and hydrophilic nature via in situ modification using SNC-ZnO, a-TiO_2, and nCS-ZL respectively due to topographical changes. Microwave synthesized ZL and ion gelation synthesized nCS has its multifunctionality towards significant antibacterial and antiviral activity. A shrinkage-free, elevated temperature tolerable and dye removable ability stereocomplex PLA electrospun nanofabric using a-TiO_2 has been fabricated for textile application. Investigations declared ZL and its utilization as a catalyst for ring-opening

polymerization of cyclic esters. Since biodegradation of PLA exclusively occurs under industrial standard composting conditions; hence another clear alternative i.e. chemical recycling has been studied using ZL as a catalyst by methanolysis to warranty increase in production of PLA. Low-molecular-weight lactate esters are touted as green solvents because of their biodegradability and low toxicity. Serve as substitutes to hydrocarbon-based solvents with applications ranging from industrial and house cleaning, paints formulations, agricultural chemicals polymer manufacturing, to pharmaceuticals. Transformation of oligolactate esters into LA can allow polymer reformation, therefore resulting in a circular economy alongwith recovery of solvent under distillation system.

Increasing product adoption in healthcare, defense, medical, and water treatment are acting as growth-inducing factor that facilitated the integration of smart nanofabrics with our day-today requirements. Thereby the studies performed described the challenges to purposefully look into the current pandemic era as well utilizing as PPE.

Existing literature shows the utilization of sustainable material in various applications thereby these fabrics prepared with PLA/nanochitosan-ZL can be used in the future for metal detector/removal sensors and PLA/SNC-ZnO agriculture sector for grafting plants. Recyclability of nanofiber membranes should become a key concern in all application fields; thereby the prepared ZL material can solve such a problem in near future. Altogether with the performance enhancement, it can provide an interesting topic of discussion in the future, since it can be highly beneficial even at the end of their life. Moreover, addition of annealing and nucleating agents can improve the crystallinity and thereby the mechanical properties of PLA. So, further research can be done on the process-mechanical property relationships for the functionalized PLA nanofabrics.

RESEARCH OUTCOME

Published research article:

1. **Hazarika, D.,** Kumar, A., & Katiyar, V. (2022). Structural Evolution of in situ Polymerized Poly(L-lactic acid) Nanocomposite for Smart Textile Application. *Scientific reports*, 12, 14724.

2. **Hazarika, D.,** Kalita, N. K., Kumar, A., & Katiyar, V. (2022). Crystalline titanium-dioxide nanofinish impregnated on electrospun stereocomplex poly (lactic acid) as non-woven nanotextile with superhydrophilic, anti-shrinkage, dark dyeing and waste dye removal ability for sustainable application. **International Journal of Biological Macromolecules**, 219, 384-394.

3. **Hazarika, D**., Kalita, N. K., Kumar, A., & Katiyar, V. (2021). Functionalized Poly(lactic acid) based Nano-fabric for Anti-Viral Application. ***RSC Advances***, **11**, 32884 -32897.

4. Kalita, N. K., Damare, N. A., **Hazarika, D.,** Bhagabati, P., Kalamdhad, A., & Katiyar, V. (2021). Biodegradation and characterization study of compostable PLA bioplastic containing algae biomass as potential degradation accelerator. ***Environmental Challenges,*** *3*, 100067.

5. Kalita, N. K., **Hazarika, D.,** Kalamdhad, A., & Katiyar, V. (2021). Biodegradation of biopolymeric composites and blends under different environmental conditions: Approach towards end-of-life panacea for crop sustainability. ***Bioresource Technology Reports***, *15*, 100705.

6. Bhagabati, P., **Hazarika, D**., & Katiyar, V. (2019). Tailor-made ultra-crystalline, high molecular weight poly (ε-caprolactone) films with improved oxygen gas barrier and optical properties: a facile and scalable approach. ***International journal of biological macromolecules***, *124*, 1040-1052.

PATENT FILLED:

1. Katiyar V, **Hazarika D**, Kumar A and Kumar S, A PROCESS OF PREPARING AN ANTIVIRAL NANO FABRIC AND AN ANTIVIRAL NANO FABRIC THEREOF, Indian Patent Application No: 202131013654.

BOOK CHAPTERS:

1. Ghosh, T., **Hazarika, D**., & Katiyar, V. (2021). Cellulose-Based Nanostructured Materials in Edible Food Packaging. In *Nanotechnology in Edible Food Packaging* (pp. 65-100). Springer, Singapore.

2. Ghosh, T., **Hazarika, D.,** Dhar, P., & Katiyar. (2020). 5. Processing techniques for nanocellulose based value-added products. In *Cellulose Nanocrystals* (pp. 119-156). De Gruyter.

3. **Hazarika, D.,** Kumar A., & & Katiyar, V. (2020). "Mimicking Smart Textile by Fabricating Stereocomplex Poly (Lactic Acid) Nanocomposite Fibers." *Advances in Sustainable Polymers*. Springer, Singapore, 341-362.

PREPARED ARTICLES:

1. **Hazarika, D.,** Chakraborty G., Kumar, A., & Katiyar, V. Non-Isothermal Crystallization Kinetics Studies on Fabrication of Highly Hydrophobic Poly(Lactic Acid)/Silk Nanocrystal-ZnO Nanofiber Composite **(to be submitted).**

2. **Hazarika, D.,** Ghosh, T., Snkhla, A., Bhonsale, S., Kumar, S., Kumar, A., & Katiyar, V. Behaviour of Nanochitosan and Zinc-Oligo-Lactate as a Nanofinish for PLA Nanofabric for application of Protective Wearables **(to be submitted).**

3. **Hazarika, D**., Kalita, N. K., Kumar, A., & Katiyar, V. Investigations on Zinc-oligo Lactate as a Catalyst for polymerization of Cyclic Esters and chemical degradation of High Molecular Weight PLA for recycling **(to be submitted).**

4. Mudenur, C., **Hazarika, D.**, Kumar, A., & Katiyar, V. Synthesis of Poly(lactic acid) using prodigiosin as catalyst (to be submitted).

ORAL and POSTER PRESENTATIONS:

1. **Hazarika, D**., Kalita, N. K., Kumar, A., & Katiyar, V., Biodegradable Antiviral Facemask **(Oral)**, participation in CHEMCON-2021 conference held in a hybrid mode from December 26-30, 2021, at CSIR-IMMT, Bhubaneswar, India.

2. **Hazarika D.**, Kumar A., and Katiyar V., Studies on non-isothermal crystallization kinetics of poly(lactic acid) PLA/ in situ PLLA- Silk nano crystal (SNC) nanocomposite films **(Poster),** International Symposium on Sustainable Polymers & National Symposium on Chemistry Education for Sustainable Engineering, August 23-25, 2019, IIT Guwahati.

3. **Hazarika D**., Kumar A., and Katiyar V., Fabrication of Stereo complex Poly (Lactic acid) (PLA) fibers reinforced with Amphiphilic Chitosan using Melt Spinning, **(Poster),** SPSI-MACRO-2018, December 19th – 22nd, 2018.

AWARDS RECEIVED

1. **"Best Oral Presentation Award" Hazarika, D**., Kalita, N. K., Kumar, A., & Katiyar, V., entitled "Biodegradable Antiviral Facemask" presented in CHEMCON-2021 conference held in a hybrid mode from December 26-30, 2021, at CSIR-IMMT, Bhubaneswar, India.

CONFERENCES AND WORKSHOP ATTENDED

1. Trilateral Symposium on Bioinspired and Biobased Materials" organized by Kyoto Institute of Technology, Ca'Foscari University of Venice, Italy, and Indian Institute of Technology Guwahati, India (5-March, 2021).

2. MatCon-2021, International Conference On materials for Millenium, organized by Department of Applied Chemistry, Cochin University of Science and Technology, Kochi -682022, Kerala. (15-19 march, 2021).

3. North East Centre for Biological Sciences and Healthcare Engineering, NECBH, Online workshop on 3D printing Techniques and their applications in Biomedical devices, 15 July 2021.

4. North East Centre for Biological and Healthcare Engineering (NECBH), Online Workshop on Nuclear Magnetic Resonance: Technique and its Applications. at IIT Guwahati, 23rd to 24th August, 2021.

5. Attended webinar on "Dynamic Mechanical Analysis (DMA)" organized by Anton Paar India Pvt. Ltd. Dated: 30th March 2021.

6. Conference on Polymer Processing and Emerging Technologies, conducted by Polymer processing Academy in association with IIT Alumni Center, Bengaluru, on 5-7 November 2020.

7. Society of Polymer Science India, Mumbai Chapter, Webinar on Journey of Polymers to Plastics: The Polyolefins, 12 September 2020.

8. Participated in 2h professional workshop on “Prior-art Search with Google Patents” conducted by Turnip Innovations Pvt. Ltd., 5th September 2020.

9. Participated in TEQIP Sponsored online national symposium on Nanomaterials for Engineering and Biomedical Applications (NEBA 2020), 27-29 July, 2020 organized by KEC, Katihar-854109.

10. Attended conference organized by Indo-Japan Bilateral Symposium on Future Perspective of Bio-resource Utilization in North-East India, IJBS-17, February 1-4, 2018.

11. Attended conference organized by International Symposium on Advances in Sustainable Polymers, International Symposium on Advances in Sustainable Polymers, ASP-17, January 8-11, 2018.

References

1. Przybylak M, Maciejewski H, Dutkiewicz A, Dąbek I, Nowicki M (2016) Fabrication of superhydrophobic cotton fabrics by a simple chemical modification. Cellulose 23:2185–2197 . https://doi.org/10.1007/s10570-016-0940-z

2. Shahid-ul-Islam, Butola BS (2019) Recent advances in chitosan polysaccharide and its derivatives in antimicrobial modification of textile materials. Int J Biol Macromol 121:905–912 . https://doi.org/10.1016/j.ijbiomac.2018.10.102

3. Busi E, Maranghi S, Corsi L, Basosi R (2016) Environmental sustainability evaluation of innovative self-cleaning textiles. J Clean Prod 133:439–450 . https://doi.org/10.1016/j.jclepro.2016.05.072

4. Ahmed T, Shahid M, Azeem F, Rasul I, Shah AA, Noman M, Hameed A, Manzoor N, Manzoor I, Muhammad S (2018) Biodegradation of plastics: current scenario and future prospects for environmental safety. Environ Sci Pollut Res 25:7287–7298 . https://doi.org/10.1007/s11356-018-1234-9

5. Ignatyev, I. A., Thielemans, W., & Vander Beke, B. (2014). Recycling of polymers: a review. *ChemSusChem*, *7*(6), 1579-1593. https:// doi: 10.1002/cssc.201300898

6. Walser T, Demou E, Lang DJ, Hellweg S (2011) Prospective environmental life cycle assessment of nanosilver T-shirts. Environ Sci Technol 45:4570–4578 . https://doi.org/10.1021/es2001248

7. Rahman MH, Bhoi PR (2021) An overview of non-biodegradable bioplastics. J Clean Prod 294: . https://doi.org/10.1016/j.jclepro.2021.126218

8. Shah AA, Hasan F, Hameed A, Ahmed S (2008) Biological degradation of

plastics: A comprehensive review. Biotechnol Adv 26:246–265 . https://doi.org/10.1016/j.biotechadv.2007.12.005

9. Plastic-the Facts 2016: an Analysis of European Plastics Production, Demand and Waste Data Plastics Europe (2016). http://www.plasticseurope.org/Document/plastics---the-facts-2016-15787.aspx?FolID=2

10. Bioplastics market data, 2020 Bioplastics market data EuropeanBioplastics . https://www.european-bioplastics.org/market/ (2020)

11. Sarif Ullah Patwary MS (2015) Smart Textiles and Nano-Technology: A General Overview. J Text Sci Eng 05. https://doi.org/10.4172/2165-8064.1000181

12. Rivero PJ, Urrutia A, Goicoechea J, Arregui FJ (2015) Nanomaterials for Functional Textiles and Fibers. Nanoscale Res Lett 10:1–22 . https://doi.org/10.1186/s11671-015-1195-6

13. Homayoni H, Ravandi SAH, Valizadeh M (2009) Electrospinning of chitosan nanofibers: Processing optimization. Carbohydr Polym 77:656–661 . https://doi.org/10.1016/j.carbpol.2009.02.008

14. Koukaras EN, Papadimitriou SA, Bikiaris DN, Froudakis GE (2012) Insight on the formation of chitosan nanoparticles through ionotropic gelation with tripolyphosphate. Mol Pharm 9:2856–2862 . https://doi.org/10.1021/mp300162j

15. Hebeish A, Sharaf S, Farouk A (2013) Utilization of chitosan nanoparticles as a green finish in multifunctionalization of cotton textile. Int J Biol Macromol 60:10–17 . https://doi.org/10.1016/j.ijbiomac.2013.04.078

16. Wang Y, Guo J, Zhou L, Ye C, Omenetto FG, Kaplan DL, Ling S (2018) Design,

Fabrication, and Function of Silk-Based Nanomaterials. Adv Funct Mater 1805305:1805305 . https://doi.org/10.1002/adfm.201805305

17. Tao Y, Xu W, Yan Y, Cao Y (2012) Preparation and characterization of silk fibroin nanocrystals. 760–767 . https://doi.org/10.1002/pi.4136

18. Patwa R, Soundararajan N, Mulchandani N, Bhasney SM, Shah M, Kumar S, Kumar A, Katiyar V (2018) Silk nano-discs: A natural material for cancer therapy. Biopolymers 109:e23231 . https://doi.org/10.1002/bip.23231

19. Jae LJ, Yamane H (2010) Role of the Stereocomplex Crystallites in the PLLA/PDLA Mixed Spinning Dope on the Stereocomplex Formation in the Wet-spun Fibers. Sen-I Gakkaishi 66:236–242. https://doi.org/10.2115/fiber.66.236

20. Liu L, Yang X, Yu H, Ma C, Yao J (2014) Biomimicking the structure of silk fibers via cellulose nanocrystal as β-sheet crystallite. RSC Adv 4:14304–14313 . https://doi.org/10.1039/c4ra01284d

21. Ahmari H, Heris SZ, Khayyat MH (2018) The effect of titanium dioxide nanoparticles and UV irradiation on photocatalytic degradation of Imidaclopride The effect of titanium dioxide nanoparticles and UV irradiation on photocatalytic. 3330: . https://doi.org/10.1080/09593330.2017.1306115

22. Gupta SM, Tripathi M (2012) A review on the synthesis of TiO 2 nanoparticles by solution route. 10: . https://doi.org/10.2478/s11532-011-0155-y

23. Becheri A, Dürr M, Lo Nostro P, Baglioni P (2008) Synthesis and characterization of zinc oxide nanoparticles: Application to textiles as UV-absorbers. J Nanoparticle Res 10:679–689 . https://doi.org/10.1007/s11051-007-9318-3

24. Behnajady MA, Modirshahla N, Hamzavi R (2006) Kinetic study on photocatalytic

degradation of C.I. Acid Yellow 23 by ZnO photocatalyst. J Hazard Mater 133:226–232 . https://doi.org/10.1016/j.jhazmat.2005.10.022

25. Dastjerdi R, Montazer M (2010) A review on the application of inorganic nano-structured materials in the modification of textiles: Focus on anti-microbial properties. Colloids Surfaces B Biointerfaces 79:5–18 . https://doi.org/10.1016/j.colsurfb.2010.03.029

26. Xu B, Cai Z (2008) Fabrication of a superhydrophobic ZnO nanorod array film on cotton fabrics via a wet chemical route and hydrophobic modification. Appl Surf Sci 254:5899–5904 . https://doi.org/10.1016/j.apsusc.2008.03.160

27. Alwan AF, Khalaf HI (2019) Synthesis of polylactic acid using Zn powder under microwave irradiation. IOP Conf Ser Mater Sci Eng 571: . https://doi.org/10.1088/1757-899X/571/1/012085

28. Turovskiy Y, Chikindas ML (2011) Zinc Lactate and Sapindin Act Synergistically with Lactocin 160 Against Gardnerella vaginalis. Probiotics Antimicrob Proteins 3:144–149 . https://doi.org/10.1007/s12602-011-9068-5

29. Skalny A V, Rink L, Ajsuvakova OP, Aschner M, Gritsenko VA, Alekseenko SI, Svistunov AA, Petrakis D (2020) Zinc and respiratory tract infections : Perspectives for COVID - 19 (Review). 19:17–26 . https://doi.org/10.3892/ijmm.2020.4575

30. Iles, A., & Martin, A. N. (2013). Expanding bioplastics production: sustainable business innovation in the chemical industry. Journal of Cleaner Production, 45, 38-49. https://doi.org/10.1016/j.jclepro.2012.05.008

31. Lim LT, Auras R, Rubino M (2008) Processing technologies for poly(lactic acid).

Prog Polym Sci 33:820–852 . https://doi.org/10.1016/j.progpolymsci.2008.05.004

32. Ahmed J, Varshney SK (2011) Polylactides-chemistry, properties and green packaging technology: A review. Int J Food Prop 14:37–58 . https://doi.org/10.1080/10942910903125284

33. R.S. B (2005) Poly (lactic acid) fibers. … Sustain Fibres. https://doi.org/10.2115/fiber.59.P_329

34. Bai H, Deng S, Bai D, Zhang Q, Fu Q (2017) Recent Advances in Processing of Stereocomplex-Type Polylactide. Macromol Rapid Commun 38:1–12 . https://doi.org/10.1002/marc.201700454

35. Yamane H, Sasai K (2003) Effect of the addition of poly(D-lactic acid) on the thermal property of poly(L-lactic acid). Polymer (Guildf) 44:2569–2575 . https://doi.org/10.1016/S0032-3861(03)00092-2

36. Furuhashi Y, Kimura Y, Yoshie N, Yamane H (2006) Higher-order structures and mechanical properties of stereocomplex-type poly(lactic acid) melt spun fibers. Polymer (Guildf) 47:5965–5972 . https://doi.org/10.1016/j.polymer.2006.06.001

37. Tu C, Cao X, Zhang R, Wang D, Cui L (2018) Effects of posttreatment on the properties of modified PLLA/PDLA fibers. Polym Adv Technol 1–10 . https://doi.org/10.1002/pat.4460

38. Tsuji H (2016) Poly(lactic acid) stereocomplexes: A decade of progress. Adv Drug Deliv Rev 107:97–135 . https://doi.org/10.1016/j.addr.2016.04.017

39. Ahmed R (2011) Poly(lactic acid) stereocomplex formation in the melt: limitations and prospectives. https://doi.org/10.6100/IR719381

40. Tan BH, Muiruri JK, Li Z, He C (2016) Recent Progress in Using

Stereocomplexation for Enhancement of Thermal and Mechanical Property of Polylactide. ACS Sustain Chem Eng 4:5370–5391 . https://doi.org/10.1021/acssuschemeng.6b01713

41. Tsuji H, Nakano M, Hashimoto M, Takashima K, Katsura S, Mizuno A (2006) Electrospinning of poly(lactic acid) stereocomplex nanofibers. Biomacromolecules 7:3316–3320 . https://doi.org/10.1021/bm060786e

42. Gao X-R, Niu B, Hua W-Q, Li Y, Xu L, Wang Y, Ji X, Zhong G-J, Li Z-M (2018) Rapid preparation and continuous processing of polylactide stereocomplex crystallite below its melting point. Polym Bull. https://doi.org/10.1007/s00289-018-2544-2

43. Yamamoto M, Nishikawa G, Afifi AM, Lee JC, Yamane H (2015) Effect of the take-up velocity on the higher-order structure of the melt-electrospun PLLA/PDLA blend fibers. J Fiber Sci Technol 71:127–133 . https://doi.org/10.2115/fiber.71.127

44. Rudnik E, Briassoulis D (2011) Degradation behaviour of poly(lactic acid) films and fibres in soil under Mediterranean field conditions and laboratory simulations testing. Ind Crops Prod 33:648–658 . https://doi.org/10.1016/j.indcrop.2010.12.031

45. Tsuji H, Suzuyoshi K (2002) Environmental degradation of biodegradable polyesters and poly (L-lactide) films in controlled static seawater. Polym Degrad Stab 75:347–355. https://doi.org/10.1016/S0141-3910(01)00240-3

46. Alaerts L, Augustinus M, Van Acker K (2018) Impact of bio-based plastics on current recycling of plastics. Sustain 10: . https://doi.org/10.3390/su10051487

47. Kumar N, Kumar M, Mudenur C, Kalamdhad A (2019) Biodegradation of modi fi ed Poly (lactic acid) based biocomposite fi lms under thermophilic composting

conditions. Polym Test 76:522–536 . https://doi.org/10.1016/j.polymertesting.2019.02.021

48. Teixeira S, Eblagon KM, Miranda F, R. Pereira MF, Figueiredo JL (2021) Towards Controlled Degradation of Poly(lactic) Acid in Technical Applications. C 7:42 . https://doi.org/10.3390/c7020042

49. Maga D, Hiebel M, Thonemann N (2019) Life cycle assessment of recycling options for polylactic acid. Resour Conserv Recycl 149:86–96 . https://doi.org/10.1016/j.resconrec.2019.05.018

50. McKeown P, Jones MD (2020) The Chemical Recycling of PLA: A Review. Sustain Chem 1:1–22 . https://doi.org/10.3390/suschem1010001

51. Schütz C, Sort J, Bacsik Z, Oliynyk V, Pellicer E, Fall A, Wågberg L, Berglund L, Bergström L, Salazar-Alvarez G (2012) Hard and Transparent Films Formed by Nanocellulose-TiO2 Nanoparticle Hybrids. PLoS One 7:1–8 . https://doi.org/10.1371/journal.pone.0045828

52. Feng X, Zhang L, Chen J, Guo Y, Zhang H, Jia C (2007) Preparation and characterization of novel nanocomposite films formed from silk fibroin and nano-TiO 2. 40:105–111 . https://doi.org/10.1016/j.ijbiomac.2006.06.011

53. Yang C, Chen S, Su H, Zhang H, Tang J, Guo C (2019) gold nanoparticles regulated by silk fi broin fi ber from Bombyx mori cocoons. 13:126–132

54. Yang Z, Peng H, Wang W, Liu T (2010) Crystallization behavior of poly(ε-caprolactone)/layered double hydroxide nanocomposites. J Appl Polym Sci 116:2658–2667 . https://doi.org/10.1002/app

55. Xu J, Su H, Han J, Chen Y, Song W, Gu Y, Moon WJ, Zhang D (2012) In situ

deposition of flower-like ZnO on silk fibroin fibers. Appl Phys A Mater Sci Process 108:235–238 . https://doi.org/10.1007/s00339-012-6882-x

56. Dhar P, Kumar A, Katiyar V (2015) Fabrication of cellulose nanocrystal supported stable Fe(0) nanoparticles: a sustainable catalyst for dye reduction, organic conversion and chemo-magnetic propulsion. Cellulose 22:3755–3771 . https://doi.org/10.1007/s10570-015-0759-z

57. Series IOPC, Science M (2019) Synthesis of polylactic acid using Zn powder under microwave irradiation. https://doi.org/10.1088/1757-899X/571/1/012085

58. Au HT, Pham LN, Ha T, Vu T, Park JS (2012) Fabrication of An Antibacterial Non-Woven Mat of a Poly (lactic acid)/ Chitosan Blend by Electrospinning. 20:51–58 . https://doi.org/10.1007/s13233-012-0010-9

59. Feng S, Zhang F, Ahmed S, Liu Y (2019) Physico-mechanical and antibacterial properties of PLA/TiO2 composite materials synthesized via electrospinning and solution casting processes. Coatings 9: . https://doi.org/10.3390/coatings9080525

60. Brake, L. D. (1993). *U.S. Patent No. 5,264,617*. Washington, DC: U.S. Patent and Trademark Office.

61. Song X, Zhang X, Wang H, Liu F, Yu S, Liu S (2013) Methanolysis of poly(lactic acid) (PLA) catalyzed by ionic liquids. Polym Degrad Stab 98:2760–2764 . https://doi.org/10.1016/j.polymdegradstab.2013.10.012

62. Román-Ramírez LA, McKeown P, Jones MD, Wood J (2019) Poly(lactic acid) Degradation into Methyl Lactate Catalyzed by a Well-Defined Zn(II) Complex. ACS Catal 9:409–416 . https://doi.org/10.1021/acscatal.8b04863

63. Zhang Z, Song K, Li Y, Wu Q (2014) Non-Isothermal Crystallization of Poly

(vinylidene fluoride)/Poly (methyl methacrylate)/Cellulose Nanocrystal Nanocomposites. Int J Polym Anal Charact 19:332–341 . https://doi.org/10.1080/1023666X.2014.902530

64. Shokeen K, Srivathsan A, Kumar S (2021) Lithium chloride functions as Newcastle disease virus-induced ER-stress modulator and confers anti-viral effect. Virus Res 292:198223 . https://doi.org/10.1016/j.virusres.2020.198223

65. Park JS (2011) Electrospinning and its applications. *Advances in Natural Sciences: Nanoscience and Nanotechnology*, *1*(4), 043002. https://doi:10.1088/2043-6262/1/4/043002.

66. Xue J, Wu T, Dai Y, Xia Y (2019) Electrospinning and electrospun nanofibers: Methods, materials, and applications. Chem Rev 119:5298–5415 . https://doi.org/10.1021/acs.chemrev.8b00593

67. Xue J, Wu T, Dai Y, Xia Y, States U, States U (2019) HHS Public Access. 119:5298–5415 . https://doi.org/10.1021/acs.chemrev.8b00593.Electrospinning

68. Gorrasi G, Sorrentino A, Lichtfouse E (2020) Back to plastic pollution in COVID times. Environ Chem Lett 1–4 . https://doi.org/10.1007/s10311-020-01129-z. https://doi.org/10.1007/s10311-020-01129-z

69. Mueller A V., Eden MJ, Oakes JM, Bellini C, Fernandez LA (2020) Quantitative Method for Comparative Assessment of Particle Removal Efficiency of Fabric Masks as Alternatives to Standard Surgical Masks for PPE. Matter 3:950–962 . https://doi.org/10.1016/j.matt.2020.07.006

70. Fadare OO, Okoffo ED (2020) Since January 2020 Elsevier has created a COVID-19 resource centre with free information in English and Mandarin on the novel

coronavirus COVID- 19 . The COVID-19 resource centre is hosted on Elsevier Connect , the company ' s public news and information. https:// doi: 10.1016/j.scitotenv.2020.140279

71. Das O, Neisiany RE, Capezza AJ, Hedenqvist MS, Försth M, Xu Q, Jiang L, Ji D, Ramakrishna S (2020) The need for fully bio-based facemasks to counter coronavirus outbreaks: A perspective. Sci Total Environ 736: . https://doi.org/10.1016/j.scitotenv.2020.139611

72. Wang Q, Zhao X, Zhu JY (2014) Kinetics of strong acid hydrolysis of a bleached kraft pulp for producing cellulose nanocrystals (CNCs). Ind Eng Chem Res 53:11007–11014 . https://doi.org/10.1021/ie501672m

73. Ali M, Ain QT (2020) Environmental Contaminants Reviews (ECR). 3:32–36 . https://doi.org/10.26480/ecr.01.2020.32.36

74. Jing Y, Zhang L, Huang R, Bai D, Bai H, Zhang Q, Fu Q (2017) Ultrahigh-performance electrospun polylactide membranes with excellent oil/water separation ability: Via interfacial stereocomplex crystallization. J Mater Chem A 5:19729–19737 . https://doi.org/10.1039/c7ta05379g

75. Tesfaye M, Patwa R, Kommadath R, Kotecha P, Katiyar V (2016) Silk nanocrystals stabilized melt extruded poly (lactic acid) nanocomposite films: Effect of recycling on thermal degradation kinetics and optimization studies. Thermochim Acta 643:41–52 . https://doi.org/10.1016/j.tca.2016.09.008

76. Al-Harbi LM, El-Mossalamy EH, Arafa HM, Al-Owais A, Shah MA (2011) TiO2nanoparticles with tetra-pad shape prepared by an economical and safe route at very low temperature. Mod Appl Sci 5:130–135 .

https://doi.org/10.5539/mas.v5n3p130

77. Mills A, Crow M (2008) A study of factors that change the wettability of titania films. Int J Photoenergy 2008: . https://doi.org/10.1155/2008/470670

78. Dai S, Wu Y, Sakai T, Du Z, Sakai H, Abe M (2010) Preparation of highly crystalline TiO 2 nanostructures by acid-assisted hydrothermal treatment of hexagonal-structured nanocrystalline titania/cetyltrimethyammonium bromide nanoskeleton. Nanoscale Res Lett 5:1829–1835 . https://doi.org/10.1007/s11671-010-9720-0

79. Rahmat M, Ghasemi I, Karrabi M, Azizi H, Zandi M, Riahinezhad M (2015) Silane crosslinking of poly (lactic acid): The effect of simultaneous hydrolytic degradation. 9:1133–1141 . https://doi.org/10.3144/expresspolymlett.2015.101

80. Tesfaye M, Patwa R, Dhar P, Katiyar V (2017) Nanosilk-grafted poly(lactic acid) films: Influence of cross-linking on rheology and thermal stability. ACS Omega 2:7071–7084 . https://doi.org/10.1021/acsomega.7b01005

81. Patwa R, Soundararajan N, Mulchandani N, Bhasney SM, Shah M, Kumar S, Kumar A, Katiyar V (2018) Silk nano-discs : A natural material for cancer therapy a. https://doi.org/10.1002/bip.23231

82. Catauro M, Tranquillo E, Dal Poggetto G, Pasquali M, Dell'Era A, Ciprioti SV (2018) Influence of the heat treatment on the particles size and on the crystalline phase of TiO2 synthesized by the sol-gel method. Materials (Basel) 11: . https://doi.org/10.3390/ma11122364

83. Mhlanga N, Ray SS, Africa S (2014) Dioxide Nanoparticles-Containing Biodegradable Polylactide Composites Synthesized by Sol – Gel Method.

https://doi.org/10.1166/jnn.2014.8271

84. Nakayama N, Hayashi T (2007) Preparation and characterization of poly(l-lactic acid)/TiO2 nanoparticle nanocomposite films with high transparency and efficient photodegradability. Polym Degrad Stab 92:1255–1264 . https://doi.org/10.1016/j.polymdegradstab.2007.03.026

85. El-Sherbiny S, Morsy F, Samir M, Fouad OA (2014) Synthesis, characterization and application of TiO2 nanopowders as special paper coating pigment. Appl Nanosci 4:305–313 . https://doi.org/10.1007/s13204-013-0196-y

86. Morsy FA, Fouad OA (2013) Synthesis , characterization and application of TiO2 nanopowders as special paper coating pigment Synthesis , characterization and application of TiO 2 nanopowders as special paper coating pigment. https://doi.org/10.1007/s13204-013-0196-y

87. Yuan M, Chen Y, Yuan M, Li H, Xia X, Xiong C (2018) Functionalization of graphene oxide with low molecularweight poly (lactic acid). Polymers (Basel) 10:1–16 . https://doi.org/10.3390/polym10020177

88. Yuan M, Xiong C, Jiang L, Li H, Yuan M (2018) The preparation, characterization, mechanical and antibacterial properties of GO-ZnO nanocomposites with a poly(L-lactide)-modified surface. Materials (Basel) 11: . https://doi.org/10.3390/ma11020323

89. Ohgo K, Bagusat F, Asakura T, Scheler U (2008) Investigation of structural transition of regenerated silk fibroin aqueous solution by Rheo-NMR spectroscopy. J Am Chem Soc 130:4182–4186 . https://doi.org/10.1021/ja710011d

90. Gupta A, Prasad A, Mulchandani N, Shah M, Ravi Sankar M, Kumar S, Katiyar V

(2017) Multifunctional Nanohydroxyapatite-Promoted Toughened High-Molecular-Weight Stereocomplex Poly(lactic acid)-Based Bionanocomposite for Both 3D-Printed Orthopedic Implants and High-Temperature Engineering Applications. ACS Omega 2:4039–4052 . https://doi.org/10.1021/acsomega.7b00915

91. Suphankij S, Mekprasart W, Pecharapa W (2013) Photocatalytic of N-doped TiO2 nanofibers prepared by electrospinning. Energy Procedia 34:751–756 . https://doi.org/10.1016/j.egypro.2013.06.810

92. Gupta A, Katiyar V (2017) Cellulose Functionalized High Molecular Weight Stereocomplex Polylactic Acid Biocomposite Films with Improved Gas Barrier, Thermomechanical Properties. ACS Sustain Chem Eng 5:6835–6844 . https://doi.org/10.1021/acssuschemeng.7b01059

93. Dhar P, Tarafder D, Kumar A, Katiyar V (2015) Effect of cellulose nanocrystal polymorphs on mechanical, barrier and thermal properties of poly(lactic acid) based bionanocomposites. RSC Adv 5:60426–60440 . https://doi.org/10.1039/c5ra06840a

94. Monshi A, Foroughi MR, Monshi MR (2012) Modified Scherrer Equation to Estimate More Accurately Nano-Crystallite Size Using XRD. World J Nano Sci Eng 02:154–160 . https://doi.org/10.4236/wjnse.2012.23020

95. Treacy JPW, Hussain H, Torrelles X, Grinter DC, Cabailh G, Bikondoa O, Nicklin C, Selcuk S, Selloni A, Lindsay R, Thornton G (2017) Geometric structure of anatase Ti O2(101). Phys Rev B 95:1–7 . https://doi.org/10.1103/PhysRevB.95.075416

96. Hardcastle FD (2011) Raman spectroscopy of titania (TiO 2) nanotubular water-splitting catalysts. *Journal of the Arkansas academy of science*, *65*(1), 43-48.

97. Gupta KK, Mishra PK, Srivastava P, Gangwar M, Nath G, Maiti P (2013) Hydrothermal in situ preparation of TiO 2 particles onto poly(lactic acid) electrospun nanofibres. Appl Surf Sci 264:375–382 . https://doi.org/10.1016/j.apsusc.2012.10.029

98. Faungnawakij K (2019) New understanding of crystal control and facet selectivity of titanium dioxide ruling photocatalytic performance. 7: . https://doi.org/10.1039/c8ta11475g

99. Miyauchi M, Nakajima A, Watanabe T, Hashimoto K (2002) Photocatalysis and Photoinduced Hydrophilicity of Various Metal Oxide Thin Films. 2812–2816 . https://doi.org/10.1021/cm020076p

100. Yao J, Wang C (2010) Decolorization of Methylene Blue with TiO 2 Sol via UV Irradiation Photocatalytic Degradation. 2010: . https://doi.org/10.1155/2010/643182

101. Subha PP, Jayaraj MK (2015) Solar photocatalytic degradation of methyl orange dye using TiO 2 nanoparticles synthesised by sol – gel method in neutral medium. J Exp Nanosci 10:1106–1115 . https://doi.org/10.1080/17458080.2014.969338

102. Gorrasi G, Sorrentino A, Lichtfouse E (2020) Back to plastic pollution in COVID times. Environ Chem Lett 1–4 . https://doi.org/10.1007/s10311-020-01129-z

103. Zhao Y, Chen R, Ni R, Liu H, Li J, Huang C (2020) Fabrication and characterization of a novel facial mask substrates based on thermoplastic polyester elastomer fibers. J Text Inst 111:1231–1237 .

https://doi.org/10.1080/00405000.2019.1702612

104. Huang X, Jiao T, Liu Q, Zhang L, Zhou J, Li B, Peng Q (2019) Hierarchical electrospun nanofibers treated by solvent vapor annealing as air filtration mat for high-efficiency PM2.5 capture. Sci China Mater 62:423–436 . https://doi.org/10.1007/s40843-018-9320-4

105. Chellamani KP, Veerasubramanian D, Vignesh Balaji RS (2013) Surgical Face Masks: Manufacturing Methods and Classification. J Acad Ind Res 2:320

106. Jiang S, Chen Y, Duan G, Mei C, Greiner A, Agarwal S (2018) Electrospun nanofiber reinforced composites: A review. Polym Chem 9:2685–2720 . https://doi.org/10.1039/c8py00378e

107. Ullah S, Ullah A, Lee J, Jeong Y, Hashmi M, Zhu C, Joo K Il, Cha HJ, Kim IS (2020) Reusability Comparison of Melt-Blown vs Nanofiber Face Mask Filters for Use in the Coronavirus Pandemic. ACS Appl Nano Mater 3:7231–7241 . https://doi.org/10.1021/acsanm.0c01562

108. Kreiser-Saunders I, Kricheldorf HR (1998) Polylactones, 39: Zn lactate-catalyzed copolymerization of L-lactide with glycolide or ε-caprolactone. Macromol Chem Phys 199:1081–1087 . https://doi.org/10.1002/macp.1998.021990623

109. Singh CP, Vaishna RL, Kakkar A, Arunkumar KP, Nagaraju J (2014) Characterization of antiviral and antibacterial activity of Bombyx mori seroin proteins. Cell Microbiol 16:1354–1365 . https://doi.org/10.1111/cmi.12294

110. Parlin AF, Stratton SM, Culley TM, Guerra PA (2020) A laboratory-based study examining the properties of silk fabric to evaluate its potential as a protective barrier for personal protective equipment and as a functional material for face

coverings during the COVID-19 pandemic. PLoS One 15:1–19 . https://doi.org/10.1371/journal.pone.0239531

111. Zhang DS, Liu XY, Li JL, Xu HY, Lin H, Chen YY (2013) Design and fabrication of a new class of nano hybrid materials based on reactive polymeric molecular cages. Langmuir 29:11498–11505 . https://doi.org/10.1021/la4023085

112. Kalita NK, Bhasney SM, Kalamdhad A, Katiyar V (2020) Biodegradable kinetics and behavior of bio-based polyblends under simulated aerobic composting conditions. J Environ Manage 261:110211 . https://doi.org/10.1016/j.jenvman.2020.110211

113. Murariu M, Dubois P (2016) PLA composites: From production to properties. Adv Drug Deliv Rev 107:17–46 . https://doi.org/10.1016/j.addr.2016.04.003

114. Farah S, Anderson DG, Langer R (2016) Physical and mechanical properties of PLA, and their functions in widespread applications — A comprehensive review. Adv Drug Deliv Rev 107:367–392 . https://doi.org/10.1016/j.addr.2016.06.012

115. Tripathi N, Katiyar V (2016) PLA / functionalized-gum arabic based bionanocomposite films for high gas barrier applications. 43458:1–8 . https://doi.org/10.1002/app.43458

116. Buluş E, Buluş GS, Yakuphanoğlu F (2020) Production of polylactic acid-activated charcoal nanofiber membranes for COVID-19 pandemic by electrospinning technique and determination of filtration efficiency. J Mater Electron devices 4:21–26. https://orcid.org/0000-0002-2045-2499

117. Pal AK, Katiyar V (2017) Melt processing of biodegradable poly(lactic acid)/functionalized chitosan nanocomposite films: mechanical modeling with

improved oxygen barrier and thermal properties. J Polym Res 24: . https://doi.org/10.1007/s10965-017-1305-5

118. Orozco FG, Valadez-González A, Domínguez-Maldonado JA, Zuluaga F, Figueroa-Oyosa LE, Alzate-Gaviria LM (2014) Lactic acid yield using different bacterial strains, its purification, and polymerization through ring-opening reactions. Int J Polym Sci 2014: . https://doi.org/10.1155/2014/365310

119. Florczak M, Michalski A, Kacprzak A, Brzeziński M, Biedroń T, Pajak A, Kubisa P, Biela T (2016) MALDI-TOF analysis of lactide oligomers with functional end groups. React Funct Polym 104:71–77 . https://doi.org/10.1016/j.reactfunctpolym.2016.05.010

120. Qi L, Weng X, Yuan L, Wei B, Wu X, Huang G, Du X, Liu H (2020) Improved thermal expansion performance of Aluminum/polysiloxane/glass coatings with low infrared emissivity by zinc powder. Infrared Phys Technol 110:103458 . https://doi.org/10.1016/j.infrared.2020.103458

121. Pal AK, Katiyar V (2016) Nanoamphiphilic Chitosan Dispersed Poly(lactic acid) Bionanocomposite Films with Improved Thermal, Mechanical, and Gas Barrier Properties. Biomacromolecules 17:2603–2618 . https://doi.org/10.1021/acs.biomac.6b00619

122. Li M, Zhu L, Lin D (2011) Toxicity of ZnO nanoparticles to escherichia Coli: Mechanism and the influence of medium components. Environ Sci Technol 45:1977–1983 . https://doi.org/10.1021/es102624t

123. Almoudi MM, Hussein AS, Abu Hassan MI, Mohamad Zain N (2018) A systematic review on antibacterial activity of zinc against Streptococcus mutans.

Saudi Dent J 30:283–291 . https://doi.org/10.1016/j.sdentj.2018.06.003

124. Hewawaduge C, Senevirathne A, Jawalagatti V, Kim JW, Lee JH (2021) Copper-impregnated three-layer mask efficiently inactivates SARS-CoV2. Environ Res 196:110947 . https://doi.org/10.1016/j.envres.2021.110947

125. Çakir BA, Budama L, Topel Ö, Hoda N (2012) Synthesis of ZnO nanoparticles using PS-b-PAA reverse micelle cores for UV protective, self-cleaning and antibacterial textile applications. Colloids Surfaces A Physicochem Eng Asp 414:132–139 . https://doi.org/10.1016/j.colsurfa.2012.08.015

126. Gali KK, Soundararajan N, Katiyar V, Sivaprakasam S (2021) Electrospun chitosan coated polylactic acid nanofiber: A novel immobilization matrix for α – Amylase and its application in hydrolysis of cassava fibrous waste. J Mater Res Technol 13:686–699 . https://doi.org/10.1016/j.jmrt.2021.05.001

127. Dhiman G, Chakraborty JN (2015) Antimicrobial performance of cotton finished with triclosan, silver and chitosan. Fash Text 2: . https://doi.org/10.1186/s40691-015-0040-y

128. Oh JW, Chun SC, Chandrasekaran M (2019) Preparation and in vitro characterization of chitosan nanoparticles and their broad-spectrum antifungal action compared to antibacterial activities against phytopathogens of tomato. Agronomy 9: . https://doi.org/10.3390/agronomy9010021

129. Abdallah Y, Liu M, Ogunyemi SO, Ahmed T, Fouad H, Abdelazez A, Yan C, Yang Y, Chen J, Li B (2020) Bioinspired green synthesis of chitosan and zinc oxide nanoparticles with strong antibacterial activity against rice pathogen xanthomonas oryzae pv. oryzae. Molecules 25: .

https://doi.org/10.3390/molecules25204795

130. Salama, AHM ED (2018) Chitosan/Silk Fibroin/Zinc Oxide Nanocomposite as a Sustainable and Antimicrobial Biomaterial. *Cell. Chem. Technol*, *52*, 903-907.

131. Villegas-Peralta Y, López-Cervantes J, Madera Santana TJ, Sánchez-Duarte RG, Sánchez-Machado DI, Martínez-Macías M del R, Correa-Murrieta MA (2021) Impact of the molecular weight on the size of chitosan nanoparticles: characterization and its solid-state application. Polym Bull 78:813–832 . https://doi.org/10.1007/s00289-020-03139-x

132. Gupta KC, Jabrail FH (2006) Effects of degree of deacetylation and cross-linking on physical characteristics, swelling and release behavior of chitosan microspheres. Carbohydr Polym 66:43–54 . https://doi.org/10.1016/j.carbpol.2006.02.019

133. Wijesena RN, Tissera ND, De Silva KMN (2015) Coloration of cotton fibers using nano chitosan. Carbohydr Polym 134:182–189 . https://doi.org/10.1016/j.carbpol.2015.07.088

134. Souza VGL, Pires JRA, Rodrigues C, Rodrigues PF, Lopes A, Silva RJ, Caldeira J, Duarte MP, Fernandes FB, Coelhoso IM, Fernando AL (2019) Physical and morphological characterization of chitosan/montmorillonite films incorporated with ginger essential oil. Coatings 9:1–20 . https://doi.org/10.3390/coatings9110700

135. Tawfik TM, El-Masry AMA (2021) Preparation of chitosan nanoparticles and its utilization as novel powerful enhancer for both dyeing properties and antimicrobial activity of cotton fabrics. Biointerface Res Appl Chem 11:13652–13666 . https://doi.org/10.33263/BRIAC115.1365213666

136. Idumah CI (2021) Influence of nanotechnology in polymeric textiles, applications, and fight against COVID-19. The Journal of the Textile Institute, 112(12), 2056-2076. https://doi.org/10.1080/00405000.2020.1858600

137. Behzadinasab S, Chin A, Hosseini M, Poon L, Ducker WA (2020) A Surface Coating that Rapidly Inactivates SARS-CoV-2. ACS Appl Mater Interfaces 12:34723–34727 . https://doi.org/10.1021/acsami.0c11425

138. Hosseini M, Chin AWH, Behzadinasab S, Poon LLM, Ducker WA (2021) Cupric Oxide Coating That Rapidly Reduces Infection by SARS-CoV-2 via Solids. ACS Appl Mater Interfaces. https://doi.org/10.1021/acsami.0c19465

139. Bar G, Biswas D, Pati S, Chaudhary K, Bar M (2021) Antiviral finishing on textiles - An overview. Text Leather Rev 4:5–22 . https://doi.org/10.31881/TLR.2020.17

140. Faten F, Rania Ibrahim S (2018) Comparing Surface Chemical Modifications of Zinc Oxide Nanoparticles for Modulating their Antiviral Activity against Herpes Simplex Virus Type-1. Int J Nanoparticles Nanotechnol 4: . https://doi.org/10.35840/2631-5084/5521

141. Otsuki K, Ito T, Murase T, Ito H, Wakabayashi K, Yakura M,Yamana H (2009). U.S. Patent Application No. 10/567,968.

142. Loutfy SA, Elberry MH, Farroh KY, Mohamed HT, Mohamed AA, Mohamed EB, Faraag AHI, Mousa SA (2020) Antiviral activity of chitosan nanoparticles encapsulating curcumin against hepatitis C virus genotype 4a in human hepatoma cell lines. Int J Nanomedicine 15:2699–2715 . https://doi.org/10.2147/IJN.S241702

143. Duan Y, Chen X, Shao ZZ (2018) The Silk Textile Embedded in Silk Fibroin

Composite: Preparation and Properties. Chinese J Polym Sci (English Ed 36:1043–1046 . https://doi.org/10.1007/s10118-018-2117-8

144. Augustine R, Hasan A (2020) Emerging applications of biocompatible phytosynthesized metal/metal oxide nanoparticles in healthcare. J Drug Deliv Sci Technol 56:101516 . https://doi.org/10.1016/j.jddst.2020.101516

145. Suryani SEI, Sa'Adah U, Amini WNL, Suprayogi T, Mustikasari AA, Taufiq A, Sunaryono, Diantoro M, Nur H (2018) Effect of ZnO and Annealing on the Hydrophobic Performance of x(ZnO)-CA-PLA. J Phys Conf Ser 1093: . https://doi.org/10.1088/1742-6596/1093/1/012003

146. Murariu M, Doumbia A, Bonnaud L, Dechief AL, Paint Y, Ferreira M, Campagne C, Devaux E, Dubois P (2011) High-performance polylactide/ZnO nanocomposites designed for films and fibers with special end-use properties. Biomacromolecules 12:1762–1771 . https://doi.org/10.1021/bm2001445

147. Papageorgiou GZ, Achilias DS, Nanaki S, Beslikas T, Bikiaris D (2010) PLA nanocomposites: Effect of filler type on non-isothermal crystallization. Thermochim Acta 511:129–139 . https://doi.org/10.1016/j.tca.2010.08.004

148. Bussiere PO, Therias S, Gardette JL, Murariu M, Dubois P, Baba M (2012) Effect of ZnO nanofillers treated with triethoxy caprylylsilane on the isothermal and non-isothermal crystallization of poly(lactic acid). Phys Chem Chem Phys 14:12301–12308 . https://doi.org/10.1039/c2cp41574g

149. Nam JY, Sinha Ray S, Okamoto M (2003) Crystallization behavior and morphology of biodegradable polylactide/layered silicate nanocomposite. Macromolecules 36:7126–7131 . https://doi.org/10.1021/ma034623j

150. Zou H, Wu S, Shen J (2008) Polymer/silica nanocomposites: preparation, characterization, properties, and applications. Chemical reviews, 108(9), 3893-3957. https://doi.org/10.1021/cr068035q

151. Ding C, Guo Y, Liu J, Kent GB, Jobson BT, Fu X, Yang X, Zhong WH (2020) A Super-breathable “woven-like” Protein Nanofabric. ACS Appl Bio Mater 3:2958–2964 . https://doi.org/10.1021/acsabm.0c00008

152. Zhang R, Lan W, Ji T, Sameen DE, Ahmed S, Qin W, Liu Y (2021) Development of polylactic acid/ZnO composite membranes prepared by ultrasonication and electrospinning for food packaging. Lwt 135:110072 . https://doi.org/10.1016/j.lwt.2020.110072

153. Patwa R, Singh M, Kumar A, Katiyar V (2018) Kinetic modelling of thermal degradation and non-isothermal crystallization of silk nano-discs reinforced poly (lactic acid) bionanocomposites. Springer Berlin Heidelberg. https://doi.org/10.1007/s00289-018-2434-7

154. Rinawa K, Maiti SN, Sonnier R, Cuesta JL (2015) Non-isothermal crystallization kinetics and thermal behaviour of PA12 / SEBS- g -MA blends. 38:1315–1327

155. Zhang L, Dong H, Li M, Wang D, Liu M, Wang C, Fu S (2020) Synthesis and characterization of carbon black modified by polylactic acid (PLA-g-CB) as pigment for dope dyeing of black PLA fibers. J Appl Polym Sci 137:1–9 . https://doi.org/10.1002/app.48784

156. Varol N, Monnier X, Delbreilh L, Saiter A, Fatyeyeva K, Dargent E (2020) Highlight of primary and secondary relaxations in amorphous stereocomplex polylactides. Express Polym Lett 14:48–62 .

https://doi.org/10.3144/expresspolymlett.2020.5

157. Zhang J, Sato H, Tsuji H, Noda I, Ozaki Y (2005) Infrared spectroscopic study of CH 3···O=C interaction during poly(L-lactide)/Poly(D-lactide) stereocomplex formation. Macromolecules 38:1822–1828 . https://doi.org/10.1021/ma047872w

158. Shao J, Xiang S, Bian X, Sun J, Li G, Chen X (2015) Remarkable melting behavior of PLA stereocomplex in linear PLLA/PDLA blends. Ind Eng Chem Res 54:2246–2253 . https://doi.org/10.1021/ie504484b

159. Hirata J, Kurokawa N, Okano M, Hotta A, Watanabe S (2020) Evaluation of Crystallinity and Hydrogen Bond Formation in Stereocomplex Poly(lactic acid) Films by Terahertz Time-Domain Spectroscopy. Macromolecules 53:7171–7177 . https://doi.org/10.1021/acs.macromol.0c00237

160. Tsuji H, Yamamoto S (2011) Enhanced stereocomplex crystallization of biodegradable enantiomeric poly(lactic acid)s by repeated casting. Macromol Mater Eng 296:583–589 . https://doi.org/10.1002/mame.201000397

161. Alghoraibi I, Alomari S (2019) Handbook of Nanofibers

162. Sadegh H, Ali GAM, Gupta VK, Makhlouf ASH, Shahryari-ghoshekandi R, Nadagouda MN, Sillanpää M, Megiel E (2017) The role of nanomaterials as effective adsorbents and their applications in wastewater treatment. J Nanostructure Chem 7:1–14 . https://doi.org/10.1007/s40097-017-0219-4

163. Mei L, Ren Y, Gu Y, Li X, Wang C, Du Y, Fan R, Gao X, Chen H, Tong A, Zhou L, Guo G (2018) Strengthened and Thermally Resistant Poly(lactic acid)-Based Composite Nanofibers Prepared via Easy Stereocomplexation with Antibacterial Effects. ACS Appl Mater Interfaces 10:42992–43002 .

https://doi.org/10.1021/acsami.8b14841

164. Wang S, Zhu ZH, Coomes A, Haghseresht F, Lu GQ (2005) The physical and surface chemical characteristics of activated carbons and the adsorption of methylene blue from wastewater. J Colloid Interface Sci 284:440–446 . https://doi.org/10.1016/j.jcis.2004.10.050

165. Zhong Y, Li T, Lin H, Zhang L, Xiong Z, Fang Q, Zhang G, Liu F (2018) Meso-/macro-porous microspheres confining Au nanoparticles based on PDLA/PLLA stereo-complex membrane for continuous flowing catalysis and separation. Chem Eng J 344:299–310 . https://doi.org/10.1016/j.cej.2018.03.080

166. Lv R, Peng N, Jin T, Na B, Wang J, Liu H (2017) Stereocomplex mesophase and its phase transition in enantiomeric polylactides. Polymer (Guildf) 116:324–330 . https://doi.org/10.1016/j.polymer.2017.04.004

167. Naga N, Yoshida Y, Noguchi K (2019) Crystallization of poly(L-lactic acid)/poly(D-lactic acid) blend induced by organic solvents. Polym Bull 76:3677–3691 . https://doi.org/10.1007/s00289-018-2563-z

168. Wojtczak E, Biedroń T, Bednarek M (2019) Hydrolytic stability of polylactide stereocomplex microparticles containing metal ions. Polym Bull 76:1135–1149 . https://doi.org/10.1007/s00289-018-2432-9

169. Srisuwan Y, Baimark Y (2018) Controlling stereocomplexation, heat resistance and mechanical properties of stereocomplex polylactide films by using mixtures of low and high molecular weight poly(D-lactide)s. E-Polymers 18:485–490 . https://doi.org/10.1515/epoly-2018-0115

170. Zhang ZM, Gan ZQ, Bao RY, Ke K, Liu ZY, Yang MB, Yang W (2020) Green

and robust superhydrophilic electrospun stereocomplex polylactide membranes: Multifunctional oil/water separation and self-cleaning. J Memb Sci 593:117420 . https://doi.org/10.1016/j.memsci.2019.117420

171. Castilhos S, de Souza FM, Colpini LMS, de Mattos Jorge LM, dos Santos OAA (2020) Assessment comparison of commercial TiO2 and TiO2 sol-gel on the degradation of caffeine using artificial radiation. Environ Sci Pollut Res 27:22155–22168 . https://doi.org/10.1007/s11356-020-07748-x

172. Haque FZ, Nandanwar R, Singh P (2017) Evaluating photodegradation properties of anatase and rutile TiO2 nanoparticles for organic compounds. Optik (Stuttg) 128:191–200 . https://doi.org/10.1016/j.ijleo.2016.10.025

173. Soltani N, Saion E, Hussein MZ, Erfani M, Abedini A, Bahmanrokh G, Navasery M, Vaziri P (2012) Visible light-induced degradation of methylene blue in the presence of photocatalytic ZnS and CdS nanoparticles. Int J Mol Sci 13:12242–12258 . https://doi.org/10.3390/ijms131012242

174. Araújo ES, Libardi J, Faia PM, De Oliveira HP (2015) Hybrid ZnO/TiOLoaded in Electrospun Polymeric Fibers as Photocatalyst. J Chem 2015: . https://doi.org/10.1155/2015/476472

175. Luo F, Fortenberry A, Ren J, Qiang Z (2020) Recent Progress in Enhancing Poly(Lactic Acid) Stereocomplex Formation for Material Property Improvement. Front Chem 8:1–8 . https://doi.org/10.3389/fchem.2020.00688

176. Thamer BM, Aldalbahi A, Meera Moydeen A, Rahaman M, El-Newehy MH (2021) Modified electrospun polymeric nanofibers and their nanocomposites as nanoadsorbents for toxic dye removal from contaminated waters: A review.

Polymers (Basel) 23:1–37 . https://doi.org/10.3390/polym13010020

177. Jem KJ, Tan B (2020) The development and challenges of poly (lactic acid) and poly (glycolic acid). Adv Ind Eng Polym Res 3:60–70 . https://doi.org/10.1016/j.aiepr.2020.01.002

178. Ajioka M, Enomoto K, Suzuki K, Yamaguchi A (1995) The basic properties of poly(lactic acid) produced by the direct condensation polymerization of lactic acid. J Environ Polym Degrad 3:225–234 . https://doi.org/10.1007/BF02068677

179. Yu TL, Wu CC, Chen CC, Huang BH, Wu J, Lin CC (2005) Catalysts for the ring-opening polymerization of ε-caprolactone and L-lactide and the mechanistic study. Polymer (Guildf) 46:5909–5917 . https://doi.org/10.1016/j.polymer.2005.04.079

180. Bhagabati P, Hazarika D, Katiyar V (2019) Tailor-made ultra-crystalline, high molecular weight poly(ε-caprolactone) films with improved oxygen gas barrier and optical properties: a facile and scalable approach. Int J Biol Macromol 124:1040–1052 . https://doi.org/10.1016/j.ijbiomac.2018.11.199

181. Pandey AK (2014) Ring opening polymerization of lactide by using zinc prolinate catalyst. Adv Mater Lett 5:44–51 . https://doi.org/10.5185/amlett.2013.6493

182. Balla E, Daniilidis V, Karlioti G, Kalamas T, Stefanidou M, Bikiaris ND, Vlachopoulos A, Koumentakou I, Bikiaris DN (2021) Poly(lactic acid): A versatile biobased polymer for the future with multifunctional properties-from monomer synthesis, polymerization techniques and molecular weight increase to PLA applications. Polymers (Basel) 13: . https://doi.org/10.3390/polym13111822

183. Upare PP, Hwang YK, Chang JS, Hwang DW (2012) Synthesis of lactide from alkyl lactate via a prepolymer route. Ind Eng Chem Res 51:4837–4842 .

https://doi.org/10.1021/ie202714n

184. Song X, Bian Z, Hui Y, Wang H, Liu F, Yu S (2019) Zn-Acetate-Containing ionic liquid as highly active catalyst for fast and mild methanolysis of Poly(lactic acid). Polym Degrad Stab 168:108937 . https://doi.org/10.1016/j.polymdegradstab.2019.108937

185. Bhagabati P, Hazarika D, Katiyar V (2019) Tailor-made ultra-crystalline, high molecular weight poly (ε-caprolactone) films with improved oxygen gas barrier and optical properties: a facile and scalable approach. *International journal of biological macromolecules*,124, 1040-1052.

186. Payne J, McKeown P, Mahon MF, Emanuelsson EAC, Jones MD (2020) Mono- and dimeric zinc(II) complexes for PLA production and degradation into methyl lactate-a chemical recycling method. Polym Chem 11:2381–2389 . https://doi.org/10.1039/d0py00192a

187. Araújo A, Oliveira M, Oliveira R, Botelho G, Machado A V. (2014) Biodegradation assessment of PLA and its nanocomposites. Environ Sci Pollut Res 21:9477–9486 . https://doi.org/10.1007/s11356-013-2256-y